MECHANOBIOLOGY: EMERGING TOOLS AND METHODS

EDITED BY: Sara Baratchi, Khashayar Khoshmanesh, Charles David Cox and Guillermo Alberto Gomez

PUBLISHED IN: Frontiers in Bioengineering and Biotechnology

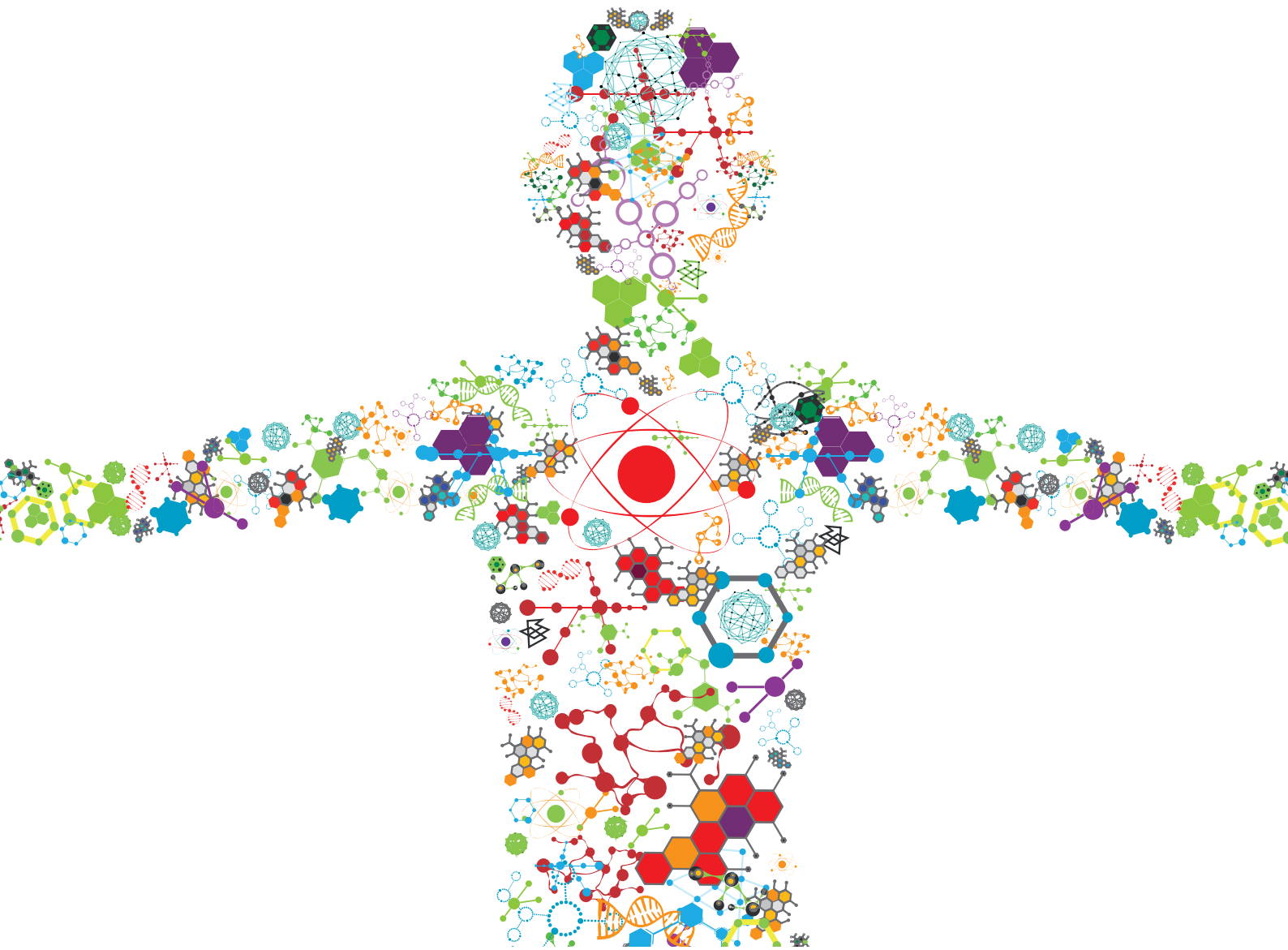

frontiers Research Topics

frontiers

ISSN 1664-8714
ISBN 978-2-88963-755-3
DOI 10.3389/978-2-88963-755-3

About Frontiers

Frontiers is more than just an open-access publisher of scholarly articles: it is a pioneering approach to the world of academia, radically improving the way scholarly research is managed. The grand vision of Frontiers is a world where all people have an equal opportunity to seek, share and generate knowledge. Frontiers provides immediate and permanent online open access to all its publications, but this alone is not enough to realize our grand goals.

Frontiers Journal Series

The Frontiers Journal Series is a multi-tier and interdisciplinary set of open-access, online journals, promising a paradigm shift from the current review, selection and dissemination processes in academic publishing. All Frontiers journals are driven by researchers for researchers; therefore, they constitute a service to the scholarly community. At the same time, the Frontiers Journal Series operates on a revolutionary invention, the tiered publishing system, initially addressing specific communities of scholars, and gradually climbing up to broader public understanding, thus serving the interests of the lay society, too.

Dedication to Quality

Each Frontiers article is a landmark of the highest quality, thanks to genuinely collaborative interactions between authors and review editors, who include some of the world's best academicians. Research must be certified by peers before entering a stream of knowledge that may eventually reach the public - and shape society; therefore, Frontiers only applies the most rigorous and unbiased reviews.
Frontiers revolutionizes research publishing by freely delivering the most outstanding research, evaluated with no bias from both the academic and social point of view. By applying the most advanced information technologies, Frontiers is catapulting scholarly publishing into a new generation.

What are Frontiers Research Topics?

Frontiers Research Topics are very popular trademarks of the Frontiers Journals Series: they are collections of at least ten articles, all centered on a particular subject. With their unique mix of varied contributions from Original Research to Review Articles, Frontiers Research Topics unify the most influential researchers, the latest key findings and historical advances in a hot research area! Find out more on how to host your own Frontiers Research Topic or contribute to one as an author by contacting the Frontiers Editorial Office: researchtopics@frontiersin.org

MECHANOBIOLOGY: EMERGING TOOLS AND METHODS

Topic Editors:
Sara Baratchi, RMIT University, Australia
Khashayar Khoshmanesh, RMIT University, Australia
Charles David Cox, Victor Chang Cardiac Research Institute, Australia
Guillermo Alberto Gomez, University of South Australia, Australia

Citation: Baratchi, S., Khoshmanesh, K., Cox, C. D., Gomez, G. A., eds. (2020). Mechanobiology: Emerging Tools and Methods. Lausanne: Frontiers Media SA. doi: 10.3389/978-2-88963-755-3

Table of Contents

frontiers in Bioengineering and Biotechnology

EDITORIAL
published: 09 April 2020
doi: 10.3389/fbioe.2020.00289

Editorial: Mechanobiology: Emerging Tools and Methods

Sara Baratchi[1]*, *Khashayar Khoshmanesh*[2], *Charles David Cox*[3] and *Guillermo Alberto Gomez*[4]

[1] School of Health and Biomedical Sciences, RMIT University, Bundoora, VIC, Australia, [2] School of Engineering, RMIT University, Melbourne, VIC, Australia, [3] Molecular Cardiology and Biophysics Division, Victor Chang Cardiac Research Institute, Sydney, NSW, Australia, [4] Centre for Cancer Biology, University of South Australia and SA Pathology, Adelaide, SA, Australia

Keywords: modeling, mechanobiology, molecular/cellular biology, biomaterials, bioengineering, micro/nanotechnologies

Editorial on the Research Topic

Mechanobiology: Emerging Tools and Methods

The effect of mechanical forces on tissue development was proposed more than one hundred years ago (Wolff, 1892; E. W. M, 1896; Thompson, 1992). During recent decades, with the advancement of tools and methods that allow us to mimic and measure mechanical forces, we have begun to understand how cells and tissues sense and respond to their physical surroundings. This understanding will provide fundamental knowledge on the role of mechanobiology in health and disease and new perspectives for the development of future therapies for their treatment.

Particularly, biomechanical forces play a crucial role in the development of different pathologies, as changes in physical forces of blood flow, shear stress, and pressure, play a significant role in the development of cardiovascular diseases (Baratchi et al., 2017). Likewise, tissue stiffness and solid stress as a result of abnormal tumor growth and resistance from the surrounding tissues affect tumor growth, metastasis, and treatment (Kalli and Stylianopoulos, 2018).

Mechanosensation and mechanotransduction are also key in the development and normal physiology (García-Añoveros and Corey, 1997; Lewin and Moshourab, 2004; Marshall and Lumpkin, 2012). For example, evolutionarily effective limb moment relies on limb biomechanics as well as mechanosensory feedback (Aiello et al., 2017), the sense of touch (Lumpkin et al., 2010) and ability to feel pain relies on the detection of mechanical stimuli by sensory neurons (Lewin and Moshourab, 2004) and cell fate, proliferation, differentiation, and death all rely on cell mechanics (Keller, 2012).

Therefore, we aimed this Research Topic to provide to the scientific community an overview of different techniques that have been developed to study the effect of mechanical forces on cells and tissues and provide an insight into different methods that have been developed to measure forces at the cellular and subcellular level.

The original research articles of this issue report the effect of aging on the viscosity of tendons fascicles and fibers (Karathanasopoulos and Ganghoffer) uniaxial dynamic loading on cultured microtissues (van Kelle et al.) and cyclic compressive stress on epithelial cells (Ho et al.). Method papers published in this issue include a novel microfluidic channel with integrated ridges to investigate the effect of disturbed flow on endothelial cells (Tovar-Lopez et al.) and a detailed protocol to adopt the Doppler echocardiography platform to analyse cardiac function (Benslimane et al.). Furthermore, Sianati et al. describes a protocol for investigating the response of mechanosensitive ion channels using pillar arrays and whole-cell patch-clamp techniques, and (Kriesi et al.) provides a technology report on an integrated flow chamber for *in vitro* quantification of mechanical stress using live-cell microscopy.

OPEN ACCESS

Edited and reviewed by:
Stefan Scheiner,
Vienna University of Technology, Austria

***Correspondence:**
Sara Baratchi
sara.baratchi@rmit.edu.au

Specialty section:
This article was submitted to Biomechanics, a section of the journal Frontiers in Bioengineering and Biotechnology

Received: *06 September 2019*
Accepted: *19 March 2020*
Published: *09 April 2020*

Citation:
Baratchi S, Khoshmanesh K, Cox CD and Gomez GA (2020) Editorial: Mechanobiology: Emerging Tools and Methods. Front. Bioeng. Biotechnol. 8:289. doi: 10.3389/fbioe.2020.00289

In addition, this issue hosts comprehensive review articles on *in vitro* platforms to study the mechanobiology of cardiomyocytes (Chin et al.) and stretch technologies to investigate the mechanotransduction of cells in the cardiovascular system (Friedrich et al.). Furthermore, it features a comprehensive review of computation and experimental approaches to study abdominal aortic aneurysms (Salman et al.) and methods to investigate outside-in and inside-out mechanotransduction (Mohammed et al.).

Collectively, these articles provide a broad overview of different tools and methods that can be used to apply and study mechanical forces at cell and tissue levels, yet this is not a exhaustive list. The editors hope that the articles compiled in this issue will be worthwhile for researchers in the field of mechanobiology and that they will contribute to the advancement of knowledge.

Lastly, we would like to thank the efforts of all authors, co-authors, reviewers, and the Frontiers in Bioengineering and Biotechnology team who made this collection possible.

AUTHOR CONTRIBUTIONS

All authors listed have made a substantial, direct and intellectual contribution to the work, and approved it for publication.

ACKNOWLEDGMENTS

SB was supported by the Australian Research Council (DE170100239 and DP200101248).

REFERENCES

Aiello, B. R., Westneat, M. W., and Hale, M. E. (2017). Mechanosensation is evolutionarily tuned to locomotor mechanics. *Proc. Natl. Acad. Sci. U.S.A.* 114, 4459–4464. doi: 10.1073/pnas.1616839114

Baratchi, S., Khoshmanesh, K., Woodman, O. L., Potocnik, S., Peter, K., and McIntyre, P. (2017). Molecular sensors of blood flow in endothelial cells. *Trends Mol. Med.* 23, 850–868. doi: 10.1016/j.molmed.2017.07.007

E. W. M (1896). Gesammelte abhandlungen über entwicklungsmechanik der organismen. *Nature* 54, 217–219.

García-Añoveros, J., and Corey, D. P. (1997). The molecules of mechanotransduction. *Annu. Rev. Neurosci.* 20, 567–594.

Kalli, M., and Stylianopoulos, T. (2018). Defining the role of solid stress and matrix stiffness in cancer cell proliferation and metastasis. *Front. Oncol.* 8:55. doi: 10.3389/fonc.2018.00055

Keller, R. (2012). Developmental biology. Physical biology returns to morphogenesis. *Science* 338, 201–203. doi: 10.1126/science.1230718

Lewin, G. R., and Moshourab, R. (2004). Mechanosensation and pain. *J. Neurobiol.* 61, 30–44. doi: 10.1002/neu.20078

Lumpkin, E. A., Marshall, K. L., and Nelson, A. M. (2010). The cell biology of touch. *J. Cell Biol.*191, 237–248. doi: 10.1083/jcb.201006074

Marshall, K. L., and Lumpkin, E. A. (2012). The molecular basis of mechanosensory transduction. *Adv. Exp. Med. Biol.* 739, 142–155. doi: 10.1007/978-1-4614-1704-0_9

Thompson, D. A. W. (1992). *On Growth and Form*. Cambridge: Cambridge University Press.

Wolff, J. (1892). *Das Gesetz der Transformation der Knochen*. Berlin: Hirschwald.

Conflict of Interest: The authors declare that the research was conducted in the absence of any commercial or financial relationships that could be construed as a potential conflict of interest.

frontiers in Bioengineering and Biotechnology

ORIGINAL RESEARCH
published: 16 October 2018
doi: 10.3389/fbioe.2018.00148

Advanced Microfluidic Device Designed for Cyclic Compression of Single Adherent Cells

Kenneth K. Y. Ho[1†], *Ying Lin Wang*[1†], *Jing Wu*[1,2] *and Allen P. Liu*[1,3,4,5*]

[1] Department of Mechanical Engineering, University of Michigan, Ann Arbor, MI, United States, [2] Department of Mechanical Engineering, University of Hong Kong, Hong Kong, China, [3] Department of Biomedical Engineering, University of Michigan, Ann Arbor, MI, United States, [4] Cellular and Molecular Biology Program, University of Michigan, Ann Arbor, MI, United States, [5] Biophysics Program, University of Michigan, Ann Arbor, MI, United States

Cells in our body experience different types of stress including compression, tension, and shear. It has been shown that some cells experience permanent plastic deformation after a mechanical tensile load was removed. However, it was unclear whether cells are plastically deformed after repetitive compressive loading and unloading. There have been few tools available to exert cyclic compression at the single cell level. To address technical challenges found in a previous microfluidic compression device, we developed a new single-cell microfluidic compression device that combines an elastomeric membrane block geometry to ensure a flat contact surface and microcontact printing to confine cell spreading within cell trapping chambers. The design of the block geometry inside the compression chamber was optimized by using computational simulations. Additionally, we have implemented step-wise pneumatically controlled cell trapping to allow more compression chambers to be incorporated while minimizing mechanical perturbation on trapped cells. Using breast epithelial MCF10A cells stably expressing a fluorescent actin marker, we successfully demonstrated the new device design by separately trapping single cells in different chambers, confining cell spreading on microcontact printed islands, and applying cyclic planar compression onto single cells. We found that there is no permanent deformation after a 0.5 Hz cyclic compressive load for 6 min was removed. Overall, the development of the single-cell compression microfluidic device opens up new opportunities in mechanobiology and cell mechanics studies.

Keywords: microfluidics, cell mechanics, mechanobiology, compression, single-cell analysis, microcontact printing

OPEN ACCESS

Edited by:
Guillermo Alberto Gomez, University of South Australia, Australia

Reviewed by:
Maurizio Ventre, Università degli Studi di Napoli Federico II, Italy
Huseyin Cagatay Yalcin, Qatar University, Qatar

***Correspondence:**
Allen P. Liu
allenliu@umich.edu

†Present Address:
Kenneth K. Y. Ho, Biocrede, Plymouth, MI, United States
Ying Lin Wang, Trust Bio-sonics, Hsinchu, Taiwan

Specialty section:
This article was submitted to Biomechanics, a section of the journal Frontiers in Bioengineering and Biotechnology

Received: *26 June 2018*
Accepted: *26 September 2018*
Published: *16 October 2018*

Citation:
Ho KKY, Wang YL, Wu J and Liu AP (2018) Advanced Microfluidic Device Designed for Cyclic Compression of Single Adherent Cells. Front. Bioeng. Biotechnol. 6:148. doi: 10.3389/fbioe.2018.00148

INTRODUCTION

Cells and tissues in our body experience various kinds of chemical and mechanical signals in physiological and pathological conditions. Due to the complex environment and multiple interactions with neighboring cells, cells experience different combinations of compressive, tensile and shear stresses in different directions. Most living cells exhibit viscoelastic deformation under mechanical stress (Fabry et al., 2001). When the mechanical load is removed, the cell usually recovers partially to its original undeformed shape. The incomplete shape recovery is mainly due to the rupture of bonds within the cytoskeleton when the cells experience tensile stress, leading to the observed plasticity (Bausch et al., 2001; Bonakdar et al., 2016). Repetitive tensile loading and

unloading was found to result in an increase in residual deformation, which was suggested to be an adaptive process for cells to protect themselves against mechanical damage (Bonakdar et al., 2016). However, little is known how cells respond to repetitive compressive loading and unloading.

The study of cellular responses to compression, tension and shear has a long history, particularly in musculoskeletal (Grodzinsky et al., 2000) and vascular (Shyy and Chien, 2002; Gupta and Grande-Allen, 2006) tissues. In many cases, bioengineering tools have played a central role in deciphering mechanotransduction pathways (Polacheck et al., 2013; Liu et al., 2017). However, there is a growing interest in studying the response of cells from compressive stress in other physiological environments, for example during development (Mammoto and Ingber, 2010) and in cancer (Jain et al., 2014; Ricca et al., 2018). Mechanical forces, such as compression generated by living cells are crucial for the control of embryonic development. Solid stress is developed in tumor microenvironment because uncontrolled proliferation of cancer cells leads to an increase in compressive stress. Dense extracellular matrix and endothelial barriers also present physiological scenarios where cells experience significant compression (Reymond et al., 2013). Several recent studies have utilized microfabricated channels with narrow constriction that lead to compression as cells migrate in these microchannels (Denais et al., 2016; Raab et al., 2016; Heureaux et al., 2018). Different structures inside the cells, such as actin cortex beneath the plasma membrane, vertical actin fibers connecting the apical and basal surfaces of the cells and the mechanical stiffness of the nucleus, are responsible for withstanding planar compressive deformation. Thus, cells with different stiffnesses, particularly between healthy and diseased cells, may respond differently to compression. Despite a general understanding, how cells withstand and respond to planar compression is not as well-understood compared to cellular responses to tension or shear. The development of a microengineering device that applies uniform and well-controlled compression will aid the investigation of how cells recover after compression.

Different experimental techniques were developed to apply compression on cells (Van Vliet et al., 2003). Modified atomic force microscopy (AFM) probes was developed to apply compressive forces to single cells (Lulevich et al., 2006, 2010; Rosenbluth et al., 2006; Weafer et al., 2013). While AFM is a powerful approach to apply compressive forces and measure deformation of cells, this sophisticated method has a low throughput (e.g., one cell at a time) and requires expensive equipment and technical expertise. Microfluidics holds great promise as a next generation tool for mechanically perturbing single cells (Liu, 2016). With the integration of microsized and fast-operating valves in the microfluidic system, several microfluidic platforms have been developed for studying biological responses of cells under a compressive stress (Kim et al., 2007; Hosmane et al., 2011; Si et al., 2015). These microengineering devices allow the application of compression to cells.

Our lab previously developed a microfluidic aspiration and compression device and demonstrated compression of double emulsion droplets (Ho et al., 2016). However, there were two critical challenges that prevented the use of the same device for single-cell compression. First, the concave deflection profile of the polydimethylsiloxane (PDMS) membrane does not provide a controlled contact area between the membrane and the cells (**Figure S1A**), thus affecting the forces applied to each cell. Second, despite the high cell trapping efficiency, cells randomly spread inside the microfluidic device and were rarely directly underneath the deflection membrane for compression (**Figure S1B**).

To overcome the first challenge of the concave PDMS membrane deflection profile, we spatially varied bending rigidity across the membrane by increasing the thickness of the membrane in the middle. This was accomplished by including a block of PDMS in the middle of the membrane. In this case, the membrane in the middle has a higher resistance to deform comparing to the membrane at the side. This creates a flat deflection profile in the middle of the membrane, while having a concave deflection profile on the side. To control where cells spread within the compression chambers, we implemented microcontact printing of fibronectin islands that are positioned directly underneath the deflection membrane. In this work, we describe our effort in developing a microfluidic device for single-cell static and cyclic compression. We will first describe the design process and experimental validation of the block in the PDMS membrane. Then, we explain our newly designed two-step, pneumatically controlled cell trapping to further facilitate trapping. With the fabrication process flow, we demonstrated the alignment of the microcontact printed fibronectin island to control the cell spreading location. Finally, we showed the device capability to apply cyclic compression on cells and found that there is no permanent change in the height of the breast epithelial MCF-10A cells after cyclic compression.

MATERIALS AND METHODS

Device Overview and Design

The microfluidic device, made out of PDMS, is specifically designed for single-cell compression. The microfluidic device is designed to trap single cells in different chambers, confine cell spreading on microcontact printed islands, and apply planar compression onto the cells. The device consists of two layers, the flow layer (magenta) and the control layer (blue and orange) (**Figure 1A**), similar to the previously designed microfluidic device in our group (Ho et al., 2016). The flow layer has a comparable design, where fluid and cells flow from two inlets through the microfluidic channel to one outlet. An extra inlet was added to reduce the possibility of air bubble injection during addition of cell suspension and cell culture medium. In our current implementation, the device has four columns each containing 9 compression chambers. The compression chamber provides a shear-free space for cells to spread and be compressed. Each compression chamber is connected to the opposing end of the main microfluidic channel through a small microchannel (**Figure 1B**). The dimensions of microfluidic channel are designed so that the flow resistance of the main microfluidic channel is 20 times smaller than that of the small microchannel. This allows the majority of fluid to flow into the

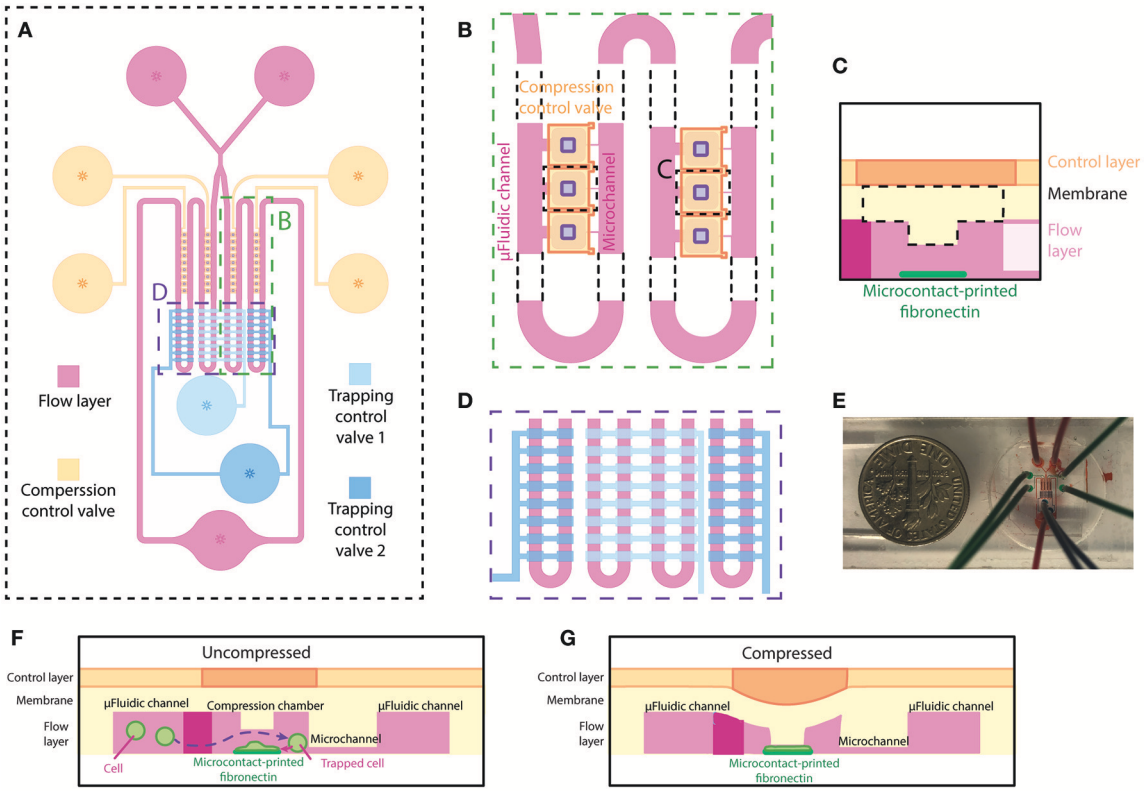

FIGURE 1 | Overview and design of the microfluidic device for single-cell compression. **(A)** The top view of overall design of the device. The flow layer is labeled in magenta, and the control layer consists of trapping control valves (blue) and compression control valve (orange). **(B)** The zoomed-in top view of the compression chamber (marked in A) and the meandering microfluidic channel in the device. The orange compression control valve is on top of the compression chamber in the flow layer. The purple rectangles are the designed block attached to the deflection membrane for compression. **(C)** Side view schematic of the compression chamber. A rectangular block and fibronectin island are unique features of this device. **(D)** The zoomed-in top view of the main meandering microfluidic channel (marked in A) and trapping control valve (blue). The inside two columns and outside two columns are controlled separately by two different trapping control valves. **(E)** A picture of the device. **(F,G)** Side view schematics of the device when the compression control valve is uncompressed **(F)** or compressed **(G)** on a cell spread on the fibronectin island.

main microfluidic channel and that less pressure is applied to the cells when they are trapped inside the compression chamber. A thin PDMS membrane separates the microfluidic channel (flow layer) and the control layer. The center of the membrane inside the compression chamber is designed to be thicker by adding a rectangular block underneath the membrane for applying planar compression (**Figure 1C**). Fibronectin is microcontact-printed underneath the block so that the cell spreads in the middle of the compression chamber (**Figure 1C**). Two pneumatically controlled valve sets, trapping control valve (light and dark blue) and compression control valve (orange), are located above the main microfluidic channel and above the compression chambers, respectively. These two sets of microfluidic control valves contained two and four independent inlets, respectively. Each controlled valve set is independently controlled using a pressure regulation setup (with an electro-regulator, Proportion-Air, QBX and a pressure regulator, Norgren R07-200-RGEA) to direct flow to the compression chambers or to compress cells. Two trapping control valves feature rectangular patterns across the main microfluidic channels for controlling cell capture (**Figure 1D**). The main microfluidic channels with trapping control valves are shown in **Figure 1E** in different color dyes. Compression control valve features rectangular patterns directly above each compression chamber for compressing cell (**Figures 1F,G**).

Imaging

A spinning disk confocal microscope (Olympus IX73 with Yokogawa CSU-X1) or an epi-fluorescence microscope (Nikon, Ti Eclipse) were used for brightfield and fluorescence imaging. The spinning disk confocal microscope has an Andor IXON DU897 EMCCD camera and the epifluorescence microscope has a Hamamatsu Flash 4 cMOS camera.

For measuring cell size and height, z-stack fluorescence confocal images were acquired using the spinning disk confocal microscope and the images were reconstructed in ImageJ to generate side view images of the cells.

Preparation of Cell Lines

Non-tumorigenic breast epithelial cell MCF-10A cells were cultured in growth media DMEM premixed 1:1 with Ham's F12 nutrient mixture with 5% horse serum, 1% pen-strep, 2.5 μg/ml

amphotericin B (fungizone), 5 μg/ml gentamycin, 10 μg/ml insulin, 0.5 μg/ml hydrocortisone, 0.02 μg/ml epidermal growth factor, and 0.1 μg/ml cholera toxin at 5% CO_2 and 37°C until about 70% confluency. 5 μg/ml Hoechst dye in PBS was used to label the nucleus. Stable cell lines expressing eGFP and Lifeact-RFP were generated *via* lentiviral transduction for labeling the cell volume and filamentous actin, respectively. Cells were resuspended at 10^6 cells/ml in the growth media to minimize cell clumping and possible pressure fluctuation during the experiment due to clumped cells blocking up small channels.

Membrane Deflection Simulation

Membrane deflection in the compression chamber of the microfluidic device was simulated using COMSOL 4.4 (COMSOL Multiphysics). The simplified three-dimensional model of the membrane and block was constructed in COMSOL and was simulated using the solid mechanics module. PDMS was modeled as a linear elastic material with elastic modulus of 0.3 MPa, a Poisson's ratio of 0.49 and a density of 970 kg/m^3. A uniform pressure of 10 psi was applied as boundary load on top of the membrane, while the four sides of the membrane were fixed.

The three-dimensional model of the complete device model was constructed in Solidworks. The deflection of the membrane and the block was simulated using COMSOL 4.4 with the same simulation module, material properties, and pressure applied as in the membrane deflection simulation.

Device Fabrication–PDMS Casting

The microfluidic device was fabricated using multilayer soft lithography technique (Xia and Whitesides, 1998). The SU-8 patterning of the four silicon molds were described in the **Supplementary Material**. The microfluidic device is composed of a PDMS control layer, a PDMS flow layer and a fibronectin printed, PDMS-coated glass coverslip, which were sequentially aligned and bonded permanently together. Schematic of the fabrication process flow of the microfluidic device is illustrated in **Figure S2**.

Before PDMS casting or spin-coating onto the silicon molds, all four wafers were first oxygen plasma-treated and then silanized with trichloro(1H,1H,2H,2H-perfluorooctyl)silane (Sigma-Aldrich) in a desiccator for 2 h or overnight. The silicon mold for the control layer was casted with PDMS (Sylgard-184) with a mixing ratio of 7:1 (base:curing agent), while both the silicon mold for the bottom alignment layer and the microcontact printing layer were casted with PDMS with a mixing ratio of 10:1. After degassing in a desiccator, the control layer, bottom alignment layer and microcontact printing layer PDMS substrate were then cured at 60°C overnight before demolding from the wafer. The control layer PDMS substrate was then diced and holes were punched with 1 mm diameter at the inlets of the microfluidic control valves, while the bottom alignment layer and microcontact printing layer PDMS substrates were also diced. The flow channel membrane was generated by spin-coating PDMS with a mixing ratio of 20:1 (base:curing agent) on the flow layer silicon mold at rotational speeds 1,200 rpm for 60 s. After this, the PDMS flow layer membrane was cured at 60°C for 2 h. The membrane thickness was measured using a stylus profilometer (Dektak 6M). Both the diced PDMS control substrate and the PDMS flow layer membrane on the silicon mold were placed in an oxygen plasma etcher (Femto, Covance) to render the PDMS surfaces hydrophilic for the preparation of bonding procedure described as follows. The flow layer silicon mold containing the PDMS membrane was mounted on a customized alignment platform on an optical microscope. The diced PDMS control layer substrate was then carefully aligned and bonded with the PDMS flow layer membrane. Permanent bonding between the control layer substrate and PDMS flow layer membrane was achieved by heating in the oven at 60°C overnight with the aid of gentle pressing between the two substrates.

The day after, the bonded control layer substrate with the flow layer membrane was then cut out and peeled off from the flow layer silicon wafer. Inlet and outlet holes (1 mm diameter) for the main microfluidic flow channel were punched through the layer PDMS control/flow substrate. The bottom alignment substrate which had the similar channel of flow layer was used to align the fibronectin with flow layer. First, PDMS microcontact printed substrate (see *Microcontact Printing* section) was aligned with the bottom alignment substrate to print the fibronectin on a PDMS-coated glass coverslip. Then the PDMS microcontact printed substrate was removed. Immediately after, the PDMS control/flow substrate was placed in an oxygen plasma etcher to render the PDMS surface hydrophilic before aligning with the bottom alignment substrate and permanently bonding to the fibronectin-printed glass coverslip. The device was kept in 4°C until use.

Microcontact Printing

To confine single MCF-10A cells, we used circular micropatterns with 16 μm diameter (area of 800 μm^2). 40 μg/ml fibronectin in PBS was incubated on the PDMS stamp for 1–2 h to coat fibronectin on its surface. Then, the PDMS stamp was dried with an air gun. A PDMS-coated coverslip was oxidized by UV-ozone. The bottom alignment substrate would be placed under a PDMS-coated coverslip and aligned with a fibronectin-coated PDMS stamp. The fibronectin is printed onto the PDMS-coated coverslip when the pattern comes into conformal contact with it. We used a mixture of fibrinogen conjugated with Alexa Fluor 647 (Thermo Fisher Scientific, F35200) and fibronectin in a ratio of 1:10 and checked the positions of fibronectin island by fluorescence imaging under a spinning disk confocal microscope. The fibronectin-printed surface was washed with 0.1% (w/v) Pluronic F127 solution for 1 h to passivate the remaining surface and then washed with PBS for 1 h.

Imaging Membrane Deflection and 3D Image Reconstruction

A dilute solution of rhodamine succinimidyl dye (Fisher scientific, 50-851-056) was perfused into the device in order to characterize membrane deflection as a function of applied pressure. The dye solution was imaged using spinning disk confocal microscopy at 20× magnification. The control layer inlets (compression control valve) of the microfluidic device

was connected to the pressure regulation setup. The membranes above the chambers were deflected by changing the air pressure in the compression control valve between 0 and 30 psi. A z-series of fluorescence images, excited at 561 nm, was captured at a step size of 500 nm and was reconstructed in ImageJ to generate 3D and side view images.

Visualization of Flow Streamlines

1 μm Y (yellow)-G (green) fluorescent beads (Invitrogen; 1:1,000 dilution in DI water) were introduced into the device at a flow rate of 1 μl/min and were imaged at 500 ms exposure to observe the flow streamlines. The PDMS microfluidic device was perfused with DI water first to eliminate any trapped air bubbles before use. Fluorescence images were captured using an epi-fluorescence microscope.

Two-Step, Pneumatically Controlled Cell Trapping

The PDMS microfluidic device was perfused with warm medium before MCF-10A cells at a concentration of 10^6 cells/ml were introduced into device at 0.5–1 μl/min for trapping single cells. To trap cells in the trapping chambers, trapping control valve 1 was pressurized at 20–30 psi to block the first column of the main microfluidic channel, which increased the flow resistance. This led to a change in the flow profile to direct the flow to the compression chambers of the first column, thereby trapping cells. After cells were trapped in the first column, trapping control valve 1 was set back to 0 psi immediately, while trapping control valve 2 was pressurized at 20–30 psi to block the second column of the main microfluidic channel. After cells were trapped in the second column, trapping control valve 2 was set back to 0 psi immediately.

Cell Seeding and Compression

After the cells were trapped, heights of the inlet and outlet tubings were adjusted to direct the cells to the middle of each compression chamber by hydrostatic pressure-induced flow. Then all the inlet and outlet tubings were clamped to stop the flow. The device was placed in an incubator for 4 h to allow cell attachment and spreading on the fibronectin-patterned surface. The pressure regulation setup was controlled by a computer program to modulate the pressure. Pressure from 0 to 15 psi was applied to the compression control valve that deflected the membrane for cell compression. Each pressure was maintained for 3 min and z-series of fluorescence images were acquired at excitations of 488, 561, and 405 nm with 500 ms exposure time, at a step size of 500 nm.

Imaging Cyclic Membrane Deflection

The cyclic membrane deflection was imaged in a similar way as described above. The fluorescence images of the rhodamine succinimidyl dye and the brightfield images of the block in the membrane were captured using spinning disk confocal microscopy at 20× magnification. The microscope was set to image at a time interval of 0.3 s. The compression control valve inlets were connected to the pressure regulation setup with an alternation of pressure between 0 and 10 psi at 0.25 and 0.5 Hz. The timelapse images were reconstructed into a real time video using ImageJ. The fluorescence intensity at the middle of the compression chamber was measured using ImageJ.

Cyclic Compression on Live Cells

Cyclic compression was applied on cells with the pressure of the compression control valve alternating between 10 and 15 psi at 0.5 Hz for 6 min . The cell height before compression and 6 min after cyclic compression were measured using the reconstructed side view images from the z-stack images.

RESULTS AND DISCUSSION

Optimization of Compression Chamber Design

To design the compression chamber for applying uniform compression on cells (e.g., MCF-10A cells), we sought to optimize four different geometric parameters of the compression chamber by using simulation. The membrane and the block in the compression chamber can be characterized by block width, compression chamber width (w), block thickness (h_b) and membrane thickness (h_m) (**Figure 2A**). In order to design a device that is suited for compressing MCF-10A cells, we first measured MCF-10A cell size and height in suspension and attached on a substrate (**Figures S3A,B**). The size and height of free or attached MCF-10A cells provide a guidance for determining the geometric parameters of the device. Attached MCF-10A cells spread over 20–40 μm lengthwise. Therefore, the block width was set at 40 μm to ensure that the cells are spread underneath the block even there is some misalignment of the microcontact printed surface during device fabrication. MCF-10A cells in suspension have an average height of 18.8 μm, while attached MCF-10A cells have an average height of 14.1 μm (**Figure S3C**). The separation between the block and the bottom cell attachment surface was set to be around 20–25 μm to accommodate for the size of MCF-10A in suspension. While the height of attached MCF-10A cells is around 14 μm, we desired the optimal membrane deflection to be around 10–15 μm when a pressure of 10 psi is applied, yielding a cell compression of 4 μm for an average cell.

To optimize the other three design parameters for compression, we performed solid mechanics simulation of a simplified membrane and block model using COMSOL (see Methods for detail). PDMS membrane was modeled as a linearly elastic material. It was shown previously that PDMS with base and curing agent ratio of 20:1 is linearly elastic even under large deformation (Li et al., 2016). The block displacements were determined for 27 conditions where we permutated the values of the three variables (**Figure 2B**). Based on the simulation results, the compression chamber width and membrane thickness were set as 80 and 30 μm, respectively to achieve a membrane deflection of around 10–15 μm. For the block thickness, we plotted the displacement of the membrane and block with respect to the horizontal position across the compression chamber (**Figure 2C**). We can readily see that the original concave deflection profile (black line, 0 μm) became flat when

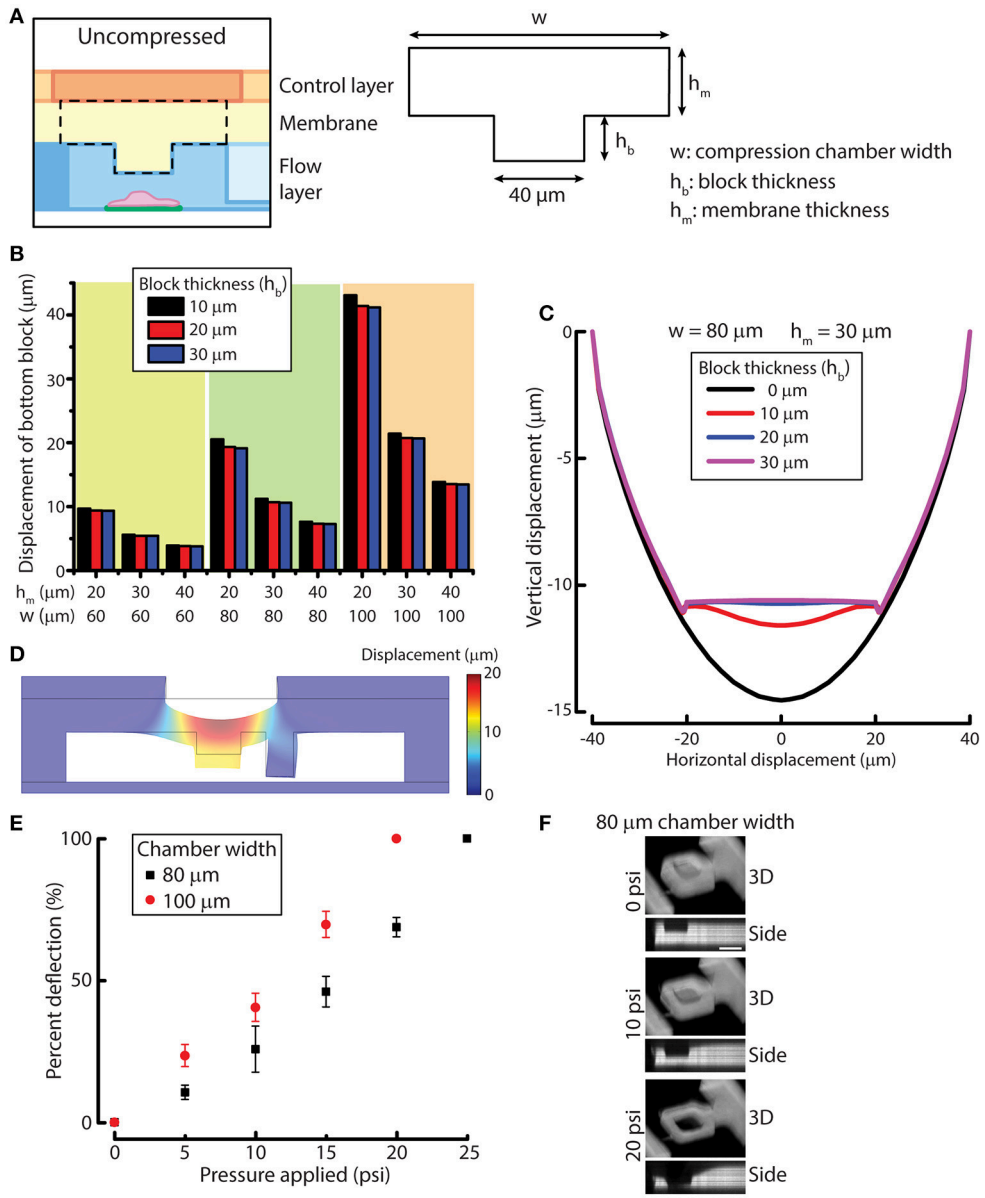

FIGURE 2 | Simulation and experimental results for designing and verifying the PDMS membrane block design of the device for cell compression. **(A)** A simplified model of membrane and block for simulation. Three geometric parameters were defined: compression chamber width (w), block thickness (h_b) and membrane thickness (h_m). **(B)** Displacement of the simplified membrane and block model at different values of geometric parameters. **(C)** Vertical displacement of the membrane and block at different horizontal positions across the compression chamber with different block thicknesses. **(D)** Displacement of the simulated result for the complete device model. **(E)** Membrane deflection of different compression chamber widths as a function of applied pressure. $n = 3$ for each chamber width. Error bar denotes the standard error of mean. **(F)** Reconstructed 3D and side view images of 80 μm chamber width at different compression control valve pressures. Scale bar = 40 μm.

the block thickness was increased to 20 μm (blue line) or higher. Therefore, the block thickness was set at 20 μm.

After the block width, compression chamber width, block thickness and membrane thickness were set at 40, 80, 20, and 30 μm, respectively, we performed simulation of the complete device model to evaluate if the deformation of membrane behaves as we expect. At a pressure of 10 psi, the membrane and block deflected between 12 and 13 μm across the block as designed (**Figure 2D**), suggesting that the simulated results of the simplified membrane and block model can be used to provide design guidelines for fabricating the microfluidic device.

We next examined membrane deflections as a function of different applied pressures, using the optimized parameters determined from our simulation studies. As a comparison, we also fabricated a device with a compression chamber width of 100 μm (instead of 80 μm) while keep all the

other parameters the same. The microfluidic channel volume was labeled with rhodamine succinimidyl dye since the PDMS membrane cannot directly be labeled easily. When compression control valve was pressurized, the membrane deflected and displaced the fluid in the compression chamber so that we could indirectly visualize membrane deflection. The 3D and side view images of the compressed compression chamber showed the increase in membrane deflection with increasing compression chamber widths (**Figure 2E**), where the deflection was greater in 100 μm chamber than in 80 μm chamber, as expected. The thickness of the PDMS membrane spun-coated on the flow layer at 1,200 rpm was 36.1 ± 3.0 μm, which was slightly thicker than the designed membrane thickness of 30 μm. Therefore, membrane deflection in the 80 μm chamber, 6.2 μm at 10 psi, was smaller than designed. However, membrane deflection at 15 psi reached 11.0 μm, fulfilling the design requirement. More importantly, when the membrane deflected, the bottom of the block remained flat while the side membrane is concave (**Figure 2F**), demonstrating the block design was effective at providing a uniform compression.

Two-Step, Pneumatically Controlled Cell Trapping

Due to the increased number of trapping chambers compared with a previous design (Lee et al., 2016), the pressure difference between different chambers of each column will become larger and might affect the trapping efficiency or result large pressure applied to trapped cells. To increase the chances of a trapped cell landing on the fibronectin-printed island, we included more compression chambers in the present design by including two more columns of trapping chambers. To accommodate the new design, the trapping control valve is separated into two individually controlled sets: one controlling the first column (trapping control valve 1) and the other one controlling the second column (trapping control valve 2) of the main microfluidic channel (**Figure 1D**).

Since the microfluidic device is symmetric we consider one side in our analysis for simplicity. The trapping control valve 1 controls the first column of the main microfluidic channel, while the trapping control valve 2 controls the second column of the main microfluidic channel. In theory, the main microfluidic channel can meander into n columns and the trapping control valve can be separated into n individually controlled sets, with each set controlling each column of the main microfluidic channel, where n is larger than 1. In the following, we will describe volume flow rate as Q, fluid flow resistance as R and pressure difference as ΔP. The subscripts under Q, R, and ΔP denote the path in which $2i-1$ refer to the main microfluidic channel and $2i$ refer to the small microchannel of the i-th column, where $i = 1, 2, 3, \ldots, n$ (**Figure 3A**).

When all n control sets are not actuated, the main microfluidic channel will have a 20-times smaller resistance than the small microchannel connecting the compression chamber and the main microfluidic channel on the other side. By the least flow resistance theory, the volume flow rate through the main microfluidic channel Q_{2i-1} will be higher than the volume flow rate through the small microchannels Q_{2i} in the i-th column, respectively (**Figure 3A**). Therefore, the volume flow rate ratios Q_{2i-1}/Q_{2i} should exceed 1.

If all n columns of main microfluidic channel are controlled by a single valve, the increase in fluid flow resistance of the main microfluidic channel will lead to a reduction of the volume flow rate ratios Q_{2i-1}/Q_{2i} of each column at the same time. Since cell loading occurs sequentially, while waiting for cells to be trapped in the $(i+1)$-th column of chambers, high fluid flow resistance in the k-th column (k is a number less than i) of the main microfluidic channel R_{2k-1} will result in a high pressure difference across two sides of the small microchannels in the k-th column ΔP_{2k-1}, hence a high aspiration pressure on trapped cells in the k-th column, where $k = 1, 2, \ldots, i$ and $i = 1, 2, \ldots, n-1$ (**Figure 3B**). This might result a difference in mechanical perturbation to difference cells between compressing them.

We next consider a scenario where the n control sets are separately controlled. When only the i-th control set is actuated to block the i-th column of the main microfluidic channel, only volume flow rate ratio Q_{2i-1}/Q_{2i} will reduce and only cells in the i-th column of chambers will be trapped. After one cell is trapped in each chamber of the i-th column, the i-th control set is turned to OFF and only then is the $(i+1)$-th control set turned to ON. In this case, only volume flow rate ratio Q_{2i+1}/Q_{2i+2} will reduce and cells will be trapped in the $(i+1)$-th column of chambers. Thus, ΔP_{2k-1} can be kept as minimum, since R_{2k-1} and Q_{2k-1} are both small, where $k = 1, 2, \ldots, i$ and $i = 1, 2, \ldots, n-1$ (**Figure 3C**). With the n control sets are separately controlled, trapped cells experience less mechanical perturbation while other cells are being trapped.

Before demonstrating the two-step, pneumatically controlled cell trapping, we first examined the trapping efficiency of the device when the trapping control valve was pressurized. We imaged the flow streamline inside the main microfluidic channel and the compression chamber by following the trajectories of small fluorescent beads. With increasing pressure applied in the trapping control valve, the fluid flow resistance in the main microfluidic channel increased. By the least flow resistance theory, more fluid was directed into the compression chamber and passed through the small microchannel, as shown in **Figure 4A**.

Next, we separately control the trapping control valves, by applying 30 psi to the trapping control valve 1 and 2 separately, to achieve the two-step pneumatically controlled cell trapping (**Figure 4B**). When only trapping control valve 1 was actuated, cells became trapped in the compression chamber in the first column (**Figure 4C**, middle). After that, trapping control valve 1 was turned to OFF and trapping control valve 2 was actuated, which facilitated cell trapping in the second column (**Figure 4C**, right). This control sequence demonstrated the two-step, pneumatically controlled cell trapping and a similar design strategy can be applied for a larger number of columns (i.e., increasing the number of cell trapping steps) while minimizing aspiration to the already trapped cells.

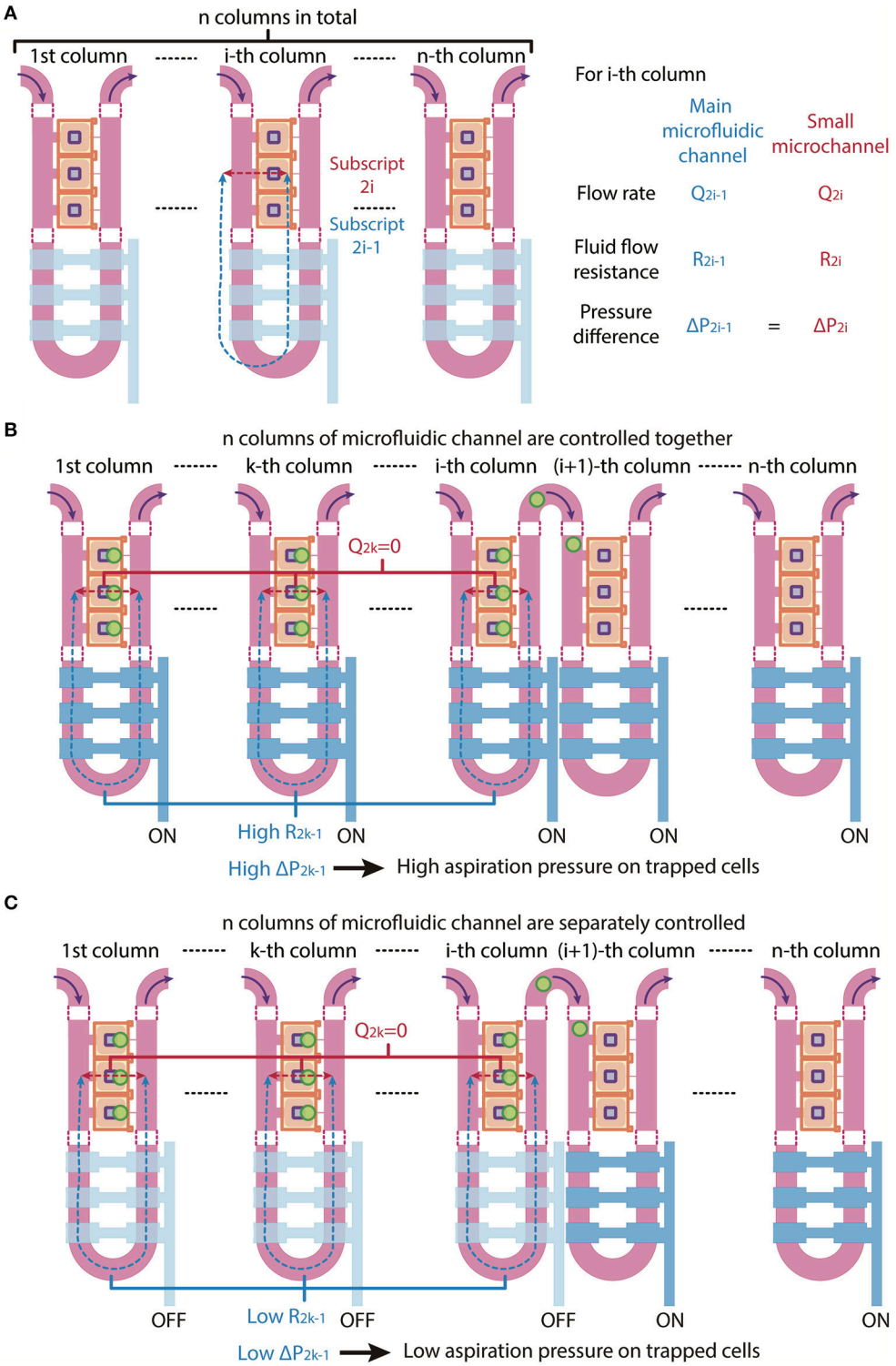

FIGURE 3 | Schematic of multi-column, separately-controlled cell trapping. **(A)** A schematic of a microfluidic channel with *n* individually controlled columns. Each column consists of two channels, so subscripts 2*i* and 2*i*-1 (with $i = 1,2,3,\ldots, n$) address individual channels. Pressures (*P*), flow rates (Q), and resistances (*R*) of the main microfluidic channel and the small microchannel were denoted in blue and red and are shown in the figure as blue and red dotted lines, respectively. **(B,C)** A schematic of the same microfluidic channel when the *n* columns of microfluidic channel are **(B)** controlled altogether (i.e., all values are *ON*) or **(C)** separately controlled (i.e., valves 1 to *i* are *OFF* and valves $i + 1$ to *n* are *ON*). The consequential changes in fluid flow resistance and pressure difference across cells are shown.

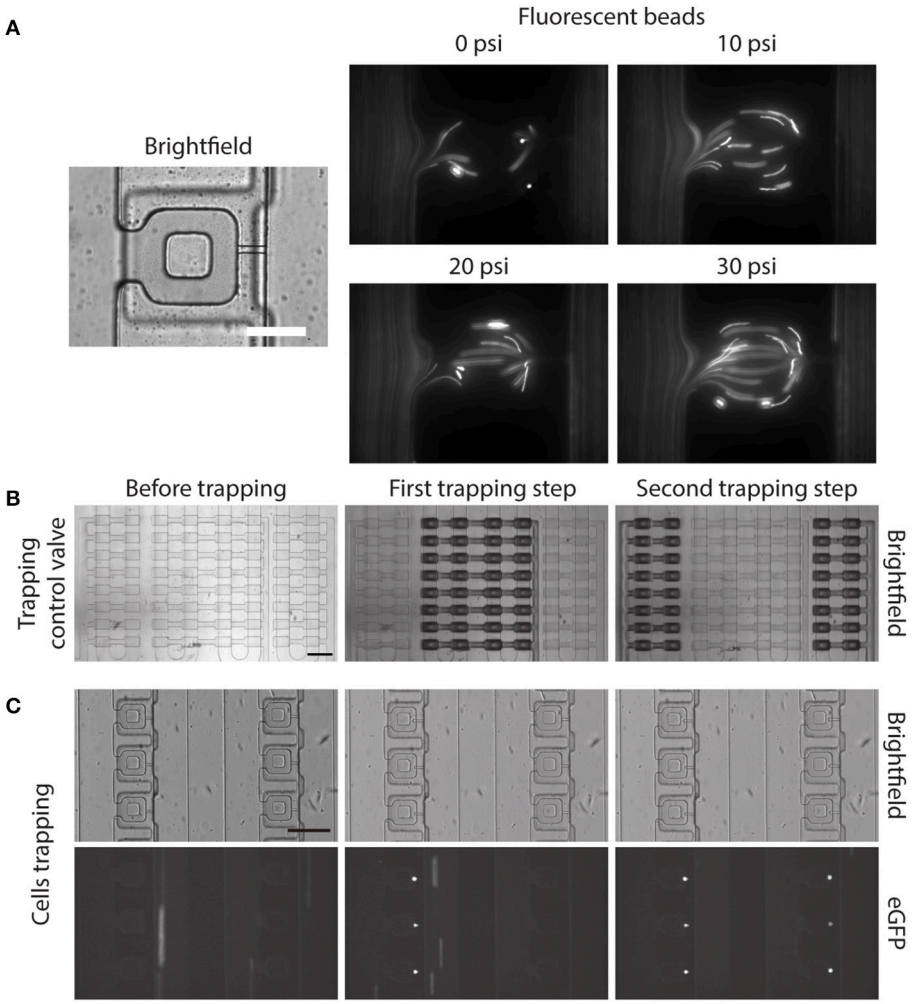

FIGURE 4 | Two-step, pneumatically controlled cell trapping. **(A)** Brightfield image of the compression chamber and fluorescence images of the 1 μm Y (yellow)-G (green) fluorescent beads when the trapping control valve was pressurized at different pressures. Scale bar = 60 μm. **(B,C)** Brightfield images of the compression chamber **(B)** and fluorescence images of the trapped eGFP expressing MCF-10A cells **(C)** when the trapping control valve was changed from before trapping (**C**, left) to after first trapping step (**C**, middle) and second trapping step (**C**, right). Scale bar = 200 μm.

Alignment of Fibronectin Island With Compression Block

The alignment of microcontact printed fibronectin islands with the compression block within the compression chamber is very important, as the cells need to be positioned beneath the compression block for uniform compression. Since our customized alignment platform does not support fluorescence imaging, the alignment between microcontact printed fibronectin islands and the compression chambers was achieved *via* a two-step alignment process by using a reference bottom alignment layer (detail described in the Methods section). The procedure was effective and fluorescent fibronectin colocalized well with the compression block in a fully assembled device (**Figure 5A**).

Following the alignment of the microcontact printed fibronectin to the compression chamber, we verified that the fabrication steps and cell trapping methods did not affect cell spreading on the fibronectin islands. MCF-10A stably expressing Lifeact-RFP was introduced to the compression device and found spread on fibronectin islands (**Figure 5B**). Since two different alignment steps and human eyes were involved in assembling the device, misalignment happens and the microcontact printed island does not always align in the center (**Figure 5B**). The PDMS block was designed to be larger than the microcontact printed island (40 μm comparing to 16 μm). It was designed to remain flat when the membrane deflects, and we further verified that in simulation and experiment (**Figures 2C,D,F**). Therefore, small misalignment was allowed. As long as the cell is adhered underneath the block, it will be compressed as desired. This demonstrated that the device is suitable for single-cell capture and subsequent compression.

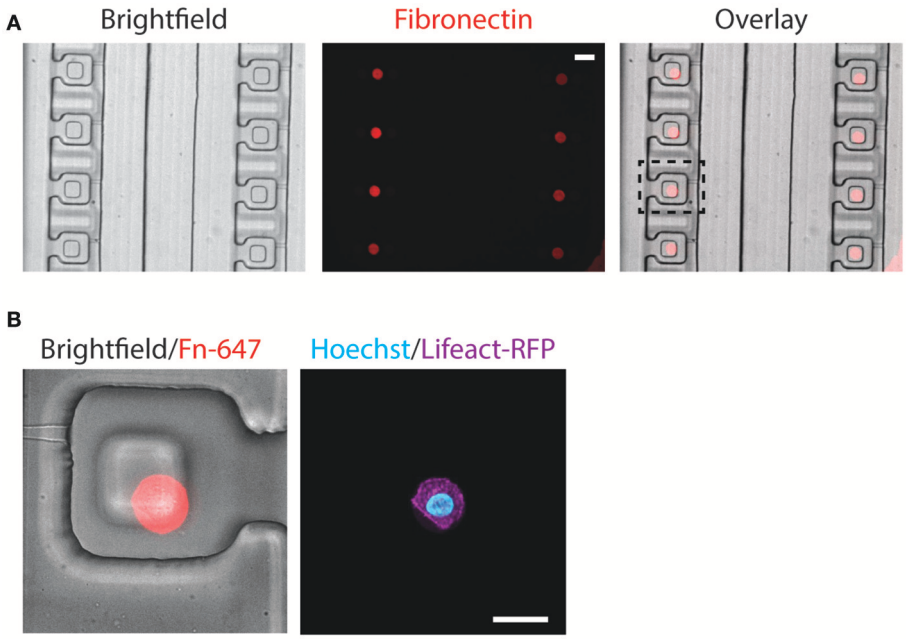

FIGURE 5 | Alignment of microcontact-printed fibronectin for the attachment and compression of cells. **(A)** Brightfield and fluorescence images of the device and fibronectin, respectively. Scale bar = 50 μm. **(B)** Zoomed-in brightfield and fluorescence image of the device and fibronectin, respectively (left). Fluorescence image of the MCF-10A cell, labeling the DNA (cyan) and actin (magenta) (right). Scale bar = 20 μm.

Despite cells can spread well on microcontact printing islands, and our cell trapping efficiency is nearly 100%, we typically do not find too many cells on fibronectin islands within a fully assembled device. We attribute this low efficiency to the fact that cells that entered the trapping chamber needed to land on the fibronectin island by chance. When moving the device back to the incubator after cell trapping, cells may escape from the trapping chamber. We typically found one out of four trapped cells successfully spread on the microcontact printing islands. Even though this is not ideal, having a large number of trapping chambers helped increase the chance of having cells positioned on microcontact printed islands within the trapping chambers.

Live Cell Cyclic Compression

The new microfluidic device was designed to apply uniform compression on cells by increasing the air pressure applied to the compression control valve. This allows the cell to be compressed by the deflection of the PDMS membrane. As the pressure of the compression control valve increases, the PDMS membrane first deflected and touched the top of the cell. Then, the cell was compressed at 10 psi slightly and further compressed at 15 psi, as shown in the reconstructed side view images of the MCF-10A cell at different applied pressures (**Figure 6A**). This demonstrated the ability of the device to control different extent of compression on cells. The compression of cells was determined by the PDMS block pressing down on top of the cells. Therefore, due to the differences in cell height between different cells, the compressive strain that is applied to each cell will be different (may range from 0.2 to 0.8). However, all cells will have the same deformed height which is determined by the pressured applied to the compression control valve. Hence, this device will control for the same deformed height among a group of cells with different initial heights.

When the pressure in the compression control valve is alternating between high and low values, the cell can experience repetitive compression and relaxation cycle. We demonstrated that the PDMS membrane can alternate between deflected and relaxed states at different frequencies (**Figure 6B**). With a fluorescent dye perfused into the microfluidic device, the deflection of the membrane can be visualized. When the membrane is deflected, the fluorescence intensity in the middle of the compression chamber will reduce because the deflected PDMS block displaces the fluorescent dye. The fluorescence intensity at the middle of the compression chamber cycled between low and high intensities at a frequency of pressure application to the compression control valve (**Figures 6B,C**).

The mechanical behavior of living cells depends on the organization and dynamics of the cytoskeleton. The tensegrity model of living cells prescribes an interconnected network of actin filaments and microtubules that stabilizes prestress and bear compression (Wang et al., 2001). Mechanical behaviors of cells have also been compared to colloidal glass transition, in which osmotically compressed cells become stiffer and have slow intracellular relaxation (Zhou et al., 2009). In this model, the cytoskeleton is thought to have an independent and additive contribution to the stiffness changes of a cell. As a proof-of-demonstration experiment of our new compression device, we carried out cyclic compression between 10 and 15 psi on MCF-10A cells. Following 6 min of cyclic compression at 0.5 Hz, we found no statistically significant difference in cell height

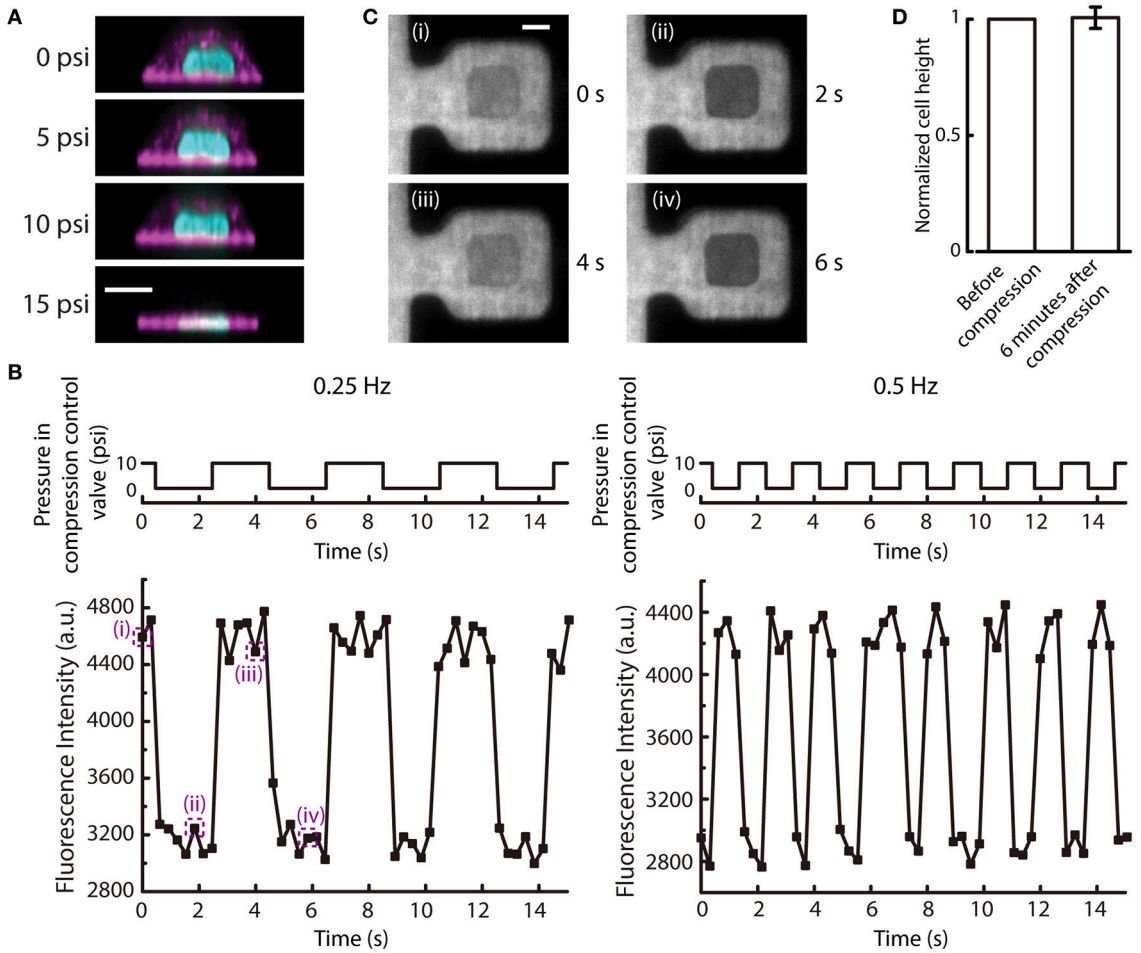

FIGURE 6 | Cyclic deflection of the membrane and compression of cells. **(A)** Reconstructed side view images of a MCF-10A cell at different applied pressures to compression control valve. Cyan: DNA; Magenta: actin. Scale bar = 10 μm. **(B)** (Top) The applied cyclic pressure in the compression control valve over time at 0.25 Hz (left) and 0.5 Hz (right). (Bottom) The measured fluorescence intensity of the rhodamine succinimidyl dye at the middle of the compression chamber over time when the compression control valves were pressurized at the corresponding frequencies. **(C)** Fluorescence images of the compression chamber at different time points, as indicated in **(B)**. Scale bar = 20 μm. **(D)** The normalized cell height before and 6 min after 6-min cyclic compression alternating between 10 and 15 psi at 0.5 Hz ($n = 6$). Error bar denotes the standard error of mean. No statistical significance by *t*-test.

compared to before compression (**Figure 6D**), suggesting that MCF-10A cells do not experience permanent change in cell height after of cyclic compression under this condition. This result is different from the previous findings that showed cells have plastic response when a cyclic load was removed (Bonakdar et al., 2016). Since the cytoskeleton in a cell is anisotropic, with cytoskeletal filaments organized in different directions (Hu et al., 2003), cyclic loading will stretch and compress cytoskeletal fibers. When a cyclic mechanical loading is applied, tensed regions will undergo plastic deformation due to rupture of bonds, while compressed regions will not recover completely due to the inability to generate sufficient restoring forces after most of the elastic stresses have been evaded through buckling of cytoskeletal fibers (Bonakdar et al., 2016). The difference between our findings could be due to a number of reasons. First, in our device, the cells were seeded on fibronectin printed islands, which could impair the assembly of actin cytoskeleton. However, we have imaged the actin structures inside the cells when they were seeded on the fibronectin printed islands before and after being compressed. Actin stress fibers were found to form at the adhered surface (**Figure S4**). Second, in the Bonakdar et al. study, force was applied to a magnetic bead in both push and pull directions, rather than planar compression over a large cell area as in our case. Further, the magnetic tweezer approach was operated in a constant force mode, thus allowing the observation of increased residual deformation with increasing force cycle numbers. Our microfluidic compression device provides a distance clamp (assuming the cell does not provide a strong resistance force against the deflection membrane). When MCF-10A cells experienced cyclic planar compression, the height of the cells recovered fully. Here, we did not have high vertical resolution and temporal resolution in imaging and it was thus

difficult to determine the rate of viscoelastic relaxation. We also did not have a large number of samples. This was mainly limited by the low seeding efficiency and long 3D image acquisition time of a single cell, reducing the number of cells that can be compressed and imaged at the same time. As a proof-of-concept device, one can imagine expanding the number of trapping structures to compensate for the low seeding efficiency (trapping efficiency is 100%) in the future. More detailed investigation of cytoskeleton responses during and after cyclic compression would also be an interesting future direction.

Finally, it is worth noting that there are analogous studies with cell stretching. Static cell stretching has been shown to reinforce focal adhesions at short time scale as well as delay focal adhesion disassembly at long time scale (Chen et al., 2013; Shao et al., 2013). Interestingly, the delayed response depends on the orientation of cell stretching (Chen et al., 2013). Cyclic stretching, on the other hand, elicits cell reorientation to a uniform angle that is driven by minimizing the cells' elastic energy (Livne et al., 2014). Cellular response to static or cyclic compression may also elicit different responses, and these remain to be thoroughly investigated.

CONCLUSION

In this work, we developed a valve-based microfluidic device for applying compression on single adherent cells. The microfluidic device was engineered with PDMS block in the membrane to ensure optimal compression on cells and microcontact printed fibronectin in the compression chamber to control the cell spreading location. The microfluidic device was also equipped with two-step, pneumatically controlled cell trapping, to increase the number of cells that can be trapped in a device, while reducing the applied aspiration on cells during cell trapping. We have also demonstrated the application of cyclic compression on normal breast epithelial cells. The device has a unique property of compressing different cells to the same deformed height and can be easily combined with fluorescence live cell imaging. It can be used to compress different cell types with similar cell sizes used in the present work. Thus, it is possible to compare normal vs. diseased cell types to gain further insights into specific diseases. The development provides new opportunities for investigating mechanical compression in cell mechanics and mechanobiology.

AUTHOR CONTRIBUTIONS

KH conceived the study, designed and fabricated the device, carried out experiments, analyzed data, prepared figures, and wrote the manuscript. YW performed experiments, analyzed data, and prepared figures. JW performed experiments, analyzed data, and prepared figures. AL conceived the study and wrote the manuscript.

ACKNOWLEDGMENTS

This work is supported by the NIH Director's New Innovator Award (DP2 HL117748-01) and NSF CMMI-1561794. We acknowledge the support from Lurie Nanofabrication Center (LNF) at the University of Michigan.

SUPPLEMENTARY MATERIAL

The Supplementary Material for this article can be found online at: https://www.frontiersin.org/articles/10.3389/fbioe.2018.00148/full#supplementary-material

REFERENCES

Bausch, A. R., Hellerer, U., Essler, M., Aepfelbacher, M., and Sackmann, E. (2001). Rapid stiffening of integrin receptor-actin linkages in endothelial cells stimulated with thrombin: a magnetic bead microrheology study. *Biophys. J.* 80, 2649–2657. doi: 10.1016/S0006-3495(01)76234-0

Bonakdar, N., Gerum, R., Kuhn, M., Spörrer, M., Lippert, A., Schneider, W., et al. (2016). Mechanical plasticity of cells. *Nat. Mater.* 15, 1090–1094. doi: 10.1038/nmat4689

Chen, Y., Pasapera, A. M., Koretsky, A. P., and Waterman, C. M. (2013). Orientation-specific responses to sustained uniaxial stretching in focal adhesion growth and turnover. *Proc. Natl. Acad. Sci. U.S.A.* 110, E2352– E2361. doi: 10.1073/pnas.1221637110

Denais, C. M., Gilbert, R. M., Isermann, P., McGregor, A. L., te Lindert, M., Weigelin, B., et al. (2016). Nuclear envelope rupture and repair during cancer cell migration. *Science* 352, 353–358. doi: 10.1126/science.aad7297

Fabry, B., Maksym, G. N., Butler, J. P., Glogauer, M., Navajas, D., and Fredberg, J. J. (2001). Scaling the microrheology of living cells. *Phys. Rev. Lett.* 87:148102. doi: 10.1103/PhysRevLett.87.148102

Grodzinsky, A. J., Levenston, M. E., Jin, M., and Frank, E. H. (2000). Cartilage tissue remodeling in response to mechanical forces. *Annu. Rev. Biomed. Eng.* 2, 691–713. doi: 10.1146/annurev.bioeng.2.1.691

Gupta, V., and Grande-Allen, K. J. (2006). Effects of static and cyclic loading in regulating extracellular matrix synthesis by cardiovascular cells. *Cardiovasc. Res.* 72, 375–383. doi: 10.1016/j.cardiores.2006.08.017

Heureaux, J., Luker, K. E., Haley, H., Pirone, M., Lee, L. M., and Liu, A. P. et al. (2018). The effect of mechanosensitive channel MscL expression in cancer cells on 3D confined migration. *APL Bioeng.* 2:032001. doi: 10.1063/1.5019770

Ho, K. K., Lee, L. M., and Liu, A. P. (2016). Mechanically activated artificial cell by using microfluidics. *Sci. Rep.* 6:32912. doi: 10.1038/srep32912

Hosmane, S., Fournier, A., Wright, R., Rajbhandari, L., Siddique, R., Yang, I., et al. (2011). Valve-based microfluidic compression platform: single axon injury and regrowth. *Lab Chip* 11, 3888–3895. doi: 10.1039/c1lc20549h

Hu, S., Chen, J., Fabry, B., Numaguchi, Y., Gouldstone, A., Ingber, D., et al. (2003). Intracellular stress tomography reveals stress focusing and structural anisotropy in cytoskeleton of living cells. *Am. J. Physiol. Cell Physiol.* 285, C1082–C1090. doi: 10.1152/ajpcell.00159.2003

Jain, R. K., Martin, J. D., and Stylianopoulos, T. (2014). The Role of mechanical forces in tumor growth and therapy. *Annu. Rev. Biomed. Eng.* 16, 321–346. doi: 10.1146/annurev-bioeng-071813-105259

Kim, Y. C., Kang, J. H., Park, J-S., Yoon, E-S, and Park, K-J. (2007). Microfluidic biomechanical device for compressive cell stimulation and lysis. *Sens. Actuators B Chem.* 128, 108–116. doi: 10.1016/j.snb.2007.05.050

Lee, L. M., Lee, J. W., Chase, D., Gebrezgiabhier, D., and Liu, A. P. (2016). Development of an advanced microfluidic micropipette aspiration device for single cell mechanics studies. *Biomicrofluidics* 10:054105. doi: 10.1063/1.4962968

Li, Z., Li, X., McCracken, B., Shao, Y., Ward, K., and Fu, J. (2016). A miniaturized hemoretractometer for blood clot retraction testing. *Small* 12, 3926–3934. doi: 10.1002/smll.201600274

Liu, A. P. (2016). Biophysical tools for cellular and subcellular mechanical actuation of cell signaling. *Biophys. J.* 111, 1112–1118. doi: 10.1016/j.bpj.2016.02.043

Liu, A. P., Chaudhuri, O., and Parekh, S. H. (2017). New advances in probing cell-extracellular matrix interactions. *Integr. Biol.* 9, 383–405. doi: 10.1039/C6IB00251J

Livne, A., Bouchbinder, E., and Geiger, B. (2014). Cell reorientation under cyclic stretching. *Nat. Commun.* 5:3938. doi: 10.1038/ncomms4938

Lulevich, V., Yang, H. Y., Rivkah Isseroff, R., and Liu, G. Y. (2010). Single cell mechanics of keratinocyte cells. *Ultramicroscopy* 110, 1435–1442. doi: 10.1016/j.ultramic.2010.07.009

Lulevich, V., Zink, H-T., Chen, H. Y., Liu, T., and Liu G. Y. (2006). Cell mechanics using atomic force microscopy-based single-cell compression. *Langmuir* 22, 8151–8155. doi: 10.1021/la060561p

Mammoto, T., and Ingber, D. E. (2010). Mechanical control of tissue and organ development. *Development* 137, 1407–1420. doi: 10.1242/dev.024166

Polacheck, W. J., Li, R., Uzel, S. G., and Kamm, R. D. (2013). Microfluidic platforms for mechanobiology. *Lab Chip* 13, 2252–2267. doi: 10.1039/c3lc41393d

Raab, M., Gentili, M., de Belly, H., Thiam, H. R., Vargas, P., Jimenez, A. J. et al. (2016). ESCRT III repairs nuclear envelope ruptures during cell migration to limit DNA damage and cell death. *Science* 352, 359–362. doi: 10.1126/science.aad7611

Reymond, N., d'Agua B. B., and Ridley, A. J. (2013). Crossing the endothelial barrier during metastasis. *Nat. Rev. Cancer* 13, 858–870. doi: 10.1038/nrc3628

Ricca, B. L., Venugopalan, G., Furuta, S., Tanner, K., Orellana, W. A., Reber, C. D. et al. (2018). Transient external force induces phenotypic reversion of malignant epithelial structures via nitric oxide signaling. *Elife* 7:e26161. doi: 10.7554/eLife.26161

Rosenbluth, M. J., Lam, W. A., and Fletcher, D. A. (2006). Force microscopy of nonadherent cells: a comparison of leukemia cell deformability. *Biophys. J.* 90, 2994–3003. doi: 10.1529/biophysj.105.067496

Shao, Y., Tan, X., Novitski, R., Muqaddam, M., List, P., Williamson, L. et al. (2013). Uniaxial cell stretching device for live-cell imaging of mechanosensitive cellular functions. *Rev. Sci. Instrum.* 84:114304. doi: 10.1063/1.4832977

Shyy, J. Y., and Chien, S. (2002). Role of integrins in endothelial mechanosensing of shear stress. *Circ. Res.* 91, 769–775. doi: 10.1161/01.RES.0000038487.19924.18

Si, F., Li, B., Margolin, W., and Sun, S. X. (2015). Bacterial growth and form under mechanical compression. *Sci. Rep.* 5:11367. doi: 10.1038/srep 11367

Van Vliet, K. J., Bao, G., and Suresh, S. (2003). The biomechanics toolbox: experimental approaches for living cells and biomolecules. *Acta Mater.* 51, 5881–5905. doi: 10.1016/j.actamat.2003.09.001

Wang, N., Naruse, K., Stamenović, D., Fredberg, J. J., Mijailovich, S. M., Tolić-Nørrelykke, I. M. et al. (2001). Mechanical behavior in living cells consistent with the tensegrity model. *Proc. Natl. Acad. Sci. U.S.A.* 98, 7765–7770. doi: 10.1073/pnas.141199598

Weafer, P. P., Ronan, W., Jarvis, S. P., and McGarry, J. P. (2013). Experimental and computational investigation of the role of stress fiber contractility in the resistance of osteoblasts to compression. *Bull. Math. Biol.* 75, 1284–1303. doi: 10.1007/s11538-013-9812-y

Xia, Y., and Whitesides, G. M. (1998). Soft lithography. *Annu. Rev. Mater. Sci.* 28, 153–184. doi: 10.1146/annurev.matsci.28.1.153

Zhou, E. H., Trepat, X., Park, C. Y., Lenormand, G., Oliver, M. N., Mijailovich, S. M. et al. (2009). Universal behavior of the osmotically compressed cell and its analogy to the colloidal glass transition. *Proc. Natl. Acad. Sci. U.S.A.* 106, 10632–10637. doi: 10.1073/pnas.09014 62106

Conflict of Interest Statement: The authors declare that the research was conducted in the absence of any commercial or financial relationships that could be construed as a potential conflict of interest.

frontiers in Bioengineering and Biotechnology

ORIGINAL RESEARCH
published: 12 March 2019
doi: 10.3389/fbioe.2019.00041

Increased Cell Traction-Induced Prestress in Dynamically Cultured Microtissues

Mathieu A. J. van Kelle[1,2], *Nilam Khalil*[1], *Jasper Foolen*[1], *Sandra Loerakker*[1,2]* *and Carlijn V. C. Bouten*[1,2]

[1] *Department of Biomedical Engineering, Eindhoven University of Technology, Eindhoven, Netherlands,* [2] *Institute for Complex Molecular Systems, Eindhoven University of Technology, Eindhoven, Netherlands*

Prestress is a phenomenon present in many cardiovascular tissues and has profound implications on their *in vivo* functionality. For instance, the *in vivo* mechanical properties are altered by the presence of prestress, and prestress also influences tissue growth and remodeling processes. The development of tissue prestress typically originates from complex growth and remodeling phenomena which yet remain to be elucidated. One particularly interesting mechanism in which prestress develops is by active traction forces generated by cells embedded in the tissue by means of their actin stress fibers. In order to understand how these traction forces influence tissue prestress, many have used microfabricated, high-throughput, micrometer scale setups to culture microtissues which actively generate prestress to specially designed cantilevers. By measuring the displacement of these cantilevers, the prestress response to all kinds of perturbations can be monitored. In the present study, such a microfabricated tissue gauge platform was combined with the commercially available Flexcell system to facilitate dynamic cyclic stretching of microtissues. First, the setup was validated to quantify the dynamic microtissue stretch applied during the experiments. Next, the microtissues were subjected to a dynamic loading regime for 24 h. After this interval, the prestress increased to levels over twice as high compared to static controls. The prestress in these tissues was completely abated when a ROCK-inhibitor was added, showing that the development of this prestress can be completely attributed to the cell-generated traction forces. Finally, after switching the microtissues back to static loading conditions, or when removing the ROCK-inhibitor, prestress magnitudes were restored to original values. These findings show that intrinsic cell-generated prestress is a highly controlled parameter, where the actin stress fibers serve as a mechanostat to regulate this prestress. Since almost all cardiovascular tissues are exposed to a dynamic loading regime, these findings have important implications for the mechanical testing of these tissues, or when designing cardiovascular tissue engineering therapies.

Keywords: prestress, microtissue, *in vitro*, experiments, tissue-engineering

OPEN ACCESS

Edited by:
Sara Baratchi,
RMIT University, Australia

Reviewed by:
Huaping Wang,
Beijing Institute of Technology, China
Kristen L. Billiar,
Worcester Polytechnic Institute, United States

***Correspondence:**
Sandra Loerakker
S.Loerakker@tue.nl

Specialty section:
This article was submitted to Biomechanics, a section of the journal Frontiers in Bioengineering and Biotechnology

Received: *24 December 2018*
Accepted: *19 February 2019*
Published: *12 March 2019*

Citation:
van Kelle MAJ, Khalil N, Foolen J, Loerakker S and Bouten CVC (2019) Increased Cell Traction-Induced Prestress in Dynamically Cultured Microtissues. Front. Bioeng. Biotechnol. 7:41. doi: 10.3389/fbioe.2019.00041

1. INTRODUCTION

Cardiovascular tissues display significant levels of prestress. This prestress is an intrinsic stress which is relieved when the particular tissues are isolated from their *in vivo* environment. The presence of prestress has profound implications for the *in vivo* functioning of cardiovascular tissues. First, prestress directly influences the apparent *in vivo* mechanical properties of, heart valves (Amini et al., 2012; Rausch and Kuhl, 2013) and arteries (Dobrin et al., 1975; Chuong and Fung, 1986; Cardamone et al., 2009), for example. It therefore largely dictates the functioning of these cardiovascular tissues. Second, prestress development has shown to increase tissue extracellular matrix (ECM) alignment and increased matrix deposition in tissue engineered (TE) sheets (Grenier et al., 2005) and heart valves (Mol et al., 2005), respectively, hence influencing structural adaptation in the long run. Finally, abnormal levels of prestress can give rise to serious pathologies which, among others, include vascular hypertension caused by excessive prestress-induced vasoconstriction (Fagan et al., 2004), and aneurysm formation caused by insufficient levels of prestress in tissue-engineered vascular grafts (Tara et al., 2015). In this context, gaining insight into the factors influencing the development of tissue prestress is of paramount importance.

The development of tissue prestress in cardiovascular tissues typically arises due to complex growth and remodeling phenomena, which are only partially understood (Ambrosi et al., 2011). One particularly interesting mechanism for prestress development is the ability of cells to apply traction forces to their surroundings. These forces are generated by contraction of cellular actin stress fibers. Subsequently, these actively generated forces are transferred to the surrounding ECM by means of focal adhesions, leading to the development of tissue prestress. Van Vlimmeren et al. (2012) showed that these cell-mediated traction forces are accountable for roughly 40% of the prestress present in statically cultured tissue-engineered strips.

Many previous studies have investigated the effect of cellular traction forces on the development of tissue prestress. For instance van Loosdregt et al. (2018) studied the relationship between intrinsically generated cell stress and cellular organization in 2D, and found the two to be independent from each other. In addition, Legant et al. (2009) developed a platform in which micrometer-scale cantilevers were used to simultaneously culture 3D microtissues and measure the generated stress. This stress increased with higher cantilever stiffness, but decreased with increasing collagen concentrations. Kural and Billiar (2014) used similar microtissues to study the effect of boundary stiffness, and TGF-β exposure to the developed cell-generated forces. Finally, Boudou et al. (2012) also created a microfabricated platform to measure the dynamic contraction of cardiac microtissues, which was later adapted by van Spreeuwel et al. (2014), who studied the influence of matrix (an)isotropy on this intrinsic contraction. The main advantages of these micrometer scale setups over conventional platforms are the relatively short culture times, and the option of accommodating a large number of samples. However, these particular setups were only used to study cell-generated stress under static external loading which is not physiological for cardiovascular tissues, since these are constantly being exposed to dynamic loading conditions.

There is evidence that external dynamic loading can alter (micro)tissue organization and potentially the degree of developed prestress. Like Legant et al. (2009) and Foolen et al. (2012) also used cantilever-suspended tissues, but in this particular case the cantilevers were mounted on top of a stretchable membrane, enabling dynamic loading of the constructs. They found that uniaxial and biaxial cyclic stretch differentially affected active actin and collagen (re)organization in 3D. However, as the cantilevers were relatively stiff, tissue prestress could not be quantified. A similar study by Gould et al. (2012) found that dynamic loading of collagen hydrogels, in addition to regulating collagen fiber alignment and cellular orientation, is a potent regulator of cellular phenotype. Finally, Zhao et al. (2013) cyclically loaded microtissues for 15 min using electromagnetic tweezers and found increased tissue stiffness due to increased cellular traction forces. However, it remains unclear whether long-term exposure to dynamic mechanical stimuli also induces a cell traction-mediated increase in prestress. This can be especially important in cardiovascular tissue-engineering therapies, which introduce a previously unloaded construct into a continuously dynamic loaded *in vivo* environment. If this is the case, prestress-induced changes in TE construct mechanical properties can alter its *in vivo* functionality, ultimately determining the success or failure of the therapy.

Delvoye et al. (1991) showed that in constrained collagen gels, seeded fibroblasts will compact the ECM until the tensile stress reaches a steady state. After subsequent perturbations in the gel, the cells will again strive to restore the same mechanical steady state. In analogy with this phenomenon, we hypothesize that cells will also mediate tissue prestress in response to dynamic stimulation by increasing their actin-generated cell traction forces.

To investigate the validity of this hypothesis, in this study 3D microtissues were exposed to long-term dynamical loading, after which the cell traction-induced prestress was quantified. To this end, a microfabricated tissue gauge (μTUG) platform (van Spreeuwel et al., 2014) was combined with the commercial available Flexcell system to create a μFlex-TUG setup and facilitate 24 h cyclic stretching of the microtissues. First, the setup was validated by measuring the microtissue stretches during dynamic culture using digital image correlation. Subsequently, microtissues were dynamically cultured for 24 h, which increased the cell traction-induced tissue prestress almost two-fold. Next, the origin of the increased prestress levels was investigated. First, a ROCK-inhibitor, temporary inhibiting stress fiber contractility, was added after 48 h to both dynamically and statically cultured experimental groups. In both groups, prestress levels were comparable and almost completely abated after ROCK-inhibition, showing that the elevated prestress levels after 24 h dynamical culture can solely be attributed to increased stress fiber contraction. Second, after subsequent removal of the ROCK-inhibitor, prestress magnitudes returned to static control levels. In addition, in another dynamically cultured group, the elevated prestress levels returned to magnitudes comparable to static controls after removal of the dynamic cue. These findings show

that intrinsic tissue prestress is a highly regulated parameter, in which the actin stress fibers serve as a mechanostat to control this prestress.

Since cardiovascular tissues are experiencing everlasting hemodynamic loading, and the fact that prestress influences a tissue's mechanical behavior, these findings have important implications for accurately determining (*in vivo*) mechanical properties. Additionally, tissue-engineering therapies aimed at replacing such cardiovascular tissues often use cells with a contractile phenotype. The findings suggest that dynamic stimulation after implantation of the TE constructs could alter their *in vivo* function and subsequent success of the therapy.

2. METHODS

2.1. μFlex-TUG and μTUG Fabrication

The setup consists of eighty microfabricated tissue gauges (μTUGs), where each of these μTUGs contains four compliant polydimethylsiloxane (PDMS) microposts embedded in a microwell (**Figures 1A,B**). Fabrication of the μTUGs was performed according to van Spreeuwel et al. (2014). Briefly, positive masters were created by spincoating SU-8 photoresist (Microchem, Berlin, Germany) on a silicon wafer, which was subsequently UV-exposed. Alignment of different layers was performed using a Suss MJB3 mask aligner (Suss Microtec, Garching, Germany). The masters were then made non-adhesive through overnight silanization with (tridecafluoro-1,1,2,2-tetrahydrooctyl)-1-trichlorosilane (Abcr, Karlsruhe, Germany) under vacuum. Negative PDMS templates were made by casting PDMS, with prepolymer to curing agent ratio of 10 : 1 w/w (Sylgard 184; Dow-Corning, Midland, USA) on the masters, followed by overnight incubation at 65°C. These negative PDMS templates were then treated in a plasma oxydizer (1 min at 100 watt) and again made non-adhesive by overnight silanization. Subsequently, PDMS was cast on these templates which was then degassed in a vacuum oven. The PDMS-covered negative templates were either stamped in Flexcell BioFlex plates (Flexcell International Corporation, Burlington, NC, USA) to create μFlex-TUGs for dynamic culture, or in regular petri dishes to create static μTUGs. Finally, both setups were cured overnight at 65°C followed by careful removal of the negative template.

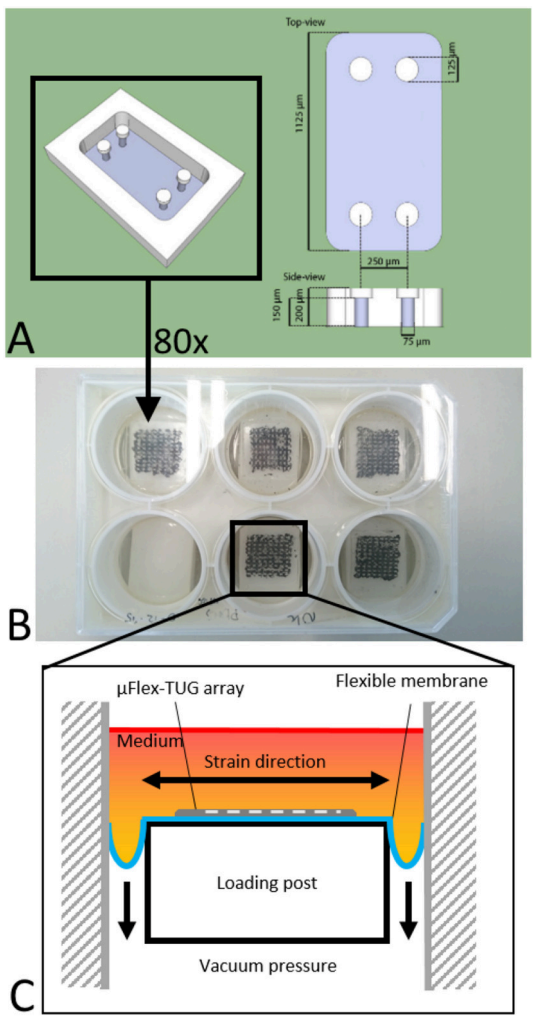

FIGURE 1 | (A) Design of the microwell containing four PDMS microposts (courtesy of Alex Bastiaens). **(B)** μTUGs created on a Flexcell plate to create a μFlex-TUG. **(C)** Application of uniaxial dynamic loading to the μFlex-TUGs.

2.2. Cell and Microtissue Culture

Human vena saphena cells (HVSCs) were cultured until passage 7 using culture medium containing advanced Dulbecco's Modified Eagle Medium (DMEM, Invitrogen, Carlsbac, CA, USA), supplemented with 10% Fetal Bovine Serum (FBS, Greiner Bio One, Frinckenhausen, Germany), 1% Glutamax (Invitrogen) and 1% penicillin/streptomycin (Lonza, Basel, Switzerland). These cells have previously been characterized as myofibroblasts (Mol et al., 2006) and exhibit a contractile phenotype. Microtissues were created according to the protocol described by van Spreeuwel et al. (2014). In short, first the μFlex-TUGs and μTUGs were sterilized by immersion in 70% ethanol for 15 min, followed by 15 min UV radiation. To impair cell adhesion, the PDMS was treated with 0.2% Pluronic F127 (BASF, Ludwigshafen am Rhein, Germany) in PBS for 15 min. A gel mixture containing 50% collagen (Rat tail collagen type 1, BD biosciences, New Jersey, US, 3.2 mg ml^{-1}), 39% culture medium, 8% growth factor-reduced Matrigel (BD Biosciences) and 3% 0.25 M NaOH was prepared and centrifuged into the microwells (1 min, 2,000 RPM). Residual gel which was not in the microwells was used to resuspend harvested HVSCs, after which this suspension was centrifuged again into the microwells (1 min, 1000 RPM) (**Figure 2A**). Excessive gel was removed and the remaining cell/gel suspension in the microwells was allowed to polymerize for 10 min at 37°C. Finally, 0.25 mg/mL L-ascorbic 2-phosphate acid (Sigma-Aldrich, St. Louis, MO, USA) supplemented standard culture medium was added on top of the microwells. After seeding, the setups were placed in an incubator for 24 h at 37°C, 100% humidity and 5% CO_2 to allow for initial microtissue formation (**Figure 2B**).

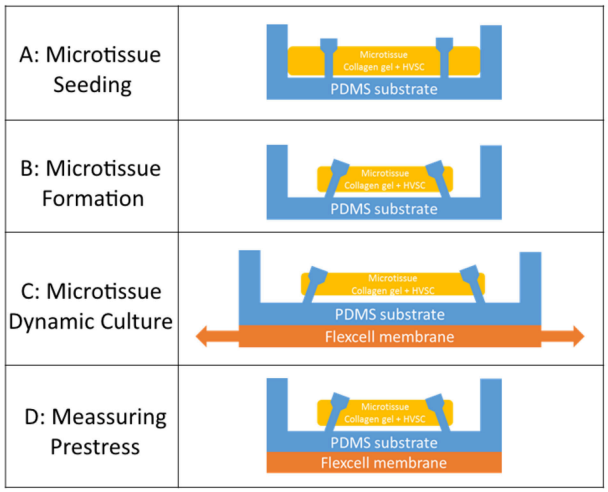

FIGURE 2 | (A) Seeding of the cell/gel suspension in a microwell. **(B)** Formation of a microtissue. **(C)** Dynamic stretching of a microtissue. **(D)** Measuring prestress by tracking the micropost displacement.

2.3. Validation of Microtissue Strain in μFlex-TUG

To cyclically stretch the microtissues, the seeded μFlex-TUGs were placed in the Flexcell FX-4000 system supported by rectangular posts (**Figure 1B**). This system enables application of uniaxial dynamic loading conditions by applying a vacuum to the flexible membrane of the Flexcell plates and stretching it over the posts (**Figure 1C**). The PDMS microposts connected to the membrane translate these stretches to the connected microtissue (**Figure 2C**). It is unknown how the Flexcell membrane stretches translate to actual microtissue stretches. In this regard, Colombo et al. (2008) showed that accurate calibration and measurements of Flexcell strains are recommended given the viscoelastic nature of the Flexcell system. Therefore, the strains in the microtissues in the μFlex-TUG were validated by means of digital image correlation (DIC). Toward this end, microtissues were seeded in the μFlex-TUG system and 5,10,15 and 20% Flexcell strains with a frequency of 0.5 Hertz were applied. Videos of the stretched microtissues were recorded with a camera mounted on a Zeiss stereo discovery v8 (Oberkochen, Germany) and analyzed using previously developed DIC software by Neggers et al. (2012) to obtain the Green-Lagrange strains (in the constrained tissue direction) in one rectangular middle section of the microtissue for each of the applied Flexcell strains.

2.4. Confocal Microscopy

To visualize microtissue structure at the end of the experiments, the microtissues were incubated with a collagen-specific CNA35 probe (Boerboom et al., 2007) for 30 min, after which Z-stack images were made using a confocal laser scanning microscope (TCS SP5X; Leica Microsystems, Wetzlar, Germany, excitation 488 nm, emission 520 nm, magnification 10x, Z-step= 3 μm). Next, microtissues were fixed for 10 min using 10% formalin, followed by permeabilization with 0.5% Triton X-100 in PBS. The cell nuclei and actin network were stained with DAPI and Atto 488 Phalloidin (Sigma-Aldrich) dyes, respectively, and imaged using the confocal microscope.

2.5. Prestress Measurements

In order to quantify the tissue prestress (**Figure 2D**), first the generated forces on the four PDMS microposts were determined. Toward this end brightfield images of the microtissues were made on every time point on an EVOS XL Core microscope (Thermo Fisher, Waltham, MA, USA). Using a semi-automatic, custom-made Matlab script (Mathworks, Natick, USA), the four strongest circles in each image were detected using Matlab's *imfindcircles* function. The position of these circles corresponded to the top of the four microposts. The displacement of the center of each circle with respect to its original position was used to determine the displacement of the top of these posts (u). Next, the spring constant K [= 1.22 N m^{-1}] of a single micropost was determined by means of finite element simulations (Abaqus, Dassault Systèmes Simulia Corp., Providence, RI, USA, version 6.14-1). First, a force was applied to the part of a single micropost where the tissue is attached, which is just below the relatively large cap of the post. Next, the displacement of the top middle node in the direction of the force was determined (for more information see the **Supplementary Material**). Second, using this spring constant and the micropost displacement, the force exerted on one micropost (F^i_{post}) was determined:

$$F^i_{post} = Ku_{post} \qquad and \qquad F_{tissue} = \frac{\sum_{n=1}^{4} F^i_{post}}{2} \tag{1}$$

Since the force generated by the microtissue is equal and opposite on the microposts on both side of the tissue, the total microtissue force F_{tissue} is the sum of the individual forces on each of the four posts divided by two. It needs to be noted that only the component of the total force in the constrained direction was considered. To acquire the prestress in the microtissues, the measured forces need to be translated into stresses. Toward this end, the cross-sectional area (CSA) from each microtissue was obtained. First from all the images made during the force measurements, Matlab's *imdistline* function was used to obtain the width in the middle part of the microtissue, which we define as the "Cross-Sectional Length" (A_{CSL}). Second, at the end of the experiment the "real" CSA (A_{CSA}) from the collagen stained microtissues (section Confocal Microscopy) was determined. All slices of the Z-stack were imported into Matlab, and from the middle image the main orientation of the largest connected component (which is the microtissues) was obtained using the *regionprops* Matlab function. This main orientation was used to rotate all individual slices so that the images align in the horizontal direction (**Figure 3A**). Next, each lateral slice form the 3D image was binarized. A convex hull was wrapped around the images, where the pixels within this convex hull compose the CSA (**Figure 3B**). The lateral slice with the smallest convex hull was obtained and used together with the dimension data from each voxel to obtain the microtissue CSA in μm^2. This real CSA was plotted against the microtissue width at the end of the experiment, for which a strong correlation (R^2=0.91) was

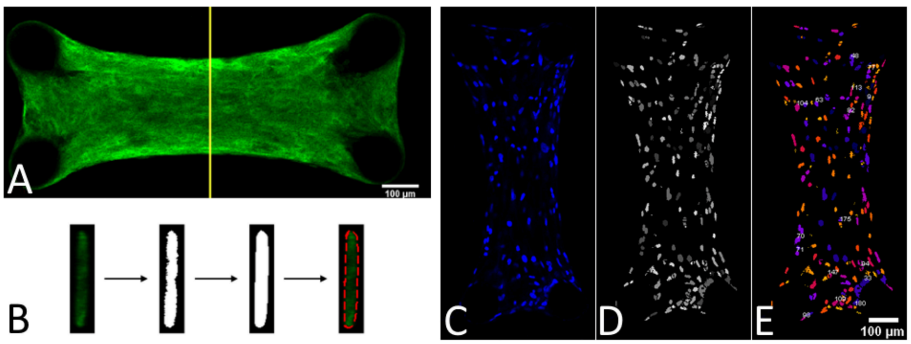

FIGURE 3 | (A) Middle slice of a 3D image form a collagen-stained microtissue. **(B)** Determining the cross-sectional area by using a convex hull on the middle lateral slice form the 3D image. **(C)** DAPI stained a microtissue. **(D)** Watershed filtering of cell nuclei. **(E)** Segmenting and counting the cell nuclei in 3D, where every individual nucleus has a different color.

found when fitting a linear model (**Figure 4**). Finally, the real CSA was determined by applying the obtained linear model to the measured microtissues widths at each previous time point of the experiment. All the forces (F_{tissue}, μN) were divided by the CSA (A_{CSA}, μm^2) to obtain the microtissue prestress (σ) in kPa, i.e.,

$$\sigma = \frac{F_{tissue}}{A_{CSA}}. \quad (2)$$

2.6. Number of Cells

To determine the prestress magnitude per cell, the number of cells per microtissue was counted. This was done by importing the Z-stacks of the DAPI channel from the confocal images into ImageJ (NIH, Bethesda, MD, USA) (**Figure 3C**). First the stacks were filtered with a 3D watershed algorithm (Ollion et al., 2013) (**Figure 3D**). Next the amount of cells in the binarized images were counted using a 3D object counter plugin (Bolte and Cordelières, 2006) (**Figure 3E**).

2.7. Experimental Design

Microtissues were seeded in two μTUGs as a static control, and additionally two wells in a μFlex-TUG were seeded as a dynamic group. An overview of the experimental design can be found in **Figure 5**. Initially, all four groups were cultured under static conditions for 24 h to allow the formation of microtissues, after which the force and CSA were determined. To determine the effect of dynamic loading on the generated prestress, subsequently the two dynamic groups were switched to dynamic culture conditions by applying 10% strain to the Flexcell plate at 0.5 Hz (Foolen et al., 2012). After another 24 h, the force and CSA was determined again for all groups. To analyse the cell traction-mediated fraction of the total prestress, a ROCK-inhibitor (Y-27632, Sigma-Aldrich) was added to one static and one dynamic group and forces and CSA were measured again after 30 min. Finally, to determine whether differences in prestress were reversible, the ROCK-inhibitor was removed by adding fresh culture medium and switching all dynamic groups back to static culture conditions.

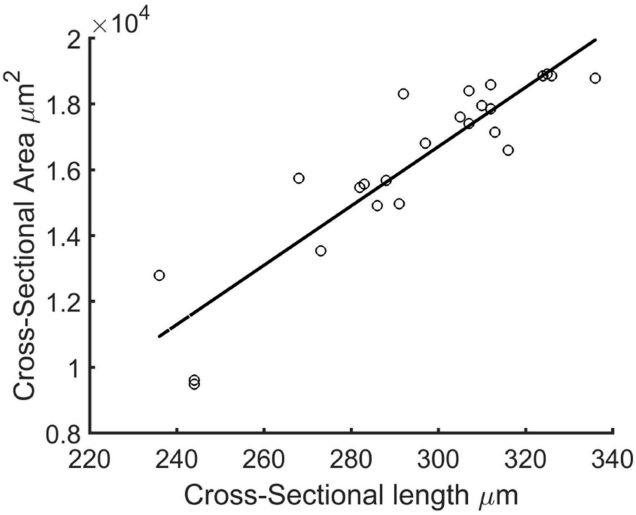

FIGURE 4 | Cross-sectional length (A_{CSL}) plotted against actual microtissue CSA A_{CSA}. The black line is the fitted linear model with equation: A_{CSA}=90.09*A_{CSL}-10323.41 (R^2=0.91).

After a final 24 h the prestress was measured again for all groups.

2.8. Statistical Analysis

Only microtissues which were still attached to all four posts at the end of the experiment (72h) were included in the analysis. For the static control group and the ROCK-inhibited static group, sample numbers were 21 and 24, respectively, while for the dynamic and ROCK-inhibited dynamic group the sample sizes were 10 and 13, respectively. All data were reported as mean ± standard error of mean. Statistical analysis of the data was performed with a many-to-one Dunnett test, comparing all conditions to one control group, accounting for heterogeneous variances and unequal samples sizes using the methods and implementation into the statistical software package R (R Core Team, Vienna, Austria) described in

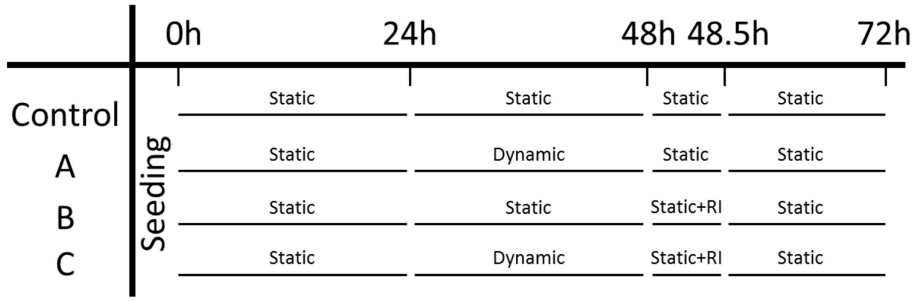

FIGURE 5 | Experiment design: the left column indicates the three experimental groups and the control group. Each time point is indicated on the top row.

Herberich et al. (2010). For analyzing the number of cells per microtissue, a Wilcoxon signed-rank statistical test was performed in MATLAB.

3. RESULTS

3.1. Microtissue Strains Are One-Third of the Applied Flexcell Strains

The applied Flexcell strains clearly translated to a strain in the microtissues (**Figures 6A,B**). During one cycle (2 s), these microtissues strains followed a homogeneous inverse parabolic profile (**Figure 6C**), reaching a maximum value halfway through the cycle. When quantifying the maximal microtissue Green-Lagrange strains, it was found that they increased with the applied Flexcell strains (**Figures 6C,D**). However, the applied Flexcell strains did not equal the microtissue strains. As a rule of thumb, the actual microtissue strain was assessed to be one-third of the applied Flexcell strain.

3.2. The Microtissues Have a Uniform Distribution of Cells, and Collagen and Stress Fibers Are Aligned in the Constrained Direction

The cells are uniformly spaced inside the microtissues (**Figure 7A**). Also the collagen (**Figure 7B**) and actin (**Figure 7C**) are homogenously distributed in the microtissue, where the fibers are oriented in the longitudinal direction.

3.3. Increased Prestress in Dynamically Cultured Microtissues

The prestress in the static control group remained constant during 72 h of culture (**Figure 8A**, blue). Although initially the prestress was similar after 24 h, following dynamic stimulation, the microtissue prestress increased significantly to levels over twice that of the statically cultured controls after 48 h of culture (**Figure 8A**, red). Upon removal of the dynamic mechanical cue, prestress levels went back to equal magnitudes as that of static controls at 72 h of culture.

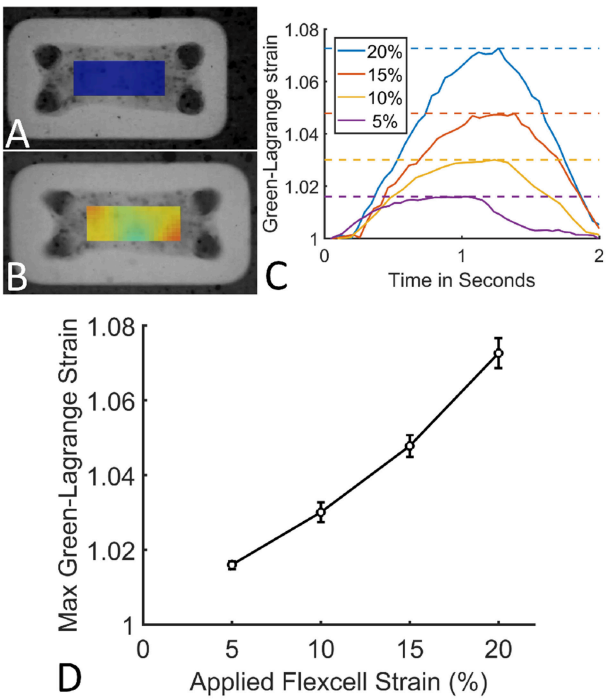

FIGURE 6 | (A) A microtissue without externally applied mechanical cues. **(B)** A dynamically cultured microtissue at 10% Flexcell strain. **(C)** Average actual microtissue Green-Lagrange strains during one cycle (2 s) for different applied Flexcell strains (legend). The dotted lines indicate the maximal strains during the cycles. **(D)** Maximum Green-Lagrange strains (averaged over the mid-section of the microtissues in **B**) for increasing applied Flexcell strains.

3.4. Prestress Increase Is Caused by the Stress Fibers and Is Reversible

The statically cultured microtissues which were exposed to the ROCK-inhibitor showed a similar prestress magnitude at 24 and 48 h of culture. However, after addition of the inhibitor, the prestress dropped significantly (**Figure 8B**, red), leaving only a small amount of residual stress. After subsequent removal of the ROCK-inhibitor, within 24 h the prestress again reached comparable levels compared to the control group.

A similar phenomenon was observed in the ROCK-inhibited dynamically cultured microtissues. Upon dynamic culture, the

stretched microtissue prestress again increased significantly to levels over twice that of the statically cultured controls at 48 h of culture (**Figure 8C**, blue). Addition of the ROCK-inhibitor diminished that higher prestress almost completely, leading to levels of residual stresses comparable to the statically ROCK-inhibited microtissues (**Figure 8B**). In line with earlier observations, removal of the ROCK-inhibitor and subsequent static culture resulted in similar prestress levels as statically cultured controls after 72 h.

3.5. Prestress Per Cell Is Similar in Statically and Dynamically Cultured Groups at the End of Culture

The number of cells per individual microtissue was determined using a DAPI staining (section Number of cells) at the end of culture. The number of cells differed substantially within the experimental groups for both conditions (**Figure 9**). However no statistical differences between the statically and dynamically cultured groups were found ($p = 0.5614$).

When plotting the stress in each microtissue against the number of cells, an increasing linear relationship was found for both the statically (R^2=0.55) and dynamically (R^2=0.62) cultured groups (**Figure 10**).

4. DISCUSSION

In this study it was investigated how long-term exposure to dynamic loading will influence cell traction-induced prestress in 3D microtissues. To facilitate this, a microfabricated tissue gauge platform was combined with the commercially available Flexcell system to enable 24 h cyclic stretching of the microtissues.

4.1. Setup Validation

First the developed system was validated by measuring the actual microtissue strains with DIC. As already stated by Colombo et al. (2008), the applied Flexcell strains do not necessarily translate one-to-one to actual microtissue strains. On average, the actual microtissue strain was one third of the applied Flexcell strains. Possible reasons for this are two-fold: first, addition of a PDMS layer to the Flexcell membrane makes the entire base of the μFlex-TUGs more stiff, and thus with the same vacuum

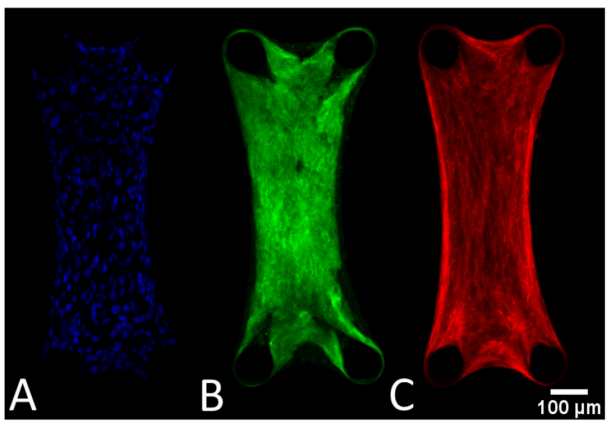

FIGURE 7 | General tissue organization depicted in these confocal images of a DAPI **(A)**, collagen **(B)**, and actin-stained **(C)** microtissue after 72 h of culture.

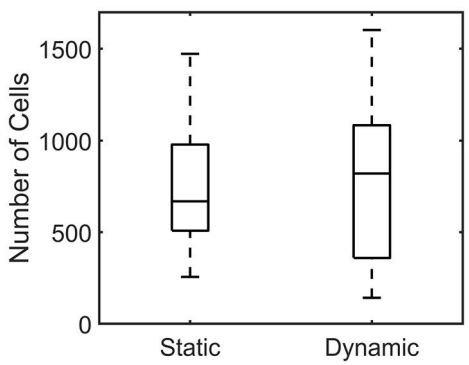

FIGURE 9 | Boxplot of the number of cells per microtissue for the statically **(Left)** and dynamically **(Right)** cultured groups at the end of the experiment.

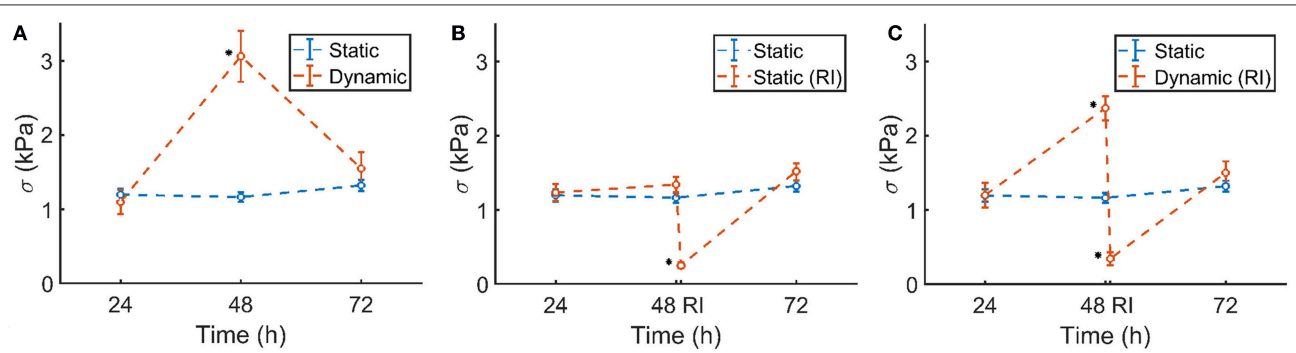

FIGURE 8 | (A) Static control group (blue) and dynamically cultured microtissues (red). **(B)** Static control group (blue) and ROCK-inhibited (RI, red, at 48 h) microtissues over the course of 72 h. **(C)** Static control group (blue) and dynamically stretched microtissues (red). A ROCK-inhibitor was added to the dynamically cultured microtissues after 48 h (RI), which was again removed after 30 min. Significant changes (p<0.05) between the two groups are indicated by a *. Note that the blue controls in **(A–C)** are the same experimental group in all figures. The characters of subfigures **(A–C)** correspond to the characters used in **Figure 5**.

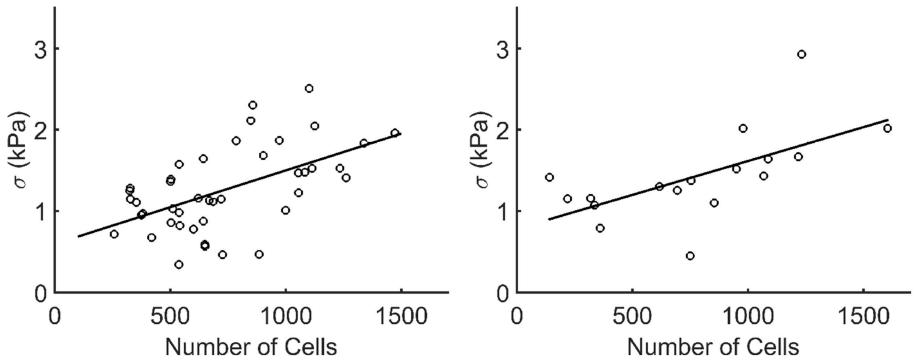

FIGURE 10 | Stress plotted against the number of cells (N_{cells}) per microtissue for the statically (left) and dynamically (right) cultured groups at 72 h of culture (after recovery). Each dot corresponds to one microtissue. The black lines indicate a linear fit through all data points. The equations for these lines are $\sigma = 0.0009 * N_{cells} + 0.5957$ and $\sigma = 0.00085 * N_{cells} + 0.7825$ for the statically (R^2=0.55) and dynamically (R^2=0.62) cultured microtissues, respectively.

magnitude the membrane yields less displacement. Second, the microtissues are connected to compliant microposts, which contrary to for example Foolen et al. (2012), bend when the cyclic stretch is applied, making the strain in the microtissues even smaller.

4.2. Cell Traction Forces Are a Mechanostat for Tissue Prestress

After validation of the setup, experiments were performed to determine the effect of dynamic loading on cell traction-mediated prestress. In the first 24 h, all groups were cultured statically to ensure microtissue formation. The prestress after 24 h was similar for all four groups. This confirms that merely culturing the microtissues in a different setup (μFlex-TUG or static μTUGs) without applying cyclic stretch did not affect the prestress. For static controls, prestress remains constant over the entire experiment. Upon dynamic culture, the prestress roughly increased two-fold compared to the static controls. This prestress increase is entirely caused by cell traction forces, as ROCK-inhibition almost completely diminishes the prestress. In fact, both the statically and dynamically cultured microtissues returned to similar values of prestress (0.25 and 0.34 kPa, respectively) after ROCK-inhibition. This passive residual stress in the static group contributes 19% to the total prestress, and 14% in the dynamic group. When comparing the percentual contribution in the static group to statically cultured TE strips by Van Vlimmeren et al. (2012), this percentage is significantly lower (60%). However, in this particular study the culture times were considerably shorter, so very little matrix production could have taken place. Therefore, this discrepancy could be explained by the fact that the only residual matrix prestress is caused by the relatively compliant collagen gel, which is far less stiff compared to the fibrous collagenous matrix in TE strips.

After switching the dynamically cultured microtissues back to static conditions, or upon removal of the ROCK-inhibitor, prestress in all groups is again normalized and comparable to the control group after 72 h. The typical timescales (smaller than 24 h) at which the increase and decrease of prestress lay within the typical turnover rate of actin stress fiber, which is approximately minutes (Peterson et al., 2004; Mbikou et al., 2006; Livne and Geiger, 2016). These results show that cyclic load-induced elevated prestress levels, and the restoration to baseline levels after removal of the ROCK-inhibitor or dynamic cue are regulated only by the actin stress fiber generated cell traction forces. It appears that in these relatively immature microtissues, the actin stress fibers serve as a mechanostat to regulate the prestress in response to perturbations in the environment.

4.3. Microtissue Structure and Increasing Prestress With Cell Number

At the experimental timepoints, both statically and dynamically cultured microtissues were stained for actin stress fibers, collagen and cell nuclei. **Figures 7B,C** show that the collagen, and cellular actin fibers are present uninterruptedly between the four microposts. This means that all cell-generated forces can be translated within the tissue. Both the actin and collagen fibers are aligned in the longitudinal direction of the microtissues. This phenomenon is not surprising since this is the only constrained direction of the constructs.

The DAPI-stained microtissues affirm a homogeneous distribution of cells with the microtissue (**Figure 7A**). However, cell numbers among microtissues varied up to 10-fold (± 150–1,500). This is possibly caused by the fact that during seeding, the cells are centrifuged into 80 different microwells at once. This makes it impossible to control how many cells end up per microtissue. Regardless of this fact, successful microtissues formation—attached to all four posts—could occur with such a varying number of cells per construct. The effect of the varying numbers of cells per microtissue is also noticeable in microtissue prestress. Since prestress differences in this study are mainly caused by cell traction forces, larger cell numbers in microtissues cause higher prestress magnitudes. However, a two-fold increase in cell number for instance does not yield a prestress of the double magnitude. It appears that the cells cooperatively regulate the tissue prestress in response to altering cell numbers. This coincides with the findings by Canovi et al. (2016), who showed that cellular traction forces in 2D culture decrease with increasing confluency. Again in this case, cellular traction forces serve as a

mechanostat for the total tissue prestress in response to changing numbers of cells.

4.4. Challenges and Future Directions

In these experiments, the microtissues were loaded uniaxially. Since many cardiovascular tissues are loaded in multiple directions, a biaxial loading regime as used in Foolen et al. (2012) would mimic the *in vivo* situation more closely. Moreover, this setup could enable testing prestress development in anisotropically organized tissues. In addition, currently it was not investigated how the dynamic loading might affect cellular morphology and phenotype. Regardless of the relatively short time of the experiments, such morphological and phenotypic changes are known to occur, for instance under the influence of micropost stiffness Kural and Billiar (2016). With this platform, a thorough investigation of morphology and/or phenotype could be conducted using this platform. Moreover, although the large range of cells per tissue can at first be perceived as a drawback of the current method, it could be utilized to investigate the effect of cell number on generated tissue force and prestress more thoroughly. For instance, a comprehensive analysis of the force or stress per cell could help to determine the cooperative behavior of cells to reach a tensional homeostasis. Also, in the current experiments the applied microtissue strains were relatively low ($3.01\% \pm 0.26$), whereas higher levels of strain would be more realistic to the native situation of many cardiovascular tissues. Additionally, tracking prestress levels in real-time, instead of at discrete time points can give more insight into the rate of change in prestress. Currently, it is unknown how prestress changes in between the discrete time points (hence the dotted lines in **Figure 8**). Finally, the microtissues were created using a collagen gel, supplemented with matrigel. Such collagenous gels are subject to significant degradation and remodeling, which can alter the mechanical properties, and therefore the cellular response (Allison et al., 2009; Smithmyer et al., 2014). However, since collagen gels tend to be stable for culture times shorter than 1 week (Smithmyer et al., 2014), the degree of degradation is probably negligible in the current experiments, which only last 72 h. In that regard, little to no matrix production could occur during these experiments, which explains the relatively small contribution of the residual stress to the total tissue prestress. Yet, it is known that prolonged dynamic loading induces elevated levels of ECM production and cross-linking (Boerboom et al., 2008; van Geemen et al., 2013), which is expected to generate more prestress. It would therefore be interesting to increase the culture time of the experiments to study the effect of ECM-induced prestress.

4.5. Implications

The implications of increased cell traction-induced prestress under dynamic loading conditions and subsequent relatively quick recovery, are numerous. This phenomenon should for instance be considered when mechanically testing cardiovascular tissues. Rausch and Kuhl (2013) already reported that neglecting tissue prestress explained differences in reported stiffness values in literature of up to four orders of magnitude for the same types of tissues, showing the importance of accurate prestress quantification. Usually, these prestress measurements involve isolating the tissue in question from its native situation and determining the retraction (Chuong and Fung, 1986; Amini et al., 2012; Horny et al., 2013). However since this study shows that the prestress drops relatively quickly after removal of the dynamic cues, prestress measurements in these dynamically loaded cardiovascular tissues could yield different outcomes depending on the time of the measurement after excision.

Increased cell-induced prestress could also influence tissue-engineering therapies. Since these therapies rely on cell-seeded scaffolds where these cells often have a contractile phenotype (Mol et al., 2006; Tara et al., 2015), substantial prestress magnitudes are ought to be expected. Introducing such a construct from a previously unloaded environment into a continuously dynamic loaded *in vivo* environment, can lead to prestress-induced changes in the construct's mechanical behavior. This can lead to subsequent alterations in its *in vivo* functionality, determining the success or failure of the therapy.

Several factors associated with tissue-engineering strategies can influence these cell-generated prestress levels. For instance, the mechanical properties of the scaffold dictate the biomechanical behavior of the construct, thus also influence the mechanical strains experienced by the cells. A relatively compliant scaffold would induce larger cellular strains, and subsequent higher tissue prestress, whereas a stiff scaffold could shield the cells from the dynamic loads, yielding a lower prestress. Furthermore, temporal changes in scaffold degradation, ECM accumulation and organization will influence dynamic cues sensed by the cells, and hence the tissue prestress, which then again alters the functioning of the TE construct.

4.6. Conclusions

This study investigated how 24 h dynamic loading influences cell traction-induced prestress in 3D microtissues. Toward this end, a setup to culture microtissues was combined with the commercially available Flexcell system to facilitate dynamic culture of the constructs. First, the setup was validated to determine the peak microtissue stretches during the experiment, after which the effect of the applied dynamic microtissue stretch on the generated prestress was quantified. After 24 h, prestress increased significantly compared to static controls. However, after subsequent removal of the dynamic cue, prestress again dropped to levels comparable to static controls. With the addition of a ROCK-inhibitor, the prestress in these microtissues vanished almost completely, confirming that the prestress in these microtissues can be completely attributed to the cellular traction forces. Finally, after removal of the ROCK-inhibitor, prestress magnitudes restored to baseline levels. In conclusions, this study systematically and quantitatively investigated the effect of dynamic loading on cell traction-mediated tissue prestress. The results indicate that intrinsic tissue prestress is a highly controlled parameter, where the actin stress fibers serve as a mechanostat by regulating tissue prestress levels in response to perturbations in the environment. These findings can have important implications for mechanical testing of native cardiovascular tissues, and tissue-engineering therapies.

DATA ACCESSIBILITY

All data and numerical code have been stored at SURFdrive, a personal cloud storage service for the Dutch education and research community, and are available upon request.

DATA AVAILABILITY

The datasets generated for this study are available on request to the corresponding author.

AUTHOR CONTRIBUTIONS

MvK, NK, SL, and CB conceptualized the idea behind this study. MvK and NK conducted the experiments and numerical simulations and analyzed the data. MvK wrote the manuscript. JF was involved in developing the experimental setup. SL and CB supervised the project. All authors reviewed the manuscript.

ACKNOWLEDGMENTS

We acknowledge the funding from the Netherlands Cardiovascular Research Initiative (CVON 2012-01): The Dutch Heart Foundation, Dutch Federation of University Medical Centres, the Netherlands Organization for Health Research and Development and the Royal Netherlands Academy of Sciences. We furthermore acknowledge Maike Werner for her help with the ROCK-inhibitor experiments.

SUPPLEMENTARY MATERIAL

The Supplementary Material for this article can be found online at: https://www.frontiersin.org/articles/10.3389/fbioe.2019.00041/full#supplementary-material

REFERENCES

Allison, D. D., Braun, K. R., Wight, T. N., and Grande-Allen, K. J. (2009). Differential effects of exogenous and endogenous hyaluronan on contraction and strength of collagen gels. *Acta Biomater.* 5, 1019–1026. doi: 10.1016/j.actbio.2008.11.013

Ambrosi, D., Ateshian, G., Arruda, E., Cowin, S., Dumais, J., Goriely, A., et al. (2011). Perspectives on biological growth and remodeling. *J. Mech. Phys. Solids* 59, 863–883. doi: 10.1016/j.jmps.2010.12.011

Amini, R., Eckert, C. E., Koomalsingh, K., McGarvey, J., Minakawa, M., Gorman, J. H., et al. (2012). On the *in vivo* deformation of the mitral valve anterior leaflet: effects of annular geometry and referential configuration. *Ann. Biomed. Eng.* 40, 1455–1467. doi: 10.1007/s10439-012-0524-5

Boerboom, R. A., Krahn, K. N., Megens, R. T. A., van Zandvoort, M. A., Merkx, M., and Bouten, C. V. C. (2007). High resolution imaging of collagen organisation and synthesis using a versatile collagen specific probe. *J. Struct. Biol.* 159, 392–399. doi: 10.1016/j.jsb.2007.04.008

Boerboom, R. A., Rubbens, M. P., Driessen, N. J. B., Bouten, C. V. C., and Baaijens, F. P. T. (2008). Effect of strain magnitude on the tissue properties of engineered cardiovascular constructs. *Ann. Biomed. Eng.* 36, 244–253. doi: 10.1007/s10439-007-9413-8

Bolte, S. and Cordelières, F. (2006). A guided tour into subcellular colocalization analysis in light microscopy. *J. Microsc.* 224, 213–232. doi: 10.1111/j.1365-2818.2006.01706.x

Boudou, T., Legant, W. R., Mu, A., Borochin, M. A., Thavandiran, N., Radisic, M., et al. (2012). A microfabricated platform to measure and manipulate the mechanics of engineered cardiac microtissues. *Tissue Eng. Part A* 18, 910–919. doi: 10.1089/ten.tea.2011.0341

Canovi, E. P., Zollinger, A. J., Tam, S. N., Smith, M. L., and Stamenovi, D. (2016). Tensional homeostasis in endothelial cells is a multicellular phenomenon. *Am. J. Physiol. Cell Physiol.* 311, 528–535. doi: 10.1152/ajpcell.00037.2016

Cardamone, L., Valentín, A., Eberth, J. F., and Humphrey, J. D. (2009). Origin of axial prestretch and residual stress in arteries. *Biomech. Model. Mechanobiol.* 8, 431–446. doi: 10.1007/s10237-008-0146-x

Chuong, C. J., and Fung, Y. C. (1986). On residual stresses in arteries. *J. Biomech. Eng.* 108, 189–192. doi: 10.1115/1.3138600

Colombo, A., Cahill, P. A., and Lally, C. (2008). An analysis of the strain field in biaxial Flexcell membranes for different waveforms and frequencies. *Proc. Inst. Mech. Eng. Part H J. Eng. Med.* 222, 1234–1245. doi: 10.1243/09544119JEIM428

Delvoye, P., Wiliquet, P., Levêque, J. L., Nusgens, B. V., and Lapière, C. M. (1991). Measurement of mechanical forces generated by skin fibroblasts embedded in a three-dimensional collagen gel. *J. Invest. Dermatol.* 97, 898–902. doi: 10.1111/1523-1747.ep12491651

Dobrin, P., Canfield, T., and Sinha, S. (1975). Development of longitudinal retraction of carotid arteries in neonatal dogs. *Experientia* 31, 1295–1296. doi: 10.1007/BF01945788

Fagan, K. A., Oka, M., Bauer, N. R., Gebb, S. A., Ivy, D. D., Morris, K. G., et al. (2004). Attenuation of acute hypoxic pulmonary vasoconstriction and hypoxic pulmonary hypertension in mice by inhibition of Rho-kinase. *Am. J. Physiol. Cell. Mol. Physiol.* 287, L656–L664. doi: 10.1152/ajplung.00090.2003

Foolen, J., Deshpande, V. S., Kanters, F. M. W., and Baaijens, F. P. T. (2012). The influence of matrix integrity on stress-fiber remodeling in 3D. *Biomaterials* 33, 7508–7518. doi: 10.1016/j.biomaterials.2012.06.103

Gould, R. A., Chin, K., Santisakultarm, T. P., Dropkin, A., Richards, J. M., Schaffer, C. B., et al. (2012). Cyclic strain anisotropy regulates valvular interstitial cell phenotype and tissue remodeling in three-dimensional culture. *Acta Biomater.* 8, 1710–1719. doi: 10.1016/j.actbio.2012.01.006

Grenier, G., Rémy-Zolghadri, M., Larouche, D., Gauvin, R., Baker, K., Bergeron, F., et al. (2005). Tissue reorganization in response to mechanical load increases functionality. *Tissue Eng.* 11, 90–100. doi: 10.1089/ten.2005.11.90

Herberich, E., Sikorski, J., and Hothorn, T. (2010). A robust procedure for comparing multiple means under heteroscedasticity in unbalanced designs. *PLoS ONE* 5:e9788. doi: 10.1371/journal.pone.0009788

Horny, L., Adamek, T., and Zitny, R. (2013). Age-related changes in longitudinal prestress in human abdominal aorta. *Arch. Appl. Mech.* 83, 875–888. doi: 10.1007/s00419-012-0723-4

Kural, M. H., and Billiar, K. L. (2014). Mechanoregulation of valvular interstitial cell phenotype in the third dimension. *Biomaterials* 35, 1128–1137. doi: 10.1016/j.biomaterials.2013.10.047

Kural, M. H., and Billiar, K. L. (2016). Myofibroblast persistence with real-time changes in boundary stiffness. *Acta Biomater.* 32, 223–230. doi: 10.1016/j.actbio.2015.12.031

Legant, W. R., Pathak, A., Yang, M. T., Deshpande, V. S., McMeeking, R. M., and Chen, C. S. (2009). Microfabricated tissue gauges to measure and manipulate forces from 3D microtissues. *Proc. Natl. Acad. Sci. U.S.A.* 106, 10097–10102. doi: 10.1073/pnas.0900174106

Livne, A., and Geiger, B. (2016). The inner workings of stress fibers, from contractile machinery to focal adhesions and back. *J. Cell Sci.* 129, 1293–1304. doi: 10.1242/jcs.180927

Mbikou, P., Fajmut, A., Brumen, M., and Roux, E. (2006). Theoretical and experimental investigation of calcium-contraction coupling in airway smooth muscle. *Cell Biochem. Biophys.* 46, 233–252. doi: 10.1385/CBB:46:3:233

Mol, A., Driessen, N. J., Rutten, M. C. M., Hoerstrup, S. P., Bouten, C. V., and Baaijens, F. P. (2005). Tissue engineering of human heart valve leaflets: a novel bioreactor for a strain-based conditioning approach. *Ann. Biomed. Eng.* 33, 1778–1788. doi: 10.1007/s10439-005-8025-4

Mol, A., Rutten, M. C., Driessen, N. J., Bouten, C. V., Zünd, G., Baaijens, F. P., et al. (2006). Autologous human tissue-engineered heart valves: prospects for systemic application. *Circulation* 114, 152–158. doi: 10.1161/CIRCULATIONAHA.105.001123

Neggers, J., Hoefnagels, J., Roux, S., and Geers, M. (2012). A global digital image correlation enhanced full-field bulge test method. *Proc. IUTAM* 4, 73–81. doi: 10.1016/j.piutam.2012.05.009

Ollion, J., Cochennec, J., Loll, F., Escudé, C., and Boudier, T. (2013). TANGO: a generic tool for high-throughput 3D image analysis for studying nuclear organization. *Bioinformatics* 29, 1840–1841. doi: 10.1093/bioinformatics/btt276

Peterson, L. J., Rajfur, Z., Maddox, A. S., Freel, C. D., Chen, Y., Edlund, M., et al. (2004). Simultaneous stretching and contraction of stress fibers *in vivo*. *Mol. Biol. Cell* 15, 3497–3508. doi: 10.1091/mbc.e03-09-0696

Rausch, M. K., and Kuhl, E. (2013). On the effect of prestrain and residual stress in thin biological membranes. *J. Mech. Phys. Solids* 61, 1955–1969. doi: 10.1016/j.jmps.2013.04.005

Smithmyer, M. E., Sawicki, L. A., and Kloxin, A. M. (2014). Hydrogel scaffolds as *in vitro* models to study fibroblast activation in wound healing and disease. *Biomater. Sci.* 2, 634–650. doi: 10.1039/C3BM60319A

Tara, S., Kurobe, H., Maxfield, M. W., Rocco, K. A., Yi, T., Naito, Y., et al. (2015). Evaluation of remodeling process in small-diameter cell-free tissue-engineered arterial graft. *J. Vasc. Surg.* 62, 734–743. doi: 10.1016/j.jvs.2014.03.011

van Geemen, D., Driessen-Mol, A., Baaijens, F. P. T., and Bouten, C. V. C. (2013). Understanding strain-induced collagen matrix development in engineered cardiovascular tissues from gene expression profiles. *Cell Tissue Res.* 352, 727–737. doi: 10.1007/s00441-013-1573-2

van Loosdregt, I. A. E. W., Dekker, S., Alford, P. W., Oomens, C. W., Loerakker, S., and Bouten, C. V. (2018). Intrinsiccell stress is independent of organization in engineered cell sheets. *Cardiovasc. Eng. Technol.* 9, 181–192. doi: 10.1007/s13239-016-0283-9

van Spreeuwel, A. C., Bax, N. A. Bastiaens, A. J., Foolen, J., Loerakker, S., Borochin, M., et al. (2014). The influence of matrix (an)isotropy on cardiomyocyte contraction in engineered cardiac microtissues. *Integr. Biol.* 6, 422–429. doi: 10.1039/C3IB40219C

Van Vlimmeren, M. A., Driessen-Mol, A., Oomens, C. W., and Baaijens, F. P. (2012). Passive and active contributions to generated force and retraction in heart valve tissue engineering. *Biomech. Model. Mechanobiol.* 11, 1015–1027. doi: 10.1007/s10237-011-0370-7

Zhao, R., Boudou, T., Wang, W. G., Chen, C. S., and Reich, D. H. (2013). Decoupling cell and matrix mechanics in engineered microtissues using magnetically actuated microcantilevers. *Adv. Mater.* 25, 1699–1705. doi: 10.1002/adma.201203585

Conflict of Interest Statement: The authors declare that the research was conducted in the absence of any commercial or financial relationships that could be construed as a potential conflict of interest.

frontiers in Bioengineering and Biotechnology

PROTOCOLS
published: 22 March 2019
doi: 10.3389/fbioe.2019.00047

Analysis of Mechanically Activated Ion Channels at the Cell-Substrate Interface: Combining Pillar Arrays and Whole-Cell Patch-Clamp

Setareh Sianati[1,2], *Anie Kurumlian*[1,2], *Evan Bailey*[2] *and Kate Poole*[1,2]*

[1] *EMBL Australia Node in Single Molecule Science, School of Medical Sciences, University of New South Wales, Sydney, NSW, Australia,* [2] *Cellular and Systems Physiology, School of Medical Sciences, University of New South Wales, Sydney, NSW, Australia*

Ionic currents can be evoked by mechanical inputs applied directly at the cell-substrate interface. These ionic currents are mediated by mechanically activated ion channels, where the open probability increases with increasing mechanical input. In order to study mechanically activated ion channels directly at the interface between cells and their environment, we have developed a technique to simultaneously monitor ion channel activity whilst stimuli are applied via displacement of cell-substrate contacts. This technique utilizes whole-cell patch-clamp electrophysiology and elastomeric pillar arrays, it is quantitative and appropriate for studying channels that respond to stimuli that are propagated to an adherent cell via the physical substrate. The mammalian channels PIEZO1, PIEZO2 have been shown to be activated by substrate deflections, using this technique. In addition, TRPV4 mediated currents can be evoked by substrate deflections, in contrast to alternate stimulation methods such as membrane stretch or cellular indentation. The deflections applied at cell-substrate points mimic the magnitude of physical stimuli that impact cells *in situ*.

Keywords: mechanically-activated ion channels, cell-substrate interface, electrophysiology, pillar arrays, protocol

OPEN ACCESS

Edited by:
Sara Baratchi,
RMIT University, Australia

Reviewed by:
Oleg Yarishkin,
Korea Institute of Science and Technology (KIST), South Korea
Tam Thi Thanh Phuong,
The University of Utah, United States
Chilman Bae,
The University of Texas Medical Branch at Galveston, United States

***Correspondence:**
Kate Poole
k.poole@unsw.edu.au

Specialty section:
This article was submitted to Biomechanics, a section of the journal Frontiers in Bioengineering and Biotechnology

Received: *02 February 2019*
Accepted: *28 February 2019*
Published: *22 March 2019*

Citation:
Sianati S, Kurumlian A, Bailey E and Poole K (2019) Analysis of Mechanically Activated Ion Channels at the Cell-Substrate Interface: Combining Pillar Arrays and Whole-Cell Patch-Clamp. Front. Bioeng. Biotechnol. 7:47. doi: 10.3389/fbioe.2019.00047

INTRODUCTION

Cellular mechanoelectrical transduction is the conversion of a mechanical stimulus into an electrochemical response. Such signal transduction is mediated by ion channels (pore forming proteins) that exhibit increasing open probability with increasing mechanical input to the cell (Martinac and Poole, 2018). Diverse functions have been attributed to signaling via mechanosensitive or mechanically activated (MA) ion channels in mammals. MA channel activity underpins our senses of touch (Delmas et al., 2011; Lechner and Lewin, 2013) and hearing (Fettiplace and Kim, 2014), is required for the development and homeostatic maintenance of the vasculature (Li et al., 2014) and recent data suggest that MA channels are activated by cell-generated forces (Pathak et al., 2014). In addition to their physiological function, MA channels with both gain-of-function and loss-of-function mutations have been shown to lead to pathophysiological disruption in numerous cells and tissues (Lamandé et al., 2011; Bae et al., 2013; Coste et al., 2013).

Not only are MA channels expressed in a diverse set of tissues, the mechanical environments and stimuli applied to cells are also highly varied. For instance, the chondrocytes in articular cartilage

are impacted by compressive forces during joint movement, combined with shear forces as fluid moves through the joint. In addition, there are tensile forces propagated to the cells via the extracellular matrix within which the individual cells are embedded (Guilak et al., 1995; Sanchez-Adams and Athanasiou, 2011; Madden et al., 2013). At the cellular level, these distinct forces will lead to cellular compression, stretch of the cell membrane and pulling at regions of contact between cells and their surrounding matrix (referred to here as the cell-substrate interface). Similarly, during tumor development and metastasis cancerous cells experience varied mechanical environments. The mechanics at the primary tumor site reflect changes in matrix production, leading to a reduction in the compliance of the tumor microenvironment. Any invasive cells that metastasize away from the primary tumor must navigate complex and diverse environments that often require cells to enter a state of confinement (Paul et al., 2017; Van Helvert et al., 2018). The mechanosensitivity of non-motile cells can also be impacted by the underlying substrate. For instance, in sensory neurons the specific laminin substrate can locally polarize neuritic segments into active and inactive regions (over EHS-Laminin and Laminin-332, respectively) (Chiang et al., 2011).

Given the diversity of mechanics and forces that cells experience it is important to study whether MA channels are ubiquitously activated by a spectrum of mechanical inputs or whether they respond to a restricted set of mechanical cues. This then presents a challenge of how to study MA channel activity within the appropriate context. Ion channel activation leads to the passive diffusion of selected ions down their electrochemical gradient (Moorhouse, 2015), through the pore of the channel (most mammalian ion channels have a selectivity filter that limits the specific ions that can traverse the pore). In order to study channel activity, regardless of ionic permeability, the gold standard technique is to use patch-clamp electrophysiology. This set of related techniques enables the direct measurement of ionic flux across the membrane. However, in order to study mechanically activated ion channels, patch clamp measurements need to be combined with the application of a mechanical stimulus to the patched cell.

For many years the application of stretch to the membrane via the patch pipette itself has been used to study MA channels. The first measurement of mechanical activation of single channels in the cell membrane was conducted by Guharay and Sachs, by applying an increase in suction to membrane patches from chick skeletal muscle cells (Guharay and Sachs, 1984). Today, high-speed pressure-clamp (HSPC) (Besch et al., 2002) is used as a routine analysis to study such mammalian MA channels as PIEZO1 and TREK-1 and TRAAK (Coste et al., 2010; Brohawn et al., 2014; Moroni et al., 2018). As a complementary method to study macro currents, whole-cell patch-clamp is combined with the indentation of the cell with a glass rod (Drew et al., 2002; Hu and Lewin, 2006). The mammalian channels PIEZO1 and PIEZO2 will respond to such stimuli (Coste et al., 2010; Dubin et al., 2017). The MA channels identified to date cannot account for the diversity of currents evoked using cellular indentation, suggesting that there are additional MA channels that have not yet been identified.

Whilst both HSPC and cellular indentation have generated much interesting data and significantly advanced our understanding of the expression pattern and activity of MA channels, both approaches apply stimuli to the apical surface of the cell. As such, neither technique directly addresses MA channel activation at the interface between cells and their substrates. As mentioned above, this cellular compartment is critically important in cellular mechanosensing in a number of cells and tissues. In order to directly apply stimuli at this interface we developed a technique whereby mechanical stimuli can be applied to cells cultured on elastomeric pillar arrays (Poole et al., 2014). This technique represents a modification of the approach previously developed to quantify cell-generated forces (Tan et al., 2003; du Roure et al., 2005; Ganz et al., 2006; Desai et al., 2007). The channel activity in cells cultured on the arrays is monitored using whole-cell patch-clamp and stimuli are applied by deflecting an individual pilus subjacent to the cell. Pillar deflection has been shown to evoke PIEZO1, PIEZO2 (Poole et al., 2014) and TRPV4 (Servin-Vences et al., 2017; Tay et al., 2018) mediated currents and to evoke MA channel activity in primary cells, such as somatosensory neurons and chondrocytes (Poole et al., 2014; Servin-Vences et al., 2017, 2018; Wetzel et al., 2017). The technique is quantitative and preserves transmembrane force-sensing structures incorporating the substrate, extracellular matrix (ECM), cell attachments and intracellular components, such as STOML3, that can tune the sensitivity of the MA channels (Poole et al., 2014; Wetzel et al., 2017). As such, this technique can directly probe MA channels within the appropriate cellular context and be used to study how regulatory proteins modulate channel activity in intact force-sensing complexes.

Experimental Design

Cells are cultured on pillar arrays of defined dimensions. Once adhered, a high-resistance giga-Ohm (GΩ) seal is formed between a patch-pipette and the cell, the region of membrane within the patch pipette is then disrupted to enable direct fluid access between the solution in the pipette and the intracellular space. In this whole-cell patch-clamp mode any channel activity that leads to a net flux of ions across the plasma membrane can be measured. To apply stimuli, a glass probe driven by a precisely controlled manipulator is positioned adjacent a pilus located subjacent to the patched cell. A series of deflection stimuli is then applied to the cell by deflecting the pilus across the range of 1–1,000 nm. Images are acquired during the stimulations from which precise stimulus sizes can be calculated in a *post-hoc* analysis. Using this approach MA channels can be activated with molecular-scale inputs, that are applied directly at the interface between cells and their substrate.

Advantages and Limitations of Approach

The main limitation of this experimental approach to studying MA channel activity is that it can only be utilized to study channel activation in adherent, dissociated cells that express MA channels at sufficiently high levels to allow detection of

macroscopic currents. As such, *ex vivo* and *in vivo* recordings are not supported. In addition, whilst defined, quantifiable stimuli can be applied to cells, it is not possible to derive how much force impacts the MA channels themselves. This limitation is shared with the other well-established methods for evoking MA currents: In the case of cellular indentation, the contact area between stimulator and cell is unknown, the curvature of the indented membrane and the point at which the stimulator contacts the cell; in the case of HSPC, elegant experiments have been used to estimate the membrane tension required to activate PIEZO1 in membrane blebs (Cox et al., 2016), however this simplified system does not reflect the native environment of PIEZO1 *in situ*. The advantages of our approach lie in the fact that stimuli are applied via connections between cells and their substrates. The design of the experiment enables a dissection of the diverse factors that can regulate MA channel force sensing: that is, the mechanics of the substrate can be modulated, the pillar arrays can be coated with distinct ECM molecules and cellular components can be manipulated using standard molecular biology techniques. The preservation of these transmembrane structures means that the MA channel activity can be studied in an appropriate mechanical context. In addition, we have found that TRPV4-mediated currents are not robustly evoked by HSPC and not evoked at all by cellular indentation, yet pillar deflection evoked sensitive TRPV4 mediated currents. As such, there are MA channels that are only activated when stimuli are applied directly at the cell-substrate interface.

MATERIALS AND EQUIPMENT

Materials

- Positive, microfabricated masters to cast pillar arrays. These masters can be ordered from companies such as Bonda Technology Pte Ltd. (Singapore). Specifications of the masters that we have used are presented in **Table S1**. Key attributes are that pili should be at least 5 μm high.
- Glass coverglass, 22 × 22 mm, Thickness 2 (VWR, 631-0126)
- Glass coverglass 13 mm diameter, Thickness 1.5 (Menzel Glaeser, ThermoFisher Scientific, MENCSC1315GP)
- Fast curing, 2-component epoxy (Selley's 5 min Araldite, 9300697106391)
- Plastic petri dishes, 35 mm × 10 mm (Corning, 430165)
- Thick walled, filamented capilliary glass (SDR Scientific, 30-0060, GC150F)
- Microfil needles, 28 gauge/ 97 mm long (World Precision Instruments, MF 28 G - 5)

Reagents

- Cells: Any adherent cells can be tested using this protocol. Cells should be maintained in appropriate media. Proliferative cells should always be passaged before reaching 100% confluence and primary cells should be carefully isolated so as not to damage the cell membrane.
- Polydimethyl Siloxane (PDMS, Sylgard 184)
- Trichloro(1H,1H,2H,2H-perfluorooctyl)silane, 97% (Sigma-Aldrich, 448931). CAUTION: in both liquid and vapor phase this silane is toxic and corrosive.
- Cell dissociation solution, Non-enzymatic (Sigma-Aldrich, C5914)
- NaCl (Ajax Finechem, AJA465)
- KCl (Chem-supply, PA054)
- $CaCl_2$ (VWR Chemicals, 22317.260)
- $MgCl_2$ (Ajax Finechem, AJA296)
- D-Glucose, anhydrous (Chem-supply, GA018)
- HEPES ≥99.5% (Sigma Aldrich, H3375)
- EGTA > 97% (Sigma Aldrich, E4378)

Optional Reagents

- Recombinant human laminin (specific isoform will depend on experiment) (BioLamina, Sweden)
- Fibronectin, pure (Sigma Aldrich, 11051407001)
- Poly-L-Lysine, 0.01% (Sigma-Aldrich, P4707)
- Lucifer yellow, 3% in intracellular buffer (Sigma-Aldrich, L0259)
- Fugene HD (Promega, E2311)
- Lifeact-eGFP (e.g., #54610, Addgene), Lifeact-mCherry (e.g., #54491, Addgene) encoding plasmids

Reagent Preparation

- The intracellular buffer (IC) is prepared using ultrapure water with the following components: NaCl (10 mM), KCl (135 mM), $MgCl_2$ (1 mM), HEPES (10 mM), EGTA (1 mM).
- The extracellular buffer (EC) is prepared using ultrapure water with the following composition: NaCl (140 mM), KCl (4 mM), $CaCl_2$ (2 mM), $MgCl_2$ (1 mM), Glucose (4 mM), HEPES (10 mM)
- For both IC and EC buffers it is essential to adjust the pH and the osmolarity. For the EC solution the pH should be adjusted to 7.4 using sodium hydroxide. For the IC solution the pH should be adjusted to 7.2–7.3 using potassium hydroxide. To prepare the buffers as accurately as possible, first dissolve the reagents in 70% of the final volume of milli Q water. Once the desired pH is achieved, adjust the buffer volume in a volumetric flask. It is important to keep the pH consistent throughout the experiments, as it may affect the channel functions. Finally, adjust the osmolarity of the solutions to protect the plasma membrane from the excessive osmotic forces. The IC solution osmolarity should be 10–20 mOsm lower than for the EC solution. This difference increases the rate of success in forming a GΩ seal. The above recipe should result in an observed osmolarity of around 280 and 290 mOsm for IC and EC solutions, respectively. These values differ from the osmolarity predicted for ideal conditions (304 mOsm and 311 mOsm, respectively), due to the osmotic coefficients of the individual solutes. Osmolarity must be controlled with osmometer every time the buffers are made. Sucrose can be used to increase the osmolarity while keeping the ion concentrations constant. It is preferable to filter the solutions by passing through a 22 μm filter. IC solution can be dispensed at 1 mL aliquots and stored at −20°C until use. The EC buffer can be stored at 4°C up to 2 weeks.

Equipment

- Vacuum dessicator

- Oven
- pH meter
- Osmometer
- Low pressure plasma system (Diener electronic, Zepto ONE)
- Pipette puller (Sutter, P-1000)
- Microforge
- Whole-cell patch-clamp equipment installed on an inverted light microscope (Nikon, *Ti*U), fixed to an optical table to dampen vibrations and enclosed in a Faraday cage to minimize electrical noise. A micromanipulator is required to control the movement of the patch-clamp headstage (Scientifica, PatchStar). A long-distance 40x objective with an adjustable coat and a camera [CCD or sCMOS, (Nikon DS-Qi2 CMOS)] with pixels smaller than 8.5 × 8.5 µm are required for acquiring images. Electrophysiological recordings are obtained using an amplifier, with appropriate software and a digitizer [Axopatch 900B controlled by pClamp10 software and a Digidata 1550B digitizer (Molecular Devices)]. Electrodes made from chlorinated silver wire (99.99% purity).
- Nano-stimulator (Kleindiek, Germany, MM3A-LS).

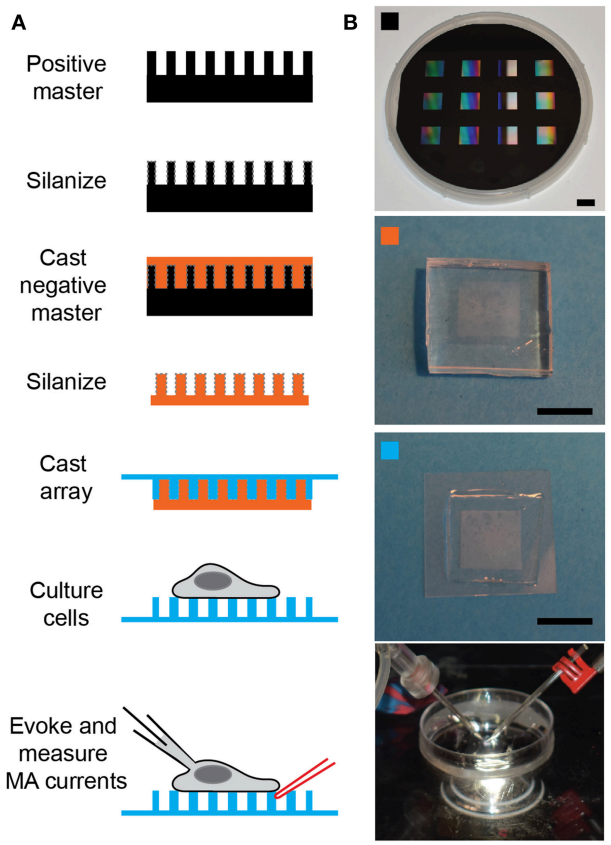

FIGURE 1 | Preparing pillar arrays. **(A)** Flow diagram outlining the steps from obtaining the positive master to analyzing MA channel activity in cells. The positive master is silanized before casting a negative master in PDMS. These negative masters are then silanized and used multiple times to cast arrays in PDMS, with a glass backing. Cells can be cultured on these arrays and then analyzed by deflecting a pilus subject to the cell with a glass probe (in red) whilst the cell is simultaneously monitored using whole-cell patch-clamp (pipette in black). **(B)** The top panel is a photograph of a positive master, then marked with an orange square is a photograph of a negative master. The panel marked with a cyan square shows a pillar array and the bottom channel shows the dish mounted on the microscope with the patch pipette on the left and the stimulating pipette mounted in the stimulator on the right. Scale bars = 10 mm.

STEPWISE PROCEDURES

Design and Order Positive Masters

Positive microfabricated masters should be designed as these silicon masters can be fragile: creating positive microfabricated masters minimizes handling. In order to culture cells and apply deflection stimuli there are some constraints on the dimensions of the elements of the array. We routinely use arrays with individual pili that are 5 µm high. The diameter and center-to-center spacing of individual pili can be varied, see **Table S1** for validated dimensions. Increasing the length and/or decreasing the diameter of pili can lead to arrays that collapse when removed from master and should be avoided.

Pause point: Once positive masters have been obtained they can be reused and will only need to be replaced if damaged or if a new design is required.

Prepare Negative Masters

In order to create negative masters from which to cast positive arrays, the positive master is first silanized (**Figure 1**). Carefully place positive master, structured side up, in a vacuum dessicator, in a fume hood. Place clean glass coverslips to either side of the master and place a 5 µl of drop of Trichloro (1H,1H,2H,2H-perfluorooctyl) silane on each of the two coverslips. Close the dessicator, apply vacuum and leave in fume hood overnight.

CRITICAL STEP: it is essential to ensure that the microfabricated master is properly silanized each time before casting negative masters. If the silanization does not create a sufficiently hydrophobic surface the negative masters will not easily peel away and the positive master may end up damaged.

CAUTION: the positive masters are fragile and should be handled with care.

CAUTION: Trichloro(1H,1H,2H,2H-perfluorooctyl)silane is toxic and corrosive in its vapor and liquid phases. Always handle in a fume hood and carefully flush the bottle with an inert gas, such as nitrogen, before storing.

After overnight silanization, remove the glass coverslips on which the Trichloro(1H,1H,2H,2H-perfluorooctyl)silane was placed and dispose of appropriately. Please note that the silane deposited on the surface of the master is no longer toxic. Carefully transfer the positive master to a disposable, flexible, heat-resistant vessel (we use 3 stacked, large weigh-boats with a high heat tolerance). Test the silanization of the master by placing a 10 µl drop of milliQ water on the surface. If the contact angle is high the silanization is effective, if the contact angle is low repeat the silanization step.

Prepare 30 mL PDMS from the two-components provided in a 1:10 ratio of curing agent:elastomer, mix extremely well and degas for 30 min. While PDMS mixture is degassing turn oven on

to 80°C. When PDMS is degassed gently pour still fluid mixture over the silanized master to a depth of 4–5 mm. Place into oven and cure for 15 min.

After curing remove from oven and very gently cut the weigh boats away from the master and PDMS. Allow to cool and turn the sandwich over. Trim excess PDMS away from the underside of the master and then turn back over so that the master is on the underside of the PDMS. Gently deform the PDMS at one edge, this should cause the PDMS to easily pull away from the master. Keep gently deforming the PDMS until the master has been completely released from the PDMS. Return master to secure, dust-free storage container until next required.

CAUTION: The PDMS should only be 4–5 mm thick and should be very gently deformed so as not to destroy the master. Take care to ensure that that when the positive master comes away from the PDMS it does not fall as it will shatter. It is recommended to have the PDMS-master sandwich sitting on a clean bench and then gently deform the PDMS up to release the master so that the master stays flat against the bench.

Immediately return the positive master to a secure, clean storage space.

Take block of PDMS and excise individual negative masters using straight-edge razor blade.

Pause point: these negative masters can be stored indefinitely in a clean environment for future use

Silanize overnight using Trichloro(1H,1H,2H,2H-perfluorooctyl)silane, as above. Note: these negative masters will be used to cast the experimental arrays, they can be used for multiple casts, but will need to periodically be re-silanized. The frequency of silanization depends on climate, in dry locations silanization every 4–5 casts is sufficient, in more humid environs silanization may need to be repeated after every use. Examples: Berlin, Germany every 5 casts, Sydney, Australia every 3 casts, Singapore, every cast.

Cast Pillar Arrays

Mix PDMS at a ratio of 1:10, curing agent:elastomer and mix thoroughly before degassing for 30 min. Whilst PDMS is degassing turn oven on to 110°C. Place silanized, negative PDMS masters patterned-side up onto a glass dish or tray. After degassing carefully drop fluid PDMS onto the top of the master (try to avoid touching the structure so that masters last longer). Spread PDMS over the top of the master and leave to sit for 30 min.

Note: 4 mL PDMS is more than sufficient to cast 12 arrays.

Activate a coverslip (22 × 22 mm, Thickness 2) for each array by placing in a plasma system and treating with oxygen plasma for 90 s. Immediately after activation place the coverslip over the PDMS-coated master and gently apply pressure so that there is a thin layer of PDMS between coverslip and master. Place the master-PDMS-coverglass sandwich in the oven for exactly 1 h.

Note: a similar elasticity (2.1 MPa) of the PDMS can be achieved by curing for 16 h at 60°C (instead of 1 h at 110°C).

After curing, remove the master-PDMS-coverglass sandwich from the oven and very carefully peel the master away from the coverslip. If the master is sufficiently silanized the PDMS should readily peel away. If, however, the silanization is insufficient, it will be more challenging to remove the PDMS and increase the likelihood of damaging the master.

Pause point: Store freshly cast pillar arrays in a clean, covered environment, such as a large petri dish and use within 1–2 weeks of casting.

Preparing Arrays for Cell Plating

Use two-component epoxy to affix array in the bottom of a dish of appropriate size to mount on the microscope fitted with patch clamp and stimulator (we use 35 mm petri dishes from Corning). Use four small dots of epoxy at the corners of the underside of the glass on which the pillar array has been cast and endeavor to apply even amounts of epoxy at each corner. Affix array in petri dish and allow to cure before moving on to next step (5 min for fast curing epoxy).

There are a number of ways to prepare the arrays for cell culture- each will depend on the cell type to be studied. We provide here options for uncoated, globally coated and coated at the tops of the arrays.

Uncoated Arrays

Adherent cells will attach to uncoated PDMS, particularly if the PDMS has been activated. Place array in plasma system and treat with oxygen plasma for 90 s. Within 30 min of this treatment, plate dissociated cells directly onto activated PDMS.

Note: this approach has been successfully used to study MA currents in chondrocytes, HEK-293T cells heterologously expressing MA channels and some cancer cell lines.

Globally-Coated Arrays

In order to investigate the role of specific ECM molecules in regulating MA channel activity, the pillar arrays can be globally coated.

Prepare a solution containing the protein of interest: laminin isoforms at a concentration of 10 μg/mL, fibronectin at 10 μg/mL or poly-L-lysine at 0.01% in PBS. Activate the arrays using oxygen plasma for 90 s and then place a drop of the protein solution on the array. Incubate for 1 h in a humidified incubator. Gently wash the array with media before plating dissociated cells on top of the array.

Coating Exclusively the Tops of the Arrays

In some cases, it is best to restrict the ECM coating exclusively to the top of the pillar structures. This approach is important when studying neuronal cells where neurite outgrowth needs to be restricted just to the tops of the array.

Option 1: Treat arrays with oxygen plasma and then leave in a sterile environment for 1 h to allow the surface to repassivate. Silanize the arrays with Trichloro(1H,1H,2H,2H-perfluorooctyl)silane for exactly 30 min. This treatment will render the array hydrophobic. Place a drop of solution containing ECM protein (see above) on the top of the array and due to the hydrophobicity the droplet will sit on top and not flow between the structured elements. Carefully cover the droplet with a small, round glass coverslip

(13 mm diameter) and leave overnight in a humidified incubator. Remove the small coverslip in the morning and then wash the array with media.

Note: it is best to leave the array submerged in cell culture media for 12–24 h to reduce the hydrophobicity of the array before plating cells.

Note: care must be taken exchanging media and buffers on these arrays as it is easy to strip all the cells off the surface if the hydrophobicity drives the liquid away from the structured area.

Option 2*:* Prepare some blocks of PDMS that are slightly larger than the structured area of the array. In this case, prepare the PDMS mixture at a ratio of 1:20 curing agent:elastomer. After degassing, cure at 110°C for 15 min. The PDMS will remain a little sticky when removed from the oven. Cut the PDMS into blocks slightly larger than the array.

Coat the PDMS blocks with the solution containing the ECM molecules (see above) and incubate for 30–60 min in a humidified incubator. Collect the excess ECM solution from the blocks (this remainder can be stored for 1 week and reused), rinse PDMS blocks with ultrapure water and dry under a stream of nitrogen. Activate the pillar array using oxygen plasma and then immediately apply the PDMS cubit, ECM coated side down, to the tops of the array. Gently apply pressure to gain a good contact between PDMS and pillar array, without disrupting the array itself. Leave for 30 min in humidified incubator before removing the PDMS cubit. These arrays are now ready for cell culture.

Note: we have found that option 1 gives a more even coating of ECM molecules [as have other researchers (Ganz et al., 2006)] but arrays prepared in this fashion are more difficult to handle, due to the increased hydrophobicity.

Culturing Cells on Arrays

Adherent cells can be studied with this technique, preparation of cells for plating on arrays will depend on timing and cell type.

For freshly isolated primary cells (Servin-Vences et al., 2017; Wetzel et al., 2017): isolate cells with standard protocols but avoid mechanical damage or disruption of membrane integrity so as to avoid disrupting the formation of a tight seal during patch-clamp analysis.

For cultured cells: If experiments are to be conducted acutely (within hours of preparation) release cells from tissue culture plastic using non-enzymatic cell dissociation solution, if experiments are to be conducted the following day, standard trypsin-based protocols can be used. A critical consideration when working with cultured cells is to ensure that they never grow past confluence, for most cultured cell lines this will reduce the ease of forming a high-resistance seal between the patch pipette and the cell membrane.

It is recommended to transfect cells with a plasmid encoding Lifeact-eGFP or Lifeact-mCherry to be able to accurately visualize the boundaries of the cell to avoid hitting the cell or any fine filopodia that may extend from the cell body. For terminally-differentiated cells that are more challenging to transfect a membrane impermeable dye, such as lucifer yellow, can be included in the patch pipette, such that the intracellular space of a cell in whole-cell mode is rendered fluorescent.

Cells should be studied within 36 h of plating to optimize patching conditions. Primary cells may need to be analyzed on the day of deposition, depending on propensity to de-differentiate (Servin-Vences et al., 2017).

Whole-Cell Patch-Clamp

Prepare glass pipettes for patching. The glass used for and shape of the patch pipettes are critical variables. We use the Sutter P-1000 puller fitted with a 2.5 mm box filament (SDR Scientific, FB255B) and thick-walled, filamentous glass (SDR Scientific, 30-0060, GC150F) to create pipettes with a resistance of 3–6 MΩ. These pipettes are fire polished with a home-made microforge before use.

Glass pipettes can be prepared the day prior to patching and stored in a dust-free container. Care should be taken to not touch the fine tip of the pipette against any surface as they are fragile and will break easily. It is critical that the end of the pipette is free from structural defects.

Prepare glass probe for pillar deflections. We convert the same types of pipettes created for patching into stimulators by heating the end with the microforge to seal the tip. Care should be taken to make sure the end is sealed, otherwise the edges of the glass can damage the cell. The tip should be no larger than 1–2 mm, if it gets too broad it is difficult to deflect pili without disrupting the cell. Glass stimulating probes can be prepared in advance and stored in a dust-free environment indefinitely until use, they can be reused until they are damaged.

Prepare both intracellular and extracellular solutions and bring to room temperature. (Pre-prepared IC buffer can be filtered, aliquoted and stored for 12 months at −20°C, EC buffer can be prepared in bulk, filtered and stored at 4°C for 1–2 weeks.)

Gently wash all media off the cells, add extracellular buffer to the dish and mount the dish on the inverted light microscope. Insert the reference electrode into the dish, making sure that it is submerged under the level of the buffer.

Change to a low power objective (10x) and select a cell that connects to pili that can be accessed with the stimulator without hitting another region of the cell. It is important to select individual cells.

Mount a glass stimulating probe in the MM3A-LS and position it so that the shadow of the glass is visible in the field of view before carefully maneuvering the stimulator close to the cell that will be patched. It is not recommended to position the stimulator directly at the pilus before patching the cell but it should be visible within the field of view to enable final positioning after the whole-cell patch configuration has been established for the selected cell.

Fill the end of a glass pipette with intracellular buffer using a syringe fitted with a very fine, long needle (only add buffer to fill the end of the pipette, as increased buffer will increase noise). Check that there are no bubbles in the pipette and mount into the pipette holder of the headstage, taking care to tighten the holding screw to ensure that the pipette is stable and sealed. Swing the manipulator over the dish and before lowering it into the extracellular buffer apply a small amount of outward pressure.

Lower the patch pipette into the extracellular buffer and note the resistance of the pipette when a test pulse is applied at a holding potential of 0 mV. If the resistance is outside 3–6 MΩ, release the positive pressure, retract and discard the pipette before starting again.

CAUTION: if the pipette does not have the desired resistance ensure that the pressure is released before trying to remove the pipette, otherwise the pipette may be expelled from the headstage holder due to the outward pressure.

Once a pipette of appropriate resistance is mounted in the headstage holder, use the course movement to position the pipette over the cell to be patched. The pipette should be oriented such that contact will be made close to the apex of the cell.

Move the 40x objective into place and ensure that the microscope is set for bright-field contrast. At this point it is essential to ensure that the camera will capture well-contrasted bright field images with the focus set to the top of the pili (**Figure 2A**). Poor bright field images will hamper the analysis of pillar movement and any adjustments of the microscope at a later stage risk disrupting the high-resistance seal between the membrane and the pipette.

Ensure that the amplifier is in "patch" mode. Approach the cell using the fine movement of the manipulator controlling the movement of the headstage until there is a 10% increase in the pipette resistance, release the outward pressure and apply inward pressure in order to form a high resistance seal between the pipette and the membrane (>1 GΩ). Use the Fast and Slow compensation to charge the pipette capacitance, adjust the holding potential to −60 mV [or appropriate voltage is the cells to be studied exhibit a different transmembrane potential, i.e., chondrocytes −40 mV (Servin-Vences et al., 2017)] and use a quick pulse of inward pressure to rupture the membrane patch. Switch the amplifier to "whole-cell" mode and use the whole-cell compensation to charge the membrane capacitance. Once the whole cell compensation has been adjusted appropriately, the series resistance should be compensated to at least 60%. For further details on the intricacies of whole-cell patch-clamp, the Axon Guide (available from the Molecular Devices website: www.moleculardevices.com) provides detailed discussion.

Applying Stimuli at the Cell-Substrate Interface

Once the cell is in whole-cell patch-clamp mode, the stimulator should be already near the cell. Start recording in voltage-clamp mode (at appropriate holding potential for the cells being studied, e.g., sensory neurons −60 mV, chondrocytes −40 mV). Finish positioning the stimulator adjacent a pilus that lies subjacent to the cell, while monitoring the voltage clamp recording to control for whether the stimulator hits the cell during the final positioning. Ensure that the stimulator will not hit any part of the cell or any fine filopodia that may extend from the cell body (cells

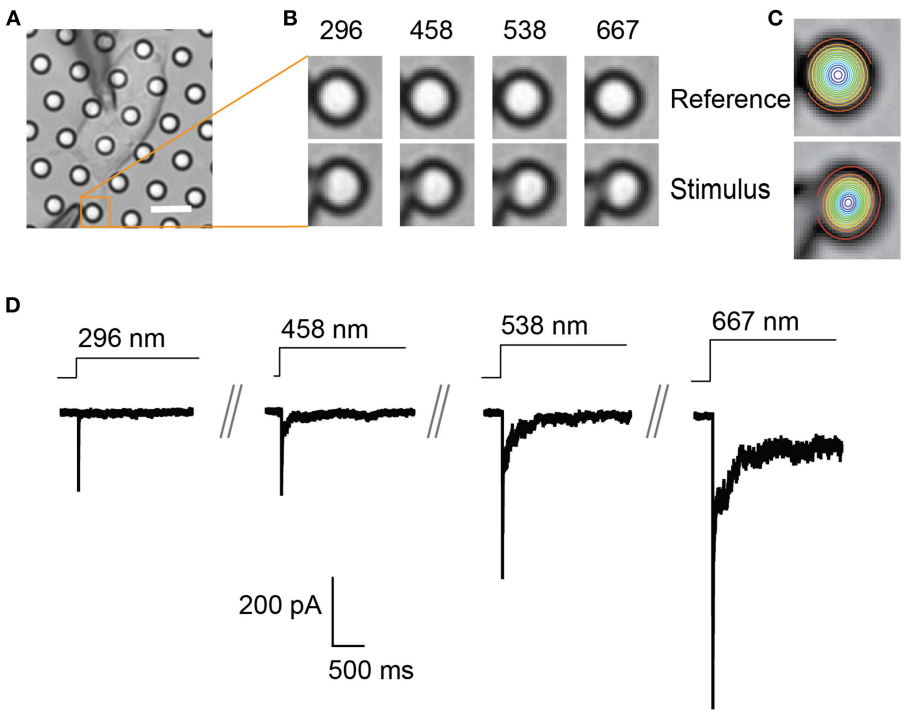

FIGURE 2 | Representative pillar deflections and corresponding TRPV4-mediated currents**. (A)** Bright-field image of a single HEK-293T cell expressing TRPV4 cultured on the pillar array, scale bar 10 μm. **(B)** Series of mechanical stimuli are applied directly at cell-substrate interface by deflecting the pilus subjacent to the cell (orange box). Middle panel shows the movement of indicated pilus in response to the stimuli of increasing magnitude from 296 to 667 nm. **(C)** The center point of the pilus is determined from a 2D Gaussian fit of intensity values in the images of before and during deflection. **(D)** Representative traces of TRPV4-mediated currents corresponding to the stimuli presented in **(B)**.

expressing a fluorescent marker such as Lifeact-eGFP or Lifeact-mCherry will enable clear visualization of the cell boundaries).

Collecting Data

Start by acquiring an image of the cell before stimulation. Begin a voltage-clamp recording and then initiate a series of deflection stimuli (**Figure 2B**). Each stimulus should be applied for a minimum of 0.5–1 s to enable acquisition of an image during each individual stimulus. A pause of 10 s between each stimulus should be employed to avoid current rundown over the course of the experiment (for each MA channel/cell type this delay should be empirically determined). It is recommended to also acquire an image between each stimulus to act as a reference for the following stimulus, thus accounting for any drift of the dish during the experiment.

In order to calculate a threshold of channel activation, apply a series of stimuli of increasing magnitude, from a few nm up to 1,000 nm. In order to generate stimulus-response curves, randomize the stimuli. It is important to apply at least 5 stimuli at a pilus that span the stimulus range. In addition, there is pilus-to-pilus and cell-to-cell variation as the stimulus region contains a restricted number of channels. As such, it is best practice to apply a series of stimuli to at least 2 pili subjacent to each individual cell. In particular, when no response is noted at an individual pilus a second pilus should be sampled.

Analyzing Data

There are two components to the analysis, characterizing the current parameters and quantifying stimulus sizes. The voltage-clamp recordings are opened in the Clampfit software and the following parameters are analyzed: current amplitude, latency, activation time constant (τ_1) and inactivation time constant (τ_2) (**Figure 3**). Current amplitudes are measured from the pre-stimulus baseline amplitude to the peak of the current. The latency is measured from the start of the stimulus to the onset of the current. The activation and inactivation time constants are calculated from a mono-exponential fit of the current rise time and current decay.

In order to quantitate the stimulus magnitude (pillar deflection) it is necessary to determine the center point of the deflected pilus from the images acquired during the experiment. Each individual pilus acts as a light guide. As such, the relative x-y co-ordinates that correspond to the center of the pilus can be calculated from a 2D Gaussian fit of intensity values. This can be achieved using the in-built analysis routines of the Igor Pro 7 analysis software (WaveMetrics Inc.). The center point of the pilus in successive images, taken before, during and after the stimulus, can then be used to calculate the exact deflection applied (**Figure 2**).

TIMING

Pre-experiment Preparation

Three weeks: design of pillar array masters and manufacture. Note, the masters generated in this step can be reused multiple times if handled with care. This step should not need to be repeated unless the masters are damaged or a new design is required.

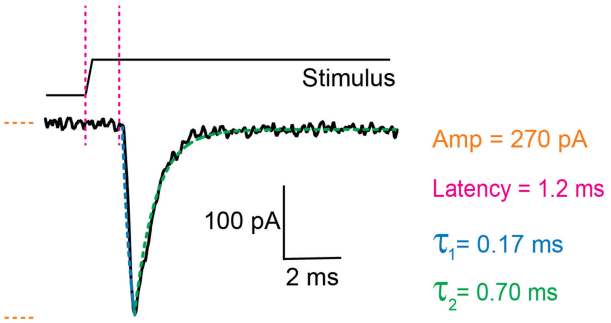

FIGURE 3 | Example trace of a mechanically activated current**.** Example trace of a deflection-gated response. Marked in orange is the amplitude of the current, in magenta the latency between stimulus and onset of the response, in blue the activation time constant (τ_1) and in green the inactivation time constant (τ_2). These data were generated in HEK-293T cells expressing TRPV4.

Sixteen hours: overnight silanization of microfabricated positive masters. critical step. do not proceed with sub-optimal silanization as the masters will be damaged

One hour: prepare negative masters using pdms. these negative masters can be used multiple times. if cared for properly they can be utilized over many months before this step will need to be repeated.

Sixteen hour: overnight silanization of negative pdms masters.

One hour: prepare IC and EC buffers for patching. CRITICAL STEP: ensure that buffers are precisely made and have the appropriate ph and osmolarity. poor buffers can lead to difficulties in forming a high resistance seal, opening the cell and maintaining a patch.

Preparation Required for Each Experiment

Two hours: casting pillar arrays

One -sixteen hours: optional coating of arrays with ECM proteins

Thirty minutes: transfer of cells to pillar arrays

Thirty minutes -sixteen hours: culture of cells on arrays before use.

Running the Experiment

Thirty minutes: preparation of patch pipettes, stimulating probe and initialization of patch-clamp rig for use, exchange of media for extracellular buffer on individual dish. CRITICAL STEP: poor pipettes will inhibit the ability to form a high resistance seal.

Two hours: maximum time any single sample should be analyzed

Five minutes: finding an appropriate cell, positioning the stimulating pipette, loading the patch pipette with IC buffer, positioning the patch pipette above the selected cell

Five seconds - Five minutes: obtaining a GΩ seal

Thirty seconds: compensating for fast and slow capacitive effects, checking patch parameters, setting a series resistance compensation

Thirty seconds: final positioning of stimulating probe

Two to five minutes: application of a series of stimuli (8–10) ranging from 1 nm−1 μm

Thirty minute: repositioning of stimulating probe adjacent a second appropriate pilus

Two to five minute: application of a series of stimuli (8–10) ranging from 1 nm−1 μm

Thirty minute: analysis of evoked currents and pillar deflections for each cell studied.

ANTICIPATED RESULTS

Currents will be evoked by pillar movements in cells expressing MA channels that can be activated by substrate deflections and increasing stimuli result in currents of increasing amplitude (**Figure 2**). To date, deflection-activated currents have been evoked in cells expressing the mechanically activated channels PIEZO1, PIEZO2, and TRPV4 (Poole et al., 2014; Servin-Vences et al., 2017; Wetzel et al., 2017; Tay et al., 2018). In addition, currents were evoked by pillar deflection in primary sensory neurons and primary chondrocytes. The primary sensory neurons contained subsets of cells with differing mechanosensitivities: a population of low-threshold mechanoreceptors and a population of high-threshold nociceptors (Poole et al., 2014). Dedifferentiated chondrocytes exhibited a decrease in the activation threshold of deflection-evoked currents in comparison with primary chondrocytes themselves (Servin-Vences et al., 2017).

There are a number of ways to compare MA currents evoked using pillar arrays. Cells can be categorized as responsive vs. non-responsive to pillar deflections within the range 1–1,000 nm. Categorical data can be compared using Fisher's exact test. A minimum of 20 cells from each condition are required (Servin-Vences et al., 2017).

In order to calculate an activation threshold, average the smallest deflection that evokes a current for each cell. These data should be assessed to determine if they exhibit a normal distribution. Parametric data can be compared using a Student's *t*-test, non-parametric with a Mann-Whitney U test. Differences can be detected with approximately 15 cells per condition (Servin-Vences et al., 2017; **Figures 4**, **5**).

The stimulus-response data collected from pillar array analysis have variation in x (deflection) and y (current amplitude); therefore, the response is grouped in bins of increasing stimulus size (0–10, 10–50, 100–250, 250–500, and 500–1,000 nm) in

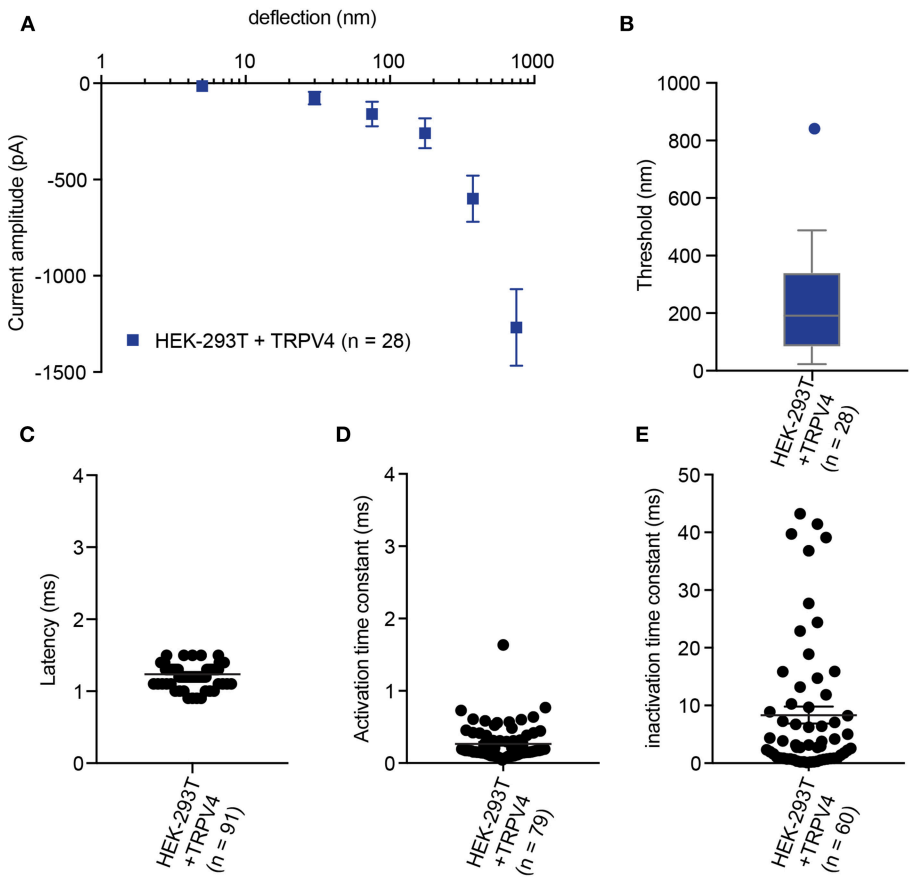

FIGURE 4 | Representative data collected using HEK-293T cells expressing TRPV4**. (A)** Stimulus-response plot of TRPV4 currents induced by pillar deflections within the range 1–1,000 nm ($n = 28$ cells) **(B)** Activation threshold of TRPV4 to substrate deflection was calculated by averaging of smallest deflection that induced current in each cell ($n = 28$ cells). **(C)** Latency of deflection-activated TRPV4 currents. **(D)** Activation time constant of TRPV4 currents evoked by substrate deflection. **(E)** Inactivation time constant of TRPV4 currents evoked by substrate deflection.

order to aid statistical comparison. For each cell, average the current amplitudes within each bin, and then average these data across cells. An ordinary two-way ANOVA with a Tukey *post-hoc* test can be used to statistically compare stimulus-response curves (Poole et al., 2014; Servin-Vences et al., 2017; Wetzel et al., 2017; Tay et al., 2018). We note that in most systems that we have tested, the stimulus-response curves of MA current amplitude exhibit large error bars. There are a number of likely reasons for this variability. The first is that the region to which stimuli are applied is delimited, corresponding to around 10 μm^2, or less. As such the contact area between cell and substrate would only contain a restricted number of activatable channels which would result in noisier data. By using fluorimetric Ca^{++} imaging we can show that the initial influx of ions in response to pillar deflection occurs at the stimulated pilus, indicating that the channels that are activated are restricted to this region of the membrane (**Figure S1**). In addition, connections between the cell and the substrate will be dynamic, likely introducing confounding factors that influence the transfer of force from the deflected pilus to the channel, such as changes in cellular adhesion and localized cytoskeletal structures. The variation within the data thus likely reflects biological variability and if sufficient cells are analyzed, differences between groups can be determined.

The comparison of thresholds and stimulus-response curves can be used to test whether specific molecules or conditions affect the sensitivity of MA currents. For instance, we used pillar array analysis to demonstrate that the membrane scaffolding protein STOML3 sensitizes both PIEZO1 and PIEZO2. In addition, STOML3 is required for the molecular-scale sensitivity of touch receptive neurons (Poole et al., 2014). In some neuropathic pain states STOML3 levels are increased, presumably leading to hypersensitivity of these neurons and we showed that blocking STOML3 oligomerization can reverse neuropathic pain-driven behaviors in a number of mouse models (Wetzel et al., 2017). Here we have presented data that demonstrates the shift in sensitivity of MA currents in the presence of STOML3 and the reduction in transduction threshold (**Figure 5**).

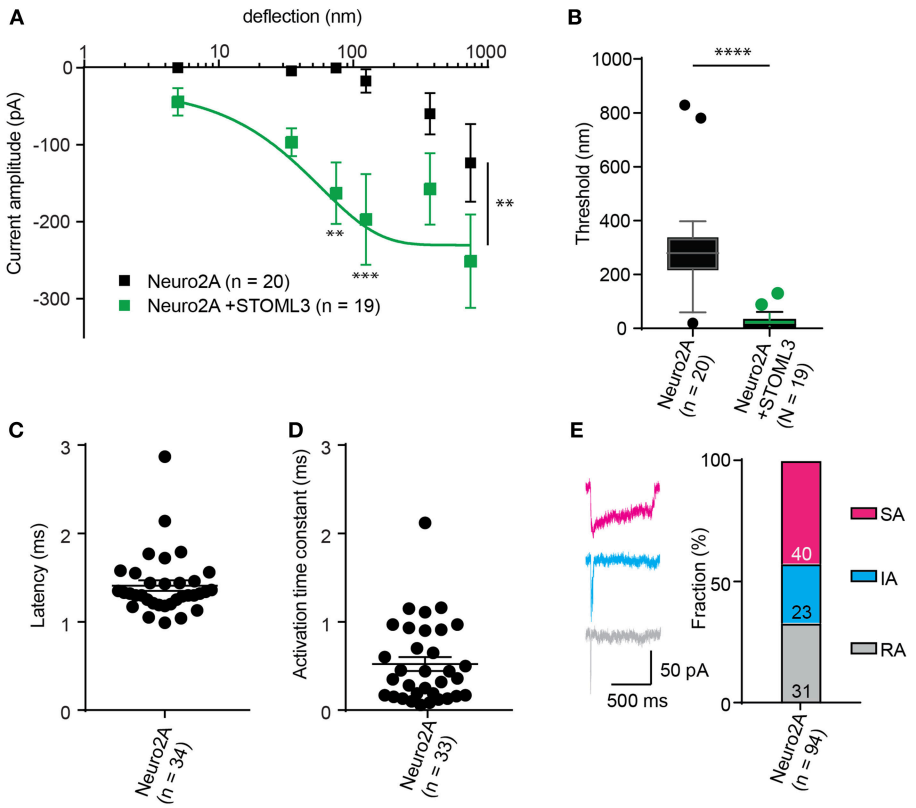

FIGURE 5 | Representative data collected using Neuro2A cells. **(A)** Stimulus-response curve generated from Neuro2A cells (endogenously expressing PIEZO1). Overexpression of STOML3 in these cells leads to a sensitization of the MA currents (Ordinary Two-way ANOVA, $n = 19$ cells and 20 cells, respectively, curve comparison $^{**}P = 0.0032$, *post-hoc* analysis of individual bins $^{**}P = 0.0043$, $^{***}P = 0.001$). Boltzmann sigmoidal fit of Neuro2A + STOML3 data (green fit line) estimates a half maximal response of ~15 nm. **(B)** An analysis of the Neuro2A cells vs. Neuro2A cells + STOML3 indicates that STOML3 significantly reduces activation threshold of deflection-activated currents in these cells (Mann Whitney *U*-Test, $^{****}P < 0.0001$, $n = 19$ cells and 20 cells, respectively). Data plotted as box and whiskey plots, Tukey. **(C)** Latency of deflection activated currents in Neuro2A cells. **(D)** Activation time constant of deflection activated currents in Neuro2A cells. **(E)** Example traces of deflection activated currents in Neuro2A cells highlighting the variability in inactivation kinetics, classed as RA ($\tau_2 < 5$ ms), IA ($5 < \tau_2 < 50$ ms), or SA ($\tau_2 > 50$ ms or non-inactivating). Categorical plot of percentage of deflection activated currents in Neuro2A cells that are classed as RA, IA, or SA (numbers correspond to number of cells in each group, total $n = 94$). A subset of these data was previously published (Poole et al., 2014).

The amplitude of currents evoked by pillar deflection in the most sensitive cells will saturate within the stimulus range, less sensitive cells do not. When the current amplitude does saturate the stimulus required for a half-maximal response can be determined from a Boltzmann sigmoidal fit of the data (calculated in GraphPad Prism 7.0) (Poole et al., 2014; **Figure 5**). In the case of touch receptive neurons or cells expressing PIEZO1 together with STOML3 the stimulus that results in a half maximal response is only ∼15 nm (Poole et al., 2014; **Figure 5**). In fact, such a deflection is less than the width of a microtubule, representing an exquisite molecular-scale sensitivity to deflections of small regions of the membrane.

In addition to the sensitivity of the evoked currents, we also analyze the kinetic parameters of individual currents. Here were present kinetics for TRPV4 (**Figure 4**) and PIEZO1-mediated currents (**Figure 5**). The anticipated latency of channels directly activated by the mechanical input should be <2 ms, and the activation time constant <1 ms. Longer latencies indicate either inhibition of the force transfer to the channel or suggest a second messenger may be required for channel activation. Slower activation time constants suggest that the transfer of force to the set of activated channels is inhibited. We have observed that the inactivation time constants vary for distinct channels. Mechanically activated TRPV4 exhibits rapid inactivation kinetics (Servin-Vences et al., 2017; Tay et al., 2018; **Figure 4**), in contrast to current kinetics observed for the osmotic activation of TRPV4 (Lechner et al., 2011). For PIEZO1-mediated currents, we observe variable inactivation kinetics. We note that a significant fraction of PIEZO1-mediated currents are non-inactivating, in contrast to much of the data published for PIEZO1-mediated currents activated by HSPC and indentation. However, Gottlieb and colleagues noted that PIEZO1 channel inactivation kinetics were labile, as they also recorded non-inactivating currents (Gottlieb et al., 2012).

SUMMARY

The technical approach to evoking MA currents described here is a powerful tool to investigate MA channel activity within an intact cell-substrate interface. This approach preserves transmembrane structures, allowing an analysis of how MA channels function within a microenvironment that mimics cellular interfaces *in vivo*. In addition, the stimulus range of 1–1000 nm is consistent with the *in vivo* magnitude of deflections and movements that cells experience. This approach can also be used to study channels such as TRPV4 that are only mechanically activated by substrate deflections (but not indentation or membrane stretch) as well as to investigate how MA channels such PIEZO1 function within intact transmembrane structures. The quantitative nature of the experiments means that subpopulations of cells with variant mechanosensitivity can be identified and the molecules that tune MA channel activity can be analyzed. This technique is appropriate for the study of ion channel mediated mechanoelectrical transduction in those systems where mechanical inputs are propagated to the cell via the surrounding microenvironment. To date, this technique has been applied to primary somatosensory neurons (Poole et al., 2014; Wetzel et al., 2017) and primary chondrocytes (Servin-Vences et al., 2017). We propose that this approach would be also appropriate for the study of mechanoelectrical transduction in additional systems, such as in tumor cells and stem cells, where changes in the physical microenvironment can impact cellular function and the balance between physiological and pathophysiological states.

DATA AVAILABILITY

All datasets generated for this study are included in the manuscript and the supplementary files.

AUTHOR CONTRIBUTIONS

Experiments were designed by KP and SS. Data were generated and analyzed by SS, AK, and EB. The manuscript was written by KP and SS with input from all of the authors.

FUNDING

This work was supported, in part, by NHMRC project grants awarded to KP, APP1122104 and APP1138595.

ACKNOWLEDGMENTS

SEM imaging was conducted by Simon Hager of the Electron Microscope Unit of the UNSW Mark Wainwright Analytical Centre.

SUPPLEMENTARY MATERIAL

The Supplementary Material for this article can be found online at: https://www.frontiersin.org/articles/10.3389/fbioe.2019.00047/full#supplementary-material

REFERENCES

Bae, C., Gnanasambandam, R., Nicolai, C., Sachs, F., and Gottlieb, P. A. (2013). Xerocytosis is caused by mutations that alter the kinetics of the mechanosensitive channel PIEZO1. *Proc. Natl. Acad. Sci. U.S.A.* 110, E1162–E1168. doi: 10.1073/pnas.1219777110

Besch, S. R., Suchyna, T., and Sachs, F. (2002). High-speed pressure clamp. *Pflugers Arch. Eur. J. Physiol.* 445, 161–166. doi: 10.1007/s00424-002-0903-0

Brohawn, S. G., Su, Z., and MacKinnon, R. (2014). Mechanosensitivity is mediated directly by the lipid membrane in TRAAK and TREK1 K+ channels. *Proc. Natl. Acad. Sci. U.S.A.* 111, 3614–3619. doi: 10.1073/pnas.1320768111

Chiang, L.-Y., Poole, K., Oliveira, B. E., Duarte, N., Sierra, Y. A. B., Bruckner-Tuderman, L., et al. (2011). Laminin-332 coordinates mechanotransduction and growth cone bifurcation in sensory neurons. *Nat. Neurosci.* 14, 993–1000. doi: 10.1038/nn.2873

Coste, B., Houge, G., Murray, M. F., Stitziel, N., Bandell, M., Giovanni, M. A., et al. (2013). Gain-of-function mutations in the mechanically activated ion channel PIEZO2 cause a subtype of Distal Arthrogryposis. *Proc. Natl. Acad. Sci. U.S.A.* 110, 4667–4672. doi: 10.1073/pnas.1221400110

Coste, B., Mathur, J., Schmidt, M., Earley, T. J., Ranade, S., Petrus, M. J., et al. (2010). Piezo1 and Piezo2 are essential components of distinct mechanically activated cation channels. *Science* 330, 55–60. doi: 10.1126/science.1193270

Cox, C. D., Bae, C., Ziegler, L., Hartley, S., Nikolova-Krstevski, V., Rohde, P. R., et al. (2016). Removal of the mechanoprotective influence of the cytoskeleton reveals PIEZO1 is gated by bilayer tension. *Nat. Commun.* 7:10366. doi: 10.1038/ncomms10366

Delmas, P., Hao, J., and Rodat-Despoix, L. (2011). Molecular mechanisms of mechanotransduction in mammalian sensory neurons. *Nat. Rev. Neurosci.* 12, 139–153. doi: 10.1038/nrn2993

Desai, R. A., Yang, M. T., Sniadecki, N. J., Legant, W. R., and Chen, C. S. (2007). Microfabricated post-array-detectors (mPADs): an approach to isolate mechanical forces. *J. Vis. Exp.* 8:e311. doi: 10.3791/311

Drew, L. J., Wood, J. N., and Cesare, P. (2002). Distinct mechanosensitive properties of capsaicin-sensitive and -insensitive sensory neurons. *J. Neurosci. Off.* 22:RC228. doi: 10.1523/JNEUROSCI.22-12-j0001.2002

du Roure, O., Saez, A., Buguin, A., Austin, R. H., Chavrier, P., Silberzan, P., et al. (2005). Force mapping in epithelial cell migration. *Proc. Natl. Acad. Sci. USA.* 102, 2390–2395. doi: 10.1073/pnas.0408482102

Dubin, A. E., Murthy, S., Lewis, A. H., Brosse, L., Cahalan, S. M., Grandl, J., et al. (2017). Endogenous piezo1 can confound mechanically activated channel identification and characterization. *Neuron* 94, 266–270.e3. doi: 10.1016/j.neuron.2017.03.039

Fettiplace, R., and Kim, K. X. (2014). The physiology of mechanoelectrical transduction channels in hearing. *Physiol. Rev.* 94, 951–986. doi: 10.1152/physrev.00038.2013

Ganz, A., Lambert, M., Saez, A., Silberzan, P., Buguin, A., Mège, R. M., et al. (2006). Traction forces exerted through N-cadherin contacts. *Biol. Cell.* 98, 721–730. doi: 10.1042/BC20060039

Gottlieb, P. A., Bae, C., and Sachs, F. (2012). Gating the mechanical channel Piezo1: a comparison between whole-cell and patch recording. *Channels* 6, 282–289. doi: 10.4161/chan.21064

Guharay, F., and Sachs, F. (1984). Stretch-activated single ion channel currents in tissue-cultured embryonic chick skeletal muscle. *J. Physiol.* 352, 685–701. doi: 10.1017/S0009838810000340

Guilak, F., Ratcliffe, A., and Mow, V. C. (1995). Chondrocyte deformation and local tissue strain in articular cartilage: A confocal microscopy study. *J. Orthop. Res.* 13, 410–421. doi: 10.1002/jor.1100130315

Hu, J., and Lewin, G. R. (2006). Mechanosensitive currents in the neurites of cultured mouse sensory neurones. *J. Physiol.* 577, 815–828. doi: 10.1113/jphysiol.2006.117648

Lamandé, S. R., Yuan, Y., Gresshoff, I. L., Rowley, L., Belluoccio, D., Kaluarachchi, K., et al. (2011). Mutations in TRPV4 cause an inherited arthropathy of hands and feet. *Nat. Genet.* 43, 1142–1146. doi: 10.1038/ng.945

Lechner, S. G., and Lewin, G. R. (2013). Hairy sensation. *Physiology* 28, 142–150. doi: 10.1152/physiol.00059.2012

Lechner, S. G., Markworth, S., Poole, K., Smith, E. S. J., Lapatsina, L., Frahm, S., et al. (2011). The molecular and cellular identity of peripheral osmoreceptors. *Neuron* 69, 332–344. doi: 10.1016/j.neuron.2010.12.028

Li, J., Hou, B., Tumova, S., Muraki, K., Bruns, A., Ludlow, M. J., et al. (2014). Piezo1 integration of vascular architecture with physiological force. *Nature* 515, 279–282. doi: 10.1038/nature13701

Madden, R., Han, S. K., and Herzog, W. (2013). Chondrocyte deformation under extreme tissue strain in two regions of the rabbit knee joint. *J. Biomech.* 46, 554–560. doi: 10.1016/j.jbiomech.2012.09.021

Martinac, B., and Poole, K. (2018). Mechanically activated ion channels. *Int. J. Biochem. Cell Biol.* 97. doi: 10.1016/j.biocel.2018.02.011

Moorhouse, A. J. (2015). "Membrane potential: concepts," in *Encyclopedia of Cell Biology,* eds R. A. Bradshaw and P. D. Stahl (Elsevier Ltd.), 218–236. doi: 10.1016/B978-0-12-394447-4.10027-6

Moroni, M., Servin-Vences, M. R., Fleischer, R., Sánchez-Carranza, O., and Lewin, G. R. (2018). Voltage gating of mechanosensitive PIEZO channels. *Nat. Commun.* 9, 1–15. doi: 10.1038/s41467-018-03502-7

Pathak, M. M., Nourse, J. L., Tran, T., Hwe, J., Arulmoli, J., Le, D. T. T., et al. (2014). Stretch-activated ion channel Piezo1 directs lineage choice in human neural stem cells. *Proc. Natl. Acad. Sci. U.S.A.* 111, 16148–16153. doi: 10.1073/pnas.1409802111

Paul, C. D., Mistriotis, P., and Konstantopoulos, K. (2017). Cancer cell motility: Lessons from migration in confined spaces. *Nat. Rev. Cancer* 17, 131–140. doi: 10.1038/nrc.2016.123

Poole, K., Herget, R., Lapatsina, L., Ngo, H.-D., and Lewin, G. R. (2014). Tuning Piezo ion channels to detect molecular-scale movements relevant for fine touch. *Nat. Commun.* 5:4520. doi: 10.1038/ncomms4520

Sanchez-Adams, J., and Athanasiou, K. A. (2011). "Biomechanical characterization of single chondrocytes," in *Cellular and Biomolecular Mechanics and Mechanobiology*, ed. A. Gefen (Berlin, Heidelberg: Springer Berlin Heidelberg), 247–266.

Servin-Vences, M. R., Moroni, M., Lewin, G. R., and Poole, K. (2017). Direct measurement of TRPV4 and PIEZO1 activity reveals multiple mechanotransduction pathways in chondrocytes. *Elife* 6. doi: 10.7554/eLife.21074

Servin-Vences, M. R., Richardson, J., Lewin, G. R., and Poole, K. (2018). Mechanoelectrical transduction in chondrocytes. *Clin. Exp. Pharmacol. Physiol.* 45, 481–488. doi: 10.1111/1440-1681.12917

Tan, J. L., Tien, J., Pirone, D. M., Gray, D. S., Bhadriraju, K., and Chen, C. S. (2003). Cells lying on a bed of microneedless: an approach to isolate mechanical force. *Proc Natl Acad Sci U.S.A.* 100, 1484–1489. doi: 10.1073/pnas.0235407100

Tay, A., Sohrabi, A., Poole, K., Seidlits, S., and Di Carlo, D. (2018). A 3D magnetic hyaluronic acid hydrogel for magnetomechanical neuromodulation of primary dorsal root ganglion neurons. *Adv. Mater.* 30, 1–8. doi: 10.1002/adma.201800927

Van Helvert, S., Storm, C., and Friedl, P. (2018). Mechanoreciprocity in cell migration. *Nat. Cell. Biol.* 20, 8–20. doi: 10.1038/s41556-017-0012-0

Wetzel, C., Pifferi, S., Picci, C., Gök, C., Hoffmann, D., Bali, K. K., et al. (2017). Small-molecule inhibition of STOML3 oligomerization reverses pathological mechanical hypersensitivity. *Nat. Neurosci.* 20, 209–218. doi: 10.1038/nn.4454

Conflict of Interest Statement: The authors declare that the research was conducted in the absence of any commercial or financial relationships that could be construed as a potential conflict of interest.

frontiers in Bioengineering and Biotechnology

REVIEW
published: 27 March 2019
doi: 10.3389/fbioe.2019.00055

Stretch in Focus: 2D Inplane Cell Stretch Systems for Studies of Cardiac Mechano-Signaling

Oliver Friedrich[1,2,3,4]*, *Anna-Lena Merten*[1,3,4], *Dominik Schneidereit*[1,3,4], *Yang Guo*[2,5], *Sebastian Schürmann*[1,3] *and Boris Martinac*[2,5]*

[1] Institute of Medical Biotechnology, Friedrich-Alexander-University Erlangen-Nürnberg, Erlangen, Germany, [2] Mechanosensory Biophysics Laboratory, Victor Chang Cardiac Research Institute, Darlinghurst, NSW, Australia, [3] Erlangen Graduate School in Advanced Optical Technologies, Friedrich-Alexander-University Erlangen-Nürnberg, Erlangen, Germany, [4] Muscle Research Center Erlangen, Friedrich-Alexander University Erlangen-Nürnberg, Erlangen, Germany, [5] Faculty of Medicine, St Vincent's Clinical School, University of New South Wales, Darlinghurst, NSW, Australia

OPEN ACCESS

Edited by:
Sara Baratchi,
RMIT University, Australia

Reviewed by:
Shamik Sen,
Indian Institute of Technology Bombay, India
Allen Liu,
University of Michigan, United States
Ken Takahashi,
Okayama University, Japan

***Correspondence:**
Oliver Friedrich
oliver.friedrich@fau.de
Boris Martinac
b.martinac@victorchang.edu.au

Specialty section:
This article was submitted to Biomechanics, a section of the journal Frontiers in Bioengineering and Biotechnology

Received: 18 January 2019
Accepted: 04 March 2019
Published: 27 March 2019

Citation:
Friedrich O, Merten A-L, Schneidereit D, Guo Y, Schürmann S and Martinac B (2019) Stretch in Focus: 2D Inplane Cell Stretch Systems for Studies of Cardiac Mechano-Signaling. Front. Bioeng. Biotechnol. 7:55. doi: 10.3389/fbioe.2019.00055

Mechanobiology is a rapidly growing interdisciplinary research field, involving biophysics, molecular and cell biology, biomedical engineering, and medicine. Rapid progress has been possible due to emerging devices and tools engineered for studies of the effect of mechanical forces, such as stretch or shear force, impacting on biological cells and tissues. In response to such mechanical stimuli, cells possess various mechanosensors among which mechanosensitive ion channels are molecular transducers designed to convert mechanical stimuli into electrical and/or biochemical intracellular signals on millisecond time scales. To study their role in cellular signaling pathways, devices have been engineered that enable application of different strain protocols to cells allowing for determination of the stress-strain relationship or other, preferably optical, readouts. Frequently, these devices are mounted on fluorescence microscopes, allowing simultaneous investigation of cellular mechanotransduction processes combined with live-cell imaging. Mechanical stress in organs/tissues can be complex and multiaxial, e.g., in hollow organs, like lung alveoli, bladder, or the heart. Therefore, biomedical engineers have, in recent years, developed devices based on elastomeric membranes for application of biaxial or multiaxial stretch to 2D substrate-adhered or even 3D-embedded cells. Here, we review application of stretch technologies to cellular mechanotransduction with a focus on cardiovascular systems. We also present new results obtained by our *IsoStretcher* device to examine mechanosensitivity of adult ventricular cardiomyocytes. We show that sudden isotropic stretch of cardiomyocytes can already trigger arrhythmic Ca^{2+} transients on the single cell level.

Keywords: mechanotransduction, mechanosensitive (MS) ion channel, cardiac mechano-electric coupling, arrhythimas, PDMS (polydimethylsiloxane)

INTRODUCTION

The heart is an electro-mechanical organ able to transform mechanical stimuli into electrical signals (Kohl et al., 1999). The heart is pumping blood and thus, supplies organs with oxygen and nutrients. By acting at the cellular level, mechanical forces alter the cardiac electrical function in a process referred to as mechano-electric feedback (MEF). The conversion of mechanical force into

electrical and biochemical intracellular signals is, e.g., mediated by mechanosensitive (MS) ion channels. To date, the molecular identity of MS ion channels underlying cardiac MEF has not been well-characterized, although several TRP-(transient receptor potential)-type ion channels have been implied in cardiac function (Ward et al., 2008; Dyachenko et al., 2009), particularly in mechano-pathologies including cardiac hypertrophy and congestive heart failure (Seo et al., 2014; Nikolova-Krstevski et al., 2017). Although there are many potential candidates among known MS channels that could underlie and contribute to cardiac MEF, there is currently no direct evidence for their role in MEF, except for the TRPC6 and TRPC3 channels (Dyachenko et al., 2009; Seo et al., 2014; Yamaguchi et al., 2017). In other cases, it remains unclear whether ion channels correlated with pathological stress responses were inherently mechanosensitive and thus, directly involved or indirectly activated by G-protein coupled receptors (Gottlieb et al., 2008; Hill-Eubanks et al., 2014; Wilson and Dryer, 2014).

Discovery of the Piezo family of MS ion channels presents one of the recent breakthroughs in eukaryotic mechanobiology (Coste et al., 2010). Given the recent evidence showing the important role that Piezo1 mechanosensitive channels play in cardiovascular mechanosensing (Li et al., 2014), the underlying molecular mechanisms have attracted growing interest, including further studies of the respective mechanosensors in cardiac signaling, i.e., MEF, and their associated signaling pathways. To allow direct investigation of the mechanosensory signaling *in vitro* by applying stretch or shear forces to cardiomyocytes and cardiac or vascular endothelial cells, it is important to employ devices for application of different mechanical strain protocols mimicking as close as possible those experienced by cardiac and vascular cells *in vivo*. Such investigations should also help to reconcile previous correlative studies of ion channel expression and function under conditions of heart disease with single cell models (Friedrich et al., 2012, 2017). Hemodynamic volume/pressure load in the heart, as a hollow organ, is associated with multiaxial wall distension. A volume/pressure overload causes *inplane* 2D stretching of individual cardiomyocytes in multiple directions (Friedrich et al., 2017). This challenge prompted biomedical engineers to design and further develop multiaxial cell stretch systems, which have enabled studies of chronic heart distension on a cellular level.

In this paper, we briefly review recent approaches in biomedical engineering toward development of stretch devices enabling application of biaxial or multiaxial stretch to cells. We further discuss the advantages of the *IsoStretcher* (**Figure 1A**), a new cell stretch system engineered by the authors that overcomes some previous limitations (Schürmann et al., 2016). In addition, we show that single adult ventricular cardiomyocytes can be stretched isotropically when following a 3D-hydrogel embedding approach that allows for inplane cell stretch to be applied and Ca^{2+} transient activity to be immediately observed with minimum z-shift of the optical axis.

PULLING THE STRINGS AND BEYOND

Stretching single cells can be a tedious and cumbersome undertaking, in particular with smaller cell geometries. Given their large sizes with diameters up to ∼100 μm and lengths from several hundreds of μm up to exceeding 10 cm, depending on the species, skeletal muscle single fibers have been a first prototype of cells subjected to longitudinal stretch. Since skeletal muscle serves predominantly as a linear bioactuator, uniaxial stretch systems were the obvious design. Early systems were research-designed machines, mostly consisting of an opposing configuration of a force transducer pin and a static counter-pin of infinite stiffness, the latter of which could be actuated to stretch the preparation, while the former served to measure passive restoration forces and/or active force generation upon fiber activation (e.g., Ter Keurs et al., 1978; Moss, 1979). The dissection, handling, and fixing of single muscle fibers into such biomechatronics systems for subsequent biomechanics recordings still is a tedious procedure confined to a few labs worldwide with also limited throughput due to manual handling of the systems (Lamb and Stephenson, 2018). As for their lengths, single muscle fibers can well be manually tied to macroscopic needles for stretching using micro-knots from braided silk or tweezer clamps with a long portion of the single cell preparation still intact between the stretch posts (Roche et al., 2015). Recently, such a biomechatronics system capable of directly assessing stress-strain relationships has been automated in a robotized environment to increase throughput (Haug et al., 2018).

However, in cases where cell types become substantially smaller than skeletal muscle fibers, the concept of manually tying/clamping cells to stretch posts/needles becomes non-feasible. This applies to most other cellular systems of the body where cells mostly fall into the range of tens of microns up to just exceeding 100 μm. For rod-shaped human ventricular cardiomyocytes that are at the upper end of the spectrum, typical diameters are ∼25 μm and lengths range 60–140 μm (Tracey and Sander, 2011). Bioengineers around Jonathan Lederer from Fischell Department of Bioengineering of University of Maryland drove the engineering and validation of a so-called *Cell Tester* device, together with a small enterprise from Heidelberg, Germany (Scientific Instruments, SI Heidelberg). This system that is now commercialized by World Precision Instruments (https://www.wpiinc.com/blog/category/cell-tester/) enables to manually grab individual cardiomyocytes by their ends and stretch them uniaxially. The system contains a chamber holding a 35 mm glass bottom dish containing, e.g., cardiomyocytes, and a rotational cuvette around the dish rim to also apply jets of solution to facilitate positioning of a single CM in the XY plane with their long axis in between an optical force transducer pin and an actuator-pin connected to a stepper motor for stretching cells. An electrically-driven clamp-tweezer mechanism allows one to grab and squeeze both ends of a single cell tightly. The whole system fits on top of inverted research-microscopes to perform, for instance, fluorescence recordings. The optical path of the microscope remains undisturbed and z-focus is adjusted with actuating the focus lens. Applying 8% uniaxial stretch to single cardiomyocytes and recording Fluo-4 Ca^{2+} sparks, Prosser et al. were able to identify a "stretch-induced tuning of RyR2 to increase Ca^{2+} signaling sensitivity in healthy cardiomyocytes" and trigger Ca^{2+} sparks in a nicotinamide adenine nucleotide phosphate oxidase 2 (NOX2)-reactive oxygen species (ROS)-dependent process (Prosser et al., 2011). Although an elegant

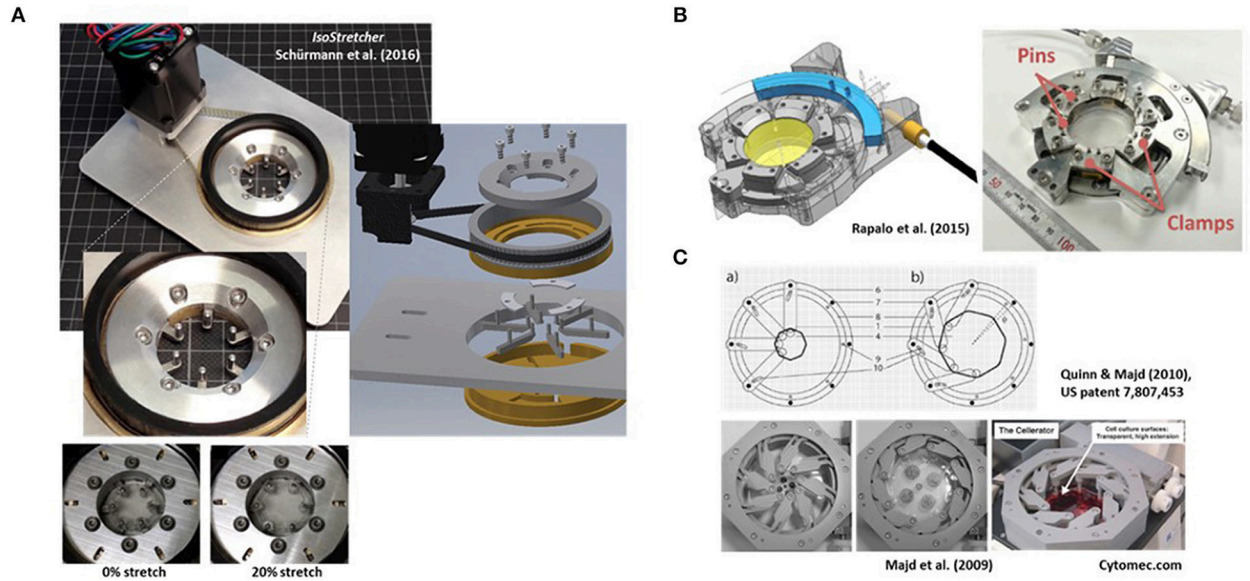

FIGURE 1 | Examples of research-built and—inspired commercial inplane stretch systems that can be suitable for studies of cardiac cells and mechano-electric feedback. **(A)** The *IsoStretcher* device, first described in Schürmann et al. (2016) that uses a V-belt driven, swivel motor actuated rotational-to-radial translation for displacement of six hook-sliders to stretch a PDMS-cast biochamber. Maximum radial stretch of the system is ∼20%. An improved current version (2018) is shown. **(B)** Radial displacement PDMS chamber lip clamp system introduced by Rapalo et al. (2015) to combine isotropic stretch of cells in large culture dishes (about 4 cm diameter) for confocal of atomic force microscopy. Maximum linear strain was 20%. Taken with permission from Rapalo et al. (2015). **(C)** An iris-like actuated system that uses eight PDMS substrate (HERS: high-extension silicon rubber) holding arms that are screwed to an outer frame allowing rotational degree of freedom of movement while the inner substrate pillar will be pulled toward the outer frame once the outer ring is actuated. For details see Quinn and Majd (2010). Isotropic surface expansions up to 1,000% have been described (Majd et al., 2009). The system was commercialized as Cellerator by the Swiss company Cytomec until 2017. (Adapted from Majd et al., 2009).

bioengineering solution to an emerging problem of studying mechano-chemical coupling in the heart, the system has several limitations: (i) it is bulky and represents a major investment (roughly 50 kUSD), (ii) through squeezing the cells at the end, parts of the cell may be strongly damaged, (iii) it can only be used for acute or short-term observations, investigating either freshly bioseparated or cultured cardiomyocytes/cells (i.e., it has no bioreactor chamber), (iv) handling is still limited to one cell at a time thus, limiting throughput and moreover, (v) cells are investigated in a free-floating environment void of any cell-cell contact or extracellular matrix which is important when addressing questions involving focal adhesion complex (FAC) regulation, and (vi) stretch is purely uniaxial. Although some points can be worked around, e.g., for (ii) using a bioadhesive glue to attach cells (Prosser et al., 2011) or (v) by using organoids, the limitations of throughput, restriction to uniaxial stretch and unavailability of FACs in single cells are of a system-inherent nature.

2D INPLANE CELL STRETCH SYSTEMS FOR HIGH-CONTENT MICROSCOPY

In order to increase throughput in so-called high-content assays, engineers have explored alternative ways of developing silicon-elastomer-based methodologies to allow adherence of many cells on flexible substrates for defined stretches to cells. A detailed review of the history of poly-dimethyl-siloxane (PDMS) polymer-engineering and its properties related to biocompatibility, elasticity and hydrophobicity can be found in our previous work (Friedrich et al., 2017). Briefly, PDMS is highly biocompatible and bioinert, and its elasticity can be tuned by varying the ratios of base DMS compound and cross-linker before polymerization. Due to its high hydrophobicity, it must be functionalized prior to seeding and attachment of cells (Friedrich et al., 2017). With tuning of the substrate elasticity, the stiffness of respective tissues can be mimicked in order to facilitate FAC building of seeded cells simulating their natural environment (i.e., soft vs. stiff substrates). However, for matrices mimicking elasticity moduli of very soft tissues with values of ∼1 kPa or below (e.g., stem cells, neuronal tissue; Even-Ram et al., 2006), either use of polyacrylamide gels or PDMS blends (using commercially available such as Sylgard 527 and 184) has been shown to be superior over single PDMS types (Palchesko et al., 2012). Including these environmental mechanical cues into cell culture technologies has become an indispensable tool in mechanobiology (Engler et al., 2006; Kurpinski and Li, 2007; Wipff et al., 2009), and also for cardiac research (Galie et al., 2013). Using downstream chemical processing of custom-made PDMS membrane geometries after curing in molds, extracellular matrix proteins, e.g., collagen, fibronectin, laminin, etc., can be covalently cross-linked to the stretchable PDMS substrate following PDMS oxygenation and silanization to increase hydrophilicity, which significantly improves attachment, spreading and proliferation of, e.g., fibroblasts (Wipff et al., 2009).

The major challenge in applying strain to PDMS membranes containing an adhered cell system is to define the directionality of stretch regarding the strain axis to be actuated and the respective biological readout for the respective cell system. For a long time, pneumatically driven systems were the leading technology, commercialized e.g., by FlexCell International Corporation (http://www.flexcellint.com/). This included sealing the PDMS membrane against a closed chamber to which negative or positive pressure could be applied via an external pressure generator. Obviously, the bulging of the membrane, although allowing for extended cyclic stretch trains, precluded use of imaging due to vast focus shifts of the substrate membrane (e.g., Kreutzer et al., 2014). A detailed discussion of those systems is given in Friedrich et al. (2017).

In order to pursue bioengineering of stretchable substrates for a more *inplane* stretch suitable for simultaneous microscopy, uniaxial stretch systems were developed as the predominant mode of actuation at the time. Those PDMS chambers were slid over polymer or metal rods on the outer chamber rim, fixing them to the base plate of a stepper motor geometry for strain applications and mounted on inverted microscopes. Using such an approach for 2D strain-culture of endothelial (HUVEC, human umbilical vein endothelial cells) cells, a preferential alignment of cells perpendicular to the main strain axis was observed (Matsumoto et al., 2007). This was also confirmed in our recent studies using atrial endothelial cells (Nikolova-Krstevski et al., 2017). Applied to endothelial cells in 3D, uniaxial strain direction was found to regulate directionality of cellular process sprouting within the hydrogel (fibrin-gel) (Matsumoto et al., 2007). In another study focusing on human bone osteosarcoma cells, a custom-made stretch device applying 5% uniaxial stretches to 50 kPa stiff elastic silicone films to which cells were adhered via fibronectin-coating was able to demonstrate rapid focal adhesion growth within seconds after stretching (Chen et al., 2013). All those biological processes were accessible to live-imaging, proving the inplane stretch criterion for associated imaging. However, one must keep in mind that z-focus shifts are inevitable due to volume conservation considerations of the material upon stretch in the elastic deformability regime thus, with stretch, the substrate membrane will always become thinner and the focus eventually shift. Although uniaxial PDMS substrate stretch systems suitable for reproducible cyclic stretch and live cell imaging have been employed, for instance, to visualize YFP-paxilin FAC remodeling in rat embryonic fibroblasts, the thinning of PDMS membranes in simple clamp-stretch devices usually requires manual re-adjustment of focus before acquiring cell images after each stretch (Shao et al., 2013). As detailed below, designing a chamber geometry with adequate mass distribution on the walls to dissipate the strain in order to minimize focal shifts of the thin membrane window portion has become the most challenging engineering aspect which becomes more eminent with higher optical resolution imaging techniques. One of the current market leaders in distributing PDMS stretch chambers with actuators for uniaxial stretch applications is STREX Inc. in Osaka, Japan (http://strex.co.jp/).

INDENTER RING-BASED INPLANE CELL STRETCH SYSTEMS WITH FLEXIBLE STRAIN GEOMETRIES

In the last few years, biophysical considerations regarding wall tension in hollow organs have led to a refinement of more physiological requirements toward strain applied to cellular systems (Huang et al., 2010; Friedrich et al., 2012). It was hypothesized that physiological wall tension at least was multiaxial in most cases, and even equibiaxial or isotropic in some case, for instance lung alveoli, bladder urothelia, etc. (Arold et al., 2007; Friedrich et al., 2012). Also, for more complex hollow organs like the heart, equibiaxial stretch during diastole might be a first approximation, while in skeletal muscle as linear bioactuator, uniaxial strain certainly remains the primary mechanical stressor. With these considerations came the necessity for new bioengineered systems to routinely apply multiaxial stretch to cells on flexible elastomer membranes while additionally allow for high-resolution microscopy with minimum focal shift. The very first systems employed the concept of actuating indenter rings over the PDMS membrane up and down an underneath indentation post to stretch and de-stretch the membrane as the indenter pulled the membrane down and up, respectively (Hung and Williams, 1994; Sotoudeh et al., 1998). By employing indenter rings with either central circular or rectangular geometry, Huang et al. (2010) were able to switch between uniaxial and equibiaxial (isotropic) stretch by simply exchanging the indenter rings. Mounting this system on top of an inverted microscope, they were able to show that equibiaxial (isotropic) stretch induced more focal adhesion complexes between cells and fibronectin-coated PDMS substrate when applying biaxial over uniaxial cyclic stretch in a 2D culture of bovine aortic endothelial cells, demonstrating the differential effects of both stretch regimes (Huang et al., 2010). By inclusion of tracking particles in the PDMS layer of known substrate stiffness, traction force microscopy can even be applied by evaluating the displacement distribution of tracking particles and calculating local strain fields (Wipff et al., 2009; Legant et al., 2010). Although equibiaxial stretch systems had been refined in the last few years for strain homogeneity (Urseka et al., 2014), those systems have to our knowledge largely remained confined to the academic community with no larger attempts for commercialization. One shortcoming of indenter-based systems is in the permanent direct contact of the PDMS membrane with the post material. This can readily lead to elastomer damage and pre-mature rupture in long-term tests. Some reports have mentioned use of lubricants between loading posts and PDMS membrane to reduce friction (Kreutzer et al., 2014) which, however, may also limit visualization attempts. Given those considerations, a free-floating substrate, rather than a direct contact configuration through indentation of the PDMS membrane, might be preferable.

In order to follow such an approach, we and others have bioengineered isotropic stretch systems based on either radial displacement of point-fixations on the outer periphery of a circular stretch-chamber (Rapalo et al., 2015; Schürmann et al.,

2016) or an iris-like mechanism (Majd et al., 2009). Those will be the focus of the following sections, followed by new application data from our *IsoStretcher* system to ventricular cardiomyocytes. One pneumatically-driven equibiaxial stretch system containing elastomeric PDMS micropost arrays suitable to convert pneumatically controlled negative pressure to bending of microposts and thus, traction forces on point attachments to cell membranes in a lab-on-a-chip format for high content imaging, shall be mentioned here for completeness (Mann et al., 2012).

RADIAL DISPLACEMENT ACTUATION TECHNOLOGIES (E.G. *ISOSTRETCHER*)

In 2016, we described the first generation of the *IsoStretcher*, an inplane isotropic stretch system. This employs equitriaxial radial displacement of a circular PDMS membrane-designed stretch chamber by a V-belt translated, grab swivel motor-driven radial displacement of six evenly distributed pull points in the periphery of the chamber through six linear sliders (Schürmann et al., 2016). Those sliders are guided in six radially oriented grooves underneath the chamber drilled into the lower base with two upward-facing pins at each end. One end is inserted into equivalent holes of the PDMS chamber ring while the pin of the outer end is inserted into a translation ring connected to the V-belt drive, containing six oblique grooves to guide the pins to the outer radial position as the ring turns. **Figure 1A** shows an improved current version of the system, reflecting a market prototype for upcoming commercialization. Compared to the previous version (Schürmann et al., 2016), polymer materials in moving parts have been replaced by steel and aluminum parts for better durability, the microcontroller and software updated and PDMS chambers refined for larger volumes of up to 1 ml as compared with the previous low volume chamber of ∼100 µl. New casting molds were also designed and polished, resulting in better transparency of the PDMS bottom for microscopy. We have validated the system to prove isotropicity and homogeneity of stretch as well as confirming a very low z-drift during stretch in the range of ∼15 µm under optimum conditions, allowing one to follow cells during stretch in real time (see supplemental video in Schürmann et al., 2016). One conclusion from our previous study was that increase in cell surface area had to be calibrated once for each new cell line and coating combinations to make sure that cells actually follow the applied hardware stretch and did not (partially) detach from the substrate, giving rise to false interpretations (Schürmann et al., 2016). Unlike in uniaxial stretch where the sample stretch matches the hardware stretch, in isotropic systems, the percentage increase in radial displacement dr/r translates to the PDMS substrate area increase dA/A according to:

$$dA = 2\pi \cdot r \cdot dr = 2\pi \cdot \frac{r^2}{r} \cdot dr \iff \frac{dA}{A} = 2 \cdot \frac{dr}{r} \qquad (1)$$

This means that a 10% increase in membrane area is achieved by a 5% radial pin displacement in the *IsoStretcher*. The IsoStretcher comes with a base plate to fit the stage of any commercial inverted research microscope and allows excellent high content imaging with long working distance objectives (modifications toward high-resolution immersion imaging are possible). The system is very light (∼200 g) and allows hardware stretch up to 20% (membrane stretch of 40%). The system allows one to apply cyclic and static stretch application. The stretch profile can be programmed to follow any given profile (saw tooth, sinusoidal, or rectangular). Given the minimum displacement velocity of 0.1%/s, and maximum around 40%/s, we usually use 20%/s which allows a 20% stretch within a second. Velocity can be tuned in steps of 0.1%/s, where the smallest displacement resolution is at 0.05% radial displacement.

At about the same time, Rapalo et al. (2015) presented a similar, yet more bulky system, to isotropically stretch PDMS membrane chambers of ∼30 mm diameter using six evenly spaced clamp tabs containing two holes for fixation to the posts of six clamps (**Figure 1B**). A linear driver converts the motor rotation to a one-dimensional motion to control isotropic stretch of up to 20% radial displacement of clamps (Rapalo et al., 2015). Translation of radial strain to linear displacement between human bronchial epithelial cells (16HBE) cultured directly on the PDMS membrane was verified by measuring the nearest neighbor distances of fluorescently labeled (DAPI) nuclei (Rapalo et al., 2015). However, in contrast to our approach of directly measuring cell surface extension upon stretch and thus, dA/A, no affirmation of whether cells were indeed tightly adhered to the PDMS membrane was provided. Also, the report did not state any functionalization of the PDMS membrane with matrix proteins or oxygenation, which renders a tight adherence to the hydrophobic PDMS membrane questionable. So far, there is no update on further refinement of the system, nor its commercialization.

IRIS-LIKE STRETCH DEVICE SYSTEMS FOR LARGE AREA INCREASE APPLICATIONS (*CELLERATOR*)

In 2009, Majd and colleagues from the Hinz lab at EPFL, Lausanne, published a novel system for dynamic cell culture of stem cells under isotropic stretch (Majd et al., 2009), based on their US patent US 7,807, 453 B2 (issued October 5, 2010) "Device for cell culture on deformable surfaces" (**Figure 1C**). High-extension silicon rubber (HERS; elastic modulus 8–25 kPa, Majd et al., 2009) was injection-molded in the shape of a cell culture dish containing elastomer hollow pillars fitting around the periphery of the chamber. Those were slid over pins within an iris-like actuated system with eight holding arms screwed to an outer frame allowing rotational movement thus, pulling the inner substrate pillars toward the outer frame (**Figure 1C**). Using the HERS over conventional PDMS, surface expansions of up to 1,000% were described. Those were used in confluent 2D cell cultures to maintain relatively constant cell densities during proliferation and to prevent contact inhibition. Since the HERS dish was biocompatible and of very good transparent quality, it was used to keep human mesenchymal stem cells over 9 weeks in dynamic expansion culture without contact inhibition

and under optical surveillance (Majd et al., 2009). The system was further used in subsequent studies by the inventors (Majd et al., 2011; Khayat et al., 2012; Klingberg et al., 2014) and was commercialized as *Cellerator* device by the Swiss company Cytomec, founded by T.M. Quinn in 2005, until 2017 when the company was dissolved.

In summary, isotropic or biaxial stretch devices for mechanobiology research have not been widely introduced on the market for a broad audience, and with the cessation of Cytomec and the *Cellerator*, the only other company with a biaxial stretcher portfolio seems to be *CellScale Biomaterials Testing* (www.cellscale.com/products/mcb1/). Their system uses a sophisticated star-shaped mesh pulling eight connected pillars holding a PDMS dish underneath. However, since their system is enclosed in a bioreactor box with no optical access, there is currently no other commercial solution available for live-cell imaging of stretched cells. To fill the gap, attempts for commercialization of the *IsoStretcher* are underway.

APPLICATION OF THE *ISOSTRETCHER* IN HEART MECHANOBIOLOGY RESEARCH

In our initial publication, we had validated the *IsoStretcher* for reliable inplane stretch of 2D cell cultures using endothelial or epithelial cell lines (e.g., HeLa cells, HEK293 cells, atrial HL-1 cells; Schürmann et al., 2016; Friedrich et al., 2017). Since then, we have applied our system to other adherent cell lines in ongoing studies. In our hands, with the right ECM protein coating, endothelial and epithelial cells readily and tightly adhere to the substrate for microscopy assessment during isotropic stretch. As detailed in Friedrich et al. (2017), when turning to adult ventricular cardiomyocytes, we could not find any matrix-functionalization procedure allowing for tight adherence of CMs in 2D culture. Inspired by a CM "cell-in-a-gel" approach (Jian et al., 2014), we experimented with 3D-hydrogel embedding of adult CM and found polyvinyl-alcohol (PVA) hydrogels, doped with thiol groups to tune their matrix stiffness for CM ECM to be a feasible bioprocess approach (Friedrich et al., 2017). In that previous report of ours, we demonstrated reliable membrane area increase upon stretch using the *IsoStretcher* up to a linear hardware stretch of 15% in medium to strong gels containing 5–9 mM thiol groups (Friedrich et al., 2017). Stretching the gel was accompanied by a stretch-induced Ca^{2+} entry into CMs from the external bulk media, as visualized by confocal Fluo-4 Ca^{2+} fluorescence microscopy. Since this increase in fluorescence developed over a time course of several minutes, which is unusually slow for live-cell reactions, the only remaining explanation could be seen in a vast diffusion restriction even to small molecules through the PVA-hydrogel. Consequently, we revisited this hypothesis to provide experimental evidence.

First, we further optimized the hydrogel layer thickness required for reliable embedding to about 10 times the CM diameter (**Figure 2A**). When applying 5 μM ionomycin, a selective Ca^{2+} ionophore, to the bulk solution and monitoring Fluo-4 fluorescence in stained single CMs embedded in the gel, we could reduce the pharmacological action delay down to ∼2.5 min, as seen by the delay in steep fluorescence increase following the addition of the ionophore (**Figure 2B**). Thus, unlike in single cell experiments in open dishes where cell reactions are almost instantaneous, in hydrogel-embedded CMs, care needs to be taken to allow for sufficient recording time to catch the delay in drug delivery due to diffusional barriers for the applied drugs to reach their target (Amsden, 1998), here ionomycin. In a final step, by applying sudden de-stretch and re-stretch to PVA-embedded, Fluo-4 stained intact murine adult ventricular CMs, we could visualize stretch-induced arrhythmic Ca^{2+} transient activity online using our *IsoStretcher* device (**Figure 2C**). This represents the very first direct visualization of stretch-induced early after-depolarization activity of ventricular CM Ca^{2+} transients and demonstrates mechano-electric feedback on a single cellular level.

CONCLUSIONS

Our understanding of mechano-related cellular events, particularly for hollow organs, relies on novel biomechatronics technologies that mimic the wall strain profiles of the natural tissues as closely as possible. In that regard, it became apparent that uni- vs. multiaxial strains are answered by markedly different FAC remodeling patterns. Isotropic or multiaxial stretch systems are not readily available on the market for a broad user community, and so far, biomedical engineering-inspired devices have mainly evolved at research institutions. Our *IsoStretcher* allows easy-to-use and intuitive handling alongside with many cell types, either in 2D or even in 3D cultures. With adult cardiomyocytes as one of the probably most cumbersome cell types for isotropic stretch, we succeeded to employ a PVA-hydrogel-based embedding and stretch approach that allows online Ca^{2+} imaging of cellular reactions. In doing so, we could provide the first evidence of direct visualization of mechanoelectric feedback in a mechanically-actuated 3D environment. In future studies, we aim to unravel the molecular origin of the mechanosensors(s) and channels involved but we already suspect a strong candidate: Piezo1.

MATERIALS AND METHODS

Generation of Thin Gels

Murine ventricular cardiomyocytes, dissociated from adult C57BL/6 (90 d) mice in a Langendorff preparation were obtained through tissue sharing with other groups at the Victor Chang Cardiac Research Institute (institutional approval number: AEC 17-17). CMs were suspended within the uncured PEG-PVA gel precursor (recipe see below) and a 15 μl droplet was placed on the surface of an *IsoStretcher* PDMS chamber. A standard 0.15 mm thick glass coverslip with a diameter of 10 mm was placed on top of the droplet, generating a fluid layer, about 250 μm thick, between slide and chamber by forming the equilibrium between gravitational and capillary forces. After curing the PEG-PVA gel for 20 min, the chamber was filled with 300 μl cell culture medium. The glass coverslip was removed with forceps, leaving behind CMs embedded in an even hydrogel with defined height. The hydrogel height was determined with a confocal microscope

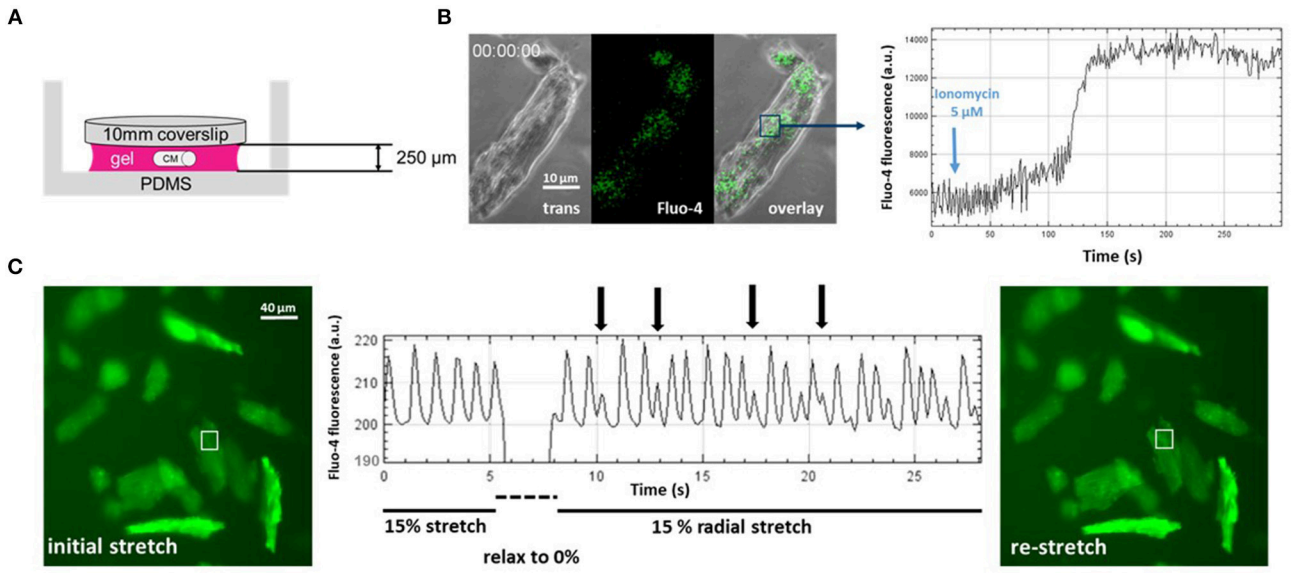

FIGURE 2 | Direct visualization of mechanoelectric feedback in cardiomyocytes through *IsoStretcher* technology. **(A)** Thin polyvinyl-alcohol gel embedding of adult cardiomyocytes allows diffusion-limited accessibility to pharmacological manipulations as shown for application of a Ca^{2+} ionophore (5 µM ionomycin) to the external solution and visualization of a maximum Fluo-4 response after ∼150 s **(B)**. **(C)** Proof-of-concept recording demonstrating mechanoelectric feedback, i.e., the direct visualization of mechanical isotropic stretch (15% radial stretch) inducing early after- depolarization spontaneous Ca^{2+} transients (vertical arrows) upon sudden re-stretch from the relaxed state. Note that the dip in fluorescence reading during the brief relaxation is mostly due to the radial displacement of the respective cardiomyocytes out of the ROI, which however, is perfectly restored upon re-stretch.

by focusing on the clearly visible upper and lower surfaces of the gel.

Hydrogel Recipe

Hydrogels were prepared from *Cellendes 3-D Life PVA-PEG Slow Gelling Hydrogel kits* (G82-1). The applied recipe is listed in **Table 1**. The components were added in sequence as they are listed in the table from top to bottom. After adding the RGD peptides, the mixture was incubated for 30 min at 37°C to allow for annealing of the peptides to the PVA thiol groups. When adding cell and PEG-Link crosslinker, the mixture was firm enough to be touched or covered by liquid without disintegrating after an incubation time of 20 min at 37°C.

TABLE 1 | Cellendes 3-D Life PVA-PEG hydrogel recipe for a gel containing 4.5 µM cross-linked thiol-groups and 0.5 µM RGD peptides.

30 µl Hydrogel med 4.5	
Water	10 µl
10 × CB	2.5 µl
PVA	5 µl
RGD	0.75 µl
Cell suspension	5 µl
PEG-Link	6.75 µl

CB buffer is a part of the G82-1 kit from Cellendes.

Determination of Diffusion Accessibility of Embedded Cardiomyocytes

Fluo-4 loading of CMs was prepared in a hydrogel of ∼250 µm thickness. The gel was covered with 100 µl medium containing 3 µM Fluo-4 AM and incubated for 2 h at 37°C and 5% CO_2. The Fluo-4 loaded (DMEM was used as cell culture medium) cells in a hydrogel were mounted into the *IsoStretcher* and imaged with a confocal microscope (Zeiss LSM 700 Inverted) using a 488 nm laser source as illumination for the fluorescence channel, while simultaneously recording a phase contrast image. A short-pass filter with a cut-off at 540 nm as well as a 488 nm notch filter were used to separate excitation from emission light. Videos with a frame time of 600 ms (512 × 512 px; 0.63 × 0.63 µm voxel size) were recorded. In the experiment shown in **Figure 2B**, the sample was stretched to 10% radial stretch and 20 s after starting a video recording, ionomycin was added into the chamber to a final concentration of 5 µM. The fluorescence intensity of an ROI in the cell is tracked, allowing one to visualize Ca^{2+} fluorescence intensity as well as the time point of terminal contracture of the cell.

Assessment of Mechanoelectric Feedback in Adult 3D-Embedded CMs

Hydrogel embedded adult murine ventricular CMs were loaded with Fluo-4 in an *IsoStretcher* chamber and mounted with the *Isostretcher* on an epifluorescence microscope. Instead of cell culture medium, the hydrogel was covered with 400 µl HBSS (Hank's Balanced Salt Solution; Thermo Fisher) solution. Fluorescence was excited by a broad band UV-source and emission light and separated by a 558 nm bandpass filter. Image sequences were recorded with a frame time of

110 ms (2,048 × 2,048; voxel size 0.59 × 0.59 μm). The chamber was stretched to 15% radial stretch and the cells were allowed to adapt to the stretched environment for 5 min. A video recording was started and after 5 s of recording, the chamber suddenly relaxed to 0% and re-stretched to 15% radial stretch within 2 s. Spontaneous calcium transients of recorded cardiomyocytes were visualized by plotting the mean fluorescence intensity of a 10 × 10 μm ROI on a cardiomyocyte.

DATA AVAILABILITY

The datasets generated for this study are available on request to the corresponding author.

AUTHOR CONTRIBUTIONS

BM and OF designed and supervised the project. A-LM, DS, and YG conducted all IsoStretcher experiments and data analysis. SS made and DS wrote the software for the IsoStretcher device. All authors discussed the results and contributed to writing of the manuscript.

FUNDING

OF acknowledges ongoing support through the Erlangen Graduate School in Advanced Optical Technologies (SAOT) through the German Excellence Initiative. OF also acknowledges funding from the Deutsche Forschungsgemeinschaft (DFG grant FR2993/23-1) as well as ongoing support through the Erlangen Graduate School in Advanced Optical Technologies (SAOT) through the German Excellence Initiative. OF and BM acknowledge funding from the National Health and Medical Research Council (grant APP1108013) as well as ongoing mobility exchange funds through the German Academic Exchange Service (DAAD #57389224 to OF) and Universities Australia (UAUNSW #RG172289 to BM).

ACKNOWLEDGMENTS

We thank Andrea Chan, Sara Holman, and Dr. Siirii Ismaa from Prof. Robert M. Graham Laboratory (VCCRI) for providing mouse cardiomyocytes for our study.

REFERENCES

Amsden, B. (1998). Solute diffusion within hydrogels. mechanisms and models. *Macromolecules* 31, 8382–8395. doi: 10.1021/ma980765f

Arold, S. P., Wong, J. Y., and Suki, B. (2007). Design of a new stretching apparatus and the effects of cyclic strain and substratum on mouse lung epithelial-12 cells. *Ann. Biomed. Eng.* 35, 1156–1164. doi: 10.1007/s10439-007-9262-5

Chen, Y., Pasapera, A. M., Koretsky, A. P., and Waterman, C. M. (2013). Orientation-specific responses to sustained uniaxial stretching in focal adhesion growth and turnover. *Proc. Natl. Acad. Sci U.S.A.* 110, E2352–E2361. doi: 10.1073/pnas.1221637110

Coste, B., Mathur, J., Schmidt, M., Earley, T. J., Ranade, S., Petrus, M. J., et al. (2010). Piezo1 and Piezo2 are essential components of distinct mechanically activated cation channels. *Science* 330, 55–60. doi: 10.1126/science.1193270

Dyachenko, V., Husse, B., Rueckschloss, U., and Isenberg, G. (2009). Mechanical deformation of ventricular myocytes modulates both TRPC6 and RG172Kir2. 3 channels. *Cell Calcium* 45, 38–54. doi: 10.1016/j.ceca.2008.06.003

Engler, A. J., Sen, S., Sweeney, H. L., and Discher, D. E. (2006). Matrix elasticity directs stem cell lineage specification. *Cell* 126, 677–689. doi: 10.1016/j.cell.2006.06.044

Even-Ram, S., Artym, V., and Yamada, K. M. (2006). Matrix control of stem cell fate. *Cell* 126, 645–647. doi: 10.1016/j.cell.2006.08.008

Friedrich, O., Schneidereit, D., Nikolaev, Y. A., Nikolova-Krstevski, V., Schürmann, S., Wirth-Hücking, A., et al. (2017). Adding dimension to cellular mechanotransduction: advances in biomedical engineering of multiaxial cell-stretch systems and their application to cardiovascular biomechanics and mechano-signaling. *Prog. Biophys. Mol. Biol.* 130, 170–191. doi: 10.1016/j.pbiomolbio.2017.06.011

Friedrich, O., Wagner, S., Battle, A. R., Schürmann, S., and Martinac, B. (2012). Mechanoregulation of the beating heart at the cellular level e mechanosensitive channels in normal and diseased heart. *Prog. Biophys. Mol. Biol.* 110, 226–238. doi: 10.1016/j.pbiomolbio.2012.08.009

Galie, P. A., Khalid, N., Carnahan, K. E., Westfall, M. V., and Stegemann, J. P. (2013). Substrate stiffness affects sarcomere and costamere structure and electrophysiological function of isolated adult cardiomyocytes. *Cardiovasc. Pathol.* 22, 219–227. doi: 10.1016/j.carpath.2012.10.003

Gottlieb, P. A., Folgering, J., Maroto, R., Raso, A., Wood, T. G., Kurosky, A., et al. (2008). Revisiting TRPC1 and TRPC6 mechanosensitivity. *Pflugers Arch.* 455, 1097–1103. doi: 10.1007/s00424-007-0359-3

Haug, M., Reischl, B., Prölß, G., Pollmann, C., Buckert, T., Keidel, C., et al. (2018). The MyoRobot: a novel automated biomechatronics system to assess voltage/Ca^{2+} biosensors and active/passive biomechanics in muscle and biomaterials. *Biosens. Bioelectron.* 102, 589–599. doi: 10.1016/j.bios.2017.12.003

Hill-Eubanks, D. C., Gonzales, A. L., Sonkusare, S. K., and Nelson, M. T. (2014). Vascular TRP channels: performing under pressure and going with the flow. *Physiology (Bethesda)* 29, 343–360. doi: 10.1152/physiol.00009.2014

Huang, L., Mathieu, P. S., and Helmke, B. P. (2010). A stretching device for high-resolution live-cell imaging. *Ann. Biomed. Eng.* 38, 1728–1740. doi: 10.1007/s10439-010-9968-7

Hung, C. T., and Williams, J. L. (1994). A method for inducing equi-biaxial and uniform strains in elastomeric membranes used as cell substrates. *J. Biomech.* 27, 227–232. doi: 10.1016/0021-9290(94)90212-7

Jian, Z., Han, H., Zhang, T., Puglisi, J., Izu, L. T., Shaw, J. A., et al. (2014). Mechanochemotransduction during cardiomyocyte contraction is mediated by localized nitric oxide signaling. *Sci. Signal.* 7:ra27. doi: 10.1126/scisignal.2005046

Khayat, G., Rosenzweig, D. H., and Quinn, T. M. (2012). Low frequency mechanical stimulation inhibits adipogenic differentiation of C3H10T1/2 mesenchymal stem cells. *Differentiation* 83, 179–184. doi: 10.1016/j.diff.2011.12.004

Klingberg, F., Chow, M. L., Koehler, A., Boo, S., Buscemi, L., Quinn, T. M., et al. (2014). Prestress in the extracellular matrix sensitizes latent TGF-β1 for activation. *J. Cell Biol.* 207, 283–297. doi: 10.1083/jcb.201402006

Kohl, P., Hunter, P., and Noble, D. (1999). Stretch-induced changes in heart rate and rhythm: clinical observations, experiments and mathematical models. *Prog. Biophys. Mol. Biol.* 71, 91–138. doi: 10.1016/S0079-6107(98)0 0038-8

Kreutzer, J., Ikonen, L., Hirvonen, J., Pekkanen-Mattila, M., Aalto-Setälä. K., and Kallio, P. (2014). Pneumatic cell stretching systems for cardiac differentiation and culture. *Med. Eng. Phys.* 36, 496–501. doi: 10.1016/j.medengphy.2013.09.008

Kurpinski, K., and Li, S. (2007). Mechanical stimulation of stem cells using cyclic uniaxial strain. *J. Vis. Exp.* 2007:242. doi: 10.3791/242

Lamb, G. D., and Stephenson, D. G. (2018). Measurement of force and calcium release using mechanically skinned fibers from mammalian skeletal muscle. *J Appl. Physiol.* 125, 1105–1127. doi: 10.1152/japplphysiol.00445.2018

Legant, W. R., Miller, J. S., Blakely, B. L., Cohen, D. M., Genin, G. M., and Chen, C. S. (2010). Measurement of mechanical tractions exerted by cells

in three-dimensional matrices. *Nat. Methods* 7, 969–971. doi: 10.1038/nmeth.1531

Li, J., Hou, B., Tumova, S., Muraki, K., Bruns, A., Ludlow, M. J., et al. (2014). Piezo1 integration of vasculature architecture with physiological force. *Nature* 515, 279–282. doi: 10.1038/nature13701

Majd, H., Quinn, T. M., Wipff, P. J., and Hinz, B. (2011). Dynamic expansion culture for mesenchymal stem cells. *Methods Mol. Biol.* 14, 175–188. doi: 10.1007/978-1-60761-999-4_14

Majd, H., Wipff, P. J., Buscemi, L., Bueno, M., Vonwil, D., Quinn, T. M., et al. (2009). A novel method of dynamic culture surface expansion improves mesenchymal stem cell proliferation and phenotype. *Stem Cells* 27, 200–209. doi: 10.1634/stemcells.2008-0674

Mann, J. M., Lam, R. H. W, Weng, S., Sun, Y., and Fu, J. (2012). A silicone-based stretchable micropost array membrane for monitoring live-cell subcellular cytoskeletal response. *Lab Chip* 12, 731–740. doi: 10.1039/C2LC20896B

Matsumoto, T., Ching Yung, Y., Fischbach, C., Kong, H. J., Nakaoke, R., and Mooney, D. J. (2007). Mechanical strain regulates endothelial cell patterning *in vitro*. *Tissue Eng.* 13, 207–217. doi: 10.1089/ten.2006.0058

Moss, R. L. (1979). Sarcomere length-tension relations of frog skinned muscle fibres during calcium activation at short lengths. *J. Physiol.* 292, 177–192. doi: 10.1113/jphysiol.1979.sp012845

Nikolova-Krstevski, V., Wagner, S., Yu, Z.-Y., Cox, C. D., Cvetkovska, J., Hill, A. P., et al. (2017). Endocardial TRPC-6 channels act as atrial mechanosensors and load-dependent modulators of endocardial/myocardial cross-talk. *JACC Basic Transl. Sci.* 2, 575–590. doi: 10.1016/j.jacbts.2017.05.006

Palchesko, R. N., Zhang, L., Sun, Y., and Feinberg, A. W. (2012). Development of polydimethylsiloxane substrates with tunable elastic modulus to study cell mechanobiology in muscle and nerve. *PLoS ONE* 7:e51499. doi: 10.1371/journal.pone.0051499

Prosser, B. L., Ward, C. W., and Lederer, W. J. (2011). X-ROS signaling: rapid mechano-chemical transduction in the heart. *Science* 333, 1440–1445. doi: 10.1126/science.1202768

Quinn, T., and Majd, H. (2010). *Device for Cell Culture on Deformable Surfaces.* US patent US 7,807,453 B2 (date of patent: Oct 5, 2010), PCT/IB2006/072911 (publ. date Jul 13, 2006).

Rapalo, G., Herwig, J. D., Hewitt, R., Wilhelm, K. R., Waters, C. M., and Roan, E. (2015). Live cell imaging during mechanical stretch. *J. Vis. Exp.* 102:e52737. doi: 10.3791/52737

Roche, S. M., Gumucio, J. P., Brooks, S. V., Mendia, C. L., and Claflin, D. R. (2015). Measurement of maximum isometric force generated by permeabilized skeletal muscle fibers. *J. Vis. Exp.* 100:e52695. doi: 10.3791/52695

Schürmann, S., Wagner, S., Herlitze, S., Fischer, C., Gumbrecht, S., Wirth-Hücking, A., et al. (2016). The *IsoStretcher*: an isotropic cell stretch device to study mechanical biosensor pathways in living cells. *Biosens. Bioelectron.* 81, 363–372. doi: 10.1016/j.bios.2016.03.015

Seo, K., Rainer, P. P., Hahn, V. S., Lee, D.-I., Jo, S.-H., Andersen, A., et al. (2014). Combined TRPC3 and TRPC6 blockade by selective small-molecule or genetic deletion inhibits pathological cardiac hypertrophy. *Proc. Natl. Acad. Sci. U.S.A.* 111, 1551–1556. doi: 10.1073/pnas.1308963111

Shao, Y., Tan, X., Novitski, R., Muqaddam, M., List, P., Williamson, L., et al. (2013). Uniaxial cell stretching device for live-cell imaging of mechanosensitive cellular functions. *Rev. Sci. Instr.* 84:114304. doi: 10.1063/1.4832977

Sotoudeh, M., Jalali, S., Shyy, J. Y., and Chien, S. (1998). A strain device imposing dynamic and uniform equi-biaxial strain to cultured cells. *Ann. Biomed. Eng.* 26, 181–189. doi: 10.1114/1.88

Ter Keurs, H. E. D. J., Iwazumi, T., and Pollack, G. H. (1978). The sarcomere length-tension relation in skeletal muscle. *J. Gen. Physiol.* 72, 565–592. doi: 10.1085/jgp.72.4.565

Tracey, R. E., and Sander, G. E. (2011). Histologically measured cardiomyocyte hypertrophy correlates with body height as strongly as with body mass index. *Cardiol. Rec. Practice* 2011:658958. doi: 10.4061/2011/658958

Urseka, C. P., Teo, S. K., Hirata, H., Harada, I., Chiam, K. H., and Sawada, Y. (2014). Design and construction of an equibiaxial cell stretching system that is improved for biochemical analysis. *PLoS ONE* 9:e90665. doi: 10.1371/journal.pone.0090665

Ward, M.-L., Williams, I. A., Chu, Y., Cooper, P. J., Ju, Y.-K., and Allen, D. G. (2008). Stretch-activated channels in the heart: contributions to length-dependence and to cardiomyopathy. *Prog. Biophys. Mol. Biol.* 97, 232–249. doi: 10.1016/j.pbiomolbio.2008.02.009

Wilson, C., and Dryer, S. E. (2014). A mutation in TRPC6 channels abolishes their activation by hypoosmotic stretch but does not affect activation by diacyglycerol of G protein signaling cascades. *Am. J. Physiol. Ren. Physiol.* 306, F1018–F1025. doi: 10.1152/ajprenal.00662.2013

Wipff, P. J., Majd, H., Acharya, C., Buscemi, L., Meister, J. J., and Hinz, B. (2009). The covalent attachment of adhesion molecules to silicone membranes for cell stretching applications. *Biomaterials* 30, 1781–1789. doi: 10.1016/j.biomaterials.2008.12.022

Yamaguchi, Y., Iribe, G., Nishida, M., and Naruse, K. (2017). Role of TRPC3 and TRPC6 channels in the myocardial response to stretch: linking physiology and pathophysiology. *Prog. Biophys. Mol. Biol.* 130, 264–272. doi: 10.1016/j.pbiomolbio.2017.06.010

Conflict of Interest Statement: The authors declare that the research was conducted in the absence of any commercial or financial relationships that could be construed as a potential conflict of interest.

frontiers in Bioengineering and Biotechnology

BRIEF RESEARCH REPORT
published: 17 April 2019
doi: 10.3389/fbioe.2019.00081

A Microfluidic System for Studying the Effects of Disturbed Flow on Endothelial Cells

*Francisco Tovar-Lopez[1], Peter Thurgood[1], Christopher Gilliam[1], Ngan Nguyen[1], Elena Pirogova[1], Khashayar Khoshmanesh[1] and Sara Baratchi[2]**

[1] School of Engineering, RMIT University, Melbourne, VIC, Australia, [2] School of Health and Biomedical Sciences, RMIT University, Bundoora, VIC, Australia

Arterial endothelium experience physical stress associated with blood flow and play a central role in maintaining vascular integrity and homeostasis in response to hemodynamic forces. Blood flow within vessels is generally laminar and streamlined. However, abrupt changes in the vessel geometry due to branching, sharp turns or stenosis can disturb the laminar blood flow, causing secondary flows in the form of vortices. Such disturbed flow patterns activate pro-inflammatory phenotypes in endothelial cells, damaging the endothelial layer and can lead to atherosclerosis and thrombosis. Here, we report a microfluidic system with integrated ridge-shaped obstacles for generating controllable disturbed flow patterns. This system is used to study the effect of disturbed flow on the cytoskeleton remodeling and nuclear shape and size of cultured human aortic endothelial cells. Our results demonstrate that the generated disturbed flow changes the orientation angle of actin stress fibers and reduces the nuclear size while increases the nuclear circularity.

Keywords: microfluidics, endothelial cells (EC), disturbed flow, shear stress, actin stress fiber

OPEN ACCESS

Edited by:
Alireza Mashaghi,
Harvard University, United States

Reviewed by:
Vincent Van Duinen,
Leiden University, Netherlands
Natalya Kizilova,
Warsaw University of Technology, Poland

***Correspondence:**
Sara Baratchi
sara.baratchi@rmit.edu.au

Specialty section:
This article was submitted to Biomechanics, a section of the journal Frontiers in Bioengineering and Biotechnology

Received: *06 February 2019*
Accepted: *01 April 2019*
Published: *17 April 2019*

Citation:
Tovar-Lopez F, Thurgood P, Gilliam C, Nguyen N, Pirogova E, Khoshmanesh K and Baratchi S (2019) A Microfluidic System for Studying the Effects of Disturbed Flow on Endothelial Cells. Front. Bioeng. Biotechnol. 7:81. doi: 10.3389/fbioe.2019.00081

INTRODUCTION

Endothelial cells, lining the inner surface of blood vessels, are in direct contact with the flowing blood, and their response to physiological as well as pathological flow dynamics affects vascular health (Chiu and Chien, 2011; Baratchi et al., 2017a). Endothelial cells experience various flow patterns and hemodynamic forces across the vascular system. Endothelial cells lining along the straight segments of the arterial trees experience a high-shear laminar flow essential for their physiological functions such as flow-mediated dilation (Chiu and Chien, 2011). In contrary, the endothelial cells lining along the arterial branches and curvatures experience a low-shear disturbed flow due to the presence of secondary flows in the form of vortices, which causes endothelial dysfunction and atherosclerosis (Caro et al., 1969, 1971; Bharadvaj et al., 1982; Suo et al., 2008).

Flow-induced alignment of the endothelial cells has been reported previously (Alenghat and Ingber, 2002; Wang et al., 2013; Yoshino et al., 2017). Recent advances in endothelial mechanobiology have also demonstrated that different classes of mechanoreceptors control the physiological function of endothelial cells, including cytoskeleton remodeling, gene expression, cell viability index and calcium homeostasis that could consequently control myogenic tone (Ingber, 2006; Chatzizisis et al., 2007; Shemesh et al., 2015). Shear-induced activation of various proteins such as RAC1 (Tzima et al., 2002) and Syndecan 4 (Baeyens et al., 2014) as well as enzymes such as RhoGTPases (Kroon et al., 2017) have also been reported to control the alignment and cytoskeleton remodeling of endothelial cells.

A variety of models have been developed to study the effect of disturbed flow on endothelial cells. These include *in vivo* models through surgical intervention (Katoh et al., 2007; Harding et al., 2018), *ex vivo* models using the endothelium at naturally occurring disturbed flow regions of the vessel (Katoh et al., 2007), and *in vitro* models using emerging microfluidic systems (Estrada et al., 2011). Among these models, microfluidic systems offer unprecedented advantages such as reduced cost and complexity of experiments, decreased volume of reagents (Katt et al., 2016; Ho et al., 2018; Yaman et al., 2018), and importantly provide predictable and controllable disturbed flow patterns based on the geometric specifications of the system (Rezvan et al., 2011; Balaguru et al., 2016). Despite these advantages, the majority of existing microfluidic systems generate localized disturbed flow patterns and thus are not suitable for studying the gene and protein expression of cultured cells under disturbed flow (Rezvan et al., 2011; Balaguru et al., 2016).

Here, we developed a microfluidic system with an array of ridge-shaped obstacles patterned along its entire surface. This allows for the generation of vortices and, in turn, low-shear disturbed flow regions in the cavities located between the successive ridges. This feature is used to quantify the effect of disturbed flow on the actin cytoskeleton remodeling, nucleus shape and size of cultured human aortic endothelial cells.

MATERIALS AND METHODS

Fabrication of 2D Parallel-Plate Flow Chambers

Ridged flow chambers were fabricated in two parts: (i) the main PDMS block consisting of a 500 μm tall channel and (ii) a PDMS film consisting of an array of 100 μm tall ridges. The main PDMS block was fabricated using a silicon wafer mold diced into a 5 mm × 50 mm × 500 μm section and adhered on to a 4-inch silicon wafer and enclosed with a 6 mm tall Teflon barrier (22 × 60 × 6 mm) (**Figure 1a**$_{i}$). PDMS (Sylgard® 184, 10:1 w/w base to curing agent) was poured into the Teflon barrier and cured at 80°C for 30 min. The PDMS block was then peeled off the mold and inlet, and outlet holes were punched using a 4 mm biopsy punch (Harris Unicore) (**Figure 1a**$_{ii}$).

The PDMS film with ridges was fabricated using a mold consisting of an array of rectangular grooves (100 μm × 100 μm × 5 mm) separated by 400 μm gaps. The mold was patterned in SU-8 3050 photoresist (MicroChem) using a high-resolution chrome mask (**Figure 1b**$_{i}$). PDMS was then poured onto the mold and spun at 100 rpm for 30 s before curing at 85°C for 5 min. The resulting PDMS film was then peeled off the mold revealing the array of rectangular obstacles. The PDMS film was cut to 22 × 60 mm prior to the assembly of the two parts (**Figure 1b**$_{ii}$). The PDMS main block and PDMS film with ridges were manually aligned and clamped together using a PMMA clamp resulting in a ridged flow chamber with rectangular obstacles (**Figure 1c**). A third mold, similar to the PDMS film mold, but without ridges was used to fabricate flat PDMS films for use as the control.

Computational Fluid Dynamics (CFD)

CFD simulations were conducted to predict the formation of vortices along the ridged microfluidic channel. This involved solving the differential equations governing the balance of mass and momentum, also known as Navier-Stokes equations. Simulations were performed using ANSYS Fluent software (ANSYS Inc.). Simulations were conducted in 3D and under steady-state conditions, considering the cell culture medium as an incompressible and Newtonian liquid. Flow was considered laminar due to its low Reynolds number. Boundary conditions included desired flow rates at the inlet, ambient pressure at the outlet and no-slip at the walls. The density and dynamic viscosity of the cell culture medium at 37°C were considered as 998 kg/m^3 and 7 × 10^{-4} Pa.s, respectively.

Cell Culture and *in-vitro* Generation of Laminar vs. Disturbed Flow

HAECs (Lonza) at early passages of 2 to 5 were used in this study. HAECs were cultured inside the microfluidic channels at the density of 5 × 10^6 cell/mL to produce a confluent layer of endothelial cells within 24 h. The volume of liquid inside the channel was ∼100 μL. The channels were pre-coated with 10 μg/mL MaxGel human extracellular matrix extracts (Sigma) according to the manufacturer's specification.

Flow experiments were carried out for 16 h at 37°C in a humidified atmosphere with 5% CO_2. The flow was applied through the channels using a peristaltic pump (OINA QP6 LAB High Accuracy) at flow rates of 20 mL/min and 6 mL/min.

Immunocytochemistry and Confocal Microscopy

Cells were fixed with 4% paraformaldehyde and permeabilised with 0.2% Triton X-100 in phosphate-buffered saline (PBS). Nonspecific binding was blocked with 2% goat serum or 5% bovine serum albumin (Sigma). F-actin was stained with Atto 565-phalloidin (94072, Sigma-Aldrich, dilution 1/500) and nuclei were stained with DAPI (Sigma-Aldrich). Image acquisition was obtained using a Nikon A1 confocal scanning microscope, as described before (Baratchi et al., 2016).

Image Processing and Analysis of Stress Fibers

The orientation of the cells and stress fibers was determined using an automated image processing algorithm written in MATLAB, as detailed elsewhere (Karlon et al., 1999; Kaunas et al., 2005; Ranade et al., 2014). Briefly, the algorithm computed the intensity gradients of the image in the horizontal and vertical directions by convolving the image with a spatial gradient filter. By treating these gradients as components of a vector field, the algorithm computed pixel-by-pixel magnitude and direction information. Local dominant orientations were then determined for each pixel by constructing a histogram of orientations from the magnitude and direction information and choosing the orientation with the largest value. Each histogram was constructed using a small subregion of 20 × 20 pixels, centered around the pixel of interest, and evaluating their deviation from a set of angles ranging

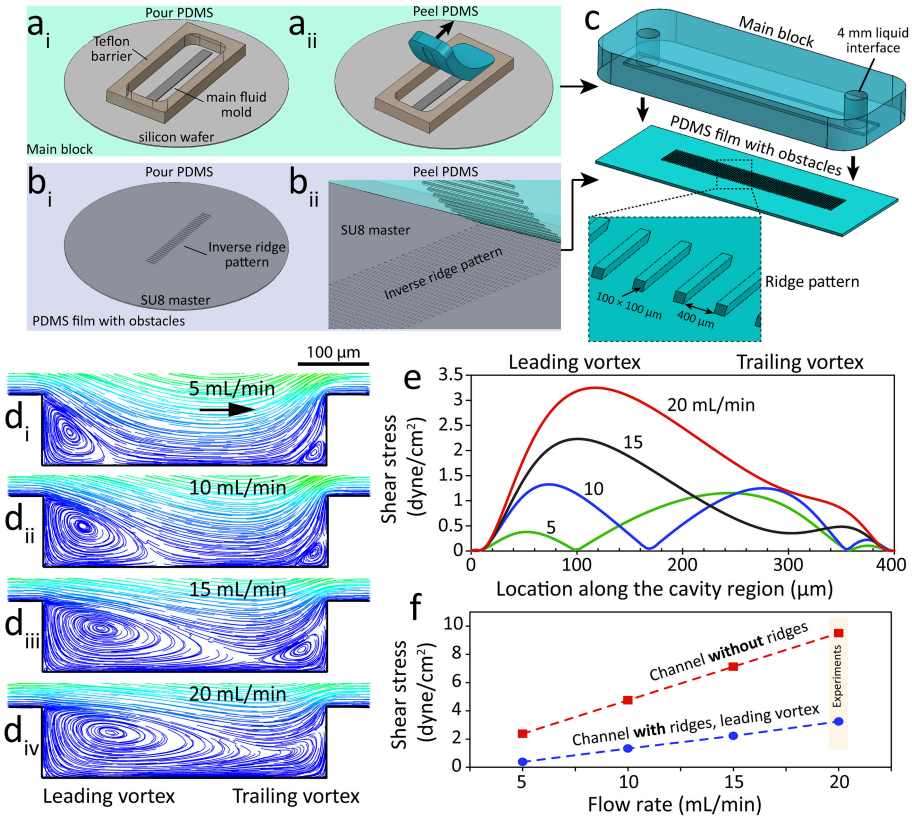

FIGURE 1 | A microfluidic system with ridge-shaped obstacles for culturing HAECs under disturbed flow. **(a_{i-ii})** The process of fabricating the main block involving a microfluidic channel with a rectangular cross-section of 5 mm × 600 µm forming the side and top walls of the system, **(b_{i-ii})** The process of fabricating the PDMS substrate with ridge-shaped obstacles patterned on its surface forming the bottom surface of the system, **(c)** The process of assembling the main block and the PDMS substrate with ridge obstacles, with the inset showing the zoomed-in PDMS substrate, **(d_{i-iv})** Flow streamlines at various flow rates of the cell culture medium applied through the microfluidic system, showing the formation and expansion of two vortices at the cavity region located between the neighboring ridges, **(e)** Variation of flow shear stress along the cavity region, **(f)** Variation of shear stress magnitude against the flow rate of the cell culture medium for the channel with ridges (disturbed flow) and the control channel without ridges (laminar flow).

from −89 to 90 degrees relative to the horizontal. For more details, we refer the reader to Kroon et al. (2017). Statistical significance was assessed with a global Watson's U2 test, and statistics were computed using the circular statistic toolbox (Berens, 2009).

Quantification of Nuclear Shape and Size

Image processing and calculations of nuclear shape and size were performed using NIS element software (Nikon Instruments Inc.). For statistical analysis, one-way ANOVA was performed using Prism 7.02 (GraphPad software) and $P < 0.05$ was considered significant.

RESULTS AND DISCUSSIONS

Characterization of Disturbed Flow

Microfluidic structures with the ridged or grooved patterns induce secondary flows in the form of vortices. This feature has been utilized for enhancing passive mixing of liquids (Stroock et al., 2002) as well as cell-based studies involving sorting (Yan et al., 2017), capturing (Manbachi et al., 2008; Stott et al., 2010; Hsiao et al., 2016; Wang et al., 2017) and forced tethering (Choi et al., 2014) of target cells.

An extensive set of numerical simulations were performed to analyze the disturbed flow patterns inside our microfluidic channel with integrated ridge-shaped obstacles. Our simulations indicated the formation of two vortices along the two corners of the cavity located between the successive ridges, which are referred to as "leading" and "trailing" vortices (**Figure 1d**). Our experiments confirmed the generation of "leading" and "trailing" vortices at the two corners of the cavity (**Supplementary Video 1**). Experiments were performed at a flow rate of 5 mL/min using a suspension of 1 µm polystyrene particles to facilitate the visualization of vortices. Increasing the flow rate of the cell culture medium led to the expansion of the vortices. In this manner, the two vortices occupied almost the entire cavity region at flow rates higher than 15 mL/min. Further increase of the flow rate led to merging of "leading" and "trailing" vortices.

The magnitude and distribution of the wall shear stress were governed by the configuration of the vortices (**Figure 1e**).

Numerical simulations revealed the existence of three localized shear peaks at 5 mL/min, corresponding to the "leading" vortex, vortex-free zone and "trailing" vortex. A similar pattern was observed at 10 mL/min. Two localized shear peaks were obtained at 15 mL/min due to the diminishing of the vortex-free zone. In comparison, only one localized shear peak was obtained at 20 mL/min due to the merging of "leading" and "trailing" vortices.

The shear stress induced by the "leading" vortex increased linearly with respect to the flow rate (**Figure 1f**). A similar trend was obtained for the control channel with no ridges (**Figure 1f**). Based on these results, the cellular experiments were performed at a flow rate of 20 mL/min to ensure (i) the endothelial cells cultured inside the "channel with ridges" experience a low shear stress under homogenous disturbed flow conditions while (ii) the endothelial cells cultured inside the "channel without ridges" experience physiological shear stress under laminar flow conditions (Chiu and Chien, 2011).

Disturbed Flow Affects the Orientation of Actin Stress Fibers and Nuclear Shape Change

Flow shear stress controls different endothelial phenotypic characteristics, including cell morphology, cytoskeleton remodeling and gene expression (Caro et al., 1969, 1971; Bharadvaj et al., 1982; Suo et al., 2008). Cytoskeleton proteins play important roles in maintaining the shape and integrity of the cells as well as transduction of shear stress from the luminal surface of endothelial cells to the cytosol (Loufrani and Henrion, 2008). Actin stress fibers consist of bundles of 10–30 actin filaments that are held together by actin crosslinking protein known as α-Actinin (Pellegrin and Mellor, 2007). Stress fibers are very important transducers of shear stress and transmit the stress to various intracellular locations (Franke et al., 1984; Wechezak et al., 1985).

HAECs were cultured overnight inside the channels with ridge-shaped obstacles (disturbed flow), without ridges (laminar flow) as well as inside Petri dishes (static condition). The flow rate of the medium was set to 20 mL/min. Under this condition, the cells cultured under disturbed flow experienced low shear stress with a maximum of 3 dyne/cm^2, whereas the cells cultured under laminar flow experienced physiological shear stress with a magnitude of ∼10 dyne/cm^2, as detailed in the previous section.

First, we studied the orientation of stress fibers developed under the laminar flow, disturbed flow, and static condition. Under the laminar flow, HAECs stress fibers were highly orientated to the direction of flow ($R^2 = 0.93$), with 71.59 ± 3.2% of stress fibers having an orientation angle of 0–30°. In contrary, in the presence of the disturbed flow, the majority of stress fibers were oriented perpendicular to the direction of flow ($R^2 = 0.92$), with 59.74 ± 1.9% of stress fibers having an orientation angle of 60–90° (**Figure 2A**). In comparison, under static condition, the orientation of stress fibers did not follow any specific trend (**Figure 2A**). This trend can be clearly seen in the contours of the stress fiber orientation angle, obtained by our automated image processing algorithm. The trend shows a transition from green-blue colors (corresponding to the orientation angles in the range of ±30°) toward red-purple colors (corresponding to orientation angles outside the range of ±70°) (**Figure 2B**). This trend can also be seen in the histograms of the stress fiber orientation angle, which clearly shows the significant changes of stress fiber orientation under disturbed flow condition (**Figure 2C**). Consistent results were obtained in five independent experiments (**Figure 2D**). Next, we conducted a control experiment, by applying a flow rate of 6 mL/min through a straight microfluidic channel without ridges, to induce a shear stress of 3 dyne/cm^2. Our experiments indicated that stress fibers were aligned perpendicular to the direction of the flow, similar to what we observed under the disturbed flow conditions inside the channel with ridges. This observation suggests that the response of HAECs to the disturbed flow is dependent on the magnitude of shear stress, rather than the flow pattern of the small vortices formed between the ridges (**Supplementary 1**).

Alignment of endothelial cells to the direction of flow has been observed previously (Alenghat and Ingber, 2002; Wang et al., 2013; Yoshino et al., 2017). It has been demonstrated that endothelial cells have the threshold of 10 dyne/cm^2 to align to the direction of flow which is similar to what we have also observed in our preliminary studies (Wang et al., 2013; Ostrowski et al., 2014). Further, porcine valvular endothelial cells have been demonstrated to orient perpendicular to the direction of flow in response to the shear stress of 20 dyne/cm^2 in comparison to the aortic endothelial cells that are aligned in parallel to the flow direction at the same shear stress level (Butcher et al., 2004; Baratchi et al., 2017b; Nguyen et al., 2018). Morphology of endothelial cells (shape and size) and actin cytoskeleton is reported to be different at the branch point of the aorta where the blood flow is disturbed compared to the regions of the aorta where blood flow is laminar (Katoh et al., 2007). This can be attributed to the different responses of endothelial cells to different shear levels, as reported in our work.

The nucleus in eukaryotic cells is the site of transcriptional regulation and receives the mechanical stress that is transmitted via the cytoskeleton. Both intra and extracellular forces affect the nuclear shape and structure (Dahl et al., 2008). To evaluate this phenomenon, we compared the nuclear shape index and size of HAECs under the laminar flow, disturbed flow and static conditions. Disturbed flow significantly increased the nucleus circularity index of HAECs compared to the laminar flow ($P < 0.001$) and static condition ($P < 0.001$) (**Figure 2E**). In comparison, the nuclear size had a significantly smaller area under the disturbed flow compared to the laminar flow ($P < 0.01$) and static condition ($P < 0.01$) (**Figure 2F**). The observed nuclear shape change in the presence of different flow dynamics can be attributed to the change in the mechanically induced signaling or macromolecular conformational changes related to change in gene expression, in the presence of different flow dynamics (Davies, 2009).

CONCLUSIONS

Here, we reported the microfluidic-based *in vitro* model for generating the disturbed flow that mimics the pathological flow patterns of arterial branch point and curvatures. The observed

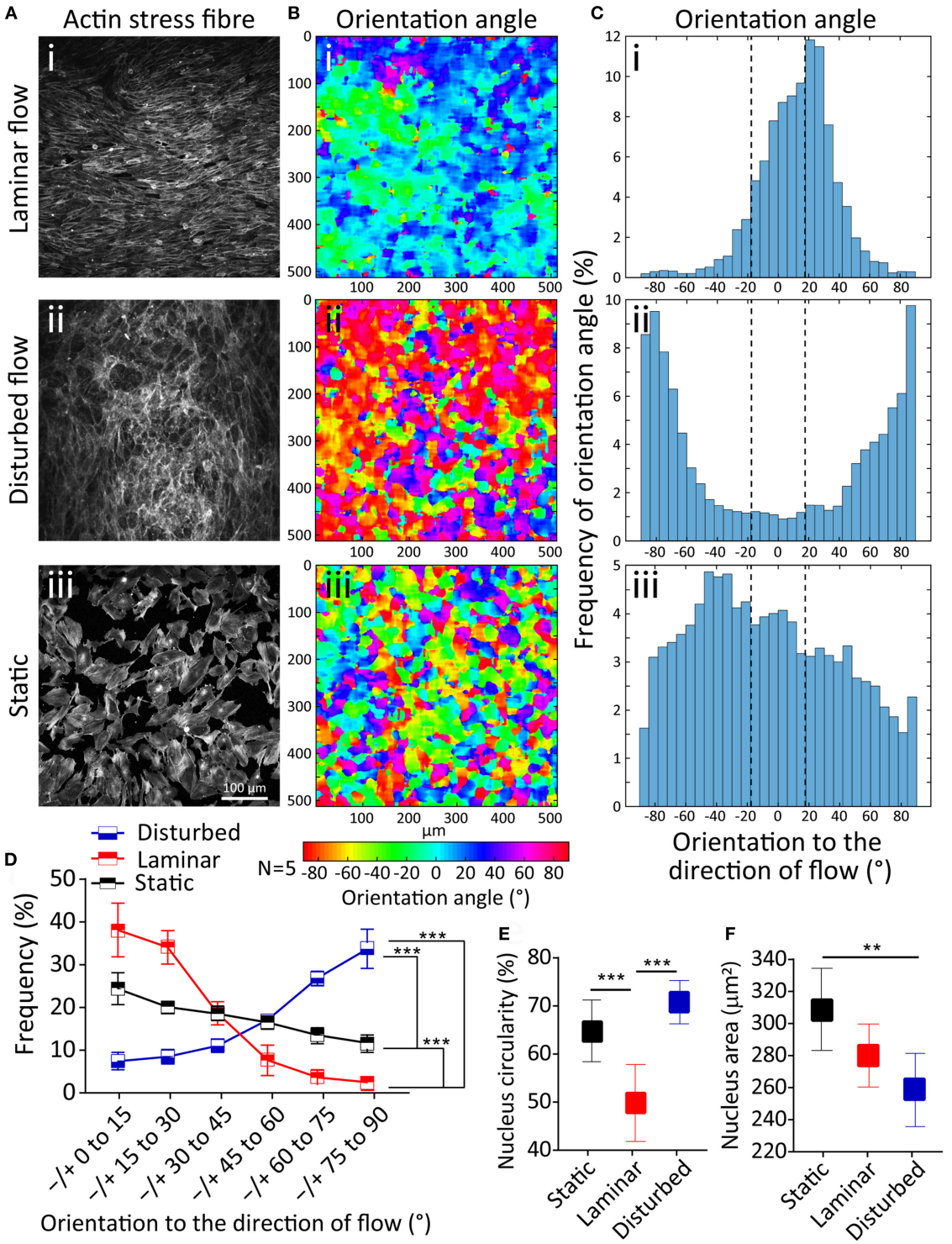

FIGURE 2 | Effect of disturbed flow on cytoskeleton remodeling, nucleus circularity and nucleus size of HAECs. **($A_{i–iii}$)** A confluent layer of HAECs cultured under laminar flow, disturbed flow and static condition, following which the actin cytoskeleton was labeled with Atto 565-phalloidin after fixation. **($B_{i–iii}$)** The contour of the orientation angle of stress fibers, and **($C_{i–iii}$)** Histogram of the frequency of the orientation angle of stress fibers, **(D)** Summary graph of the frequency of the orientation angle of stress fibers cultured under laminar flow, disturbed flow and static condition. The graph is obtained from five independent experiments. ***Indicates $P <$ 0.001, **(E)** Circularity, and **(F)** area of the nucleus of HAECs. Data are representative of five independent experiments, and error bars shown in **(D-F)** represent 95% confidence interval. 70 nuclei have been analyzed for each group. **Indicates $P < 0.01$ and *** $P < 0.001$.

flow disturbance is due to the formation of vortices along the ridges. We showed that the expansion of vortices and the magnitude of the wall shear stress can be tuned by varying the flow rate of the cell culture medium through the system. At the flow rate of 20 mL/min, the vortices filled the entire cavity region between the neighboring ridges, inducing a maximum wall shear stress of 3 dyne/cm^2 along the bottom surface of the channel where endothelial cells were cultured. To demonstrate the capability and efficacy of this model, we studied the effect of the disturbed flow on endothelial cytoskeleton remodeling and stress fiber formation as well as its nuclear shape and size. We used a MATLAB code to quantify the orientation of actin stress fibers under the laminar flow, disturbed flow and static condition.

Our results indicated that the generated disturbed flow affects the morphology and cytoskeleton remodeling of HAECs. Under the laminar flow, endothelial cells were aligned to the direction of flow and formed actin stress fibers, whereas the low-shear disturbed flow caused endothelial cells to orient perpendicular to the direction of flow. Furthermore, the HACEs exhibited a significantly higher nucleus circularity index and smaller nuclear size in the presence of disturbed flow.

These observations demonstrated the suitability of the presented microfluidic system for studying the effect of disturbed flow on the biology of endothelial cells, providing unique opportunities for evaluating the effect of the disturbed flow on the expression and function of different mechanoreceptors in endothelial cells.

AUTHOR CONTRIBUTIONS

FT-L fabricated the microfluidic device. PT conducted experiments and analyzed the results. CG wrote the MATLAB code for automated processing of images. NN conducted experiments. EP wrote the manuscript. KK performed numerical simulations and wrote the manuscript. SB designed the study, performed experiments, wrote the manuscript and supervised the work.

FUNDING

The authors wish to acknowledge RMIT's MicroNano Research Facility (MNRF) for fabrication of microfluidic devices. SB acknowledges the Australian Research Council for Discovery for Early Career Researchers Award (DE170100239). EP acknowledges the Australian National Health and Medical Research Council for funding The Australian Center for Electromagnetic Bioeffects Research (NHMRC CRE APP1135076). KK acknowledges the Australian Research Council for Discovery Grant (DP180102049).

SUPPLEMENTARY MATERIAL

The Supplementary Material for this article can be found online at: https://www.frontiersin.org/articles/10.3389/fbioe.2019.00081/full#supplementary-material

REFERENCES

Alenghat, F. J., and Ingber, D. E. (2002). Mechanotransduction: all signals point to cytoskeleton, matrix, and integrins. *Sci STKE* 2002:pe6. doi: 10.1126/stke.2002.119.pe6

Baeyens, N., Mulligan-Kehoe, M. J., Corti, F., Simon, D. D., Ross, T. D., Rhodes, J. M., et al. (2014). Syndecan 4 is required for endothelial alignment in flow and atheroprotective signaling. *Proc. Nat. Acad. Sci. U.S.A.* 111, 17308–17313. doi: 10.1073/pnas.1413725111

Balaguru, U. M., Sundaresan, L., Manivannan, J., Majunathan, R., Mani, K., Swaminathan, A., et al. (2016). Disturbed flow mediated modulation of shear forces on endothelial plane: a proposed model for studying endothelium around atherosclerotic plaques. *Sci. Rep.* 6:27304. doi: 10.1038/srep27304

Baratchi, S., Almazi, J. G., Darby, W., Tovar-Lopez, F. J., Mitchell, A., and McIntyre, P. (2016). Shear stress mediates exocytosis of functional TRPV4 channels in endothelial cells. *Cell. Mol. Life Sci.* 73, 649–666. doi: 10.1007/s00018-015-2018-8

Baratchi, S., Khoshmanesh, K., Woodman, O. L., Potocnik, S., Peter, K., and McIntyre, P. (2017a). Molecular sensors of blood flow in endothelial cells. *Trends Mol Med.* 23, 850–868. doi: 10.1016/j.molmed.2017.07.007

Baratchi, S., Knoerzer, M., Khoshmanesh, K., Mitchell, A., and McIntyre, P. (2017b). Shear stress regulates TRPV4 channel clustering and translocation from adherens junctions to the basal membrane. *Sci. Rep.* 7:15942. doi: 10.1038/s41598-017-16276-7

Berens, P. (2009). CircStat: A MATLAB Toolbox for circular *statistics. J. Stat. Soft.* 31:21. doi: 10.18637/jss.v031.i10

Bharadvaj, B. K., Mabon, R. F., and Giddens, D. P. (1982). Steady flow in a model of the human carotid bifurcation. Part II–laser-Doppler anemometer measurements. *J. Biomech.* 15, 363–378. doi: 10.1016/0021-9290(82)90058-6

Butcher, J. T., Penrod, A. M., Garcia, A. J., and Nerem, R. M. (2004). Unique morphology and focal adhesion development of valvular endothelial cells in static and fluid flow environments. *Arterioscler. Thromb. Vascu. Biol.* 24, 1429–1434. doi: 10.1161/01.ATV.0000130462.50769.5a

Caro, C. G., Fitz-Gerald, J. M., and Schroter, R. C. (1969). Arterial wall shear and distribution of early atheroma in man. *Nature* 223, 1159–1160. doi: 10.1038/2231159a0

Caro, C. G., Fitz-Gerald, J. M., and Schroter, R. C. (1971). Atheroma and arterial wall shear. Observation, correlation and proposal of a shear dependent mass transfer mechanism for atherogenesis. *Proc. Royal Soc. London Series B Biol. Sci.* 177, 109–159.

Chatzizisis, Y. S., Coskun, A. U., Jonas, M., Edelman, E. R., Feldman, C. L., and Stone, P. H. (2007). Role of endothelial shear stress in the natural history of coronary atherosclerosis and vascular remodeling - molecular, cellular, and vascular behavior. *J. Am. Coll. Cardiol.* 49, 2379–2393. doi: 10.1016/j.jacc.2007.02.059

Chiu, J. J., and Chien, S. (2011). Effects of disturbed flow on vascular endothelium: pathophysiological basis and clinical perspectives. *Physiol. Rev.* 91, 327–387. doi: 10.1152/physrev.00047.2009

Choi, S., Levy, O., Coelho, M. B., J., Cabral, M. S., Karp, J. M., and Karnik, R. (2014). A cell rolling cytometer reveals the correlation between mesenchymal stem cell dynamic adhesion and differentiation state. *Lab Chip*. 14, 161–166. doi: 10.1039/C3LC50923K

Dahl, K. N., Ribeiro, A. J., and Lammerding, J. (2008). Nuclear shape, mechanics, and mechanotransduction. *Circul. Res.* 102, 1307–1318. doi: 10.1161/CIRCRESAHA.108.173989

Davies, P. F. (2009). Hemodynamic shear stress and the endothelium in cardiovascular pathophysiology. Nature clinical practice. *Cardiovasc. Med.* 6, 16–26. doi: 10.1038/ncpcardio1397

Estrada, R., Giridharan, G. A. M, Nguyen, D., Prabhu, S. D., and Sethu, P. (2011). Microfluidic endothelial cell culture model to replicate disturbed flow conditions seen in atherosclerosis susceptible regions. *Biomicrofluidics* 5, 32006–3200611. doi: 10.1063/1.3608137

Franke, R. P., Grafe, M., Schnittler, H., Seiffge, D., Mittermayer, C., and Drenckhahn, D. (1984). Induction of human vascular endothelial stress fibres by fluid shear stress. *Nature* 307, 648–649. doi: 10.1038/307648a0

Harding, I. C., Mitra, R., Mensah, S. A., Herman, I. M., and Ebong, E. E. (2018). Pro-atherosclerotic disturbed flow disrupts caveolin-1 expression, localization, and function via glycocalyx degradation. *J. Transl. Med.* 16:364. doi: 10.1186/s12967-018-1721-2

Ho, K. K. Y., Wang, Y. L., Wu, J., and Liu, A. P. (2018). Advanced microfluidic device designed for cyclic compression of single adherent cells. *Front. Bioeng. Biotechnol.* 6:148. doi: 10.3389/fbioe.2018.00148

Hsiao, S. T., Spencer, T., Boldock L., Prosseda, S. D., Xanthis, I., Tovar-Lopez, F. J., et al. (2016). Endothelial repair in stented arteries is accelerated by inhibition of Rho-associated protein kinase. *Cardiovasc. Res.* 112, 689–701. doi: 10.1093/cvr/cvw210

Ingber, D. E. (2006). Cellular mechanotransduction: putting all the pieces together again. *FASEB J.* 20, 811–827. doi: 10.1096/fj.05-5424rev

Karlon, W. J., Hsu, P. P., Li, S., Chien, S., McCulloch, A. D., and Omens, J. H. (1999). Measurement of orientation and distribution of cellular alignment and cytoskeletal organization. *Ann Biomed. Eng.* 27, 712–720. doi: 10.1114/1.226

Katoh, K., Kano, Y., and Ookawara, S. (2007). Morphological differences between guinea pig aortic and venous endothelial cells *in situ*. *Cell Biol. Int.* 31, 554–564. doi: 10.1016/j.cellbi.2006.11.028

Katt, M. E., Placone, A. L., Wong, A. D., Xu, Z. S., and Searson, P. C. (2016). *In vitro* tumor models: Advantages, disadvantages, variables, and selecting the right platform. *Front. Bioeng. Biotechnol.* 4:148. doi: 10.3389/fbioe.2016.00012

Kaunas, R., Nguyen, P., Usami, S., and Chien, S. (2005). Cooperative effects of Rho and mechanical stretch on stress fiber organization. *Proc. Nat. Acad. Sci. U.S.A.* 102, 15895–15900. doi: 10.1073/pnas.0506041102

Kroon, J., Heemskerk, N., N., Kalsbeek, J. T. M., de Waard, V., van Rijssel, J., and van Buul, J. D. (2017). Flow-induced endothelial cell alignment requires the RhoGEF Trio as a scaffold protein to polarize active Rac1 distribution. *Mol. Biol. Cell* 28, 1745–1753. doi: 10.1091/mbc.e16-06-0389

Loufrani, L., and Henrion, D. (2008). Role of the cytoskeleton in flow (shear stress)-induced dilation and remodeling in resistance arteries. *Med. Biol. Eng. Comput.* 46, 451–460. doi: 10.1007/s11517-008-0306-2

Manbachi, A., Shrivastava, S., Cioffi, M., Chung, B. G., Moretti, M., Demirci, U., et al. (2008). Microcirculation within grooved substrates regulates cell positioning and cell docking inside microfluidic channels. *Lab Chip*. 8, 747–754. doi: 10.1039/b718212k

Nguyen, N., Thurgood, P., Zhu, J. Y., Pirogova, E., Baratchi, S., and Khoshmanesh, K. (2018). "Do-it-in-classroom" fabrication of microfluidic systems by replica moulding of pasta structures. *Biomicrofluidics* 12:044115. doi: 10.1063/1.5042684

Ostrowski, M. A., Huang, N. F., Walker, T. W., Verwijlen, T., Poplawski, C., Khoo, A. S, et al. (2014). Microvascular endothelial cells migrate, upstream, and align against the shear stress field created by impinging flow. *Biophy. J.* 106, 366-374. doi: 10.1016/j.bpj.2013.11.4502

Pellegrin, S., and Mellor, H. (2007). Actin stress fibres. *J. Cell. Sci.* 120:3491. doi: 10.1242/jcs.018473

Ranade, S. S., Qiu, Z., Woo, S. H., Hur, S. S., Murthy, S. E., Cahalan, S. M., et al. (2014). Piezo1, a mechanically activated ion channel, is required for vascular development in mice. *Proc. Natl. Acad. Sci. U.S.A* 111, 10347–10352. doi: 10.1073/pnas.1409233111

Rezvan, A., Ni, C. W., Alberts-Grill, N., and Jo, H. (2011). Animal, *in vitro*, and *ex vivo* models of flow-dependent atherosclerosis: role of oxidative stress. *Antioxidants Redox Signal.* 15, 1433–1448. doi: 10.1089/ars.2010.3365

Shemesh, J., Jalilian, I., Shi, A., Yeoh, G. H., Knothe Tate, M. L., and Warkiani, M. E. (2015). Flow-induced stress on adherent cells in microfluidic devices. *Lab Chip*. 15, 4114–4127. doi: 10.1039/C5LC00633C

Stott, S. L. C., Hsu, H., Tsukrov, D. I., Yu, M., Miyamoto, D. T., Waltman, B. A., et al. (2010). Isolation of circulating tumor cells using a microvortex-generating herringbone-chip. *Proc. Natl. Acad. Sci. U.S.A.* 107, 18392–18397. doi: 10.1073/pnas.1012539107

Stroock, A. D., Dertinger, K. W. S., Ajdari, A., Mezić, I., Stone, H. A., and Whitesides, G. M. (2002). Chaotic Mixer for microchannels. *Science* 295, 647–651. doi: 10.1126/science.1066238

Suo, J., Oshinski, J. N., and Giddens, D. P. (2008). Blood flow patterns in the proximal human coronary arteries: relationship to atherosclerotic plaque occurrence. *Mol Cell Biomech.* 5, 9–18. doi: 10.3970/mcb.2008.005.009

Tzima, E., Del Pozo, M. A., Kiosses, W. B., Mohamed, S. A., Li, S., Chien, S., et al. (2002). Activation of Rac1 by shear stress in endothelial cells mediates both cytoskeletal reorganization and effects on gene expression. *Embo J.* 21, 6791–6800. doi: 10.1093/emboj/cdf688

Wang, C., Baker, B. M., Chen, C. S., and Schwartz, M. A. (2013). Endothelial cell sensing of flow direction. *Arterioscl. Thromb. Vasc. Biol.* 33, 2130–2136. doi: 10.1161/ATVBAHA.113.301826

Wang, M., Wang, Z., Zhang, M., Guo, W., Li, N., Deng, Y., et al. (2017). microfluidic chip with double-sided herringbone microstructures for enhanced capture of rare tumor cells. *J Mater. Chem. B.* 5, 9114–9120. doi: 10.1039/C7TB02318A

Wechezak, A. R., Viggers, R. F., and Sauvage, L. R. (1985). Fibronectin and F-actin redistribution in cultured endothelial cells exposed to shear stress. *Lab Invest.* 53, 639–647.

Yaman, S., Anil-Inevi, M., Ozcivici, E., and Tekin, H. C. (2018). Magnetic force-based microfluidic techniques for cellular and tissue bioengineering. *Front. Bioeng. Biotechnol.* 6:192. doi: 10.3389/fbioe.2018.00192

Yan, S., Tan, S. H., Li, Y., Tang, S., Teo, A. J. T., Zhang, J., et al. (2017). A portable, hand-powered microfluidic device for sorting of biological particles. *Microfluid Nanofluid.* 22:8. doi: 10.1007/s10404-017-2026-0

Yoshino, D., Sakamoto, N., and Sato, M. (2017). Fluid shear stress combined with shear stress spatial gradients regulates vascular endothelial morphology. *Integr. Biol.* 9, 584–594. doi: 10.1039/C7IB00065K

Conflict of Interest Statement: The authors declare that the research was conducted in the absence of any commercial or financial relationships that could be construed as a potential conflict of interest.

frontiers in Bioengineering and Biotechnology

TECHNOLOGY REPORT
published: 01 May 2019
doi: 10.3389/fbioe.2019.00091

Integrated Flow Chamber System for Live Cell Microscopy

Carlo Kriesi[1], Martin Steinert[1], Anastasios Marmaras[2], Claudia Danzer[2], Virginia Meskenaite[2] and Vartan Kurtcuoglu[2]*

[1] TrollLABS, Department of Mechanical and Industrial Engineering, Norwegian University of Science and Technology, Trondheim, Norway, [2] The Interface Group, Institute of Physiology, University of Zurich, Zurich, Switzerland

In vitro quantification of the effect of mechanical loads on cells by live microscopy requires precise control of load and culture environment. Corresponding systems are often bulky, their setup and maintenance are time consuming, or the cell yield is low. Here, we show the design and initial testing of a new cell culture system that fits on standard light microscope stages. Based on the parallel plate principle, the system allows for live microscopy of cells exposed to flow-induced shear stress, features short setup time and requires little user interaction. An integrated feedback-controlled heater and a bubble trap enable long observation times. The key design feature is the possibility for quick exchange of the cultured cells. We present first test results that focus on verifying the robustness, biocompatibility, and ease of use of the device.

Keywords: cell culture, mechanobiology, fluid shear stress, flow chamber, device, integrated system

OPEN ACCESS

Edited by:
Sara Baratchi,
RMIT University, Australia

Reviewed by:
Takeo Minamikawa,
Tokushima University, Japan
Sungyoung Choi,
Kyung Hee University, South Korea

****Correspondence:***
Carlo Kriesi
carlo.kriesi@ntnu.no

Specialty section:
This article was submitted to Biomechanics, a section of the journal Frontiers in Bioengineering and Biotechnology

Received: *31 January 2019*
Accepted: *12 April 2019*
Published: *01 May 2019*

Citation:
Kriesi C, Steinert M, Marmaras A, Danzer C, Meskenaite V and Kurtcuoglu V (2019) Integrated Flow Chamber System for Live Cell Microscopy. Front. Bioeng. Biotechnol. 7:91. doi: 10.3389/fbioe.2019.00091

INTRODUCTION

In vivo, cells are exposed to mechanical stress in various ways (Ho et al., 2018), and exhibit cell type specific reactions to those (Davies and Tripathi, 1993). One well characterized example is how blood flow induced shear stress acts on vascular endothelial cells, thereby modulating vascular permeability (Orsenigo et al., 2012), which results in e.g., arterial blood pressure control (Wang et al., 2016). Since it is not possible to study mechanical influences in an isolated manner *in vivo*, various devices have been developed to expose cells to corresponding stimuli *in vitro*. These devices follow different fundamental principles, for instance: Mechanical deflection by the means of e.g., flexible silicone wells (Matsui et al., 2018); Flow-induced shear stress in e.g., parallel plate flow chambers (Koslow et al., 1986; Usami et al., 1993; Levitan et al., 2000) or under rotating discs (Chakraborty et al., 2016); Vibration-induced flow (Xu et al., 2018); The combination of microfluidic array and mechanical stimuli (Ho et al., 2018).

In this article, the focus lies on devices that rely on flow-induced shear stress at the cell's surface (wall shear stress or WSS). Such devices have enabled insights into for instance: How WSS activates molecular pathways in mouse embryonic stem cells (Illi et al., 2005); The impact of WSS on cell migration during wound healing (Franco et al., 2013); Cancer cell viability under WSS (Fan et al., 2016).

One popular design relies on flow between two parallel plates (Frangos et al., 1985). This design allows for well-defined, uniform shear stress on the cultured cells (Nauman et al., 1999), and also allows, in principle, for concurrent live light microscopy. One important shortcoming of current parallel plate devices is their incompatibility with high-throughput setups. This is a reflection of the time consuming, complex startup preparations needed to avoid leakage and air bubbles in these generally "bulky systems" (Salek et al., 2012). Parallel plate devices contrast

with the simple approach of placing multi-well plates on an orbital shaker to induce shear stress by swirling culture medium. The latter approach allows for high throughput, but exposes cells to inhomogeneous mechanical stresses dependent on various factors, including the amount of medium in the respective well (Salek et al., 2012). Furthermore, concurrent live microscopy is not possible. Another prominent approach relies on microfluidic devices that can be rapidly prototyped (Duffy et al., 1998) and allow for high throughput, since they can offer a high spatial density of flow paths (Thorsen et al., 2002). Despite the small form factor of microfluidic devices, the required pumps and heaters result nevertheless in bulky systems. In addition, boundary effects create inhomogeneous WSS across microchannels. Microfluidic devices further reach their limit when larger structures such as organoids need to be investigated or when mechanical access to the cells is required, e.g., in wound healing assays (Liang et al., 2007).

With the existing solutions in mind, the authors developed an integrated flow chamber system, subsequently referred to as "the device," that adopts strengths of current approaches while removing shortcomings, thereby allowing rapid, well-controlled studies of cells exposed to mechanical stimuli using live microscopy. This vision implied certain design constraints: First and foremost, the "bulkiness" of a classic parallel plate flow chamber setup, as Salek et al. (2012) put it, or any setup for that matter, had to be reduced without sacrificing accuracy and control of the imposed mechanical stimulus. One crucial element of *bulkiness* is related to the central challenge that all systems have in common, namely maintaining a temperature hospitable to the cells. Either a temperature-controlled containment for the entire microscope and its immediate surroundings must be provided, or the cell culture medium must be accurately preheated before it reaches the cells. The first approach allows for installing any equipment within the containment as long as it fits space wise. However, newly introduced elements take time to reach the target temperature, making this approach inefficient in shared microscope settings. In such an environment, the second approach allows for higher throughput, provided that compatibility with existing equipment, in particular with microscopes, is maintained. To further decrease down time, cells should be replaceable quickly, e.g., to change to a control group while maintaining experimental conditions, or to switch to a different type of experimental setup without extensive reconfiguration. Herein, we describe the development and testing of such an integrated flow chamber system.

MATERIALS AND METHODS

Design Goals and Implementation

The overarching aim throughout the development was a device usable by researchers trained in cell culture work, but without prior experience in flow cultures. This implies *soft* requirements of strong focus on user-centered design and subsequent ease of use. The technical constraints mentioned in the Introduction were translated to the following four main *hard* design requirements:

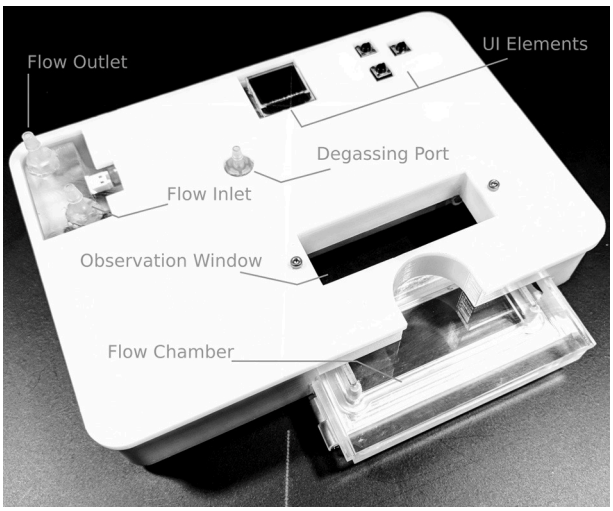

FIGURE 1 | Overview of the device. The in- and outlet ports connect to the heater and to the cell culture medium container, respectively. The degassing port is part of the bubble trap, located ahead of the flow chamber where the cells are located. The user interface (UI) elements, namely a 64 × 48 pixel OLED display and three buttons, allow the user to set the desired flow rate and temperature. During operation, the current outlet temperature, heater status, and possible sensor errors are displayed.

- The device must include a heating system that maintains the culture medium at a specific temperature and reacts rapidly to perturbations.
- The flow chamber and the cultured cells must be exchangeable without the use of tools.
- The complete system must be compatible with and fit on a standard light microscope stage.
- The device must be biocompatible in the sense that it does not harm the growth of cells and can be cleaned to remove contaminants.

The development work included multiple prototype-test-iterate rounds according to the Wayfaring principle (Steinert and Leifer, 2012), where each iteration was performed to answer specific design questions and subsequently used for guiding the focus of further development (Leifer and Steinert, 2011). The final design is shown in **Figure 1**.

Device Overview

Addressing the goal of physical compatibility with standard inverted microscope stages, the device has a footprint of 160 × 110 mm^2, and overall height of 36 mm, which is low enough for positioning under the condenser of the microscope. Within this building space, the device includes:

- User interface (UI), consisting of an OLED display and three buttons.
- Heater including two temperature sensors.
- Degassing chamber.
- Flow chamber with optical access.

- Electronic circuitry and microcontroller for regulating temperature, as well as handling the in-/output stream for the UI.

The setup in a general use case is as follows (**Figure 2**): The cell culture medium flows driven by an external peristaltic pump from an external reservoir into the device. Therein, it flows past the inlet temperature sensor, through the heater, past the outlet temperature sensor and via the bubble trap into the flow chamber and back to the reservoir. The total liquid volume within the device is 20 ml.

Production Methods

Apart from some standard components such as connectors and resistors, everything was built in-house at the prototyping facility TrollLABS at the Norwegian University for Science and Technology (NTNU, Trondheim, NO). Namely, the production relies on a laser cutter (Gravograph LS1000 XP, Gravotech Marking SAS, Rillieux-la-Pape, FR), a high-end 3D-printer (Objet30, Stratasys, Rehovot, IS, in combination with the same company's VeroWhitePlus material), a CNC mill (Mazak VCN-705E, Mazak corp., Florence, KY, US), as well as soldering equipment.

Heater and Power Control

The general design principle of the heater is that of a parallel plate heat exchanger, where each plate is a heating element made of a laser-cut nickel-chrome (NiCr) foil of 0.01 mm thickness, sandwiched between two laser-cut KU-EGF20 silicone foils (Aavid, Laconia, NH, US) of 0.22 mm thickness. The overall thickness of one heating element is thus 0.45 mm. This design creates a large surface area needed for homogenous temperature distribution within the cell culture medium within a range of flow rates. It also mitigates the risk of local overheating, which would result in medium denaturation. All other structural elements, namely the top and bottom lids as well as the spacers, are made of acrylic. The lids are CNC milled, whereas the spacers are laser cut. A CAD model cross-section of the heater assembly with annotations is presented in **Figure 3**. The entire structure is held together by ten M2 bolts, allowing for an even clamping force necessary to avoid leakage. The heating power depends on the applied voltage, as well as on the resistance of each element that can be adjusted by changing the pattern of the NiCr foil. In the current design, a single heater element has an average resistance of 47 Ohm. Therefore, following Ohm's law, the five heaters in parallel have a total resistance of 9.6 Ohm, yielding a maximum power output of roughly 40 Watts at 19.5 V. Theoretically, this is sufficient to increase the temperature of water flowing at up to 35 ml/min by 16 Kelvin, assuming adiabatic conditions and constant heat capacity of 4.2 kJ/kgK. Attached to the heater assembly is the distribution block that not only guides the flow of the cell culture medium in and out of the heater, but also includes the bubble trap. The laser-cut NiCr foil, as well as the complete heater including the distribution block, are depicted in **Figure 4**.

Sensirion STS30 temperature sensors (Sensirion AG, Staefa, CH) with a resolution of $\pm$ 0.2°C are located at the inlet and outlet of the heater. The inlet sensor enables rapid adjustment to thermal changes in the inlet and surroundings and allows for a substantially accelerated warm-up procedure by feed-forward control that relies on known flow rate, inlet temperature, and heater power. The outlet sensor is used for fine-tuning the outlet temperature to the target value by feedback control. The sensor data are processed by the control system running on a microcontroller that adjusts the heater power through a MOSFET transistor. This transistor is controlled by pulse width modulation with 8-bit resolution (256 steps), resulting in a power adjustment resolution of 0.16 W/step. By fluctuating the power level, the heater can precisely adjust to the target temperature.

Degassing

Gas bubbles within the flow chamber must be avoided, as they can damage cells and alter the mechanical stimulus. Since the solubility of the most prevalent gases in the air generally decreases with increasing temperature (Battino and Clever, 1966), gas bubbles are likely to form in the heater. Therefore, the degassing unit is placed immediately downstream of the heater and immediately upstream of the flow chamber (see **Figure 4**). The degassing unit consists of two chambers that are separated by a polytetrafluoroethylene (PTFE) membrane (TRACE Analytics, Braunschweig, DE). Its top side is in direct contact with surrounding air at atmospheric pressure and its bottom side is in contact with the medium. Gas bubbles that may develop rise within the medium up to the PTFE membrane. These gas bubbles are at the same pressure level as the surrounding medium, and thus at a slightly higher pressure than atmosphere. The actual gas removal is, therefore, a diffusion process driven by the gas partial pressure difference across the membrane (Cussler, 2009). Furthermore, the bubble trap works completely passively and is self-regulating: An increase of the flow rate implies both a larger volume of gas that is transported into the system and needs to be removed, as well as a higher gas pressure drop across the membrane that increases diffusion. This is because the cell culture medium pressure in the degassing unit increases with increasing flow rate.

Electronics

The electronic system is based on an open source Arduino Micro microcontroller (Arduino.cc). It is integrated in the electronic circuitry of the device consisting of three connected printed circuit boards (PCBs):

- The *main PCB* includes the microcontroller, MOSFET, and necessary connectors for power distribution.
- The *sensor PCB* connects both temperature sensor breakout boards and carries the necessary resistors and capacitors.
- The *display PCB* contains the UI elements and their resistors.

The microcontroller handles temperature control as well as input from and output to the UI. It also ensures shutdown of the heater in case of faulty temperature sensors.

Flow Chamber

Overall, the flow chamber is a cassette-like insert as shown in **Figure 1**. It consists of a milled acrylic body and an aluminum lid that can hold a 38 $\times$ 76 mm^2 glass slide of 1 mm thickness

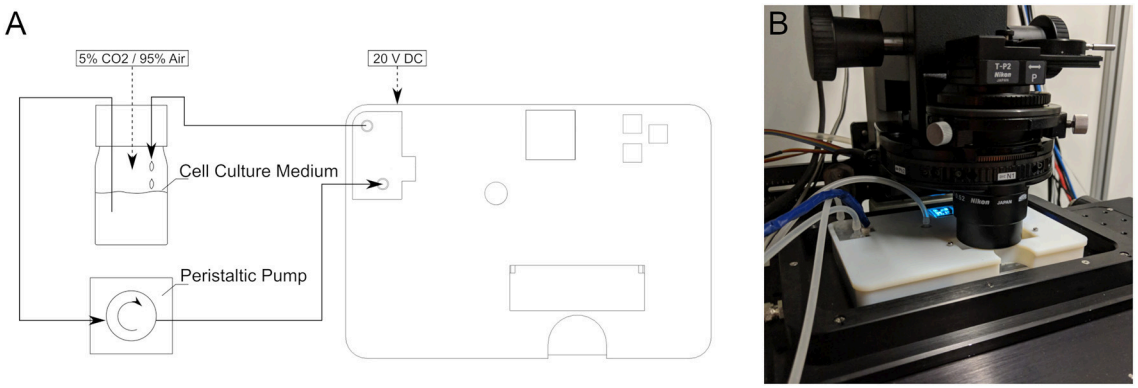

FIGURE 2 | (A) Schematic of the complete experimental circuit with the device. **(B)** The device in use on an inverted microscope.

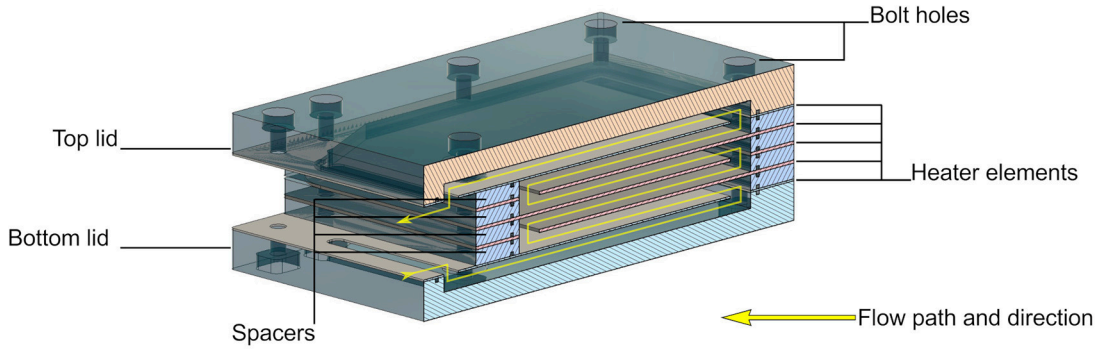

FIGURE 3 | Cross-section of the CAD model of the heater assembly showing how the five heating elements are arranged to maximize heated area per volume.

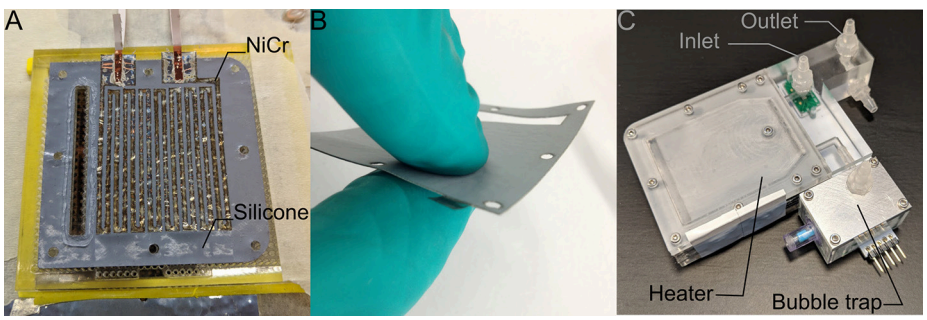

FIGURE 4 | (A) The heating elements are based on laser-cut NiCr foil sandwiched between two silicone foils. **(B)** The result is a watertight heating element with 0.45 mm thickness. **(C)** The complete heater assembly includes the in- and outlet ports, five heating elements, as well as the bubble trap upstream of a valve that leads to the flow chamber. The green plate visible under the inlet port is one of the two temperature sensor breakout boards (the second one, not visible in this picture, is located within the bubble trap).

on which cells are cultured in a regular incubator before it is placed in the flow chamber. A specifically designed, cast silicone O-ring made of Ecoflex 00-50 (Smooth-On, Macungie, PA, USA) seals the flow channel. The locking mechanism is a single pin that can be removed and inserted by hand. **Figure 5** provides a detailed view of the chamber and its individual parts. For the tests reported herein, a rectangular channel of 0.3 × 20 mm^2 cross-section was used. With the insertable glass-slide forming the bottom and the acrylic cassette the top, this corresponds to a parallel flow chamber setup. The level of shear stress τ [Pa] acting on the cells can be approximated as

$$\tau = \frac{6Q\mu}{wh^2}, \quad (1)$$

where Q is the flow-rate [m^3/s], μ is the dynamic viscosity [Pa s], and w [m] and h [m] are channel width and height,

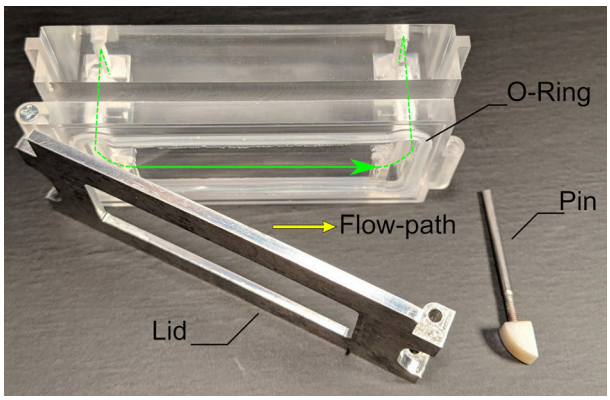

FIGURE 5 | The flow chamber that was used in all tests. The lid can hold a 38 × 76 mm^2 glass slide of 1 mm thickness on which the cells are attached. Closing the lid with the pin creates a rectangular flow-channel of 0.3 × 20 mm^2 cross-section, sealed off by the silicone O-ring.

respectively (Levitan et al., 2000). The tests reported herein were run with flow rates between 5 ml/min and 20 ml/min, resulting in shear stresses between 0.25 Pa and 1 Pa. These numbers were further validated by computational fluid dynamics (CFD) analyses (see section Flow and WSS Analysis).

Validation of Design Goals

The design goals are related to user interactions (*soft* goals) and to robustness for live cell experiments (*hard* goals). Attainment of the soft goals was validated by observing the interactions of researchers with the device, and by analyzing their feedback on its usability. Attainment of the hard goals was validated by tests performed in various settings and surroundings, with and without cells, to check for robustness, heater performance, and biocompatibility.

Ease of Use

As mentioned in the introduction, "bulkiness" had to be reduced. A proxy for the reduction in bulkiness and, therefore, for the increase in ease of use, is the number of tools and components required to run the *in vitro* flow experiments. This, in turn, is associated with the time needed to set up an experiment, which we use here as a surrogate for ease of use. Since individual research groups follow different protocols and do not use the same pump or other auxiliary equipment, our reported values only include the time the user spends in direct interaction with the device.

Robustness

Operation with expensive inverted microscopes requires robustness with respect to device integrity. In particular, leak prevention and fail-safe mechanisms must be robust, while maintaining compatibility with the microscope. Experiments with long run times require robust heating and temperature control, and day-to-day use necessitates hassle-free cleaning, loading and unloading, even as the device ages. To validate robustness, we have successfully tested the device for several 100 h under a variety of operating conditions.

TABLE 1 | Overview of cell types and shear stress levels used in the validation tests.

Cell Type	Origin	WSS [Pa]
Primary glia	Prepared from C57B6/JjRj mouse, Janvier Labs (Le Genest-Saint-Isle, FR)	0.25
Primary neurons	Prepared from C57B6/JjRj mouse, Janvier Labs	0.25
Madin-Darby canine kidney cells (MDCK)	MDCK-GAP43-YFP	0.25
Human umbilical vein endothelial cells (HUVEC)	Thermo Fisher	1.00
Meningothelial cells (MEC)	BEN-MEN-1, DSMZ no.: ACC 599 (Leibniz-Institut DSMZ-Deutsche Sammlung von Mikroorganismen und Zellkulturen GmbH, Braunschweig, DE)	0.30

Test Preparations

Device surfaces exposed to the cell culture medium are made of very stable plastics (HDPE and Acrylic) and silicones. The medium does not come in contact with any metals. All of the used materials can handle regular disinfection liquids such as 1–3% H_2O_2 and 70% ethanol. To ensure biocompatibility, we performed tests with several cell types, including sensitive primary cells as listed in **Table 1**. The following cleaning protocol was followed in preparation of the tests:

1) Flush with 70% ethanol for 15 min.
2) Drain system.
3) Flush with double distilled H_2O.
4) Drain system.
5) Flush with 3% H_2O_2 for 20 min.
6) Drain system.
7) Dry system by forced airflow.

After cleaning, the whole system was pre-filled with cell culture medium containing antibiotics, namely 100 U penicillin and 0.1 mg streptomycin/mL (Sigma-Aldrich, St. Louis, MO, USA). The cells were cultured and passaged in the appropriate culture medium. For HUVEC, this was Medium 200 plus LSGS (Thermo Fisher, Waltham, MA, USA). For MEC, it was high glucose DMEM with GlutaMAX™ and sodium pyruvate (Thermo Fisher) supplemented with 10% FCS. For primary glial cells, DMEM plus GlutaMAX (Gibco, Thermo Fisher) was used. For primary neurons, Gibco neurobasal medium (Thermo Fisher) was used. Finally, for MDCK, DMEM D5796 (Sigma-Aldrich) was utilized.

For all tests, the cells were grown in an area created by a silicone ring on 38 × 76 mm^2 glass slides until they reached the desired level of confluence (ideally 70–100%). Prior to placing the slide into the open lid of the flow chamber, the silicone ring was removed, and the glass slide was covered with additional medium to ensure that the cells were not exposed to air.

Test Procedure

Once the lid is closed and secured, the flow chamber is inserted into the prefilled main device. Two mechanically activated valves ensure that there is no leakage when the flow chamber is removed. After the flow chamber is inserted, the operator can power on the device, set a target temperature (here 37°C, maintained solely by the internal heater), and set the pump to the desired flow rate without turning it on. Finally, the device is placed on the inverted microscope stage, here on a Visitron Spinning Disk CSU-W1 (Visitron Systems GmbH, Puchheim, DE). The observation can start once the pump is turned on. The pH of the system was kept constant by gassing with 5% CO_2/95% air into the reservoir.

In addition to testing biocompatibility with a broad variety of cells, the device was used for an explorative experiment, highlighting the capability of creating a hospitable environment, as well as enabling constant observation. It investigated the effect of WSS on MECs when grown on differently coated glass slides and exposed to WSS of 0.30 Pa.

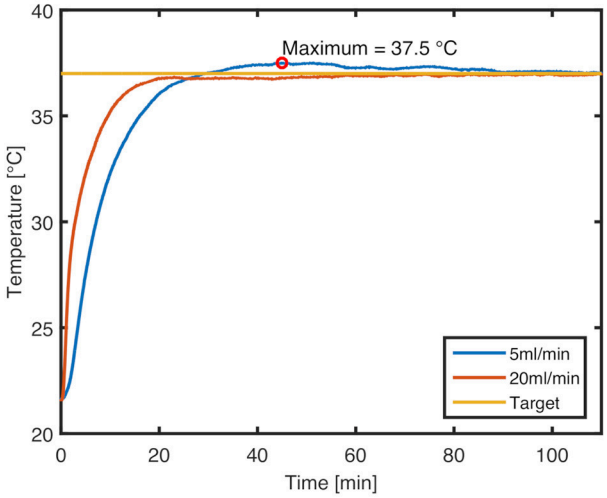

FIGURE 6 | Characteristic temperature profiles for ramp-up to 37°C set temperature at flow rates of 20 and 5 ml/min, respectively. An overshoot of 0.5°C is seen at the lower flow rate.

RESULTS

Heating and Temperature Control

The heating system proved capable of bringing the device to the desired output temperature rapidly and keeping it steady throughout the tests. Characteristic temperature profiles for ramp-up at 5 and 20 ml/min flow rate from 22°C to a target of 37°C are shown in **Figure 6** (raw sensor data available in **Supplementary Materials**). The maximum overshoot at 5 ml/min, which corresponds to the lower limit of possible flow rates, is 0.5°C. At this flow rate, the target temperature is first reached at 29 min, and equilibrium is established at 90 min. At the upper flow rate limit of 20 ml/min, there is no overshoot, and the target temperature is reached within 21 min. In both cases, the temperature stabilizes on the target value, even if the cell culture medium reservoir heats up over time.

Interactions

No tools are required to operate the device. The individual steps of user interaction are as follows (see also **Figure 2** for steps 1 and 2, and **Figure 7** for steps 3–5):

1) A tube that connects to the reservoir via the peristaltic pump is attached to the inlet port of the device.
2) The outlet port is connected to a tube that drains either back to the reservoir or into a waste container.
3) The flow chamber is removed from the device and opened by removing the pin.
4) The glass slide with the cells is placed in the flow chamber and extra cell culture medium is added.
5) The flow chamber is closed by reinserting the pin and placed back in the device.
6) The power cord is connected to the device and the target temperature, as well as the utilized flow rate are set on the UI unit.
7) Once the experiment is done, the power cord is removed. The device can now be flushed, or the next culture slide can be inserted following the steps above.

The design ensures that neither the glass slide, nor the flow chamber, nor the pin can slide out while the device is in use, since they are physically blocked by the microscope stage. Multiple biologists have used the device accordingly, and a completely new user that had not interacted with the device before required minimal training (completed within 1 h) before being able to operate the device.

Biocompatibility

The five cell types listed in **Table 1** were exposed to shear stress they typically encounter *in vivo*. The cells underwent mitosis throughout the tests and behaved in line with what has been reported in the literature and/or what we have observed in previous experiments with standard parallel plate flow devices. **Figure 8** shows five images that were recorded in these tests. Some cells survived for 72 h under flow (MEC), at which time the test was stopped, while others detached from the glass slide 30 min after onset of flow (glia). Overall, however, there were no signs of early cell death due to toxins or incompatible materials. Finally, the cleaning protocol listed in subsection Test Preparations was confirmed to be successful by observing the elimination of bacterial contamination within the device.

The results of an explorative test, comparing two coatings (**Figure 9**), show that the MEC cells grown on poly-d-lysine start rounding up and loosing attachment soon after the onset of flow. Grown on fibronectin, however, they mostly keep their initial morphology, at least up until the first 5 h of shear exposure. All images were recorded on the device described in this article.

Flow and WSS Analysis

In order to verify WSS values and shear stress homogeneity, as well as flow distribution, CFD analyses were conducted using SolidWorks Flow Simulation (Dassault Systèmes, Vélizy-Villacoublay, FR). They showed WSS of 0.26 Pa and 1.07 Pa on

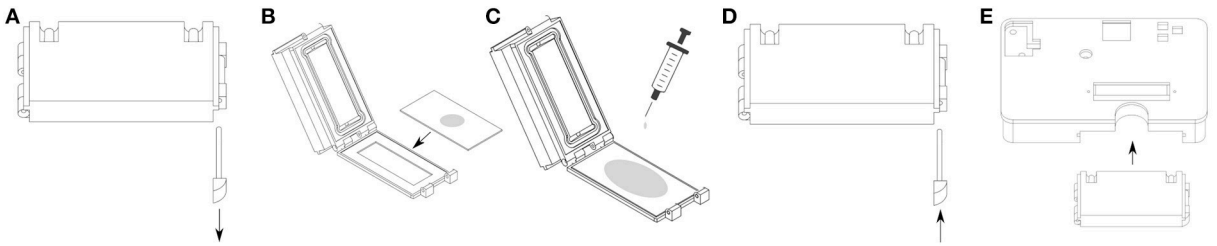

FIGURE 7 | An overview of the user interactions when unloading and loading cells for an experiment. **(A)** Removing the pin opens the flow chamber. **(B)** The glass slide hosting the incubated cells is placed in the lid. **(C)** Extra cell culture medium is added. **(D)** Inserting the pin closes the flow chamber. **(E)** The flow chamber itself is inserted into the device.

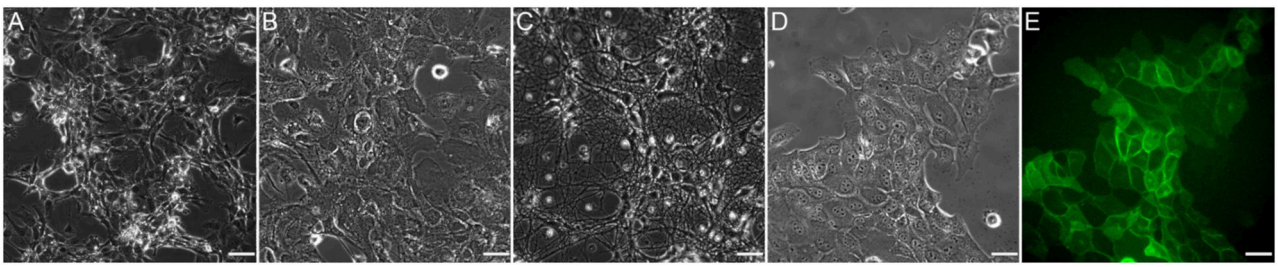

FIGURE 8 | Images of the different cell types that were used for testing as listed in **Table 1**. **(A)** HUVEC; **(B)** Primary glia; **(C)** Primary neurons; **(D)** MDCK; **(E)** MDCK GFP signal. All images were taken <1 min from onset of flow and at 40x magnification. Scale bar: 35 μm.

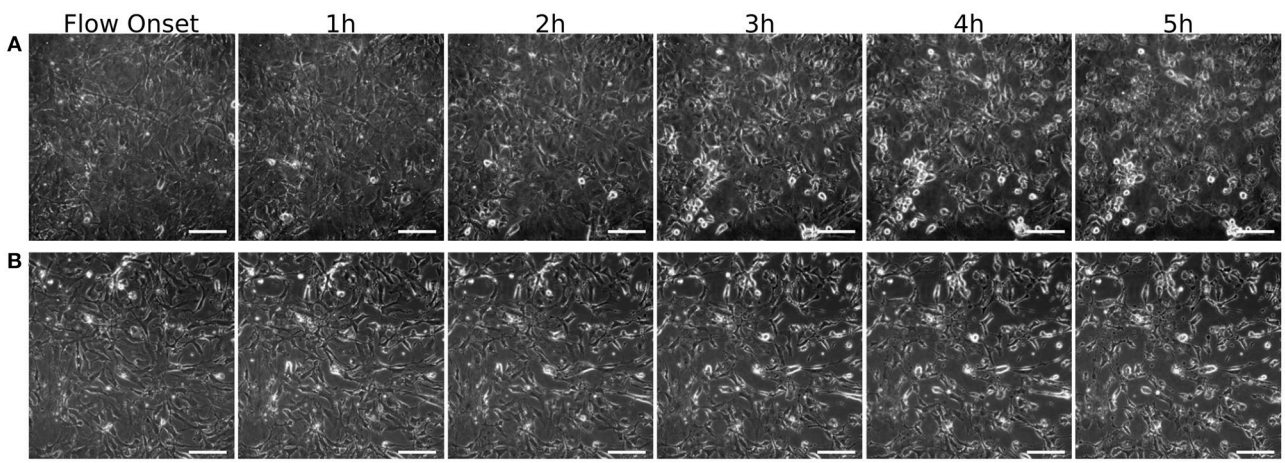

FIGURE 9 | MEC grown on different coatings. Images are taken over 5 h at one image per minute at 40x magnification. Shown here are t=0 at the onset of 6 ml/min flow (0.3 Pa WSS), and cells after 1, 2, 3, 4, and 5h of shear exposure. **(A)** Poly-d-lysine coated glass slides and **(B)** fibronectin coated glass slides. Scale bar: 50 μm.

the surface of the glass slide at steady inlet flowrates of 5 ml/min and 20 ml/min, respectively. This, as well as streamlines through the flow chamber, are illustrated in **Figure 10**.

To assess the compatibility of the device with microfluidics experiments, a microchannel insert was modeled and exposed to a simulated total flow rate of 5 and 20 ml/min, respectively. The virtual insert consisted of 30 evenly spaced channels, each with a cross-sectional area of 0.3×0.3 mm^2. The results of this simulation are illustrated in **Figure 11**. The simulation shows that such an insert would yield a homogeneous flow distribution across all channels, yet inhomogeneous WSS distribution across individual channels due to boundary effects of the channel walls. Concretely, WSS ranges from 0.29–0.95 Pa and 1.15–3.8 Pa across each channel at the lower and higher flow rate, respectively, with the minimum values occurring close to the walls and the maximum in the channel center. The WSS determined in all simulations, as well as the corresponding pressure drops between inlet and outlet are listed in **Table 2**.

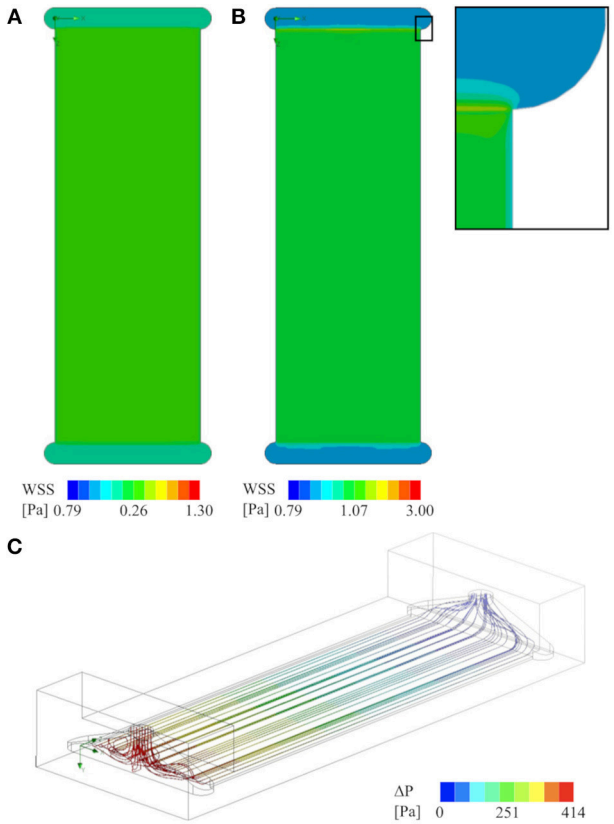

FIGURE 10 | CFD analysis of the flow chamber that was used for all experiments (cross-section of 0.3x20 mm^2): **(A)** Contour plot of WSS on the glass slide at 5 ml/min flow rate, and **(B)** at 20 ml/min, including a close up showing the boundary effects of the channel walls. **(C)** Stream lines visualizing the flow field from the inlet (red–high-pressure side) to the outlet (blue–low-pressure side) at 20 ml/min flow rate. There are no apparent zones of flow stagnation in the active area of the flow chamber.

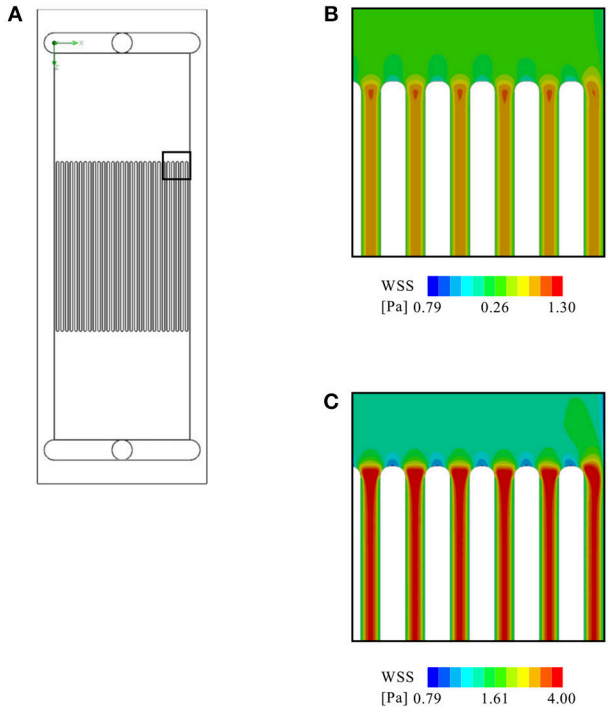

FIGURE 11 | CFD analysis of a virtual microfluidic insert consisting of 30 evenly spaced channels (each with a cross-sectional area of 0.3 × 0.3 mm^2): **(A)** The arrangement of the virtual microfluidic channels. Further shown are a close up of the contour plot of WSS on the glass slide at **(B)** 5 ml/min flow rate, and **(C)** at 20 ml/min.

DISCUSSION

This article introduces a device for flow-induced mechanical stimulation of *in vitro* cell cultures that includes a heater with controller, a bubble trap, and an insertable flow chamber. We have shown the results of first tests that focused on validating the robustness, biocompatibility, and ease of use of the device. Here, we will discuss to what extent the original design goals have been reached, and how the system can be further improved.

Validation of Main Design Goals

The *hard* goals relevant for the fundamental functionality of the device have been met. The heating system allowed fast ramp-up with little temperature overshoot and maintained target temperature for the entire test duration. Denaturation of the cell culture medium due to overheating is, therefore, not a concern. In particular, the heating system allows exchanging medium containers or topping off medium without risking a temperature shock to the cells due to the feed-forward control loop. The accuracy of the temperature control is limited by the resolution of the temperature sensors (± 0.2°C), as well as by the 8-bit resolution of the controller. The resulting power resolution of 0.16 W/step at 20 V supply voltage translates to approximately 0.46°C/step at 5 ml/min flow rate. Given the lack of insulation around the heater, the heat loss to the surroundings have a significant effect, therefore enabling the temperature to stabilize with this setup. For lower flow rates, however, either the controller must be replaced with a more precise one to ensure more accurate temperature control, or the total heating power must be adjusted to lower levels.

CFD analyses confirmed the expected homogenous WSS distribution on the glass slide, and revealed no flow stagnation zones in the active area of the flow chamber. These results are in agreement with the findings of Nauman et al. (1999). Furthermore, the WSS levels calculated by CFD are close to the values obtained by approximation with Equation (1), with a maximum deviation of 7 %.

The virtual microfluidic insert creates a roughly three times higher pressure drop than the parallel plate flow chamber at the same flow rate. At the lower flow rate of 5 ml/min, this is not expected to create any issues. However, at the higher flow rate (20 ml/min), the pressure drop across the microfluidic array may be too high for the device to handle. One can, therefore,

TABLE 2 | Calculated WSS and pressure drop across the flow chamber.

Channel cross-section [mm^2]	Total flow rate [ml/min]	WSS on cells [Pa]	Pressure drop (inlet-outlet) [Pa]
0.3 × 20 (1 channel)	5	0.26	103
0.3 × 20 (1 channel)	20	1.07	414
0.3 × 0.3 (30 channels)	5	0.29–0.95	295
0.3 × 0.3 (30 channels)	20	1.15–3.8	1189

conclude that a microfluidic setup is feasible, but with certain limitations regarding the maximum flow rate, especially since with 0.3 × 0.3 mm^2 the virtual microchannels still have a relatively large cross-section. A reduction in cross-sectional area would further increase the pressure drop. While the heater itself has enough power for a flow rate of up to 35 ml/min, the pressure drop at this flow rate across the flow chamber might cause leakage and/or ruptures along the flow path. Destructive testing will be required to determine the maximum pressure the system can withstand. Independent of the pressure-related limitations, microchannels never offers the same homogeneity of WSS across the cells as a larger parallel plate setup. This is due to boundary effects within individual channels, as visible in **Figure 11**.

The tests with live cells have proven that the device is compatible with the dimensional requirements of standard inverted microscope stages. It allows for continuous observation at 40x magnification, limited by the thickness of the glass slide that needs to withstand the internal hydraulic pressure without buckling. All observed behavior of the cells further indicates a healthy environment. In addition, the successful removal of a bacterial infection indicates that the cleaning protocol fulfills its task and, therefore, makes the device safely re-usable. While the explorative test comparing slide coating with poly-d-lysine and fibronectin was not intended to provide quantitative data on their relative performance, it does serve as a qualitative demonstration of how differences between two test settings can be optically observed. Given the fact that the device is compatible with phase contrast and fluorescent imaging techniques, analysis of metrics such as cell alignment over time as shown in e.g., Gong et al. (2017) is possible.

The *soft* design goals relating to user interaction and overall ease of use have also been reached. Integrating the heater, control system and degassing unit has reduced time required for setup compared to classic parallel plate devices. The *hard* design requirement of no tools plays into the ease of use of the whole device. If needed, the cells in the flow chamber can be exchanged within 2 min or the complete flow chamber can be exchanged in under 30 s. This is negligible compared to the duration of most flow experiments. In addition, the device also creates a safe environment for transporting cells to and from, e.g., cell culture and microscopy rooms. The small opening of the inlet and outlet parts are easily temporarily sealed. It is also possible to prepare multiple flow chambers for sequential microscopic imaging under flow, thus enabling higher throughput than with classic parallel plate systems.

Vision

On a more abstract level, the device presents a platform that takes care of the well-being of cells, and the cassette-like flow chamber creates an experimental environment that can be adjusted to individual needs. Although the here presented flow chamber follows a parallel plate design, other chamber designs could be used as well. For instance, 3D-bioprinted structures could be perfused in the available space, and microfluidic structures could be integrated. Since the production of the structures itself, e.g., 3D-bioprinting, requires multiple hours if not days to begin with, a stable environment rather than high throughput is the main objective.

The device could become even easier to use if it required no external machinery and auxiliary devices at all. As shown in **Figure 2**, the device currently relies on an external pump and reservoir, as well as a gassing system. The enclosure offers some unused space that could be utilized to integrate a pump. However, this would also require integrated flow control, meaning that a flow-sensor and corresponding electronics would need to be added as well.

To compete with high-throughput setups, e.g., with ones based on orbital shakers, parallel operation would be required. This can be achieved to some extent by designing flow chamber inserts with multiple micro-channels, such as the virtual one analyzed herein. Together with the option of an injection port, the device could allow for drug testing on organoids connected in series, thereby taking in account possible *in vivo* intercommunications of the tissues upon drug intake.

The next level will be a system with automated cell culturing directly on the glass slides, as well as automated exchange of flow chambers, allowing to standardize and multiplex the research on the effect of fluid flow on cells and organoids. It seems unreasonable to assume that this approach will ever compete with the cost-efficient throughput of stacks of multi-well plates. However, the better control of mechanical stimuli and thus higher reliability of results may justify the higher cost of an automated parallel plate setup. Such a setup could be further used to connect multiple flow chambers, either in parallel to a central cell culture medium supply, or in series in order to observe downstream effects.

In conclusion, the device presented here is a flexible platform for the study of cells under flow-induced mechanical stimuli, potentially also with microfluidic inserts. Its key advantages are that it is easy to operate, time effective in its use, and biocompatible as indicated by tests with several cell types, including sensitive primary neurons.

AUTHOR CONTRIBUTIONS

All authors contributed ideas and concepts throughout the development of the device. CK did the physical implementation. VM, CD, AM, and CK performed

the tests. MS and VK provided laboratories. All authors contributed and agreed to the final wording of the submission.

FUNDING

This research was supported by the Research Council of Norway through its user-driven research (BIA) funding scheme, project number 236739/O30, and by the Swiss National Science Foundation through NCCR Kidney.CH.

SUPPLEMENTARY MATERIAL

The Supplementary Material for this article can be found online at: https://www.frontiersin.org/articles/10.3389/fbioe.2019.00091/full#supplementary-material

REFERENCES

Battino, R., and Clever, H. L. (1966). The solubility of gases in liquids. *Chem. Rev.* 66, 395–463.

Chakraborty, A., Chakraborty, S., Jala, V. R., Thomas, J. M., Sharp, M. K., Berson, R. E., et al. (2016). Impact of bi-axial shear on atherogenic gene expression by endothelial cells. *Ann. Biomed. Eng.* 44, 3032–3045. doi: 10.1007/s10439-016-1665-8

Cussler, E. L. (2009). *Diffusion: Mass Transfer in Fluid Systems*. Cambridge: Cambridge University Press.

Davies, P. F., and Tripathi, S. C. (1993). Mechanical stress mechanisms and the cell. An endothelial paradigm. *Circ. Res.* 72, 239–245.

Duffy, D. C., McDonald, J. C., Schueller, O. J., and Whitesides, G. M. (1998). Rapid prototyping of microfluidic systems in poly (dimethylsiloxane). *Anal. Chem.* 70, 4974–4984.

Fan, R., Emery, T., Zhang, Y., Xia, Y., Sun, J., and Wan, J. (2016). Circulatory shear flow alters the viability and proliferation of circulating colon cancer cells. *Sci. Rep.* 6:27073. doi: 10.1038/srep27073

Franco, D., Milde, F., Klingauf, M., Orsenigo, F., Dejana, E., Poulikakos, D., et al. (2013). Accelerated endothelial wound healing on microstructured substrates under flow. *Biomaterials* 34, 1488–1497. doi: 10.1016/j.biomaterials.2012.10.007

Frangos, J. A., Eskin, S. G., McIntire, L. V., and Ives, C. (1985). Flow effects on prostacyclin production by cultured human endothelial cells. *Science* 227, 1477–1479.

Gong, X., Zhao, X., Li, B., Sun, Y., Liu, M., Huang, Y., et al. (2017). Quantitative studies of endothelial cell fibronectin and filamentous actin (F-Actin) coalignment in response to shear stress. *Microsc. Microanal.* 23, 1013–1023. doi: 10.1017/S1431927617012454

Ho, K. K. Y., Wang, Y.-L., Wu, J., and Liu, A. (2018). Advanced microfluidic device designed for cyclic compression of single adherent cells. *Front. Bioeng. Biotechnol.* 6:148. doi: 10.3389/fbioe.2018.00148

Illi, B., Scopece, A., Nanni, S., Farsetti, A., Morgante, L., Biglioli, P., et al. (2005). Epigenetic histone modification and cardiovascular lineage programming in mouse embryonic stem cells exposed to laminar shear stress. *Circ. Res.* 96, 501–508. doi: 10.1161/01.RES.0000159181.06379.63

Koslow, A. R., Stromberg, R. R., Friedman, L. I., Lutz, R. J., Hilbert, S. L., and Schuster, P. (1986). A flow system for the study of shear forces upon cultured endothelial cells. *J. Biomech. Eng.* 108, 338–341.

Leifer, L. J., and Steinert, M. (2011). Dancing with ambiguity: causality behavior, design thinking, and triple-loop-learning. *Inf. Knowl. Syst. Manag.* 10, 151–173. doi: 10.1007/978-3-319-01056-4_11

Levitan, I., Helmke, B. P., and Davies, P. F. (2000). A chamber to permit invasive manipulation of adherent cells in laminar flow with minimal disturbanceof the flow field. *Ann. Biomed. Eng.* 28, 1184–1193. doi: 10.1114/1.1317529

Liang, C.-C., Park, A. Y., and Guan, J.-L. (2007). *In vitro* scratch assay: a convenient and inexpensive method for analysis of cell migration *in vitro*. *Nat. Protoc.* 2:329. doi: 10.1038/nprot.2007.30

Matsui, T. S., Wu, H., and Deguchi, S. (2018). Deformable 96-well cell culture plate compatible with high-throughput screening platforms. *PLoS ONE* 13:e0203448. doi: 10.1371/journal.pone.0203448

Nauman, E. A., Risic, K. J., Keaveny, T. M., and Satcher, R. L. (1999). Quantitative assessment of steady and pulsatile flow fields in a parallel plate flow chamber. *Ann. Biomed. Eng.* 27, 194–199.

Orsenigo, F., Giampietro, C., Ferrari, A., Corada, M., Galaup, A., Sigismund, S., et al. (2012). Phosphorylation of VE-cadherin is modulated by haemodynamic forces and contributes to the regulation of vascular permeability *in vivo*. *Nat. Commun.* 3:1208. doi: 10.1038/ncomms2199

Salek, M. M., Sattari, P., and Martinuzzi, R. J. (2012). Analysis of fluid flow and wall shear stress patterns inside partially filled agitated culture well plates. *Ann. Biomed. Eng.* 40, 707–728. doi: 10.1007/s10439-011-0444-9

Steinert, M., and Leifer, L. J. (2012). "Finding One's Way": re-discovering a hunter-gatherer model based on wayfaring. *Int. J. Eng. Educ.* 28, 251–252. Available online at: https://www.ijee.ie/contents/c280212.html

Thorsen, T., Maerkl, S. J., and Quake, S. R. (2002). Microfluidic large-scale integration. *Science* 298, 580–584. doi: 10.1126/science.1076996

Usami, S., Chen, H.-H., Zhao, Y., Chien, S., and Skalak, R. (1993). Design and construction of a linear shear stress flow chamber. *Ann. Biomed. Eng.* 21, 77–83.

Wang, S., Chennupati, R., Kaur, H., Iring, A., Wettschureck, N., and Offermanns, S. (2016). Endothelial cation channel PIEZO1 controls blood pressure by mediating flow-induced ATP release. *J. Clin. Invest.* 126, 4527–4536. doi: 10.1172/JCI87343

Xu, J., Mathur, J., Vessières, E., Hammack, S., Nonomura, K., Favre, J., et al. (2018). GPR68 senses flow and is essential for vascular physiology. *Cell* 173:e16. doi: 10.1016/j.cell.2018.03.076

Conflict of Interest Statement: The authors declare that the research was conducted in the absence of any commercial or financial relationships that could be construed as a potential conflict of interest.

frontiers in Bioengineering and Biotechnology

METHODS
published: 14 May 2019
doi: 10.3389/fbioe.2019.00096

Adaptation of a Mice Doppler Echocardiography Platform to Measure Cardiac Flow Velocities for Embryonic Chicken and Adult Zebrafish

Fatiha M. Benslimane[1], *Maha Alser*[1], *Zain Z. Zakaria*[1,2], *Anju Sharma*[1], *Hana A. Abdelrahman*[1] *and Huseyin C. Yalcin*[1]*

[1] Biomedical Research Center, Qatar University, Doha, Qatar, [2] Department of Biological and Environmental Sciences, College of Arts and Science, Qatar University, Doha, Qatar

OPEN ACCESS

Edited by:
Sara Baratchi,
RMIT University, Australia

Reviewed by:
Corinna Singleman,
Queens College (CUNY), United States
Dimitris Beis,
Biomedical Research Foundation of the Academy of Athens, Greece
Louis C. Leung,
Stanford University, United States

***Correspondence:**
Huseyin C. Yalcin
hyalcin@qu.edu.qa

Specialty section:
This article was submitted to Biomechanics, a section of the journal Frontiers in Bioengineering and Biotechnology

Received: 25 December 2018
Accepted: 16 April 2019
Published: 14 May 2019

Citation:
Benslimane FM, Alser M, Zakaria ZZ, Sharma A, Abdelrahman HA and Yalcin HC (2019) Adaptation of a Mice Doppler Echocardiography Platform to Measure Cardiac Flow Velocities for Embryonic Chicken and Adult Zebrafish. Front. Bioeng. Biotechnol. 7:96. doi: 10.3389/fbioe.2019.00096

Ultrasonography is the most widely used imaging technique in cardiovascular medicine. In this technique, a piezoelectric crystal produces, sends, and receives high frequency ultrasound waves to the body to create an image of internal organs. It enables practical real time visualization in a non-invasive manner, making the modality especially useful to image dynamic cardiac structures. In the last few decades, echocardiography has been applied to *in vivo* cardiac disease models, mainly to rodents. While clinical echocardiography platforms can be used for relatively large animals such as pigs and rats, specialized systems are needed for smaller species. Theoretically, as the size of the imaged sample decreases, the frequency of the ultrasound transducer needed to image the sample increases. There are multiple modes of echocardiography imaging. In Doppler mode, erythrocytes blood flow velocities are measured from the frequency shift of the sent ultrasound waves compared to received echoes. Recorded data are then used to calculate cardiac function parameters such as cardiac output, as well as the hemodynamic shear stress levels in the heart and blood vessels. The multi-mode (i.e., b-mode, m-mode, Pulsed Doppler, Tissue Doppler, etc.) small animal ultrasound systems in the market can be used for most *in vivo* cardiac disease models including mice, embryonic chick and zebrafish. These systems are also associated with significant costs. Alternatively, there are more economical single-mode echocardiography platforms. However, these are originally built for mice studies and they need to be tested and evaluated for smaller experimental models. We recently adapted a mice Doppler echocardiography system to measure cardiac flow velocities for adult zebrafish and embryonic chicken. We successfully assessed cardiac function and hemodynamic shear stress for normal as well as for diseased embryonic chicken and zebrafish. In this paper, we will present our detailed protocols for Doppler flow measurements and further cardiac function analysis on these models using the setup. The protocols will involve

detailed steps for animal stabilization, probe orientation for specific measurements, data acquisition, and data analysis. We believe this information will help cardiac researchers to establish similar echocardiography platforms in their labs in a practical and economical manner.

Keywords: Doppler echocardiography, blood flow velocity, chick embryo, zebrafish, cardiac function, mechanobiology

INTRODUCTION

Cardiovascular diseases (CVDs) are disorders of the heart and blood vessels. They are the leading cause of mortality, constituting 31% of all fatalities globally (Kendir et al., 2018). CVDs can occur prenatally, known as congenital heart defects (CHDs), or develop at later stages of life. CHDs account for around 25% of all human congenital abnormalities (Roger et al., 2011) and it affects 1–2% of infants globally. Although prenatal cardiac malformations are linked to genetics, the etiology is highly complex and involves multiple factors (Lindsey et al., 2014). Recently, it has been shown that genetics accounts for <20% of heart defects. Other environmental factors, such as hyperglycemia during maternal diabetes, or disturbed hemodynamics are thought to play a crucial role in CHD development (Midgett et al., 2017). Hemodynamics are the mechanical forces applied by blood flow, such as pressure or shear stress. Primarily, blood is pumped during development and remodeling, which suggests that hemodynamics governs cardiac development (Hove et al., 2003; Forouhar et al., 2006; Culver and Dickinson, 2010; Yalcin et al., 2011). The constant interactions between blood flow dynamics and cardiac tissue motion signals the endothelial cells lining the chambers and the valves. Deviations from normal hemodynamic conditions lead to cardiac malformations as the heart is very sensitive to biomechanical cues at the early embryonic stages (Goenezen et al., 2012). Clinical observations and animal experiments have shown that when hemodynamics are disturbed, fetal cardiac defects develop, consequently leading to CHDs at birth (Goenezen et al., 2012). Disturbed hemodynamics also contribute to formation of CVDs that develop later in life. For instance, it was shown that heart valve/blood vessel calcification localize to flow regions (i.e., oscillatory flow regions) that deviate from normal hemodynamics (Balachandran et al., 2011; Mahler et al., 2014; Fernández Esmerats et al., 2016; Amindari et al., 2017).

Animal models are very useful to investigate how disturbed hemodynamics contribute to CVDs (Zaragoza et al., 2011). Their use in relevant research facilitated to unravel various aspects of the diseases including etiology, pathophysiology, progression, and underlying biological pathways. Consequently, this knowledge led to the advancement of new diagnostic techniques and the discovery of new potential therapeutic approaches (Chorro et al., 2009). Vertebrate species, particularly, are favored models because of their highly conserved developmental processes. Their lifespan is relatively short, by 3 months they are considered as adults and in captivity they reach to 2 years of age, which allows investigators to monitor the disease at an accelerated pace. The genetically modified models that can be developed allows the rapid establishment of proof-of-principle (Camacho et al., 2016). For instance, rodent knockouts models have been extensively used for assessing the effects of genes on normal cardiac development and CVDs (Phoon et al., 2004; Bruneau, 2008). Furthermore, rodent models are used to assess the mother's nutrition effects on cardiovascular conditions and placental development on embryonic growth as well as cardiac formation (James et al., 1998; Yu et al., 2008). However, rodent embryos are not considered ideal models to study hemodynamic effects on cardiac development; they lack the ability to develop *ex utero* beyond early stages and accessing the embryo *in utero* during development is challenging (Piliszek et al., 2011). Additionally, certain genetic knockdowns are lethal either during embryogenesis or at the early stage of adulthood limiting the ability of the investigator to understand its molecular mechanism, which in turn limits the window for developing therapeutics. It is for all of these reasons that zebrafish and embryonic avian models have been more widely used to monitor hemodynamic conditions throughout development. In the case of adult zebrafish, these investigations extend to include some genes that cause severe phenotypes or are lethal in mammals (Hove et al., 2003; Jenkins et al., 2010; Lindsey et al., 2014; Yalcin et al., 2017; Yalcin, 2018). Although these models are being used extensively by researchers, the available cardiac imaging systems that allow the study of cardiac function in small animals are complex and highly expensive.

Doppler echocardiography is a popular tool for assessing cardiac function. The technique enables the measurement of blood velocities through blood vessels, heart valves, and cardiac chambers, which is then used to diagnose CVDs (Spencer et al., 2013). Doppler echocardiography is also very useful to apply to *in vivo* CVD models to investigate disturbed hemodynamics. Most current small imaging echocardiography platforms are designed for mouse studies and can be applied to other animal models. For example, previously, we have adapted B-mode-guided Doppler ultrasound visual sonic *in vivo* 770 platform (Vevo 770, Visualsonics, Inc., Toronto, Candad) for embryonic chick studies and documented evolving atrio-ventricular canal and outflow tract (Yalcin et al., 2011; Bharadwaj et al., 2012). Such high cost systems involve multiple modalities including Doppler, m-mode, b-mode, and tissue strain. Alternatively, there are also lower cost single mode Doppler echocardiography platforms, used mainly for mice imaging. Adaptation of these mice Doppler systems for use in other animal models requires testing and evaluation of these platforms. Here, we explain how we have adapted a mice Doppler echocardiography system to embryonic chick and adult zebrafish studies. We believe this information will help cardiac researchers to establish similar

echocardiography platforms in their labs in a practical and economical manner.

The studies were carried out in accordance with the recommendations of "Use of Zebrafish" and "Use of Avian Embryos" policies, Qatar University—Institutional Animal Care and Use Committee (QU-IACUC). The protocol was approved by the QU-IACUC.

THEORY OF BLOOD VELOCITY MEASUREMENTS VIA DOPPLER ECHOCARDIOGRAPHY

Typically, echocardiography imaging systems have three modes: b-mode, m-mode, and Doppler. B-mode (brightness-mode) and M-mode (motion-mode) are used for the assessment of morphology and movement of the tissue, whereas Doppler mode is used for the evaluation of cardiac function (Gregg and Butcher, 2012). More specifically, Doppler mode is used to measure blood flow velocity and determine flow direction. The technique is based on detecting the change in the frequency of sound waves that occur as they are reflected off a moving object, known as Doppler shift. Doppler echocardiography *in vivo* measures blood flow by detecting the frequency shift due to movement of erythrocytes (Gregg and Butcher, 2012; Kowalski et al., 2014). In this technique, a piezoelectric crystal produces and sends short impulse high frequency ultrasound waves to the body. Blood flow velocities are then calculated from the sound waves as scattered echoes received by the same crystal. It enables practical real time flow measurement in a non-invasive manner, making the modality especially useful to image dynamic cardiac flows. The frequency required reflects the size of the sample, as the size of the sample to be imaged decreases, the frequency of the ultrasound transducer increases. The clinical platforms available have transducers with maximum frequency of about 15 MHz, while advanced imaging systems can go up to 90 MHz making these systems more expensive.

Doppler mode utilizes real time spectral display, also known as waveforms. These spectral waveforms are indication of the dynamic nature of the blood flow through the heart and they reflect the elasticity of heart chambers and blood vessels. Therefore, obtaining these waveforms are very useful to monitor the cardiac function. The spectra is generated based on the Doppler shift according to Equation (1), where *fd* is the Doppler shift, *ft* is the transmitted beam, *V* is the velocity of the blood, θ is the angle between the transducer and the blood flow direction and *c* is the speed of sound in tissue (**Figure 1**).

$$Doppler\ Frequency\ (fd) = \frac{2\,.\,ft\,.\,V\,.\,\cos\theta}{c} \qquad (1)$$

Here, the factor two is for the round trip of the traveling sound waves, from the transducer, hitting the sample and reflecting back to the transducer. The direction of blood flow and the Doppler wave angle between the ultrasound beam and vessel are important factors in determining the velocity (**Figure 2**). The bigger the angle the more interference with the recorded

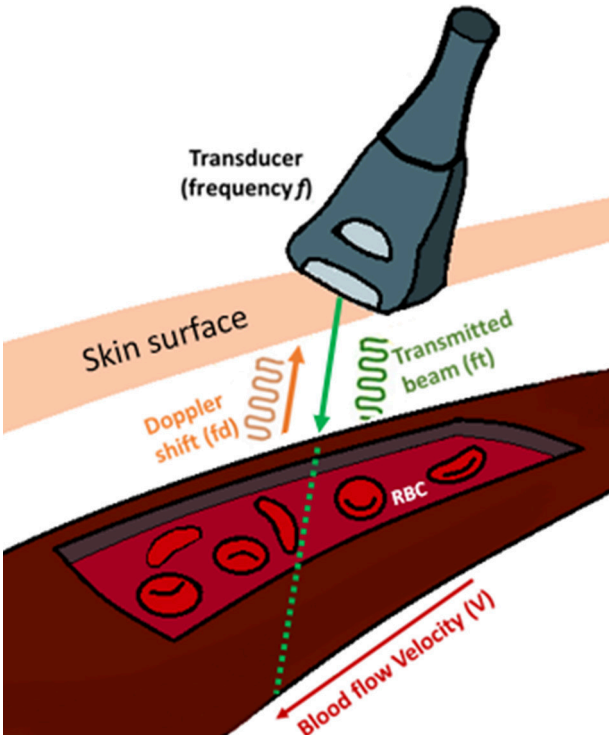

FIGURE 1 | Blood flow velocity (V) measurement using an ultrasound transducer. Doppler signal transmits a frequency (F_t) and receives the backscattered signals from the moving erythrocytes within the vessel at a frequency (F_d) known as Doppler shift. The angle (θ) is the angle between the transmitted signal and blood flow.

spectra. To obtain the largest Doppler shift using ultrasound, the transducer must be placed at an angle of zero degrees to the vessel of interest, however due to practical considerations, clinically the angle is placed at around 60 degrees. For animal experimentation, because of the small sizes of the animals, it is easier to align the probe with flow so that the angle is zero (please see relevant sections below and **Figure 2**). The direction of the blood flow, away or toward, the transducer is another important factor that interferes with the way the signal is digitized (**Figure 2**). Once the spectrogram is obtained, the blood flow velocities can be extracted from the waveforms and the heart rate is calculated by the frequency analysis of velocity waveform (Kowalski et al., 2014).

Doppler imaging modality is practical, and inexpensive in comparison with other modalities like Magnetic resonance imaging (MRI), Computed tomography (CT) and Optical coherence tomography (OCT). In addition, Doppler platforms are portable, facilitating image acquisition. Echocardiography is completely non-invasive and it has not been associated with any adverse effects (Spencer et al., 2013). Furthermore, Doppler blood velocity parameters are particularly important in direct translational studies. Cardiac parameters that are gathered with other techniques include, the heart weight, left ventricular volume, stroke volume, cardiac output, and aortic diameter are all proportional to body weight. This means that as the body size

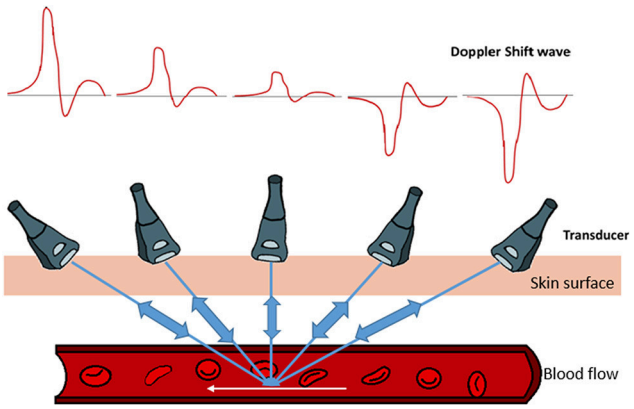

FIGURE 2 | Graphical demonstration of the relationship between Doppler's shifted frequency with respect to the insonation angle of Doppler's ultrasound beam. Pointing the Doppler ultrasound beam toward the direction of vessel's blood flow results in observing a positive Doppler shifted signal. As the Doppler ultrasound beam points away from the blood flow direction, a negative Doppler shift signal is noted. The smaller the angle between the blood vessel flow and Doppler ultrasound beam, the larger the Doppler shift signal. As the Doppler ultrasound beam approaches a 90° angle, very small signals are produced. Therefore, for any given blood flow, the larger the angle, the smaller the Doppler shift.

changes these parameters vary. As such, translating some of these measurements to other larger species or even humans would be difficult and direct translation would be challenging. On the other hand, aortic velocity and pulse wave velocity that can be obtained via Doppler are independent of body size. Aortic velocity and pulse wave velocity of a mouse, rat or a human, without the timing scale, are very similar. Their values across species do not vary that much allowing for a direct translation (Dawson, 1991).

Doppler echocardiography has been widely used in relatively larger mammalian animal models for *in vivo* cardiac function assessment (Watson et al., 2004; Locatelli et al., 2011). However, studying a small organism with a length size that ranges from 20 to 40 mm is challenging, nonetheless, it is now possible through the use of advanced high-frequency ultrasonography (up to 70 MHz, 30 μm axial resolution). The use of high frequency echocardiography in assessing cardiac function in small animals has recently begun to be explored. However, standardized approaches for image acquisition and data analysis are critically lacking. To date, reported studies displayed substantial differences in the methodologies including the choice and concentration of anesthetic agent, scanning environment and scanning views and analyzing techniques. Furthermore, there was limited data on reproducibility and quality control (Ho et al., 2002; Sun et al., 2008; Parente et al., 2013; González-Rosa et al., 2014; Lee et al., 2014; Hein et al., 2015; Huang et al., 2015; Kang et al., 2015; Wilson et al., 2015; Ernens et al., 2016). There are several systems available that could be utilized for Doppler echocardiography analysis for small animal imaging. In this study, we aimed to adapt a commonly used mice Doppler platform for embryonic chick and adult zebrafish models, which are two common models of cardiac research. Below are the details of our image acquisition and image analysis practice using the system.

Mice Doppler System

There are multiple Doppler systems used primarily on anesthetized mice and rats for noninvasive evaluation of the cardiovascular physiology (Hinton et al., 2016). They allow investigators to follow changes that occur due to disease progression, remodeling, aging, and the effects of pharmacological or surgical interventions. These systems consists of four components: two hardware component boxes, the Pulsed Doppler Transceiver (PDT) and Doppler Signal Digitizer (DSD), as well as a Handheld transducer and Doppler Workstation (DW). Here, as an example, we will present Indus Doppler System (Indus Instruments, USA.). System components and data acquisition for other similar systems do not differ. The transceiver has two channels and the digitizer takes the signal and transfers it to the computer. The PDT channels gives the option to set the direction of the flow, the range, the filters and the type of the transducer probe used. The range is the distance from the tip of the transducer probe to the location where velocity is measured and filter is selected to minimize noise in the measurement. There are three different probes available for measurements: 5, 10, and 20 megahertz (MHz). We have added a probe holder for micromanipulations (WPI 3301 micromanipulator), to facilitate the probe's orientation, and stabilization. The system component is displayed in **Figure 3**. As mentioned above, the angle is quite important when calculating the velocity. Ideally, it is preferred to fade to zero so that it has no effect on the velocity calculation. This means the Doppler probe has to be aligned with the blood flow as much as possible either with the blood moving toward or away from the probe. The probe on the Indus system is quite small, 1.0 mm diameter, which facilitates aligning it with the flow without creating an angle (**Figure 3**). The software setup and the data analysis are similar however, Doppler velocity measurements, data acquisition using this system will differ according to the species studied. The reason is that the structure and location of the heart and blood vessels differ across the species. The details of the measurements for the chick embryo and zebrafish will be discussed later on in this paper.

Doppler Signal Processing Workstation software is used to process the signal from the DSD. One important parameter that needs to be set prior to acquisition is the crystal frequency; this will depend on the probe being used (**Figure 4**, setups, system). Another important parameter that needs to be adjusted, although not important during acquisition but crucial during analysis, is the angle between the probe and the blood flow direction (**Figure 4**, Setups, Doppler, angle). Fast Fourier transform (FFT) parameters in Doppler setting tab controls the way the signal is presented (**Figure 4**, Setups, Doppler, FFT window). For best image signal, specifically for applications presented here, Blackman view along with central alignment and 1,024 samples can be selected. No high pass filter is needed but a low pass filter of 120,000 Hz is appropriate. These settings can be found from the setup menu under system and Doppler tabs. Finally, the length of the recorded signal has to be identified. This can be done

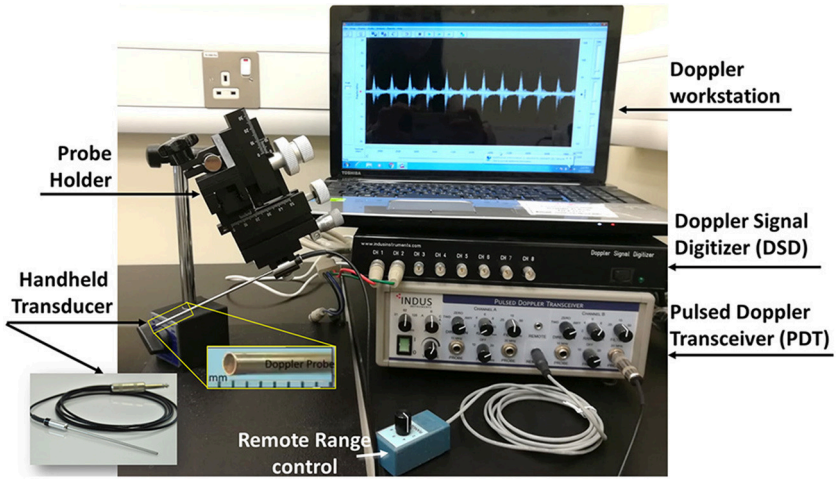

FIGURE 3 | Mice Doppler system. The system is composed of a Doppler work station, signal digitizer, transceiver, a remote range control, and a handheld transducer. The interface shows a spectrogram of a signal containing a frequency of 20 kHz.

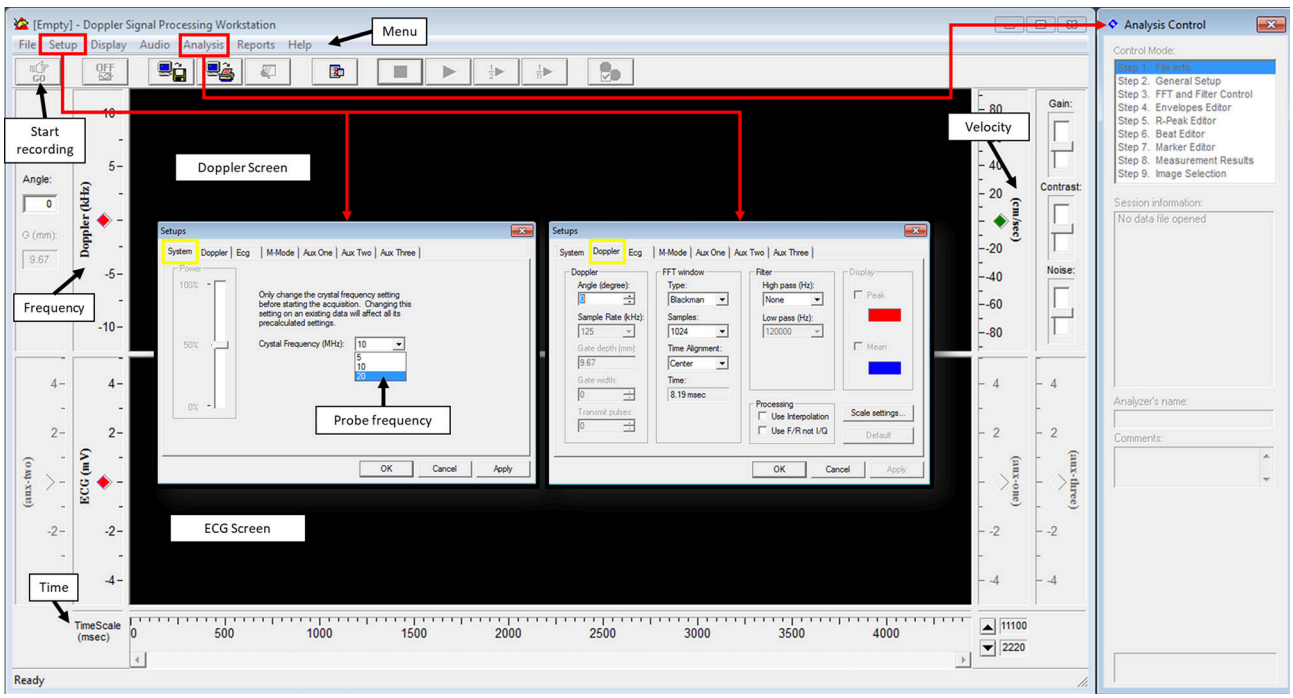

FIGURE 4 | Doppler signal processing workstation user's interphase.

from the setup menu under options. Once these parameters are set, acquisition can be started to obtain a spectrogram.

The spectrogram obtained can then be analyzed using an analysis software. Usually, software provided with the system for data acquisition is also used for data analysis. For the Indus software, from the analysis menu, analysis control window is opened to process the waveforms (**Figure 4**). The software can automatically detect the envelopes, tracing the edges of the Doppler spectrogram (**Figure 5**, yellow line), which will then be exported as a data file to be further processed. Here we will present how to make measurements for blood flow through the heart valves. Some important parameters are heart beat in beat per minute (bpm), peak velocity (cm/s), average velocity (cm/s), and ejection time (ms). Heart beat is calculated by identifying number of peaks in a known time duration. Software enables identifying peak forward velocity (shown as PFV in **Figure 5**), start of forward velocity (shown as FVS in **Figure 5**), and end of forward velocity (shown as FVE in **Figure 5**) for each beat

in the spectrogram. Ejection time is the time from FVS to FVE and represents the time duration where the valve is open. Peak velocity is calculated by averaging all peak velocities in the spectrogram. Average velocity is the average of velocity averages for each beat. For Indus software, these can be calculated directly by the software. The envelope can be exported as a data file to Microsoft Excel or other similar program to plot velocity profiles.

In the following sections, adaptation of the Indus mouse Doppler platform for chick embryo and zebrafish studies are explained in detail. We will first give a brief review on the use of these animal models in cardiac research and then will describe our approach in using the Indus Doppler system to assess cardiac function by demonstrating representative data.

ADAPTATION OF THE MICE DOPPLER SYSTEM FOR EMBRYONIC CHICK FLOW MEASUREMENTS

Chick embryos are often used as a biological model of cardiac development. The model offers several advantages, for example the embryo develops in a planar orientation on top of the egg yolk, enabling a variety of imaging and local microsurgical options to alter blood flow. Furthermore, the cardiogenic period of the chick is longer than other species enabling more detailed spatiotemporal analysis. Another major advantage is that chick can adapt to microsurgical treatments well and are of limited ethical concern. Finally, the chick embryonic heart develops similarly to the human embryonic heart, with four chamber four valve configuration (Midgett and Rugonyi, 2014). Owing to those features, embryonic chick is an ideal model to study development of CHDs under abnormal hemodynamics.

In a developing embryo, heart is the first organ that starts to function. It facilitates embryonic growth as it converts nutrients to surrounding tissues. The heart starts as a linear valve-less tube. As the embryo grows, it transforms to a multi-chambered structure that comprises of four chambers and four fibrous valves in higher species (Srivastava and Olson, 2000; Beis et al., 2005; Butcher et al., 2007; England et al., 2016). Despite some differences with human heart, for example during septation and aortic arch remodeling, avian heart resembles the human anatomy (**Supplementary Figure 1**) more closely than other non-mammalian models (Andersen et al., 2014). It was originally thought that the sole function of a beating heart during the embryonic development is pumping blood for convective transport of blood throughout the body. However, it was later shown that, diffusion is a sufficient means of transport for oxygen, nutrients, metabolic wastes, and hormones in the early embryo (Burggren, 2004). On the other hand, mechanical perturbation of blood flow causes abnormal cardiogenesis, suggesting hemodynamic forces generated by contraction of cardiomyocytes in fact act to drive cardiogenesis (Granados-Riveron and Brook, 2012; Samsa et al., 2013; Lindsey et al., 2014). During normal development, flowing blood exerts several forces on surrounding tissue. These forces include the blood pressure force on the walls, the associated circumferential stress that occurs as the walls stretch in response to pressure, and the frictional force exerted by flow along the walls, wall shear stress (Gjorevski and Nelson, 2010). These mechanical signals induce gene expression and differentiation on a cellular level, translating molecular level events into tissue-level formations that guide embryo development (Wang et al., 2009; Mammoto and Ingber, 2010; Yalcin et al., 2011; Bharadwaj et al., 2012; Buskohl et al., 2012). Therefore, disturbed hemodynamics is a major epigenetic source for congenital heart defects.

Disturbing the hemodynamics by altering blood flow in chick embryo can easily be established through surgical intervention. The micro-surgery approaches are to constrict blood flow at certain locations in the heart to recreate a hemodynamically driven clinical CHDs. A good example of inducing CHD in chick embryo is left atrial ligation (LAL). LAL is a surgical approach for studying the development of hypoplastic left heart syndrome (HLHS). In LAL, a suture is placed around the left atrium and tied in a knot to constrict the left atrioventricular (AV) orifice and to decrease the effective volume of the left atrium (Yalcin et al., 2010; Midgett and Rugonyi, 2014). LAL has been performed at day 3–4, during the looping stages and before septation (Tobita and Keller, 2000; Tobita et al., 2002; Lucitti et al., 2005; Hu et al., 2009). The partial ligation of the left atrium reduces its size, narrows the inflow area of the left ventricle (LV), and redirects blood flow from the left to the right side of the heart. The redistributed hemodynamic load results in the hypoplasia (underdevelopment) in the left side and hyperplasia (overdevelopment) in right side cardiac structures (Tobita and Keller, 2000). Since the left side hypoplasia is a characteristic of HLHS, phenotype generated via LAL is accepted as an animal model of human HLHS (Midgett and Rugonyi, 2014). Other surgical interfaces in chick embryo include vitelline vein ligation (VVL) which is a process in which one of the vitelline veins that drain blood to the embryonic heart is ligated or clipped and conotruncal banding (CTB) where the outflow tract (OFT) is narrowed with a suture (Lucitti et al., 2005; Pang et al., 2017) . Similar to LAL, also these microsurgeries are usually performed on embryonic day 3–4, since heart at this stage is very sensitive to blood flow alterations (Hove et al., 2003). All of these microsurgeries produce specific phenotypes resembling different human CHDs. These disease models help to investigate the disturbed hemodynamics during disease progression for understanding the etiology as well as for generating new therapeutic approaches.

These surgical procedures require direct access to the embryo. This can be managed by culturing the chick embryos either outside their shells (*ex-ovo*) or within their shells (*in-ovo*). *Ex-ovo* culture requires yolk and the embryo to a culture platform such as a petri dish, or a hammock like structure (Yalcin et al., 2010). *In-ovo* culturing method requires opening of a small window on the shell. For both techniques, egg shell should be cut at a stage where the vitelline vessels are not attached to the walls. Also, sufficient time should be given to the embryo to develop inside the shell. In our practice, we found out that, day 3 is the optimal time to crack the egg for *ex-ovo* culture, or open the egg window for *in-ovo* culture. For both cultures, external environmental interferences have to be minimized. In here, we use the *in-ovo* culture system to measure blood flow velocities using the mice Doppler platform.

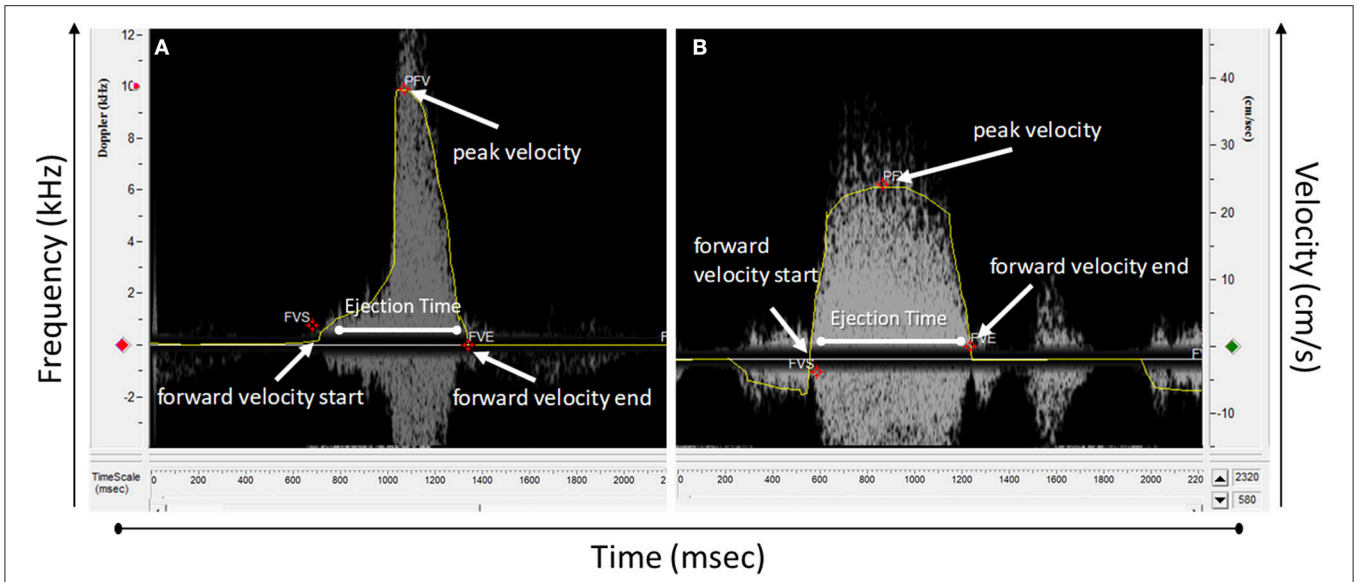

FIGURE 5 | Doppler spectrograph waveform analyzed using Doppler workstation software. **(A)** A wave from an atrioventricular valve and **(B)** outflow track valve.

In-ovo Chick Embryo Culture

Fertilized eggs should be incubated directly after laying in a 37.5°C incubator with 60% humidity; however, if there is a requirement to delay the experiments, eggs can be reserved up to 5–7 days in a 13°C cooler before the embryos start development. On day 0, eggs are placed blunt end to the top in an incubator, with continuous rocking for 72 h (3 days). On day 3, the eggs are taken out of the incubator in batches of 10 so that their temperature does not drop drastically. They are then kept laying horizontally for few minutes to allow the embryo to relocate to the top of the egg. On the blunt end, a hole is gently made with a surgical scissor. While the egg is stable, a 19-gauge needle attached to a 5 ml syringe is inserted vertically inside the egg, with caution not to poke the yolk, to remove about 5 ml of the albumin (egg white). This is done to lower the yolk with embryo for preventing rupture of the yolk with scissor penetration during cutting. The hole is then covered by clear adhesive tape. White paper tape is placed to the top of the egg to facilitate opening a widow without harming the embryo. The widow is made by creating a hole then enlarging it by cutting in a spiral form. Finally, created window is covered by a transparent tape and eggs are placed in a portable incubator under the same conditions. These steps are illustrated in **Figures 6A–I**.

Embryo Environmental Stabilization

Since the procedure of measuring blood hemodynamics is performed outside the incubator, the fluctuating temperature will almost certainly interfere with the recorded data and create variabilities across the study groups. As such, embryos must be maintained at the same temperature that they were incubated at to minimize environmental interferences. We have developed an easy and affordable setup that maintains the embryos at a temperature of 37°C during analysis. The setup requires a dry block heater, lab Armor beads, aluminum foil, water resistant tape, and water. The aluminum foil is placed in the dry block then filled with the Armor beads. The beads are then covered with foil and a groove that resembles the shape of the egg is made. These beads are good heat conductors, however to assure good conduction through the egg, the groove is covered with the water resist tape and a small amount of water is added to the groove. This way, heated water would conduct the heat through contact with the egg. For this particular setup (**Figure 6J**), we found that setting the heat block to 40°C results in a water temperature of 37°C. Once the water temperature reaches 37°C, the eggs can be placed on top of the shallow water and the experiment can be started.

Chick Embryo Blood Flow Velocity Measurement Using the Mice Doppler System

To access the embryo, the chorionic and allantoic membranes need to be removed using a dissecting stereo microscope and a pair of sharp forceps to expose the heart. For Doppler measurements, eggs are placed on the preheated dry block setup. Few drops of prewarmed Tyrode's solution is applied on the embryo near the heart to couple sound waves. The embryo's orientation is crucial and it should be set exactly as described below to reduce the angle between the probe and the detected flow to zero degrees, so that sound waves and blood flow are fully aligned. Furthermore, the channel being used in the PDT should be set to "AWAY" as the flow direction is moving away from the probe, which will result in getting positive velocity values since blood is moving away from the probe.

Here we explain Doppler blood flow measurements for embryonic day 5 as an example. This is a pre-septation stage where the heart is composed of one main ventricle, one atria, one AV valve, and one OFT valve. AV and OFT valve measurements

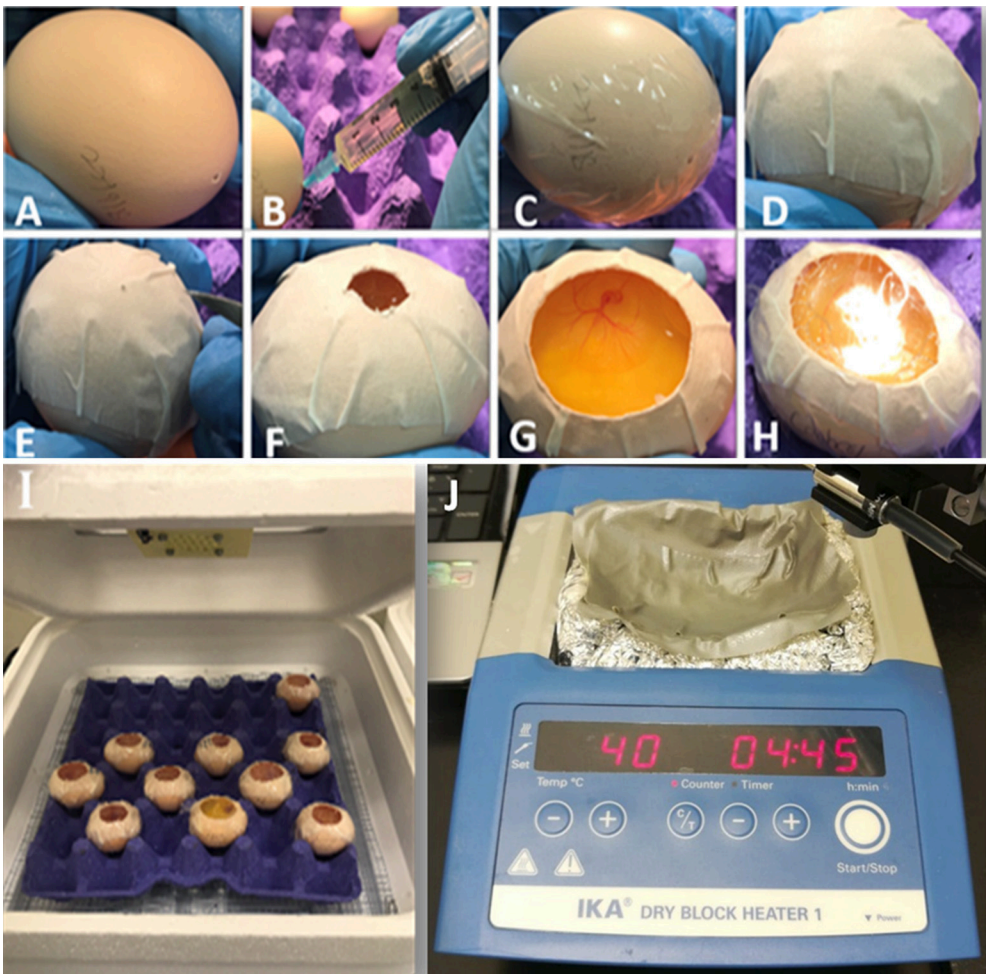

FIGURE 6 | Details of *in-ovo* culture and temperature stabilization during Doppler measurements. **(A)** The egg is kept horizontal for few minutes. **(B)** A hole is made using dissection scissors and with the aid of a needle and a syringe about 5 ml of the albumin is removed. **(C)** A clear tape is used to cover the hole. **(D)** Paper tape is placed on the top horizontal side to stabilize the egg. **(E)** Using dissection scissors, a small hole. **(F)** The hole is enlarged to locate the embryo. **(G)** Once the embryo is located, the hole is enlarged to allow access to the embryo. **(H)** Using a clear tape, the window is covered. **(I)** Eggs are then returned to the incubator. **(J)** Temperature stabilization for chick embryo using dry block heater covered by aluminum foil containing armor beads. The setup is sealed with water resistant tape. Water is added on top of the tape and to reach a water temperature of 37°C the heat block should be placed at 40°C.

are presented here. For other stages, minor adjustments to below protocol may be needed. A 20 MHz probe is suitable for this application. The chick embryo naturally lays on its left side, exposing the right side on top. To get good signal from the OFT, we found that, the natural orientation of the embryo is good. The probe is oriented toward the OFT valve from the apex, from the embryo's tail side. At that configuration, the probe is oriented at angle of around 30 degrees with the horizontal surface as shown in **Figure 7A**. To get the signal from the AV valve, we found that, Doppler transducer needs to approach the embryo from its left side on top. Therefore, the embryo is gently flipped with a blunt forceps and the probe is placed between the atria and the ventricle just near the head where the eye is located as shown in **Figure 7B**. For AV valve, the probe is again oriented at about 30 degrees to the horizontal surface. Doppler velocity signal acquisition was explained above and hence is not repeated here. It is appropriate to save a signal for about 5 s which will save about 10–15 peaks, sufficient for further analysis.

Prior to proceeding with analyzing diseased models, blood flow velocities of control embryos were measured and compared with published data obtained using different and more advanced platforms. **Figures 8B,D** illustrates velocity profiles that were extracted previously using Vevo 770 echocardiography platform for normal day 5 embryos (Yalcin et al., 2011). The data obtained from the mice Doppler system (**Figures 8A,C**) on the same day compares well. Spectrograms that represents blood flow velocities at the AV (**Figure 8A** Mice Doppler system and **Figure 8B** previous data) and OFT valves (**Figure 8C** Mice Doppler system and **Figure 8D** previous data) shows that the waveforms as well as the velocity peaks extracted from both platformers measurements are similar. The difference between advanced platforms and the mouse Doppler system is the appearance of a shadow in the

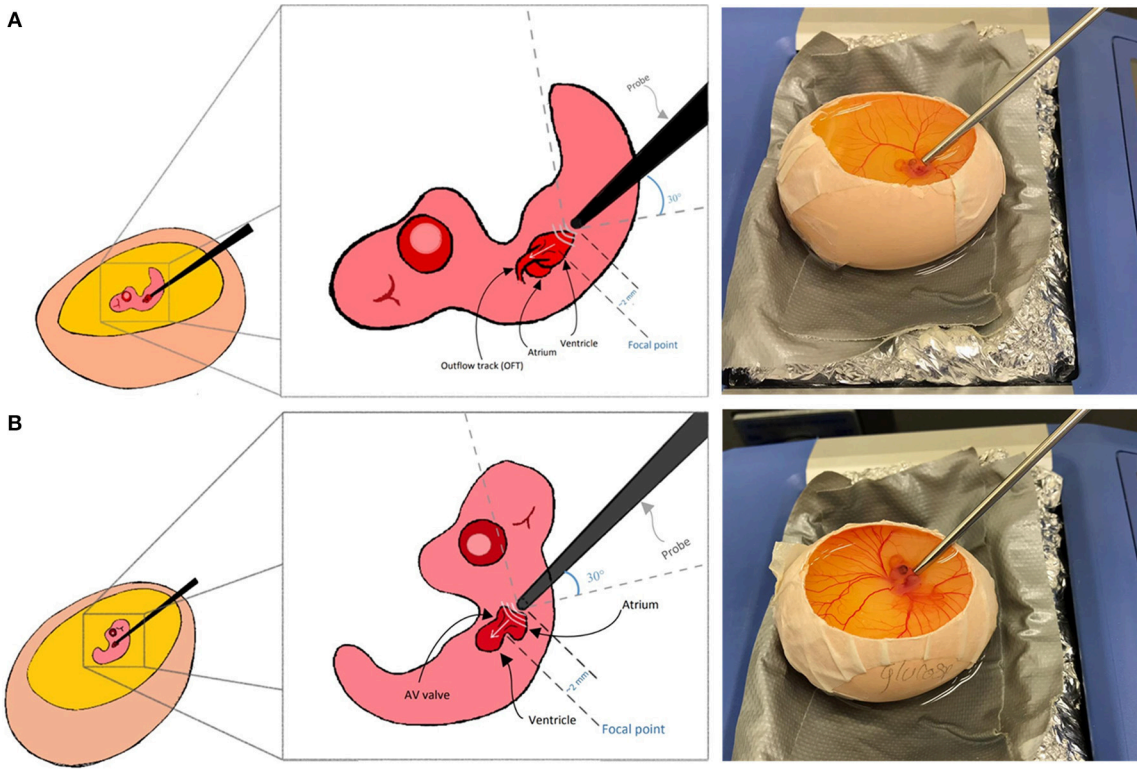

FIGURE 7 | Chick embryo orientation for Doppler echocardiography analysis. **(A)** For outflow track blood flow measurement, the embryo is kept laying on its left side and the transducer probe is oriented as shown in the figure. **(B)** For blood flow measurement at the atrioventricular valve, embryo should be gently flipped using a blunt forceps and the transducer probe should be oriented as shown in the figure.

spectrogram for the Indus system. The shadow is a mirror image of the recorded waveform with a lower brightness. However, the software recognizes this and only detects the actual signal. The velocity envelope can also be further corrected by the user with that information. **Figures 9B,C**, illustrates extracted waveforms over one cardiac cycle for blood flow velocities at the AV and the OFT canals. The reproducibility of the blood flow velocity waveforms and good comparison with the data obtained by advanced platforms validates the Indus platform as a good tool for blood flow velocities measurement in the chick embryo.

Effect of Left Atrial Ligation (LAL) Microsurgical Procedure on the Heart's Hemodynamics

To further evaluate the system for embryonic chick cardiac disease models, we studied velocity profiles after LAL. As mentioned earlier, LAL is a microsurgery where a nylon knot suture is tied around the left atrium of the heart. LAL was performed on the 4th day of incubation, during cardiac looping but ahead of septation. **Figure 9A**, summarizes the microsurgical steps. Briefly, the chorionic and allantoic membranes are removed over the embryo grown in our *in-ovo* culture. Naturally, the embryo sits on its left side; therefore, the embryo is lifted from the back and vertically rotated in order to access the left heart. Pericardium over the left atria (LA) is then cut and removed with fine forceps. Knots of approximately 0.5 mm diameters are prepared from 10-0 nylon surgical suture. These knots are aligned over the LA then tightened so that the volume of the LA is reduced to about 75%. This interference is expected to constrict the blood flow through the left side of the AV canal. The embryo is rotated back, to its original position following the procedure so that the right side is on top. Details of this procedure can be seen in our video protocol (Yalcin et al., 2010).

The changes in the hemodynamics at the AV and OFT canals was assessed 24 h following LAL. **Figures 9A**, **10B** shows the velocity profiles at the AV and OFT canals, respectively, over cardiac cycle for control as well as for LAL hearts. The velocity profile at the AV canal of the control groups showed distinct peaks representing passive (first peak) and active (second peak) contractions. On the other hand, the velocity profile at the AV canal of the LAL group had a wider spread with higher passive contraction peak and lower active contraction peak. For the OFT canal, the velocity profile of the control groups showed an initial regurgitating flow whereas the LAL group OFT canal velocity profile did not show this behavior. Both AV and OFT velocities match very well with our previous measurements with Vevo 770 system. More specifically, In AV channel, we see a dramatic decrease in peak velocity, suggesting decrease in WSS levels. However, average velocity does not differ in AV, suggesting

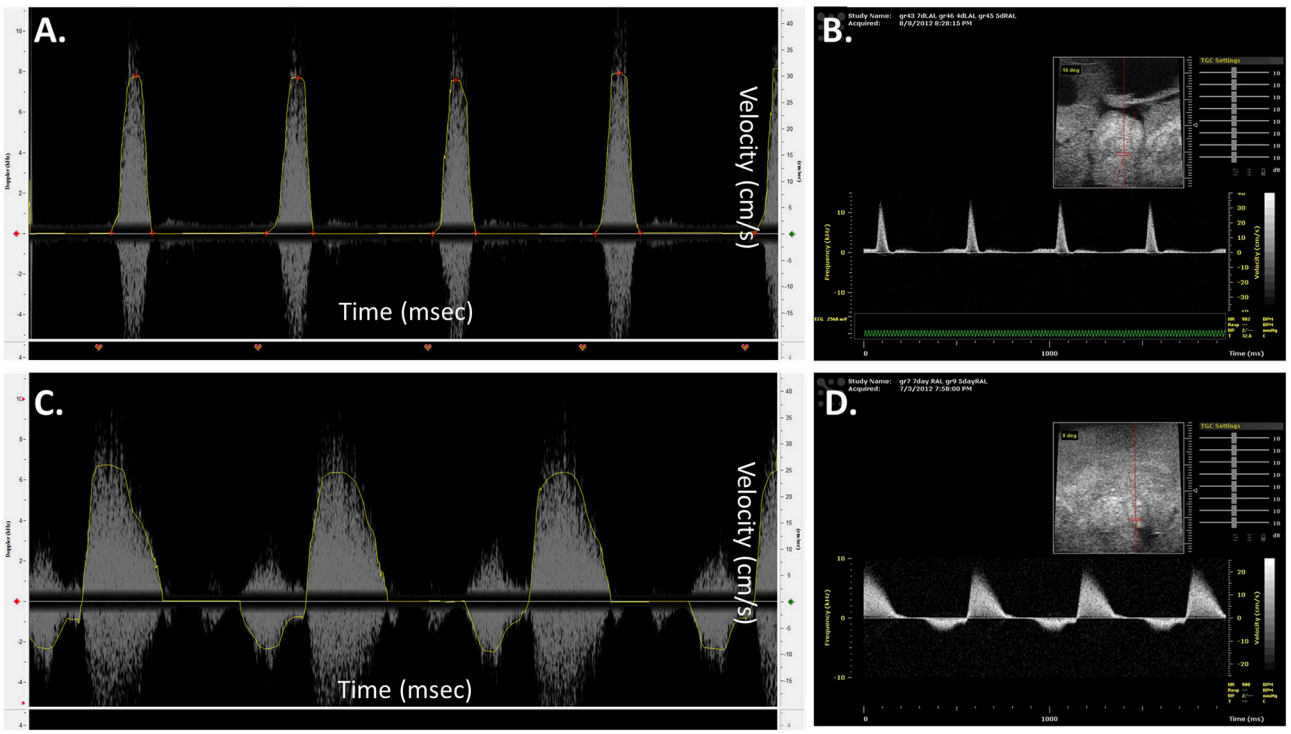

FIGURE 8 | Chick embryo blood flow velocity waveforms obtained by mice Doppler system **(A,C)** and Visualsonics *in vivo* 770 platform **(B,D).** The waveforms were measured at the atrioventricular **(A,B)** and outflow track canals **(C,D)**. The data obtained by both platforms compares well. The spectrograms from the mice Doppler system **(A,C)** shows a mirroring shadow of the recorded signal. The analysis software, however, recognizes this and detects only the correct signal, traced in a yellow line.

preservation of cardiac output. In OFT no significant change is observed rather than disappearance of initial regurgitation for LAL embryos. Tabulated data can be found in **Table 1**. These changes were expected after LAL surgery (Yalcin et al., 2011), which again validates the mice Doppler system blood flow measurements.

ADAPTATION OF MICE DOPPLER SYSTEM FOR ADULT ZEBRAFISH FLOW MEASUREMENTS

During the past two decades, zebrafish, *Danio rerio*, a small tropical freshwater fish, has become a popular vertebrate model for research. This was mainly due to the number of large-scale mutagenesis screens that have been conducted successfully with this animal model (Kari et al., 2007). Its high similarity to human gene sequence and function (87% similarity) may indicate why zebrafish can be used to model human diseases (Lieschke and Currie, 2007; Howe et al., 2013). It is estimated that 70% of the human genes have ortholog genes in the zebrafish genome (Barbazuk et al., 2000; Bournele and Beis, 2016). Compared to other mammalian models, zebrafish offer several advantages such as rapid development and reproduction, convenient genetic manipulation techniques, and low cost maintenance. These criteria rendered this small fish as an ideal organism to study the genetic basis of disease. A single female can produce ∼200 eggs weekly allowing for large scale analysis (Parng et al., 2002; Poon and Brand, 2013). Furthermore, the zebrafish embryos are fertilized externally allowing for quick collection and genetic manipulation (Miura and Yelon, 2011).

Even though zebrafish does not spontaneously develop cardiovascular disorders analogous to humans (McLeish et al., 2010), a number of conditions can be readily modeled for cardiac research. Several cardiovascular specific transgenic strains have been generated. Zebrafish have a cardiovascular system with a tubular two-chambered heart with gills instead of lungs. The heart develops early during embryogenesis, and the heart starts to beat at 24 hpf (hours post fertilization). **Supplementary Figure 2** demonstrates the stages of zebrafish heart development and compares an adult zebrafish heart to a human heart. The anatomical differences between zebrafish and humans are considerable, but the ease of studying zebrafish and rapid rate of cardiac development makes them a valuable model for heart disease. The zebrafish cardiomyocyte action potential seems almost identical to their humans' counterparts (Verkerk and Remme, 2012). Cardiac related diseases that are currently studied in zebrafish include congenital heart diseases, heart failure, cardiomyopathy, cardiac arrhythmia, myocardial infarction, and valvular heart disease (Chi et al., 2008; Bakkers, 2011; Dhillon et al., 2013; Asnani and Peterson, 2014; Liu et al., 2016). Since zebrafish heart develops rapidly, cardiac

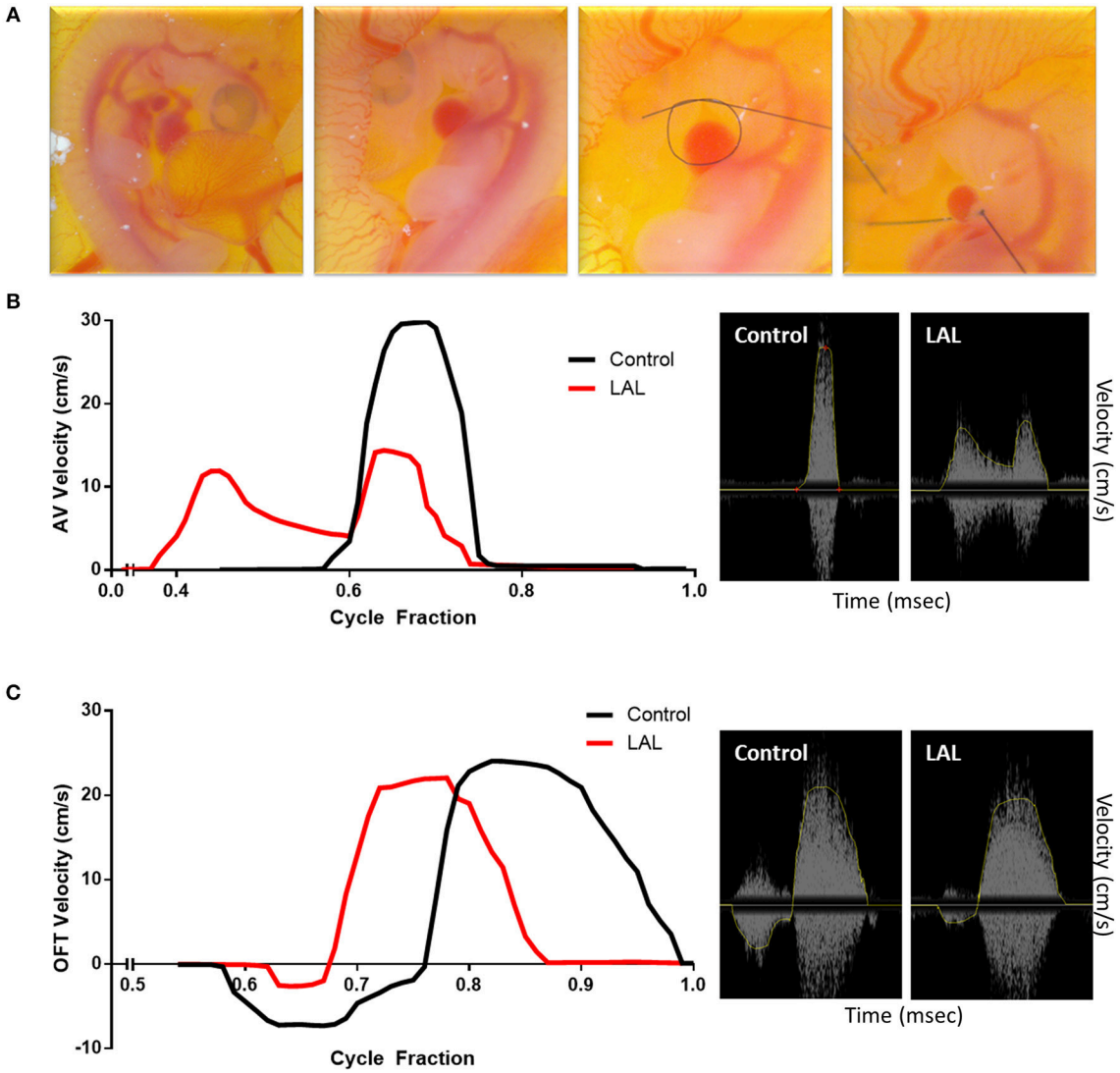

FIGURE 9 | Effect of left atrial ligation (LAL) on blood flow velocity. **(A)** Steps of LAL procedure; the embryo sits on its left side, it is flipped to have access to the left atria (LA). A pre-prepared knot using 10-0 nylon surgical suture is positioned over the left atrium then tightened so that the volume of the LA is reduced to about 75%. Extracted data of blood flow velocities at the **(B)** atrioventricular (AV) and **(C)** outflow track (OFT) canals over cycle fraction along with an example waveform peak for LAL and control embryos. The velocity profile at the AV canal of the LAL group had a wider spread with higher passive contraction peak (first peak) and lower active contraction peak (second peak). The velocity profile at the OFT canal of the control groups showed an initial regurgitating flow whereas the LAL group OFT canal velocity profile did not show this behavior.

drug screening in the zebrafish can be performed early, but is likely best done after 96 hpf. Studying how cardiac function is affected by genetic manipulation, drug or toxin exposure, or cardiac intervention in zebrafish may help to both understand the mechanism of action and reveal new therapeutic targets. Time-lapse microscopy is sufficient to study cardiac function in zebrafish embryos and larvae, since zebrafish have transparent skin at early stages, enabling the direct visualization of the heart and blood vessels. For cardiovascular assessment for zebrafish embryo/larvae, detailed protocols can be found in our previous work (Yalcin et al., 2017; Eisa-Beygi et al., 2018; Zakaria et al., 2018). As the zebrafish age and lose skin transparency the Doppler technique must be used for heart function assessment. We have also adapted a Doppler system used for mice as a tool to measure the heart valve blood flow velocities in adult zebrafish. Below is a description of our method.

Stabilization of Adult Zebrafish

Adult fish need to be immobilized to allow cardiac measurements. This can be done by anesthetization prior to the procedure. Tricaine methanesulfonate (Tricaine) is a good agent that is commonly used to sedate the fish (Carter et al.,

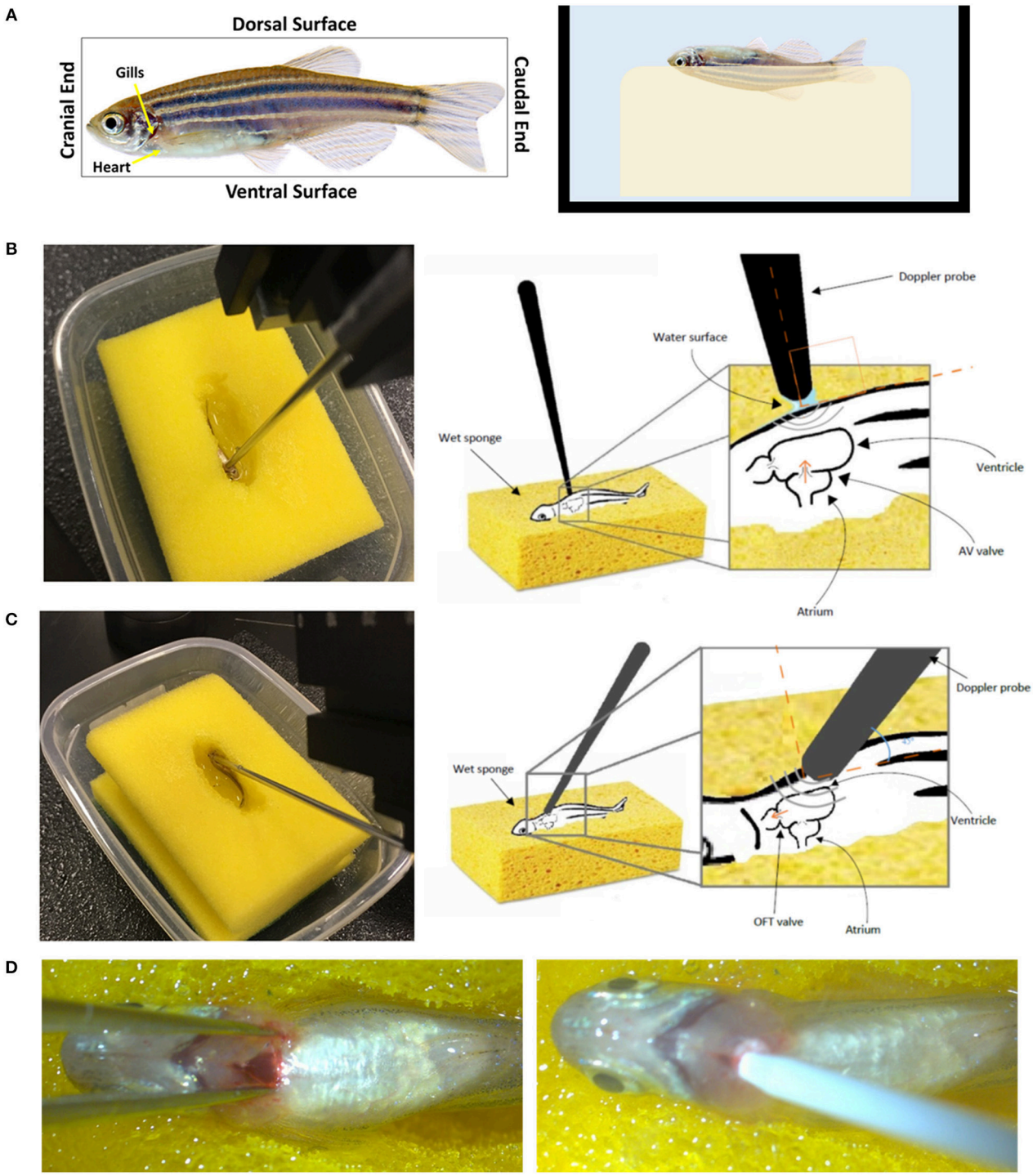

FIGURE 10 | Setup and orientation of zebrafish for Doppler echocardiography analysis. **(A)** The fish is stabilized on a wet sponge on its dorsal side toward the sponge making sure it is fully immersed in water. The 20 MHz transducer probe is positioned **(B)** perpendicular to the ventral side of the fish to obtain the atrioventricular valve (AV) flow or **(C)** at an angle to obtain the outflow rack (OFT) flow. **(D)** Myocardial infarction induction using cryoinjury. The fish in **(A)** was obtained from www.shutterstock.com.

2011). For Doppler analysis, the fish is transferred to a tank containing a final concentration of 90 mg/L Tricaine, prepared in water obtained from the fish system, for several minutes until the fish loses equilibrium and spinal reflexes. As mentioned previously, orientation is crucial when it comes to Doppler analysis, this presents a challenge when attempting to observe

TABLE 1 | Day 5 chick embryo heart rate and blood flow velocities that were obtained with Indus Doppler system.

Parameters	Control	LAL	*P*-value
Heart Rate (bmp)	166.45 ± 5.11	120.83 ± 1.69	<0.0001

Blood flow velocity	AV			OFT		
	Control	LAL	*P*-value	Control	LAL	*P*-value
Peak velocity (cm/s)	30.08 ± 0.72	15 ± 0.74	<0.0001	23.62 ± 1.40	23.38 ± 0.77	>0.9999
Ejection time (ms)	98.6 ± 4.63	261.8 ± 6.62	<0.0001	181.5 ± 3.25	208.29 ± 6.88	<0.0001
Mean velocity (cm/s)	4.48 ± 0.10	4.42 ± 0.13	>0.9999	5.99 ± 0.58	6.29 ± 0.25	>0.9999

Data is presented as mean ± SD. Analysis was by unpaired student t test. A $p < 0.05$ was considered as statistically significant. A total of 5 embryos were analyzed per group.

free-floating fish. A simple method to keep the fish in the correct orientation and in a wet environment is using a water soaked sponge. A small hole that resembles the shape of the fish is made in the middle of a sponge. The sponge is put in a tray then soaked with water from the fish system. The sponge has to be saturated with water so that the created hole is filled with water. The fish is then moved to the hole and Doppler analysis can be initiated. It is important that the fish is maintained at 25–29°C during the analysis as abnormal temperatures will interfere with cardiac measurement.

Adult Blood Flow Velocity Measurement Using the Mice Doppler System

The procedure has to be performed relatively quickly before the anesthesia wears of. Once the fish starts to flick its tail, the experiment has to be stopped and the fish has to be transferred to a tank of fresh system water to recover. Anesthetizing fish in 90 mg/L tricaine allows for a 5-min window for Doppler analysis. The breathing of the fish needs to be closely monitored during the measurement. This can be done through examining the gills. If any changes in the base line of the movement of the gills is observed, the experiment has to be stopped and the fish needs to be put back the fresh system water to recover.

The fish has to be oriented with its dorsal surface toward the sponge and its ventral surface facing upwards (**Figure 10A**). This orientation has been previously described when measuring cardiac function using more advanced platforms (Hein et al., 2015; Wang et al., 2017). It is unnatural to the fish and it might induce stress, consequently affecting the heart rhythm and cardiac output. This is a limitation about the animal model since all imaging modalities, including the one described here, require stabilizing the fish in such way to have access to the heart.

To measure the blood flow velocities at the AV valve, the probe should be perpendicular on the fish, toward the cranial end, and just below the gills (**Figure 10B**). To measure the blood flow velocities at the OFT valve, the angle of the probe has to be adjusted to 45 degree with the fish's horizontal axes. The probe's head has to be oriented toward the cranial end and the base toward the caudal end (**Figure 10C**). These orientations will assure ultrasound signals and blood flow direction are fully aligned (Instruments, 2017). The water around the fish creates an aqueous contact zone between the ultrasound probe and the animal, whereby up to 1 cm standoff can be maintained via liquid surface tension. Once the procedure is completed, the fish has to be immediately placed in a tank full of system water for recovery.

Blood flow velocities were measured at the AV and OFT valves for normal wild type (AB) zebrafish at 1 year of age. A 20 MHz Doppler probe transducer was used for this purpose. Previous Doppler echocardiography examinations on adult zebrafish showed distinct E and A waves in AV velocity profile, representing filling of the ventricle at early diastolic inflow (E) and late diastolic inflow (A) (Lee et al., 2014; Hein et al., 2015; Instruments, 2017; Packard et al., 2017). Negative OFT velocities are also detected while measuring AV velocity, as seen in **Figure 11A**. OFT velocity profile obtained from a previous study is shown in **Figure 11C**. These two velocity profiles were used as a reference for the mice Doppler measurements to confirm correct readings. For the AV profile using Indus Doppler system (**Figure 11B**), distinct E and A waves were also seen in the image, where E wave was smaller than A wave. Similar to previous studies, the OFT velocity signal was also present in the AV recording. The OFT velocity profile using Indus Doppler system (**Figure 11D**), identical to previous measurements, included a wider region of positive velocities. The heartbeat and other blood flow velocities are summarized in **Table 2**. From AV valve velocity profile, measuring E and A waves velocities are used to calculate E/A ratio. This ratio is used to assess diastolic function. Unlike human, zebrafish E/A ratio is smaller than one (Packard et al., 2017). In zebrafish cardiomyopathy and myocardial infarction models, this ratio was shown to increase (Lee et al., 2014; Hein et al., 2015; Packard et al., 2017) which suggests ventricular diastolic dysfunction. **Figures 11E,F** (blue line), illustrates extracted waveforms of the blood flow velocities at the AV and OFT canals over the cycle fraction.

Effect of Myocardial Infarction on the Zebrafish Heart's Hemodynamics

To further evaluate the system for zebrafish cardiac disease models, we studied velocity profiles after cardiac injury. Myocardial infarction was induced using cryoinjury method as described by Chablais and Jazwinska (2012). Briefly, a stainless steel rode (cryoprobe) with a diameter of 0.8 mm was cooled down by immersing the tip in liquid nitrogen for 3 min. Zebrafish was anesthetized using 90 mg/L tricaine. The fish was then

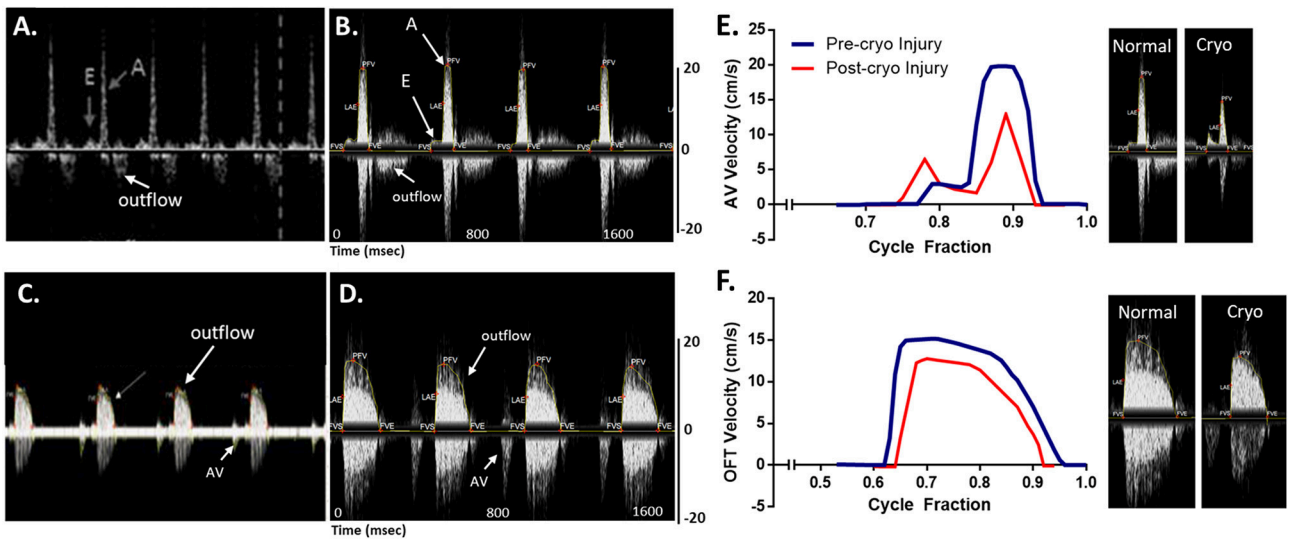

FIGURE 11 | Adult zebrafish blood flow velocity waveforms. **(A,C)** Waveforms obtained from literature (Instruments, 2017). **(B,D)** Waveforms obtained by the Indus mice Doppler system. **(A**,**B)** The waveforms were measured at the atrioventricular. **(C,D)** The waveforms were measured at the outflow track canals. Both set of data compare well, showing the same peaks with the same velocity profile. **(E,F)** Extracted data of blood flow velocities. Data was obtained from control and myocardial infarcted adult zebrafish at the **(A)** atrioventricular (AV) and **(B)** outflow track (OFT) canals over cycle fraction along with example waveform peaks.

TABLE 2 | Adult zebrafish heart rate and blood flow velocities that were obtained with Indus Doppler system.

Parameters	**Control (Pre cryo)**		**Post cryo**		***P*-value**
Heart Rate (bmp)	121.95 ± 3.70		117.08 ± 50.24		0.8427
Blood flow velocity	**AV**			**OFT**	
	Pre cryo	**Post cryo**	***P*-value**	**Pre cryo**	**Post cryo**	***P*-value**
Peak velocity (cm/s)	26.31 ± 3.89	14.71 ± 2.36	0.0155	16.52 ± 3.89	14.91 ± 2.79	0.3701
Ejection time (ms)	149.91 ± 27.58	314.9 ± 134.6	0.1162	265.7 ± 48.99	144.33 ± 8.22	0.0376
Mean velocity (cm/s)	2.79 ± 0.60	1.88 ± 0.41	0.1849	3.85 ± 0.64	2.63 ± 0.48	0.0144

Data is presented as mean ± SD. Analysis was by paired student t test. A $p < 0.05$ was considered as statistically significant. A total of 3 adult fish were analyzed per group. Cryo, Cryoinjury.

stabilized as described above. Under a stereomicroscope and using a dissecting scissors and a sharp forceps, an incision was made just below the gills to expose the heart. The cryoprobe was obtained and access liquid nitrogen was removed by shaking the probe for 10 s. The incision was spread laterally using forceps and the heart's vertical was touched gently with the cryoprobe (**Figure 10D**). After 24 s, 2 ml of system water was added on to the surgical site to release the cryoprobe. The fish was immediate transferred to fresh system water to recover.

The changes in the hemodynamics at the AV and OFT canals was assessed 24 h following myocardial infarction. **Figures 11E,F** (red line) shows the velocity profiles at the AV and OFT canals, respectively, over cardiac cycle for control as well as for infarcted hearts. The velocity profile at the AV canal of the control groups showed distinct A peak and a smaller E peak. Myocardial infarction caused the A peak velocity to decrease and the E peak velocity to increase. These findings are comparable to that previously described (Lee et al., 2014; Hein et al., 2015; Packard et al., 2017). Tabulated data can be found in **Table 2**. These changes were expected after myocardial infarction, which validates the mice Doppler system for zebrafish blood flow measurements.

CONCLUSIONS

Doppler echocardiography is an important and powerful tool for the assessment of cardiovascular physiology and function; it plays a vital role in the comprehensive evaluation of cardiovascular system particularly in the fetal stage of life. There are several echocardiography devices that measure cardiovascular function for small animals, however, they are usually designed for rodents, including rats and mice, and due to their complexity, they come with a high cost. Here we have adapted a single mode mice Doppler echocardiography system to measure cardiac flow velocities for adult zebrafish and embryonic chickens, and successfully assessed cardiac function for normal and diseased

embryonic chicken and zebrafish. We believe that our presented approach will help cardiac researchers to establish similar echocardiography platforms in their labs in a practical and economical manner.

ETHICS STATEMENT

All experiments presented in this paper were conducted under the Qatar University's Institutional Animal Care and Use Committee (QU-IACUC) approval.

AUTHOR CONTRIBUTIONS

FB wrote the manuscript. FB, MA, AS, and HA contributed to running the chick embryo experiments. FB, MA, and ZZ contributed to running the zebrafish experiments. HY supervised the studies and reviewed the manuscript. All authors read the manuscript.

FUNDING

Qatar National Research Fund (QNRF), National Priority Research Program NPRP 10-0123-170222. The publication of this article was funded by the Qatar National Library.

SUPPLEMENTARY MATERIAL

The Supplementary Material for this article can be found online at: https://www.frontiersin.org/articles/10.3389/fbioe.2019.00096/full#supplementary-material

REFERENCES

Amindari, A., Saltik, L., Kirkkopru, K., Yacoub, M., and Yalcin, H. C. (2017). Assessment of calcified aortic valve leaflet deformations and blood flow dynamics using fluid-structure interaction modeling. *Inform. Med. Unlocked.* 9, 191–199. doi: 10.1016/j.imu.2017.09.001

Andersen, T. A., Troelsen Kde, L., and Larsen, L. A. (2014). Of mice and men: molecular genetics of congenital heart disease. *Cell. Mol. Life Sci.* 71, 1327–1352. doi: 10.1007/s00018-013-1430-1

Asnani, A., and Peterson, R. T. (2014). The zebrafish as a tool to identify novel therapies for human cardiovascular disease. *Dis. Models Mech.* 7, 763–767. doi: 10.1242/dmm.016170

Bakkers, J. (2011). Zebrafish as a model to study cardiac development and human cardiac disease. *Cardiovasc. Res.* 91, 279–288. doi: 10.1093/cvr/cvr098

Balachandran, K., Sucosky, P., and Yoganathan, A. P. (2011). Hemodynamics and mechanobiology of aortic valve inflammation and calcification. *Int. J. Inflam.* 2011:263870. doi: 10.4061/2011/263870

Barbazuk, W. B., Korf, I., Kadavi, C., Heyen, J., Tate, S., Wun, E., et al. (2000). The syntenic relationship of the zebrafish and human genomes. *Genome Res.* 10, 1351–1358. doi: 10.1101/gr.144700

Beis, D., Bartman, T., Jin, S. W., Scott, I. C., DAmico, L. A., Ober, E. A., et al. (2005). Genetic and cellular analyses of zebrafish atrioventricular cushion and valve development. *Development* 132, 4193–4204. doi: 10.1242/dev.01970

Bharadwaj, K. N., Spitz, C., Shekhar, A., Yalcin, H. C., and Butcher, J. T. (2012). Computational fluid dynamics of developing avian outflow tract heart valves. *Ann. Biomed. Eng.* 40, 2212–2227. doi: 10.1007/s10439-012-0574-8

Bournele, D., and Beis, D. (2016). Zebrafish models of cardiovascular disease. *Heart Fail. Rev.* 21, 803–813. doi: 10.1007/s10741-016-9579-y

Bruneau, B. G. (2008). The developmental genetics of congenital heart disease. *Nature* 451, 943–948. doi: 10.1038/nature06801

Burggren, W. W. (2004). What is the purpose of the embryonic heart beat? Or how facts can ultimately prevail over physiological dogma. *Physiol. Biochem. Zool.* 77, 333–345. doi: 10.1086/422230

Buskohl, P. R., Jenkins, J. T., and Butcher, J. T. (2012). Computational simulation of hemodynamic-driven growth and remodeling of embryonic atrioventricular valves. *Biomech. Model. Mechanobiol.* 11, 1205–1217. doi: 10.1007/s10237-012-0424-5

Butcher, J. T., McQuinn, T. C., Sedmera, D., Turner, D., and Markwald, R. R. (2007). Transitions in early embryonic atrioventricular valvular function correspond with changes in cushion biomechanics that are predictable by tissue composition. *Circ. Res.* 100, 1503–1511. doi: 10.1161/CIRCRESAHA.107.148684

Camacho, P., Fan, H., Liu, Z., and He, J. Q. (2016). Small mammalian animal models of heart disease. *Am. J. Cardiovasc. Dis.* 6, 70–80.

Carter, K. M., Woodley, C. M., and Brown, R. S. (2011). A review of tricaine methanesulfonate for anesthesia of fish. *Rev. Fish Biol. Fish.* 21, 51–59. doi: 10.1007/s11160-010-9188-0

Chablais, F., and Jazwinska, A. (2012). Induction of myocardial infarction in adult zebrafish using cryoinjury. *J. Vis. Exp.* e3666. doi: 10.3791/3666

Chi, N. C., Shaw, R. M., Jungblut, B., Huisken, J., Ferrer, T., Arnaout, R., et al. (2008). Genetic and physiologic dissection of the vertebrate cardiac conduction system. *PLoS Biol.* 6:e109. doi: 10.1371/journal.pbio.0060109

Chorro, F. J., Such-Belenguer, L., and Lopez-Merino, V. (2009). Animal models of cardiovascular disease. *Rev. Esp. Cardiol.* 62, 69–84. doi: 10.1016/S0300-8932(09)70023-5

Culver, J. C., and Dickinson, M. E. (2010). The effects of hemodynamic force on embryonic development. *Microcirculation* 17, 164–178. doi: 10.1111/j.1549-8719.2010.00025.x

Dawson, T. H. (1991). *Engineering Design of the Cardiovascular System of Mammals*. New Jersey, NJ: Prentice Hall.

Dhillon, S. S., Dóró, É., Magyary, I., Egginton, S., Sík, A., and Müller, F. (2013). Optimisation of embryonic and larval ECG measurement in zebrafish for quantifying the effect of QT prolonging drugs. *PLoS ONE* 8:e60552. doi: 10.1371/journal.pone.0060552

Eisa-Beygi, S., Benslimane, F. M., El-Rass, S., Prabhudesai, S., Abdelrasool, M. K. A., Simpson, P. M., et al. (2018). Characterization of endothelial cilia distribution during cerebral-vascular development in zebrafish (*Danio rerio*). *Arterioscler. Thromb. Vasc. Biol.* 38, 2806–2818. doi: 10.1161/ATVBAHA.118.311231

England, J., Pang, K. L., Parnall, M., Haig, M. I., and Loughna, S. (2016). Cardiac troponin T is necessary for normal development in the embryonic chick heart. *J. Anat.* 229, 436–449. doi: 10.1111/joa.12486

Ernens, I., Lumley, A. I., Devaux, Y., and Wagner, D. R. (2016). Use of coronary ultrasound imaging to evaluate ventricular function in adult zebrafish. *Zebrafish* 13, 477–480. doi: 10.1089/zeb.2016.1274

Fernández Esmerats, J., Heath, J., and Jo, H. (2016). Shear-sensitive genes in aortic valve endothelium. *Antioxid. Redox Signal.* 25, 401–414. doi: 10.1089/ars.2015.6554

Forouhar, A. S., Liebling, M., Hickerson, A., Nasiraei-Moghaddam, A., Tsai, H. J., Hove, J. R., et al. (2006). The embryonic vertebrate heart tube is a dynamic suction pump. *Science* 312, 751–753. doi: 10.1126/science.1123775

Gjorevski, N., and Nelson, C. M. (2010). The mechanics of development: Models and methods for tissue morphogenesis. *Birth Defects Res. C Embryo Today.* 90, 193–202. doi: 10.1002/bdrc.20185

Goenezen, S., Rennie, M. Y., and Rugonyi, S. (2012). Biomechanics of early cardiac development. *Biomech. Model Mechanobiol.* 11, 1187–1204. doi: 10.1007/s10237-012-0414-7

González-Rosa, J. M., Guzmán-Martínez, G., Marques, I. J., Sánchez-Iranzo, H., Jiménez-Borreguero, L. J., and Mercader, N. (2014). Use of echocardiography reveals reestablishment of ventricular pumping efficiency and partial ventricular wall motion recovery upon ventricular cryoinjury in the zebrafish. *PLoS ONE* 9:e115604. doi: 10.1371/journal.pone.0115604

Granados-Riveron, J. T., and Brook, J. D. (2012). The impact of mechanical forces in heart morphogenesis. *Circ. Cardiovasc. Genet.* 5, 132–142. doi: 10.1161/CIRCGENETICS.111.961086

Gregg, C. L., and Butcher, J. T. (2012). Quantitative *in vivo* imaging of embryonic development: opportunities and challenges. *Differentiation* 84, 149–162. doi: 10.1016/j.diff.2012.05.003

Hein, S. J., Lehmann, L. H., Kossack, M., Juergensen, L., Fuchs, D., Katus, H. A., et al. (2015). Advanced echocardiography in adult zebrafish reveals delayed recovery of heart function after myocardial cryoinjury. *PLoS ONE* 10:e0122665. doi: 10.1371/journal.pone.0122665

Hinton, A. O. Jr., Yang, Y., Quick, A. P., Xu, P., Reddy, C. L., Yan, X., et al. (2016). SRC-1 regulates blood pressure and aortic stiffness in female mice. *PLoS ONE* 11:e0168644. doi: 10.1371/journal.pone.0168644

Ho, Y.-L., Shau, Y.-W., Tsai, H.-J., Lin, L.-C., Huang, J., and Hsieh, F.-J. (2002). Assessment of zebrafish cardiac performance using Doppler echocardiography and power angiography. *Ultrasound Med. Biol.* 28, 1137–1143. doi: 10.1016/S0301-5629(02)00564-1

Hove, J. R., Koster, R. W., Forouhar, A. S., Acevedo-Bolton, G., Fraser, S. E., and Gharib, M. (2003). Intracardiac fluid forces are an essential epigenetic factor for embryonic cardiogenesis. *Nature* 421, 172–177. doi: 10.1038/nature01282

Howe, K., Clark, M. D., Torroja, C. F., Torrance, J., Berthelot, C., Muffato, M., et al. (2013). The zebrafish reference genome sequence and its relationship to the human genome. *Nature* 496, 498–503. doi: 10.1038/nature12111

Hu, N., Christensen, D. A., Agrawal, A. K., Beaumont, C., Clark, E. B., and Hawkins, J. A. (2009). Dependence of aortic arch morphogenesis on intracardiac blood flow in the left atrial ligated chick embryo. *Anat. Rec. (Hoboken).* 292, 652–660. doi: 10.1002/ar.20885

Huang, Y., Wang, X., Zhang, J., and Wu, K. (2015). Impact of endocrine-disrupting chemicals on reproductive function in zebrafish (*Danio rerio*). *Reprod. Domest. Anim.* 50, 1–6. doi: 10.1111/rda.12468

Instruments, I. (2017). *DFVS - Zebrafish Application Note - Noninvasive Cardiac Blood Flow Velocities*. Available online at: http://indusinstruments.com/project/dfvs-zebrafish-application-note-v1/

James, J. F., Hewett, T. E., and Robbins, J. (1998). Cardiac physiology in transgenic mice. *Circ. Res.* 82, 407–415. doi: 10.1161/01.RES.82.4.407

Jenkins, M. W., Peterson, L., Gu, S., Gargesha, M., Wilson, D. L., Watanabe, M., et al. (2010). Measuring hemodynamics in the developing heart tube with four-dimensional gated Doppler optical coherence tomography. *J. Biomed. Opt.* 15:066022. doi: 10.1117/1.3509382

Kang, Y.-F., Li, Y.-H., Fang, Y.-W., Xu, Y., Wei, X.-M., and Yin, X.-B. (2015). Carbon quantum dots for zebrafish fluorescence imaging. *Sci. Rep.* 5:11835. doi: 10.1038/srep11835

Kari, G., Rodeck, U., and Dicker, A. (2007). Zebrafish: an emerging model system for human disease and drug discovery. *Clin. Pharmacol. Ther.* 82, 70–80. doi: 10.1038/sj.clpt.6100223

Kendir, C., van den Akker, M., Vos, R., and Metsemakers, J. (2018). Cardiovascular disease patients have increased risk for comorbidity: a cross-sectional study in the Netherlands. *Eur. J. Gen. Pract.* 24, 45–50. doi: 10.1080/13814788.2017.1398318

Kowalski, W. J., Pekkan, K., Tinney, J. P., and Keller, B. B. (2014). Investigating developmental cardiovascular biomechanics and the origins of congenital heart defects. *Front. Physiol.* 5:408. doi: 10.3389/fphys.2014.00408

Lee, J., Cao, H., Kang, B. J., Jen, N., Yu, F., Lee, C. A., et al. (2014). Hemodynamics and ventricular function in a zebrafish model of injury and repair. *Zebrafish* 11, 447–454. doi: 10.1089/zeb.2014.1016

Lieschke, G. J., and Currie, P. D. (2007). Animal models of human disease: zebrafish swim into view. *Nat. Rev. Genet.* 8, 353–367. doi: 10.1038/nrg2091

Lindsey, S. E., Butcher, J. T., and Yalcin, H. C. (2014). Mechanical regulation of cardiac development. *Front. Physiol.* 5:318. doi: 10.3389/fphys.2014.00318

Liu, C. C., Li, L., Lam, Y. W., Siu, C. W., and Cheng, S. H. (2016). Improvement of surface ECG recording in adult zebrafish reveals that the value of this model exceeds our expectation. *Sci. Rep.* 6:25073. doi: 10.1038/srep25073

Locatelli, P., Olea, F. D., De Lorenzi, A., Salmo, F., Janavel, G. L. V., Hnatiuk, A. P., et al. (2011). Reference values for echocardiographic parameters and indexes of left ventricular function in healthy, young adult sheep used in translational research: comparison with standardized values in humans. *Int. J. Clin. Exp. Med.* 4, 258–264.

Lucitti, J. L., Tobita, K., and Keller, B. B. (2005). Arterial hemodynamics and mechanical properties after circulatory intervention in the chick embryo. *J. Exp. Biol.* 208 (Pt 10), 1877–1885. doi: 10.1242/jeb.01574

Mahler, G. J., Frendl, C. M., Cao, Q., and Butcher, J. T. (2014). Effects of shear stress pattern and magnitude on mesenchymal transformation and invasion of aortic valve endothelial cells. *Biotechnol. Bioeng.* 111, 2326–2337. doi: 10.1002/bit.25291

Mammoto, T., and Ingber, D. E. (2010). Mechanical control of tissue and organ development. *Development* 137, 1407–1420. doi: 10.1242/dev.024166

McLeish, J. A., Chico, T. J., Taylor, H. B., Tucker, C., Donaldson, K., and Brown, S. B. (2010). Skin exposure to micro-and nano-particles can cause haemostasis in zebrafish larvae. *Thromb. Haemost.* 104, 797–807. doi: 10.1160/TH09-06-0413

Midgett, M., and Rugonyi, S. (2014). Congenital heart malformations induced by hemodynamic altering surgical interventions. *Front. Physiol.* 5:287. doi: 10.3389/fphys.2014.00287

Midgett, M., Thornburg, K., and Rugonyi, S. (2017). Blood flow patterns underlie developmental heart defects. *Am. J. Physiol. Heart Circ. Physiol.* 312, H632–H642. doi: 10.1152/ajpheart.00641.2016

Miura, G. I., and Yelon, D. (2011). A guide to analysis of cardiac phenotypes in the zebrafish embryo. *Methods Cell Biol.* 101, 161–180. doi: 10.1016/B978-0-12-387036-0.00007-4

Packard, R. R. S., Baek, K. I., Beebe, T., Jen, N., and Ding, Y. (2017). Automated segmentation of light-sheet fluorescent imaging to characterize experimental doxorubicin-induced cardiac injury and repair. 7:8603. doi: 10.1038/s41598-017-09152-x

Pang, K. L., Parnall, M., and Loughna, S. (2017). Effect of altered haemodynamics on the developing mitral valve in chick embryonic heart. *J. Mol. Cell. Cardiol.* 108, 114–126. doi: 10.1016/j.yjmcc.2017.05.012

Parente, V., Balasso, S., Pompilio, G., Verduci, L., Colombo, G. I., Milano, G., et al. (2013). Hypoxia/reoxygenation cardiac injury and regeneration in zebrafish adult heart. *PLoS ONE* 8:e53748. doi: 10.1371/journal.pone.0053748

Parng, C., Seng, W. L., Semino, C., and McGrath, P. (2002). Zebrafish: a preclinical model for drug screening. *Assay Drug Dev. Technol.* 1, 41–48. doi: 10.1089/154065802761001293

Phoon, C. K., Ji, R. P., Aristizabal, O., Worrad, D. M., Zhou, B., Baldwin, H. S., et al. (2004). Embryonic heart failure in NFATc1-/- mice: novel mechanistic insights from *in utero* ultrasound biomicroscopy. *Circ. Res.* 95, 92–99. doi: 10.1161/01.RES.0000133681.99617.28

Piliszek, A., Kwon, G. S., and Hadjantonakis, A. K. (2011). *Ex utero* culture and live imaging of mouse embryos. *Methods Mol. Biol.* 770, 243–257. doi: 10.1007/978-1-61779-210-6_9

Poon, K. L., and Brand, T. (2013). The zebrafish model system in cardiovascular research: a tiny fish with mighty prospects. *Glob. Cardiol. Sci. Pract.* 2013, 9–28. doi: 10.5339/gcsp.2013.4

Roger, V. L., Go, A. S., Lloyd-Jones, D. M., Adams, R. J., Berry, J. D., Brown, T. M., et al. (2011). Heart disease and stroke statistics-2011 update: a report from the American heart association. *Circulation* 123, e18–e209. doi: 10.1161/CIR.0b013e3182009701

Samsa, L. A., Yang, B., and Liu, J. (2013). Embryonic cardiac chamber maturation: trabeculation, conduction, and cardiomyocyte proliferation. *Am. J. Med. Genet. C Semin. Med. Genet.* 163c, 157–168. doi: 10.1002/ajmg.c.31366

Spencer, K. T., Kimura, B. J., Korcarz, C. E., Pellikka, P. A., Rahko, P. S., and Siegel, R. J. (2013). Focused cardiac ultrasound: recommendations from the American Society of Echocardiography. *J. Am. Soc. Echocardiogr.* 26, 567–581. doi: 10.1016/j.echo.2013.04.001

Srivastava, D., and Olson, E. N. (2000). A genetic blueprint for cardiac development. *Nature* 407, 221–226. doi: 10.1038/35025190

Sun, L., Lien, C.-L., Xu, X., and Shung, K. K. (2008). *In vivo* cardiac imaging of adult zebrafish using high frequency ultrasound (45-75 MHz). *Ultrasound Med. Biol.* 34, 31–39. doi: 10.1016/j.ultrasmedbio.2007.07.002

Tobita, K., and Keller, B. B. (2000). Right and left ventricular wall deformation patterns in normal and left heart hypoplasia chick embryos. *Am. J. Physiol. Heart Circ. Physiol.* 279, H959–H969. doi: 10.1152/ajpheart.2000.279.3.H959

Tobita, K., Schroder, E. A., Tinney, J. P., Garrison, J. B., and Keller, B. B. (2002). Regional passive ventricular stress-strain relations during development of altered loads in chick embryo. *Am. J. Physiol. Heart. Circ. Physiol.* 282, H2386–H2396. doi: 10.1152/ajpheart.00879.2001

Verkerk, A. O., and Remme, C. A. (2012). Zebrafish: a novel research tool for cardiac (patho) electrophysiology and ion channel disorders. *Front. Physiol.* 3:255. doi: 10.3389/fphys.2012.00255

Wang, L. W., Huttner, I. G., Santiago, C. F., Kesteven, S. H., Yu, Z. Y., Feneley, M. P., et al. (2017). Standardized echocardiographic assessment of cardiac function in normal adult zebrafish and heart disease models. *Dis. Model. Mech.* 10, 63–76. doi: 10.1242/dmm.026989

Wang, Y., Dur, O., Patrick, M. J., Tinney, J. P., Tobita, K., Keller, B. B., et al. (2009). Aortic arch morphogenesis and flow modeling in the chick embryo. *Ann. Biomed. Eng.* 37, 1069–1081. doi: 10.1007/s10439-009-9682-5

Watson, L. E., Sheth, M., Denyer, R. F., and Dostal, D. E. (2004). Baseline echocardiographic values for adult male rats. *J. Am. Soc. Echocardiogr.* 17, 161–167. doi: 10.1016/j.echo.2003.10.010

Wilson, K., Baily, J., Tucker, C., Matrone, G., Vass, S., Moran, C., et al. (2015). Early-life perturbations in glucocorticoid activity impacts on the structure, function and molecular composition of the adult zebrafish (*Danio rerio*) heart. *Mol. Cell. Endocrinol.* 414, 120–131. doi: 10.1016/j.mce.2015.07.025

Yalcin, H. C. (2018). Hemodynamic studies for analyzing the teratogenic effects of drugs in the zebrafish embryo. *Methods Mol. Biol.* 1797, 487–495. doi: 10.1007/978-1-4939-7883-0_27

Yalcin, H. C., Amindari, A., Butcher, J. T., Althani, A., and Yacoub, M. (2017). Heart function and hemodynamic analysis for zebrafish embryos. *Dev. Dyn.* 246, 868–880. doi: 10.1002/dvdy.24497

Yalcin, H. C., Shekhar, A., McQuinn, T. C., and Butcher, J. T. (2011). Hemodynamic patterning of the avian atrioventricular valve. *Dev. Dyn.* 240, 23–35. doi: 10.1002/dvdy.22512

Yalcin, H. C., Shekhar, A., Rane, A. A., and Butcher, J. T. (2010). An *ex-ovo* chicken embryo culture system suitable for imaging and microsurgery applications. *J. Vis. Exp.* e2154. doi: 10.3791/2154

Yu, Q., Leatherbury, L., Tian, X., and Lo, C. W. (2008). Cardiovascular assessment of fetal mice by *in utero* echocardiography. *Ultrasound Med. Biol.* 34, 741–752. doi: 10.1016/j.ultrasmedbio.2007.11.001

Zakaria, Z. Z., Benslimane, F. M., Nasrallah, G. K., Shurbaji, S., Younes, N. N., Mraiche, F., et al. (2018). Using zebrafish for investigating the molecular mechanisms of drug-induced cardiotoxicity. *Biomed Res. Int.* 2018:1642684. doi: 10.1155/2018/1642684

Zaragoza, C., Gomez-Guerrero, C., Martin-Ventura, J. L., Blanco-Colio, L., Lavin, B., Mallavia, B., et al. (2011). Animal models of cardiovascular diseases. *J. Biomed. Biotechnol.* 2011:497841. doi: 10.1155/2011/497841

Conflict of Interest Statement: The authors declare that the research was conducted in the absence of any commercial or financial relationships that could be construed as a potential conflict of interest.

frontiers in Bioengineering and Biotechnology

ORIGINAL RESEARCH
published: 15 May 2019
doi: 10.3389/fbioe.2019.00107

Investigating the Effect of Aging on the Viscosity of Tendon Fascicles and Fibers

Nikolaos Karathanasopoulos[1]* *and Jean-francois Ganghoffer*[2]

[1] Chair of Computatonal Modeling of Materials in Manufacturing, ETH Zurich, Zurich, Switzerland, [2] LEM3, CNRS, Université de Lorraine, Metz, France

In the current work, we investigate the effect of aging on the viscosity of tendon subunits. To that scope, we make use of experimental relaxation curves of healthy and aged tendon fascicles and fibers, upon which we identify the viscosity parameters characterizing the time-dependent behavior of each tendon subunit. We subsequently combine the obtained results with analytical viscoelastic homogenization analysis methods to extract information on the effective viscous contribution of the embedding matrix substance at the fiber scale. The results suggest that the matrix substance plays a significant role in the relaxation process of the upper tendon subunits both for aged and healthy specimens. What is more, the viscosity coefficients computed for the fibrillar components indicate that aging leads to a viscosity reduction that is statistically significant for both fascicles and fibers. Its impact is more prominent for the lower hierarchical scale of fibers. As such, the reduced stress relaxation capability at the tendon macroscale is to be primarily attributed to the modified viscosity of its inner fibrillar subunits rather than to the matrix substance.

Keywords: tendon, relaxation, viscosity, aging, fascicle, fiber, matrix

OPEN ACCESS

Edited by:
Charles David Cox, Victor Chang Cardiac Research Institute, Australia

Reviewed by:
Elisabetta M. Zanetti, University of Perugia, Italy
Nicola Francesco Lopomo, University of Brescia, Italy

***Correspondence:**
Nikolaos Karathanasopoulos
nkaratha@ethz.ch

Specialty section:
This article was submitted to Biomechanics, a section of the journal Frontiers in Bioengineering and Biotechnology

Received: *11 January 2019*
Accepted: *29 April 2019*
Published: *15 May 2019*

Citation:
Karathanasopoulos N and Ganghoffer J-f (2019) Investigating the Effect of Aging on the Viscosity of Tendon Fascicles and Fibers. Front. Bioeng. Biotechnol. 7:107. doi: 10.3389/fbioe.2019.00107

INTRODUCTION

The multiscale structure of tendons plays a functional role in the transfer of forces from the muscles to the bones (Maceri et al., 2012; Ge et al., 2018). The fascicles contained within the tendon unit are composed of fibers immersed in a matrix substance (**Figure 1A**) (Goh et al., 2008). Disease or age-related changes taking place at the tendon's molecular scale are expressed in terms of modified mechanical properties at the upper tendon scales, namely at the fiber and fascicle scale (Bailey, 2001; Zhang et al., 2014).

In order to characterize the tendon's mechanical attributes, tensile experiments have been carried out at different inner tendon hierarchies. In particular, quasi-static stress-strain curves have been used to provide estimates for the elastic modulus of fascicles and fibers (Kato et al., 1989; Gentleman et al., 2004; Lavagnino et al., 2005; Svensson et al., 2010). However, the linear elastic stress-strain response does not suffice to describe the substantial stress relaxation capabilities observed for tendons (Salathe and Arangio, 1990). Viscoelasticity has provided the theoretical basis for the characterization of the tendon's relaxation behavior (Elliott et al., 2003; Machiraju et al., 2006; Screen, 2008; Shen et al., 2011), mathematically described as a function of both elastic and viscous parameters (Taylor et al., 1970; Christensen, 1982). The tendon's viscoelastic properties have been shown to differ among its lower and upper scales, with the embedding matrix substance to play a significant role in the multiscale effective relaxation behavior (Karathanasopoulos et al., 2019).

It is up to now well-established that the aging process, as well as deceases such as diabetes, result in functional changes, which have been directly related to increased tendon damage and injury (Dressler et al., 2002), as well as to reduced healing capacity (Bedi et al., 2010). Such phenomenological effects arise from inner structural changes, which alter the mechanical properties of the tendons's inner scales (Snedeker and Foolen, 2017). In particular, it has been shown that aging induces non-enzymatic cross-linkings upon a glycation process which modifies the loading capacity and time-dependent attributes at the tropocollagen scale (Gautieri et al., 2013; Vesentini et al., 2013; Nair et al., 2014), thus already at the innermost structural building block of tendons. What is more, it has been experimentally demonstrated that aging primarily affects the viscoelastic properties and the failure mode (Li et al., 2013) of tendon fibrils, fibers and fascicles (Gautieri et al., 2017), an observation made for both human and animal tissues (Hansen et al., 2010; Maceri et al., 2012). Contrariwise, the elastic modulus of aged tendons remains practically unaffected for all of the previously reported subunits (Legerlotz et al., 2013; Fessel et al., 2014).

While the qualitative effects of aging on tendons have been long identified and relevant stress measurements are available, quantitative estimates of the resulting modifications in the effective viscosities of the different inner tendon scales remain to be provided. Information of the kind is of primal importance, not only for the understanding of the mechanical behavior of the tendon's inner fibrillar components (Karathanasopoulos and Ganghoffer, 2019a), but also for the embedding matrix substance. The latter has been shown to play a primal role both in the relaxation process (Karathanasopoulos et al., 2019) and in the progression of tissue related deceases (Snedeker and Gautieri, 2014). However, mechanical testing at the embedding matrix substance scale is rather infeasible (Ault et al., 1992), so that no direct experimental data are available. As a result, its mechanical properties are estimated either though physics-motivated analytical models (Ault et al., 1992) or multiscale modeling inference techniques (Karathanasopoulos and Hadjidoukas, 2019b; Karathanasopoulos et al., 2019).

In the current work, we make use of experimental data which we combine with viscoelastic mechanical models to provide quantitative estimates for the effective viscosity of healthy and aged tendon subunits. In particular, in section Methodology, we summarize the theoretical framework to compute the relaxation behavior of tendon subunits. Thereupon, we compute the viscoelastic parameters that characterize the relaxation behavior of healthy and aged tendon fascicles and fibers, quantifying the relevant experimental uncertainty (see sections Relaxing Healthy and Aging Fascicles and Fiber Scale Aging Relaxation) and the statistical significance of the observed alterations (see Statistical Significance of the Effective Viscosity Alterations Upon Aging). Combing the mechanical data with analytical, homogenization analysis techniques, we furnish estimates for the effective viscosity of the embedding matrix substance at the fiber scale both for the healthy (control) and for the aged tendon specimens (see section Effective Viscosity Contributions of the Embedding Matrix). In section Discussion, we comment on the obtained results, providing considerable insights in the effect of aging at the different tendon inner scales and conclude in section Conclusions.

METHODOLOGY

The fibrous, matrix-embeded structure of fascicles and fibers (**Figure 1A**) (Ge et al., 2018) has allowed for the tendon subunits to be characterized as naturally architected, two-phase composite materials (Maceri et al., 2012). The fibrillar

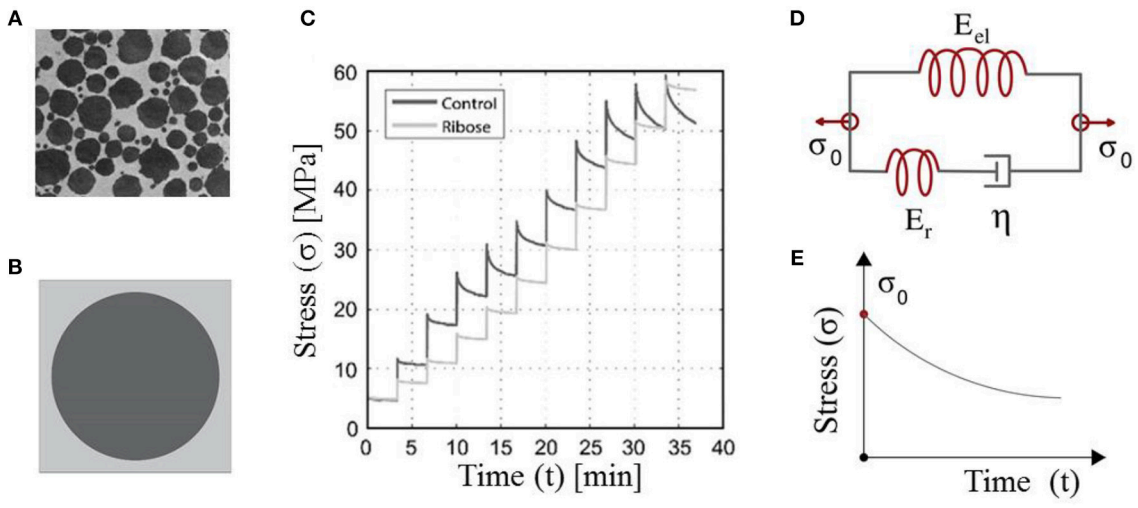

FIGURE 1 | Tendon fibers immersed in a matrix substance **(A)**. Maceri et al. (2012) and Gautieri et al. (2017) defining a certain averaged, unit-cell fiber content (Karathanasopoulos et al., 2019) **(B)**. The short-time relaxation response of *in-vitro* human tendon fascicles upon repetitive incremental loading steps **(C)**. Gautieri et al. (2017) and their theoretical representation by means of Maxwell-type relaxing elements with a primal material viscosity η (Lakes, 2009) **(D,E)**. **(A,C)** are reproduced with the permission of the copyright holder [RightsLink/Elsevier].

components are in a certain relative density to the embedding matrix substance, so that a unit-cell with a fibrous fraction f_r can be defined (**Figure 1B**) (Ganghoffer et al., 2016; Karathanasopoulos et al., 2017, 2019).

Each material phase can be considered to be in the general case of viscoelastic nature, with elastic and viscous properties E_f, E_m and η_f, η_m for the fibrillar and matrix components accordingly. As such, the effective homogenized viscoelastic response of the matrix embedded tendon fibers is characterized by the following constitutive equation (Ganghoffer et al., 2016; Karathanasopoulos et al., 2019):

$$\bar{\sigma} = \langle E\rangle\,\bar{\varepsilon} + \langle \eta\rangle\,\dot{\bar{\varepsilon}} + \langle \eta\rangle\,\frac{E_f E_m}{\eta_f \eta_m}\left(\frac{\langle \eta/E^2\rangle}{\langle 1/E\rangle} - \frac{\langle 1/E\rangle}{\langle 1/\eta\rangle}\right) \int_0^t exp\left(-\frac{E_f}{\eta_f}\frac{E_m}{\eta_m}\frac{\langle\eta\rangle}{\langle E\rangle}(t-s)\right)\dot{\bar{\varepsilon}}(s)ds \quad (1)$$

Where in Equation (1), components with a bar stand for the homogenized strain and stress $\bar{\varepsilon}$ and $\bar{\sigma}$, while brackets for the homogenized elastic and viscous moduli, $\langle E\rangle$ and $\langle\eta\rangle$ accordingly. The latter depend on the volumetric fraction of the two phases, as follows (Ganghoffer et al., 2016):

$$\langle\eta\rangle = \eta_{fasc} = \eta_f f_r + \eta_m\left(1-f_r\right), \langle E\rangle = E_{fasc} = E_f f_r + E_m\left(1-f_r\right) \quad (2)$$

Given the homogenized elastic and viscous material parameters, the time-dependent response of the tendon subunits is characterized by Maxwell-type relaxation kernels (**Figures 1D,E**) (Christensen, 1982; Lakes, 2009). The primal relaxation behavior of the viscoelastic structure is a kernel function of its elastic and viscous parameters, defined as follows (Christensen, 1982; Lakes, 2009):

$$E(t) = E_{el} + E_r e^{-\frac{E_r}{\eta}t}, E(t=0) = E_{el} + E_r \quad (3)$$

where in Equation (3), E_r stands for the relaxing modulus part, which is equal to the substraction of the elastic modulus part E_{el} (the modulus part remaining at the end of the relaxation experiment) from the initial modulus $E_r = E(t=0) - E_{el}$ (**Figure 1**). For $t = 0$, the elastic modulus is equal to its initial homogenized, non time-dependent value, as indicated by Equation (3). Equation (3) applies to both fascicles (fasc) and fibers (f), with the viscosity parameter to be denoted as η_{fasc} and η_f accordingly.

While the initial modulus can be directly retrieved out of experimental testing, information on the viscous modulus η of Equation (3) needs to be extracted making use of the relaxation curves (**Figure 1C**) . For the viscous modulus to be identified, the viscoelastic parameter η in the time-dependent modulus evolution of Equation (3) is optimized to meet the experimental modulus evolution $\hat{E}(t)$ of each relaxation curve (**Figure 3C**, Li et al., 2013; Gautieri et al., 2017) using a control timestep of ten seconds between the starting t_s and final time t_f of each relaxation experiment, upon the following loss function:

$$\arg\min L = \sum_{t_s}^{t_f}\left\|E(t) - \hat{E}(t)\right\| \quad (4)$$

For the minimization of Equation (4), a standart derivative-free method has been employed using Matlab 2018a. In the Sections to follow, we make use of the definitions of Equations (1)–(4) along with experimental data provided in Li et al. (2013) and Gautieri et al. (2017) to compute the primal viscosity coefficient of tendon fascicles (see section Relaxing Healthy and Aging Fascicles) and fibers (see section Fiber Scale Aging Relaxation), as well as to extract information on the effective viscous contribution of the embedding matrix substance (see section Effective Viscosity Contributions of the Embedding Matrix).

In order to assess the significance of the identified viscosity changes among the control and aged tendon fascicles and fibers, we carry out a Welch's t-test in section Statistical Significance of the Effective Viscosity Alterations Upon Aging. The main parameters of the t-test, namely the t value and the associated number of degrees of freedom ν are given as follows (Fagerland, 2012):

$$t = (\mu_c - \mu_a)/\sqrt{\sigma_c^2/N_c + \sigma_a^2/N_a}$$
$$\nu = \left(\sigma_c^2/N_c + \sigma_a^2/N_a\right)^2/\left(\sigma_c^4/\left(N_c^2(N_c-1)\right) + \sigma_a^4/\left(N_a^2(N_a-1)\right)\right) \quad (5)$$

where μ_c and μ_a in Equation (5) stand for the mean value (μ) of a certain control (c) and aged (a) quantity, while σ and N stand for the standard deviation and the sample size accordingly.

RESULTS

Relaxing Healthy and Aging Fascicles

In the current section, we identify the viscosity coefficient η of relaxing healthy and aged fascicles, using Equation (3) along with the experimental data provided in Gautieri et al. (2017) and depicted in **Figure 1C**. In particular, we compute the viscosity coefficient η for each of the healthy and ribosed fascicle relaxation curves, carrieη d out within the linear elastic strain range as low as 1.8% and up to 4.8%, upon strain increments of 0.6% (relaxation experiments in between 10 and 30 min in **Figure 1C**). Each relaxation experiment has been conducted for a total duration of 200 s, so that the total number N of relaxation experiments for which the viscosity value is identified is $N = 6$. The mean elastic modulus ($t = 0$) of the fascicles has been computed to be $\langle E\rangle_c = 892MPa$ and $\langle E\rangle_a = 942\,MPa$ for control (c) and aged (a) fascicles, accordingly (Li et al., 2013; Gautieri et al., 2017). In **Figure 2** (left), we provide the computed mean and standard deviation of the probability density function (pdf) for the coefficient η of the healthy and aged fascicles using Equation (4). In **Figure 2** (right), we provide the percentage reduction of the mean viscosity value η , compared to the percentage change of the elastic modulus E.

The left subplot of **Figure 2** suggests a clear separation of the probability distributions of the viscosity coefficients for the healthy and the aged fascicles. More specifically, for the

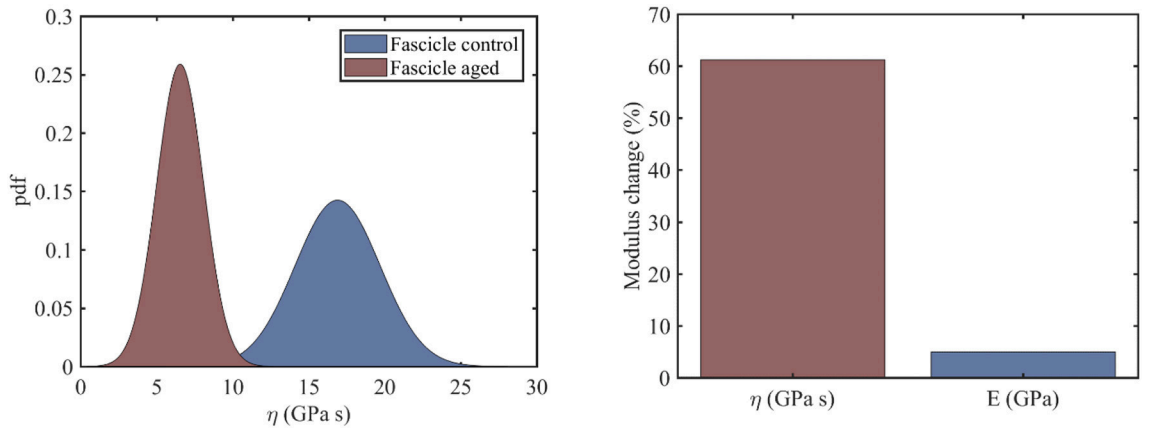

FIGURE 2 | Probability density function of the viscosity coefficients of healthy and aged tendon fascicles (left) and the percentage reduction of its mean value (right).

control healthy fascicle, a mean viscous coefficient of $\eta^c_{fasc} = 17\,GPa\,s$ has been identified with a standard deviations of 2.8 $GPa\,s$. Accordingly, for aged fascicles, a mean effective viscosity coefficient of $\eta^a_{fasc} = 6.5\,GPa\,s$ along with a standard deviation of 1.6 $GPa\,s$ has been obtained. The percentage difference for the mean value of the fascicle viscoelastic modulus η_{fasc} between the healthy and aged tendon tissue is in the order of 60% (**Figure 2**, right), contrary to the rather negligible variation of 5% for its elastic modulus $\langle E \rangle$. The relaxation curves for aged and healthy fascicles arising from the identified fascicle viscosity η_{fasc} are provided for completeness in **Appendix A**.

Fiber Scale Aging Relaxation

At the fiber scale, we identify the viscosity coefficient η_f using Equation (3), so that Equation (3) simplifies to $E_f(t) = E_{el} + E_r e^{-(\frac{E_r}{\eta_f})*t}$. The fiber scale relaxation curves for healthy and aged tendon fibers are provided in Li et al. (2013). For the fiber viscosity computations, a total of six ($N = 6$) relaxation experiments within the linear elastic strain range is used, in particular for strain magnitudes in between 2 and 4.5%, upon strain increments of 0.5%. In the left subplot of **Figure 3**, we provide the computed probability density functions for the viscosity values η of healthy and aged tendon fiber specimens, while in **Figure 3** (right) the percentage reduction in the mean viscosity values among healthy and aged tendon fiber and fascicle (see section Relaxing Healthy and Aging Fascicles) specimens.

Figure 3 (left) indicates a complete separation of the viscoelastic coefficients pertaining to healthy and aged fiber specimens. In particular, while for the control fibers, a mean viscous coefficient value of $\eta^c_f = 15.3\,GPa\,s$ is computed, for the aged ones, a value of $\eta^a_f = 1.3\,GPa\,s$ is obtained. What is more, the standard deviation of the viscosity of the aged fibers is considerably smaller (0.276 $GPa\,s$) than the one obtained for the control tendon fibers (1.05 $GPa\,s$). The mean viscosity coefficient for aged fiber specimens is considerably smaller than the corresponding η value at the fascicle scale (**Figure 3**, left). Moreover, the percentage reduction of the viscoelastic parameter upon aging is considerably higher at the fiber scale compared to the fascicle scale (**Figure 4**, right). The computed fiber-scale relaxation curves are provided for completeness in **Appendix A**.

Effective Viscosity Contributions of the Embedding Matrix

For the viscous contribution of the embedding matrix substance to be quantified, we make use of the previously obtained viscosity results at the fiber and fascicle scale (**Figures 2**, **3**), which we couple with the analytical homogenization based predictions of Equations (1) and (2). In particular, we use the mean values of the computed viscosity coefficients $\eta_{fasc} = \langle \eta \rangle$ at the fascicle scale (**Figure 2**) to infer the viscous contribution of the embedding matrix at the fiber scale η_m, using the results of **Figures 2**, **3** and Equation (2). For the computations, we allow for the fiber content entering f_r Equation (2) to vary in between 0.3 and 0.7 (Maceri et al., 2012; Li et al., 2013). In **Figure 4** (left), we depict the range of values –in red- calculated for the effective viscosity of the embedding matrix η_m for control and aged specimens, while in **Figure 4** (right), the ratio of the viscosity of the matrix to the one of the fiber (η_m/η_f) for a fibrillar fraction of $f_r = 0.3$.

Figure 4 provides an estimate of the effective viscosity of the embedding matrix η_m at the tendon fiber scale, both for the control and aged tendons. For the former, a matrix viscosity value between 18 and 22 $GPa\,s$ is obtained for low and high fiber content values accordingly (**Figure 4**, left). For their aged counterparts, a considerably wider range of values is computed, as low as 8.5 an up to 18.5 $GPa\,s$ (**Figure 4**, left). For a given fiber content value f_r (e.g., for $f_r = 0.3$, corresponding to the minimum value of the bars in **Figure 4**, left), the effective viscosity of the embedding matrix of aged specimens is considerably lower than the one of the control ones (**Figure 4**, left). However, for the aged tendons, the relative viscous embedding matrix contribution is considerably higher than the one of control fascicle specimens, as the ratio of the effective matrix viscosity to the fiber matrix viscosity η_m/η_f in **Figure 4** (right) suggests.

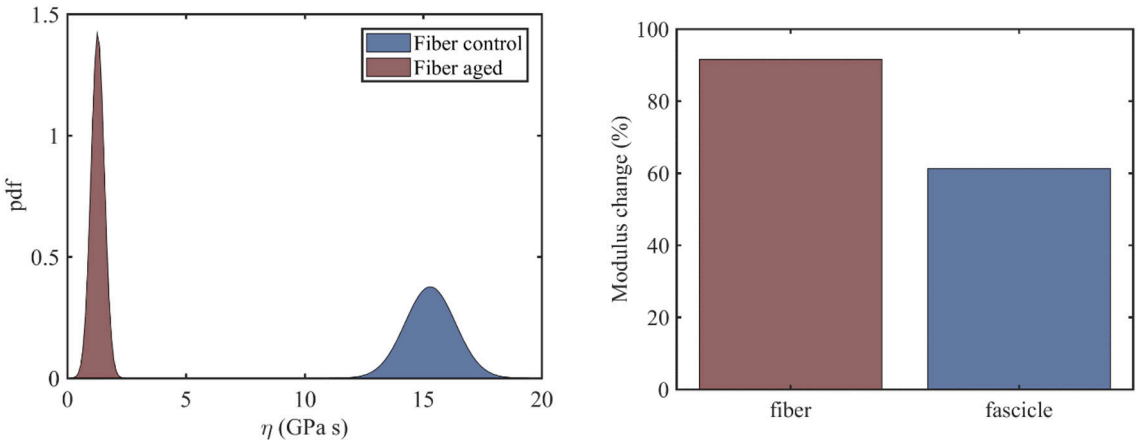

FIGURE 3 | Probability distribution of the viscosity coefficients η of healthy and aged tendon fibers (left) along with the percentage change upon aging of the mean viscous moduli value for fibers and fascicles (right).

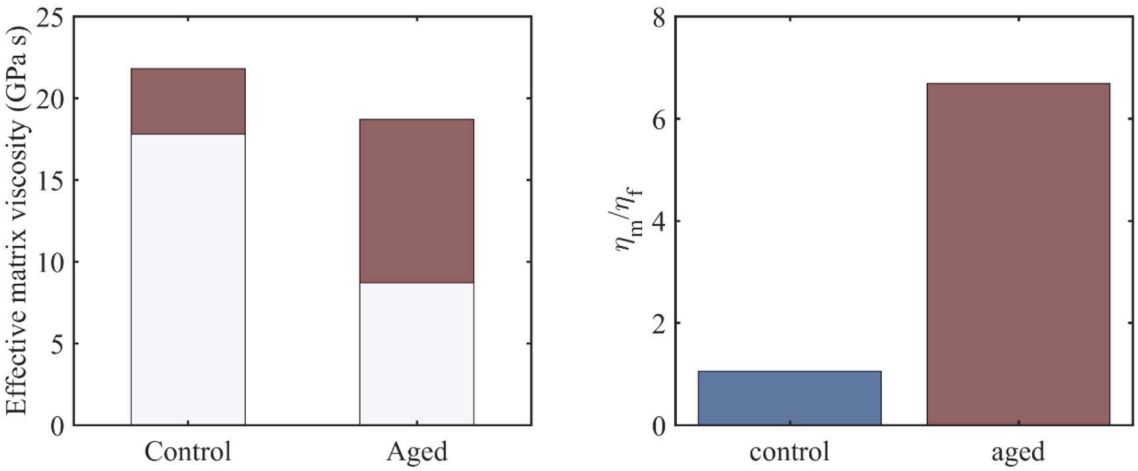

FIGURE 4 | The range of the effective viscosity of the embedding matrix –depicted in red- for control and aged tendon fascicle specimens and an f_r value in between 0.3 and 0.7 (left), along with the ratio of the fiber to the embedding matrix viscosities for a fiber fraction of $f_r = 0.3$ (right).

Statistical Significance of the Effective Viscosity Alterations Upon Aging

We subsequently assess the significance of the computed viscosity changes among the control and aged tendon fascicles and fibers, using the t-test metrics, summarized in Equation (5). At the fascicle scale, we compute a t value that is $t = 7.98$, along with an ν value of $\nu = 7.95$, using the mean viscosity η_{fasc} and standard deviation values provided in section Relaxing Healthy and Aging Fascicles. The values relate to a p-value that is lower than 0.01 within a 5% significance interval, suggesting a significant viscosity difference between the control and aged fascicle groups. Performing the same analysis for the viscosity parameters computed at the fiber scale (see section Fiber Scale Aging Relaxation), we obtain a t value that is $t = 31.5$ along with an ν value of $\nu = 5.7$. The values pair to a p-value that is lower than 10^{-4} within a 5% significance interval, indicating a highly significant difference between the control and aged tendon fiber groups. The results are summarized in **Table 1**.

DISCUSSION

The results of sections Relaxing Healthy and Aging Fascicles, Fiber Scale Aging Relaxation, and Effective Viscosity Contributions of the Embedding Matrix provide experimentally-based, quantitative estimates of the effect of aging on the time-dependent, viscous properties of tendon subunits. In particular, the viscosities at the scale of fascicles (see section Relaxing Healthy and Aging Fascicles) and fibers (see section Fiber Scale Aging Relaxation), as well as the effective viscoelastic contribution of the fiber embedding matrix substance (see section Effective Viscosity Contributions of the Embedding Matrix) are assessed.

TABLE 1 | Statistical significance of the alterations in the viscosity parameters computed for control and aged tendon fascicles (see section Relaxing Healthy and Aging Fascicles) and fibers (see section Fiber Scale Aging Relaxation) using t-test statistics.

Scale	*t*-value	ν value	*p*-value
Fascicle	7.98	7.95	<0.01
Fiber	31.5	5.7	<0.0001

The experimental data at the fascicle scale (**Figure 1C**) yield a mean viscosity value η of 17 $GPa\,s$ for the control specimens (**Figure 2**, right); a value that is 60% higher than the one computed for the aged fascicle specimens. The reduction pertains to the short-term relaxation time of fascicles, as the experimental curves (**Figure 1C**) restrain to a relaxation experiment of 200 s for each loading increment, a time-frame that is considerably shorter than the one required for a complete fascicle relaxation ($t > 400\,s$) in different studies (Machiraju et al., 2006; Davis and De Vita, 2012). Note that contrary to the substantial alteration of the time-dependent properties (see section Relaxing Healthy and Aging Fascicles), the fascicle's linear elastic attributes remain practically unaffected (**Figure 2**, right) (Gautieri et al., 2017). In particular, the elastic modulus is subject to a comparatively insignificant variation in the order of 5% (**Figure 2**, right). The rather negligible sensitivity of the elastic modulus to aging effects has been experimentally shown to apply, not only to the fascicle scale, but also to the inner scales of fibers and fibrils (Legerlotz et al., 2013; Li et al., 2013; Gautieri et al., 2017).

While the mean viscosity of control tendon fibers (**Figure 3**, left) well-compares to the short term viscosity of healthy tendon fascicles (**Figure 3**, left), the behavior of their aged counterparts differs to a large extend. More specifically, at the fiber scale, the viscosity decreases by approximately an order of magnitude (**Figure 3**, right), contrary to the 60% reduction in mean viscosity terms observed at the fascicle scale. The difference suggests that aging has a more predominant effect at the time-dependent properties of the lower tendon subunits. However, the observed viscosity changes are statistically significant both for tendon fascicles and fibers (see section Statistical significance of the Effective Viscosity Alterations Upon Aging).

The range of matrix viscosity values η_m reported in section Effective Viscosity Contributions of the Embedding Matrix constitute the first estimates –to the author's best knowledge- of the effective viscous contribution of the embedding matrix substance at the fiber scale that is based on experimental data. It needs to be noted that data-based estimates of the kind can be primarily obtained through the coupling of multiscale mechanical information (Karathanasopoulos et al., 2017, 2019; Karathanasopoulos and Ganghoffer, 2019a), as direct experimental testing is rather infeasible (Ault et al., 1992). The range of magnitudes computed for the effective embedding matrix viscosity η_m (**Figure 4**) suggests that the effective contribution of the matrix in the relaxation process at the fiber and fascicle scale is significant, both for the control and aged specimens. Analogous conclusions have been derived for the innermost tendon subunits of fibrils (Karathanasopoulos et al., 2019). What is more, for the case of aged tendon subunits, while the magnitude of the matrix viscosity is on average lower than the one obtained for the control specimens (**Figure 4**, left), their relative viscoelastic contribution is higher (**Figure 4**, right). The computed viscosity ratios (**Figure 4**, right) indicate that aging affects primarily the fibrillar components, rather than the embedding matrix substance.

We note that the current analysis has been restricted to available experimental studies on the effect of aging on the relaxation behavior of both lower and upper tendon subunits subunits (Li et al., 2013; Gautieri et al., 2017). The provided experimental information restrains to quasi-static relaxation experiments, which do not quantify the variance of the relaxation experiments for the specific strain magnitude or strain rate selected, factors that have been shown to play a role in the mechanical response of biological tissues (Zanetti et al., 2012; Natali et al., 2015). For such effects to be accounted for, further multiscale experimental data of the kind would be required, not only to decrease the reported overall experimental uncertainty (**Figures 2–4**), but also to provide experimental information that is up to now unavailable. In particular, separate short-time and long-time relaxation experiments could be carried out at different strain magnitudes and strain rates, to provide additional secondary information on the relaxation spectrum of each tendon subunit. Data of the kind could be thereafter used a basis for a more elaborate identification of the mechanical parameters at each tendon scale, as well as for the understanding of the functional role of the multiscale tendon architecture (Karathanasopoulos et al., 2019).

CONCLUSIONS

Overall, the viscosity parameters computed in sections Relaxing Healthy and Aging Fascicles and Fiber Scale Aging Relaxation have provided primal, data-based quantitative estimates of the effect of aging on the time-dependent behavior of fascicles and fibers. It has been shown that the viscosity coefficients η_{fasc} and η_f are subject to statistically significant reductions as a result of the aging process (see section Statistical Significance of the Effective Viscosity Alterations Upon Aging). What is more, the effective viscous contribution of the embedding matrix substance η_m has been quantified, using a multi-scale mechanical analysis framework (see section Effective Viscosity Contributions of the Embedding Matrix). It has been shown that the matrix effective viscosity η_m is comparable to the one computed for the tendon's fibrillar components, while its viscoelastic contribution is higher for aged rather than for control, healthy tendon subunits. The results can be used as reference viscosity mechanical parameters, factors of primal importance for the understanding of the tendon's tissue mechanics, as well as for its regeneration

(Sandri et al., 2016). We aspire that the identified viscosity parameters along with the elaborated methodology will serve as an engineering basis for the design of biocompatible restoration materials, as well as for the development of mechanically appropriate medical treatments for aged tendons (Legerlotz et al., 2013).

AUTHOR CONTRIBUTIONS

NK: conception, design, computations, and main editing. JG: analysis and interpretation of results.

ACKNOWLEDGMENTS

NK would like to acknowledge the support of the Freenovation Grant 2017 along with the support of the ETH CSE-lab in the writing of the corresponding application.

SUPPLEMENTARY MATERIAL

The Supplementary Material for this article can be found online at: https://www.frontiersin.org/articles/10.3389/fbioe.2019.00107/full#supplementary-material

REFERENCES

Ault, H. K., and Hoffman, A. H.,. (1992). A composite micromechanical model for connective tissues: part II—application to rat tail tendon and joint capsule. *J. Biomech. Eng.* 114, 142–146. doi: 10.1115/1.2895438

Bailey, A. J. (2001). Molecular mechanisms of ageing in connective tissues. *Mech. Ageing Dev.* 122, 735–755. doi: 10.1016/S0047-6374(01)00225-1

Bedi, A., Fox, A. J. S., Harris, P. E., Deng, X. H., Ying, L. A., Warren, R. F., et al. (2010). Diabetes mellitus impairs tendon-bone healing after rotator cuff repair. *J. Shoulder Elb. Surg.* 19, 978–988. doi: 10.1016/j.jse.2009.11.045

Christensen, R. M. (1982). *Theory of Viscoelasticity*. London: Academic Press. doi: 10.1016/B978-0-12-174252-2.50012-0

Davis, F., and De Vita, R. (2012). A nonlinear constitutive model for stress relaxation in ligaments and tendons. *Ann. Biomed. Eng.* 40, 1–10. doi: 10.1007/s10439-012-0596-2

Dressler, M. R., Butler, D. L., Wenstrup, R., Awad, H. A., Smith, F., and Boivin, G. P. (2002). A potential mechanism for age-related declines in patellar tendon biomechanics. *J. Orthop. Res.* 20, 1315–1322. doi: 10.1016/S0736-0266(02)00052-9

Elliott, D. M., Robinson, P. S., Gimbel, J. A., Sarver, J. J., Abboud, J. A., Iozzo, R. V., et al. (2003). Effect of altered matrix proteins on quasilinear viscoelastic properties in transgenic mouse tail tendons. *Ann. Biomed. Eng.* 31, 599–605. doi: 10.1114/1.1567282

Fagerland, M. W. (2012). T-tests, non-parametric tests, and large studies-a paradox of statistical practice? *BMC Med. Res. Methodol.* 12:78. doi: 10.1186/1471-2288-12-78

Fessel, G., Li, Y. F., Diederich, V., Guizar-Sicairos, M., Schneider, P., Sell, D. R., et al. (2014). Advanced glycation end-products reduce collagen molecular sliding to affect collagen fibril damage mechanisms but not stiffness. *PLoS ONE* 9:e110948. doi: 10.1371/journal.pone.0110948

Ganghoffer, J., Laurent, C., Maurice, G., Rahouadj, R., and Wang, X. (2016). Nonlinear viscous behaviour of the tendon's fascicles from the homogenization of viscoelastic collagen fibers. *Eur. J. Mechan. A Solids* 59, 265–279. doi: 10.1016/j.euromechsol.2016.04.006

Gautieri, A., Passini, F. S., Silvan, U., Guizar-Sicairos, M., Carimati, G., Volpi, G., et al. (2017). Advanced glycation end-products: mechanics of aged collagen from molecule to tissue. *Matrix Biol.* 59, 95–108. doi: 10.1016/j.matbio.2016.09.001

Gautieri, A., Vesentini, S., Redaelli, A., and Ballarini, R. (2013). Modeling and measuring visco-elastic properties: from collagen molecules to collagen fibrils. *Int. J. Nonlinear Mech.* 56, 25–33. doi: 10.1016/j.ijnonlinmec.2013.03.012

Ge, S. M., Alnaif, N., Azzi, A. J., and Zadeh, T. (2018). Ligaments vs tendons in joint reconstruction: a review of histology and biomechanics. *Muschle Ligaments Tendons* 8, 246–254. doi: 10.32098/mltj.02.2018.14

Gentleman, E., Lay, A. N., Dickerson, D. A., Nauman, E. A., and Livesay, G. A., Dee, K. C. (2004). Mechanical characterization of collagen fibers and scaffolds for tissue engineering. *Biomaterials* 24, 3805–3813. doi: 10.1016/S0142-9612(03)00206-0

Goh, K. L., Holmes, D. F., Lu, H. Y., Richardson, S., Kadler, K. E., Purslow, P. P., et al. (2008). Ageing changes in the tensile properties of tendons: influence of collagen fibril volume fraction. *J. Biomech. Eng.* 130:021011. doi: 10.1115/1.2898732

Hansen, P., Haraldsson, B. T., Aagaard, P., Kovanen, V., Avery, N. C., Qvortrup, K., et al. (2010). Lower strength of the human posterior patellar tendon seems unrelated to mature collagen crosslinking and fibril morphology. *J. Appl. Physiol.* 108, 47–52. doi: 10.1152/japplphysiol.00944.2009

Karathanasopoulos, N., Angelikopoulos, P., Papadimitriou, C., and Koumoutsakos, P. (2017). Bayesian identification of the tendon fascicle's structural composition using finite element models for helical geometries. *Computer Methods Appl. Mech. Eng.* 313, 744–758. doi: 10.1016/j.cma.2016.10.024

Karathanasopoulos, N., Arampatzis, G., and Ganghoffer, J.-F. (2019). Unravelling the viscoelastic, buffer-like mechanical behaviour of tendons: a numerical quantitative study at the fibril-fiber scale. *J. Mech. Behav. Biomed. Mater.* 90, 256–263. doi: 10.1016/j.jmbbm.2018.10.019

Karathanasopoulos, N., and Ganghoffer, J.-F. (2019a). Exploiting viscoelastic experimental observations and numerical simulations to infer biomimetic artificial tendon fiber designs. *Front. Bioeng. Biotechnol.* 7:85. doi: 10.3389/fbioe.2019.00085

Karathanasopoulos, N., and Hadjidoukas, P. (2019b). TendonMech: an open source high performance code to compute the mechanical behavior of tendon fascicles. *SoftwareX* 9, 324–327. doi: 10.1016/j.softx.2019.04.007

Kato, Y. P., Christiansen, D. L., Hahn, R. A., Shieh, S. J., and Goldstein, J. D., Silver, F. H. (1989). Mechanical properties of collagen fibres: a comparison of reconstituted and rat tail tendon fibers. *Biomaterials* 10, 32–42. doi: 10.1016/0142-9612(89)90007-0

Lakes, R. S. (2009). *Viscoelastic Materials*. Cambridge, UK: Cambridge University Press. doi: 10.1017/CBO9780511626722

Lavagnino, M., Arnoczky, S. P., and Frank, K., Tian, T. (2005). Collagen fibril diameter distribution does not reflect changes in the mechanical properties of *in vitro* stress- deprived tendons. *J. Biomech.* 38, 69–75. doi: 10.1016/j.jbiomech.2004.03.035

Legerlotz, K., Riley, G. P., and Screen, H. R. C. (2013). GAG depletion increases the stress-relaxation response of tendon fascicles, but does not influence recovery. *Acta Biomater.* 9, 6860–6866. doi: 10.1016/j.actbio.2013.02.028

Li, Y., Fessel, G., Georgiadis, M., and Snedeker, J. G. (2013). Advanced glycation end-products diminish tendon collagen fiber sliding. *Matrix Biol.* 32, 169–177. doi: 10.1016/j.matbio.2013.01.003

Maceri, F., Marino, M., and Vairo, G. (2012). An insight on multiscale tendon modeling in muscle-tendon integrated behaviour. *Biomech. Model. Mechanobiol.* 11, 505–517. doi: 10.1007/s10237-011-0329-8

Machiraju, C., Phan, A.-V., Pearsall, A. W., and Madanagopal, S. (2006). Viscoelastic studies of human subscapularis tendon: relaxation test and a wiechert model. *Computer Methods Programs Biomed.* 83, 29–33. doi: 10.1016/j.cmpb.2006.05.004

Nair, A. K., Gautieri, A., and Buehler, M. J. (2014). Role of intrafibrillar collagen mineralization in defining the compressive properties of nascent bone. *Biomacromolecules* 15, 2494–2500. doi: 10.1021/bm5003416

Natali, A. N., Audenino, A. L., Artibani, W., Fontanella, C. G., Carniel, E. L., and Zanetti, E. M. (2015). Bladder tissue biomechanical behavior: experimental tests and constitutive formulation. *J. Biomechan.* 48, 3088–3096. doi: 10.1016/j.jbiomech.2015.07.021

Salathe, E., and Arangio, G. (1990). The foot as a shock absorber. *J. Biomech.* 23, 655–659. doi: 10.1016/0021-9290(90)90165-Y

Sandri, M., Filardo, G., Kon, E., Panseri, S., Montesi, M., Iafisco, M., et al. (2016). Fabrication and pilot *in vivo* study of a collagen-BDDGE-elastin core-shell scaffold for tendon regeneration. *Front. Bioeng. Biotechnol.* 4:52. doi: 10.3389/fbioe.2016.00052

Screen, H. R. C. (2008). Investigating load relaxation mechanics in tendon. *J. Mech. Behav. Biomed. Mater.* 1, 51–58. doi: 10.1016/j.jmbbm.2007.03.002

Shen, Z. L., Kahn, H., Ballarini, R., and Eppell, S. J. (2011). Viscoelastic properties of isolated collagen fibrils. *Biophys. J.* 100, 3008–3015. doi: 10.1016/j.bpj.2011.04.052

Snedeker, J., and Foolen, J. (2017). Tendon injury and repair—a perspective on the basic mechanisms of tendon disease and future clinical therapy. *Acta Biomater.* 63, 18–36. doi: 10.1016/j.actbio.2017.08.032

Snedeker, J. G., and Gautieri, A. (2014). The role of collagen crosslinks in ageing and diabetes—the good, the bad, and the ugly. *Muscles Ligaments Tendons J.* 4, 303–308. doi: 10.32098/mltj.03.2014.07

Svensson, R. B., Hassenkam, T., and Grant, C. A., Magnusson, S. P. (2010). Tensile properties of human collagen fibrils and fascicles are insensitive to environmental salts. *Biophys. J.* 99, 4020–4027. doi: 10.1016/j.bpj.2010.11.018

Taylor, R. L., Pister, K. S., and Goudreau, G. L. (1970). Thermomechanical analysis of viscoelastic solids. *Int. J. Numerical Methods Eng.* 2, 45–59. doi: 10.1002/nme.1620020106

Vesentini, S., Redaelli, A., and Gautieri, A. (2013). Nanomechanics of collagen microfibrils. *Muscles Ligaments Tendons J.* 3, 23–34. doi: 10.32098/mltj.01.2013.05

Zanetti, E. M., Perrini, M., Bignardi, C., and Audenino, A. L. (2012). Bladder tissue passive response to monotonic and cyclic loading. *Biorheology* 49, 49–63. doi: 10.3233/BIR-2012-0604

Zhang, Z. J., Ng, G. Y.-F., and Lee, W. C., Fu, S. N. (2014). Changes in morphological and elastic properties of patellar tendon in athletes with unilateral patellar tendinopathy and their relationships with pain and functional disability. *PLoS ONE* 9:e108337. doi: 10.1371/journal.pone.0108337

Conflict of Interest Statement: The authors declare that the research was conducted in the absence of any commercial or financial relationships that could be construed as a potential conflict of interest.

frontiers in Bioengineering and Biotechnology

REVIEW
published: 31 May 2019
doi: 10.3389/fbioe.2019.00111

Biomechanical Investigation of Disturbed Hemodynamics-Induced Tissue Degeneration in Abdominal Aortic Aneurysms Using Computational and Experimental Techniques

Huseyin Enes Salman[1†], *Burcu Ramazanli*[2†], *Mehmet Metin Yavuz*[2*] and *Huseyin Cagatay Yalcin*[1*]

[1] Biomedical Research Center, Qatar University, Doha, Qatar, [2] Department of Mechanical Engineering, Middle East Technical University, Ankara, Turkey

OPEN ACCESS

Edited by:
Khashayar Khoshmanesh,
RMIT University, Australia

Reviewed by:
Seungik Baek,
Michigan State University,
United States
Nenad Filipovic,
University of Kragujevac, Serbia

***Correspondence:**
Mehmet Metin Yavuz
ymetin@metu.edu.tr
Huseyin Cagatay Yalcin
hyalcin@qu.edu.qa

[†]These authors have contributed equally to this work

Specialty section:
This article was submitted to Biomechanics, a section of the journal Frontiers in Bioengineering and Biotechnology

Received: 24 February 2019
Accepted: 02 May 2019
Published: 31 May 2019

Citation:
Salman HE, Ramazanli B, Yavuz MM and Yalcin HC (2019) Biomechanical Investigation of Disturbed Hemodynamics-Induced Tissue Degeneration in Abdominal Aortic Aneurysms Using Computational and Experimental Techniques. Front. Bioeng. Biotechnol. 7:111. doi: 10.3389/fbioe.2019.00111

Abdominal aortic aneurysm (AAA) is the dilatation of the aorta beyond 50% of the normal vessel diameter. It is reported that 4–8% of men and 0.5–1% of women above 50 years of age bear an AAA and it accounts for ∼15,000 deaths per year in the United States alone. If left untreated, AAA might gradually expand until rupture; the most catastrophic complication of the aneurysmal disease that is accompanied by a striking overall mortality of 80%. The precise mechanisms leading to AAA rupture remains unclear. Therefore, characterization of disturbed hemodynamics within AAAs will help to understand the mechanobiological development of the condition which will contribute to novel therapies for the condition. Due to geometrical complexities, it is challenging to directly quantify disturbed flows for AAAs clinically. Two other approaches for this investigation are computational modeling and experimental flow measurement. In computational modeling, the problem is first defined mathematically, and the solution is approximated with numerical techniques to get characteristics of flow. In experimental flow measurement, once the setup providing physiological flow pattern in a phantom geometry is constructed, velocity measurement system such as particle image velocimetry (PIV) enables characterization of the flow. We witness increasing number of applications of these complimentary approaches for AAA investigations in recent years. In this paper, we outline the details of computational modeling procedures and experimental settings and summarize important findings from recent studies, which will help researchers for AAA investigations and rupture mechanics.

Keywords: abdominal aortic aneurysm, rupture risk assessment, finite element analysis, computational fluid dynamics, fluid-structure interaction, particle image velocimetry, hemodynamics, experimental fluid mechanics

INTRODUCTION

Abdominal aortic aneurysm (AAA) is the dilatation of the abdominal aorta beyond 50% of the normal vessel diameter, due to degeneration of the arterial wall (McGloughlin Timothy and Doyle Barry, 2010). It is reported that 4–8% of men and 0.5–1% of women above 50 years of age bear an AAA and it accounts for ∼15,000 deaths per year in the United States alone (Sakalihasan et al., 2005; Kontopodis et al., 2014). AAA may result in rupture of the vessel wall, which is a fatal surgical emergency because of reduced blood flow to vital organs and hematocele (i.e., swelling caused by blood collecting in a body cavity). AAA rupture is the most catastrophic complication of the aneurysmal disease that is accompanied by a striking overall mortality of 80% (Bengtsson and Bergqvist, 1993). Unfortunately, clinical symptoms for impending AAA rupture are not observed for nearly 75% of the patients (Anjum et al., 2012).

Current clinical practice is surgical repair if the diameter of the AAA is >5.5 cm or the growth rate is over 1 cm/year and to follow up AAAs with diameters <5.5 cm at 6-month intervals (Cosford and Leng, 2007). It is reported that only 25% of AAAs ruptured in the patient's lifetime (Darling et al., 1977), and 13% of AAAs with a diameter of <5 cm are ruptured. For this reason, AAA diameter is not the sole indicator for the rupture and other factors should also be considered for the rupture risk assessment, together with the size of AAA.

The precise mechanisms leading to AAA rupture remains unclear. From a purely mechanical point of view, rupture of an AAA occurs when the mechanical stresses (i.e., internal forces per unit area) acting on the aneurysm exceeds the ability of the wall tissue to withstand these stresses (i.e., the wall's failure strength). Wall shear stress (i.e., WSS, the frictional force exerted by blood flow on the luminal surface) is also thought to play an important role (Peattie et al., 1996). While the blood flow in normal aorta (diameter within 2–2.5 cm) is mainly anterograde with high WSS, during AAA, circulatory flows emerge within the vessel. Hence, flow becomes disturbed with oscillatory characteristics leading to low WSS (Tanweer et al., 2014). The disturbance of flow in AAA is believed to contribute to the progression of the disease by activating the inflammatory markers of the endothelial cells lining the vessel wall which might lead to degeneration and weakening of the vessel wall (Franck et al., 2013). Therefore, prediction of the growth course of an AAA and precise determination of the rupture risk is a very challenging problem and attracts substantial attention.

Currently, there is no established conclusive approach for AAA rupture risk assessment, rather than the limited clinical guidelines for the AAA size. Ideally, the problem needs to be investigated from a biomechanical point of view, for a comprehensive wall stress, wall strength, and hemodynamic analyses. Computational modeling based on finite element analysis (FEA) is a powerful technique for estimating mechanical behavior of materials (i.e., mechanical behavior is the amount of stresses and deformations in a substance under external forces). This is especially beneficial in medical research where in most cases direct measurement of *in-vivo* mechanical response of diseased tissue is not possible. In this technique, first an accurate representation of the problem geometry is generated. The second step is defining the conditions in the model boundaries. The third step is defining different zones in the geometry, and assigning appropriate material properties for each zone and the fourth step is dividing zones into smaller elements (meshing). The last step is numerically solving appropriate governing equations in each small element to obtain a solution field of interest in the entire geometry. Each of these steps are critically important for solution accuracy.

Computational modeling has been used frequently in recent years to investigate rupture mechanics for AAA tissue. Comparison of ruptured and electively repaired AAA cases via FEA, revealed elevated wall stress levels for ruptured tissue (Fillinger et al., 2002). Several observations on excised tissue suggest that AAA formation is accompanied by an increase in wall stress as well as a corresponding decrease in wall strength (Vorp et al., 1996; Raghavan et al., 2000) and rupture point on AAA is usually coincides with peak wall stress locations (Fillinger et al., 2002). In very few studies where previous medical images for ruptured AAA tissue were available, patient-specific FEA could successfully identify known exact future rupture locations as high wall stress regions (Doyle et al., 2014). The FEA results prove the potential significant contribution of computational analysis for rupture risk assessment for AAA.

As computational methods have widely been used in investigation of hemodynamics and mechanical behavior of arterial tissue, the experimental techniques are also utilized in characterization of flow dynamics through AAAs. Both approaches are crucial and complement each other with offering in depth analysis where the level of its intensity and accuracy depend on the assumptions in computational models and simplifications in experimental methods. In line with the aforementioned computational studies, many experimental investigations of the hemodynamics through AAAs have been conducted in literature, and various qualitative and quantitative flow measurement techniques have been utilized for that purpose. A typical experimental set up for the analysis of hemodynamics contains physiological flow circulatory system including pump, piping, and pressure compliance, test section that contains artery model (phantoms), blood mimicking fluid, and flow measurement systems (like particle image velocimetry) to track the movement of fluid particles to calculate the velocities first, and then WSS levels on the phantoms. Previously, this approach has been adapted by several researchers to investigate AAA rupture mechanism (Tanweer et al., 2014; Wang et al., 2016).

In this paper, we will summarize the techniques utilized in experimental and computational studies of AAAs. We will briefly explain important aspects of the modeling procedure and how to set up and run relevant simulations and also, how to generate a flow circulation set up with particle image velocimetry (PIV). In addition, we will summarize important findings for experimental and computational biomechanical assessments of AAAs.

COMPUTATIONAL INVESTIGATION OF BIOMECHANICS OF AAAs

Computational models enable researchers to approximate biomechanical behavior of tissue stress and blood flow hemodynamics under realistic conditions. The models are generated by defining the conditions on the boundaries and numerically solving governing equations in fluid and solid domains. Generation of the problem geometry, setting up solid and fluid models, coupling the solutions through FSI procedure are important steps which contribute to enhance the reliability and accuracy of the biomechanical assessment as will be mentioned in the forthcoming sections.

Mathematical Details of the Problem

Geometry of the Problem

AAA has unique, patient-specific and complex geometry with a wall thickness around 1.5 mm (Raghavan et al., 2004) and mostly does not represent an axisymmetric form. Healthy abdominal aortic diameter is around 2 cm and in case of dilatation, AAA diameter can expand up to 9 cm. Proximal AAA neck angle, distal iliac bifurcation angle, heterogeneous wall thickness are patient-specific geometric parameters. Left and right renal arteries, left and right iliac arteries and superior mesenteric artery are the main branching arteries in abdominal aorta. In **Figure 1**, different patient-specific AAA geometries, branching arteries and disturbed flow in AAA sac are presented.

Main geometric parameters for a patient-specific AAA are presented in **Figure 2**. The AAA asymmetry is defined using the relation defined by Vorp et al. (1998). β is the parameter of asymmetry defined according to the central axis of undilated diameter, as shown in **Figure 2**. In Equation (1), r and R are the radii measured from center of the undilated portion to the posterior and anterior walls, respectively.

$$\beta = \frac{r}{R} \tag{1}$$

In addition to the maximum aneurysm diameter, tortuosity, curvature, proximal neck angle, iliac bifurcation angle, and complex shape of the aneurysm itself are influencing factors on the wall stress (Stringfellow et al., 1987; Vorp et al., 1998; Hua and Mower, 2001). Up to 80% of AAA rupture are observed on the posterior wall (Darling et al., 1977), demonstrating the importance of asymmetry and curved AAA geometry in rupture. Loss of curvature on the posterior wall and AAA asymmetry are suggested as dominant wall stress increasing factors (Scotti et al., 2008).

Generation of Model Geometry

Magnetic resonance imaging (MRI), three-dimensional (3D) ultrasound, computerized tomography (CT) are the most common medical imaging techniques used to extract the realistic geometry of AAAs. At present, primary imaging method is CT. However, due to its high cost, significant radiation dose, injection of ionated contrast medium associated with nephrotoxity and relatively less availability, alternative methods such as 3D ultrasound can be used to widespread the biomechanical assessments.

After obtaining patient-specific medical images in DICOM (Digital Imaging and Communications in Medicine) format, 3D AAA models can be reconstructed using segmentation software such as MIMICS (Materialize, Leuven, Belgium), VESSEG (Carniege Mellon University, Pittsburgh, PA), ImFusion Suite (ImFusion GmbH, Munich, Germany), and open-source software such as SimVascular, VMTK, and ITK-SNAP. Lumen and AAA wall are segmented separately to differentiate these zones. Segmented 3D model might include protrusions and tight internal corners, which requires application of smoothing algorithms, to prepare a suitable geometry for FEA simulations. Autodesk MeshMixer, AngioLab, and MeshLab softwares can be used for further smoothing and mesh optimization processes. For smoothing process, different algorithms can be applied such as Laplacian (Field, 1988), HC Laplacian (Vollmer et al., 2001), and Taubin's low pass filter (Taubin, 1995). In **Figure 3**, the reconstruction procedure of a patient-specific AAA model is given.

Governing Equations in Solid Domain

The governing equation in solid domain is the momentum conservation given in Equation (2) (Scotti et al., 2008).

$$\nabla . \boldsymbol{\tau}_s + \mathbf{f}_s^B = \rho_s \ddot{\mathbf{d}}_s \tag{2}$$

In Equation (2), $\boldsymbol{\tau}_s$ is solid stress tensor; $\mathbf{f}_s^B$ is body forces term per unit volume; ρ_s is AAA wall mass density; and $\ddot{\mathbf{d}}_s$ is local acceleration of solid. Lagrangian description is typically used to track the deformation of the solid domain (Donea et al., 1982; Bathe and Zhang, 2004). Neglecting the gravitational forces ($\mathbf{f}_s^B$) is a commonly used approach due to their insignificant effect on wall stresses (Wolters et al., 2005).

Important Stress Parameters for Solid Domain

For the solid domain, principal wall stresses (σ_1, σ_2, σ_3), Von Mises stress and wall displacements are critical parameters for AAA rupture risk assessment. The peak wall stresses are better indicators when compared to the maximum AAA diameter, since rupture is the mechanical failure of the wall where the strength of wall is not sufficient to withstand the peak wall stress (Fillinger et al., 2003; Wolters et al., 2005). Von Mises stress is a measure used for failure prediction based on three principal stresses as given in Equation (3).

$$\frac{1}{2}\left[(\sigma_1 - \sigma_2)^2 + (\sigma_2 - \sigma_3)^2 + (\sigma_3 - \sigma_1)^2\right] > {\sigma_y}^2 \tag{3}$$

In Equation (3), the term in the left side is square of Von Mises stress, σ_i is the local principal stress and σ_y is the uniaxial failure strength of the wall (Scotti et al., 2008).

Incorporation of Intraluminal Thrombus (ILT) to the Models

In solid domain, the presence of intraluminal thrombus (ILT) is an influencing factor for the wall stress depending on its shape,

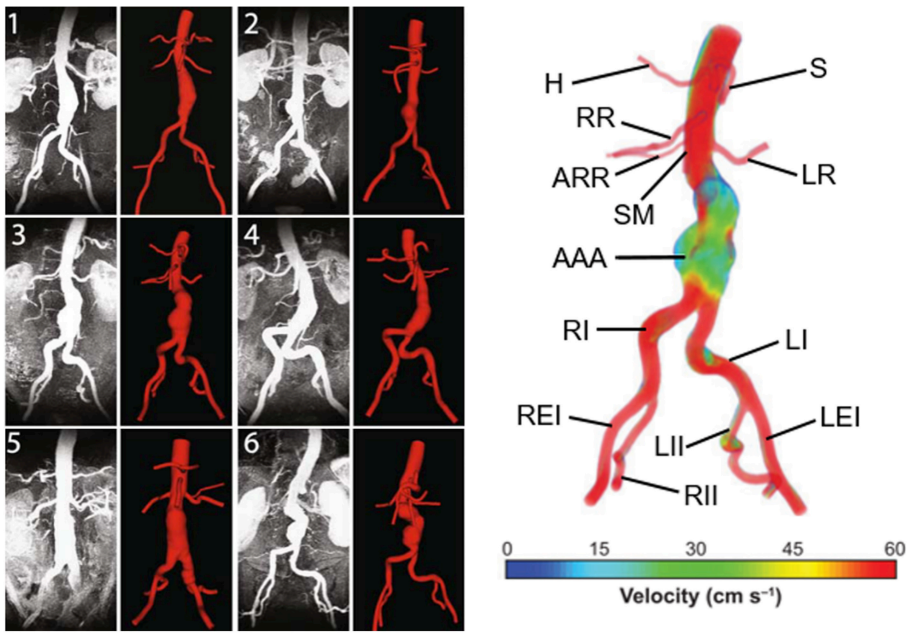

FIGURE 1 | Six different patient-specific medical images and corresponding reconstructed AAA geometries. The branching arteries and disturbed AAA flow in the 3rd patient-specific medical image are described at the right side. Compared to undilated vessel, the flow hemodynamics in the AAA sac changed significantly. The artery labels are as follows: H, Hepatic artery; S, Splenic artery; RR, Right renal artery; ARR, Accessory right renal artery; SM, Superior mesenteric artery; LR, Left renal artery; AAA, Abdominal aortic aneurysm; RI, Right iliac artery; LI, Left iliac artery; REI, Right external iliac artery; RII, Right internal iliac artery; LII, Left internal iliac artery; LEI, Left external iliac artery [The figure is adapted from Les et al. (2010) and used with permission].

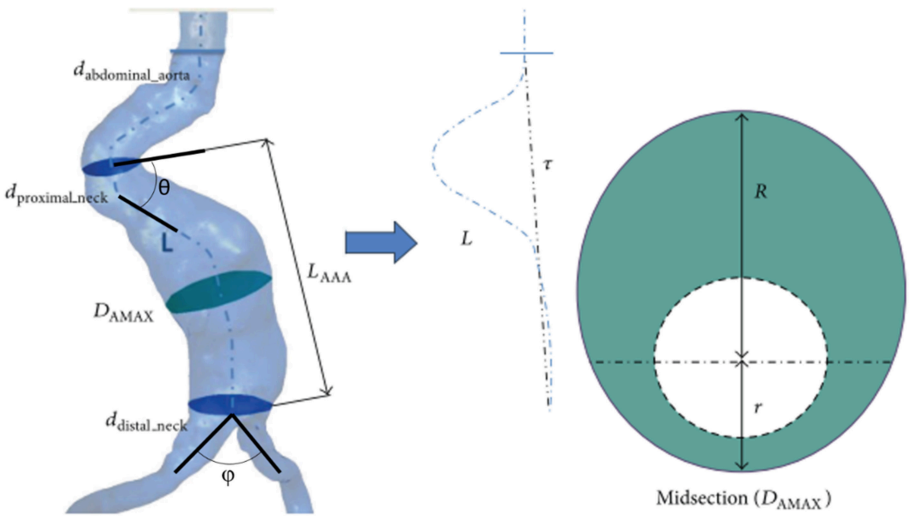

FIGURE 2 | Main geometric parameters for a patient-specific AAA geometry. L_{AAA}, Aneurysm length; D_{AMAX}, Maximum aneurysm diameter; $d_{proximal\_neck}$, Inlet diameter of AAA sac; d_{distal_neck}, Outlet diameter of AAA sac; $d_{abdominal\_aorta}$, Normal abdominal aorta diameter; θ, Proximal neck angle; ϕ, Iliac bifurcation angle; L, Absolute length of tortuous vessel; τ, Imaginary straight line starting at the center of normal abdominal aorta and ending at the iliac bifurcation. The midsection at the location of the maximum AAA diameter (D_{AMAX}) is represented at the right side. At the maximum diameter midsection, r and R are the radii measured from center of the undilated portion (i.e., normal abdominal aorta) to the posterior and anterior walls, respectively [The figure is adapted from Soudah et al. (2013) and used with permission].

size, and material properties (Mower et al., 1997; Di Martino et al., 1998; Di Martino and Vorp, 2003). Flow hemodynamics is also closely related with the ILT formation on AAA wall. ILT contains immune and inflammatory response agents affecting the evolution of the disease (Adolph et al., 1997). In a related clinical study, ILT is observed near the site of rupture for

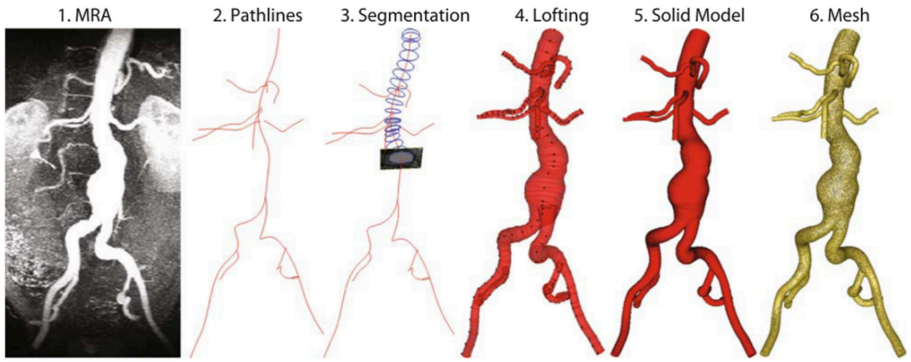

FIGURE 3 | Reconstruction procedure for a patient-specific AAA model [The figure is adapted from Les et al. (2010) and used with permission].

80% of the autopsies (Simão da Silva et al., 2000), as being a source of proteolytic activity, local wall thinning, wall weakening, and hypoxia (Swedenborg and Eriksson, 2006; Houard et al., 2007). ILT morphology can exhibit a layered structural material behavior or fluid-like homogeneous medium. It becomes a poroelastic material at a certain state of maturity which is affecting blood transport (Tong and Holzapfel, 2015). Flow stagnation and associated low WSS, high residence time of platelets and monocytes in AAA sac contribute to high potential of wall-cell adhesion forming ILT (Kelsey et al., 2016). In a recent study, Di Achille et al. (2016) predicted ILT formation and progression sites in patient-specific AAA models, using a phenomenological metric of thrombus deposition potential which is indicating a balance between the thrombogenicity and hemodynamic shear forces on the wall. The relative overlap between predicted and actual thrombus covered areas in six patient-specific AAA models was reported around 80 ± 16% (Di Achille et al., 2016). Therefore, ILT formations on vessel walls should be assigned with appropriate material constants with accurate geometric representations for model accuracy since ILT significantly affects both the wall mechanics and flow hemodynamics, indicating the importance of interactions between solid and fluid domains.

Wall Material Properties

Aorta consists of three layers: the intima, media, and adventitia (Lasheras, 2006). Intima and adventitia are the inner and outer layers, respectively. The distribution of layer thicknesses has a ratio about 20:47:33 for intima: media: adventitia (Humphrey and Holzapfel, 2012). Elastic modulus ratio for intima: media: adventitia is ∼1:3:2 (Khanafer and Berguer, 2009; Gao et al., 2013). The highest stresses are observed in the media layer due to the normal pressure of cyclic flow (Simsek and Kwon, 2015). The maximum wall deformation can reach up to 2.2 mm at the systolic phase (Canchi et al., 2018). One of the possible reasons of AAA formation is reported as the medial loss in the arterial wall with degeneration of smooth muscle cells (Humphrey and Taylor, 2008). In case of AAA wall weakening depending on the media loss, elastic modulus of the media layer can be reduced by 20 times (Feng et al., 2008). Modeling AAA wall as a single-layered structure is a commonly used approach for simplification of the problem.

Governing Equations in Fluid Domain

Flow velocity, pressure and wall shear stress (WSS) exerted by fluid viscous forces are determined by solving the Navier-Stokes and continuity equations. For an incompressible and homogeneous fluid, the Navier-Stokes equations can be defined using the Arbitrary Lagrangian Eulerian (ALE) description given in Equation (4) and continuity equation given in Equation (5) (Donea et al., 1982; Zhang et al., 2003; Scotti and Finol, 2007).

$$\rho_f \frac{\partial \mathbf{v}}{\partial t} + \rho_f (\mathbf{v} - \mathbf{w}) \cdot \nabla \mathbf{v} - \nabla \cdot \tau_f = \mathbf{f}_f^B \quad (4)$$

$$\nabla \cdot \mathbf{v} = 0 \quad (5)$$

The fluid velocity vector is denoted by $\mathbf{v}$; time is denoted by t; the velocity of the fluid domain (i.e., moving coordinate velocity primarily due to FSI) is denoted by $\mathbf{w}$; fluid stress tensor is denoted by $\boldsymbol{\tau}_f$; and body forces term is denoted by $\mathbf{f}_f^B$. The fluid stress tensor ($\boldsymbol{\tau}_f$) is defined in Equation (6), in terms of fluid pressure (p), Kronecker delta (δ_{ij}), dynamic viscosity (μ), and strain rate (ε_{ij}). The strain rate can be written in terms of velocity vector ($\mathbf{v}$), as given in Equation (7). The effect of gravitational acceleration is not critical and the body forces on the fluid ($\mathbf{f}_f^B$) can be neglected (Scotti et al., 2008).

$$\boldsymbol{\tau}_f = -p\delta_{ij} + 2\mu\varepsilon_{ij} \quad (6)$$

$$\varepsilon_{ij} = \frac{1}{2}\left(\nabla \mathbf{v} + \nabla \mathbf{v}^T\right) \quad (7)$$

Important Hemodynamic Parameters for Fluid Domain

In fluid domain, wall shear stress (WSS), oscillatory shear index (OSI), intraluminal pressure, flow path, and flow velocity are of main interest. Due to complex AAA geometries, WSS has spatially and temporally complicated distributions (Arzani and Shadden, 2015). WSS is a measure of flow-driven tangential

forces per unit area on the AAA wall. The magnitude of WSS at the fluid-structure interface can be determined by multiplying the viscosity (μ) with the local shear rate ($\dot{\gamma}$) (Wolters et al., 2005). In large arteries, WSS amplitudes typically range from 1 to 5 Pa, therefore WSS values smaller than 1 Pa are evaluated as low WSS (Ene-Iordache and Remuzzi, 2012; Qiu et al., 2018). Time averaged WSS (TAWSS) can be determined as given in Equation (8) where T is the integration period (Arzani et al., 2014; Arzani, 2018).

$$TAWSS = \frac{1}{T}\int_{t-T}^{t} |WSS|\, dt \tag{8}$$

OSI is a measure defining the unidirectionality of shear stress which is sensitive to turbulence and it can be determined as given in Equation (9) (Arzani et al., 2017).

$$OSI = \frac{1}{2}\left(1 - \frac{\left|\frac{1}{T}\int_{t-T}^{t} WSS dt\right|}{\frac{1}{T}\int_{t-T}^{t} |WSS|\, dt}\right) \tag{9}$$

When OSI is zero, it is indicating that shear stress is unidirectional. If OSI is 0.5, it means that time average of shear stress is zero. Endothelial cell activation potential (ECAP) is the ratio of OSI and TAWSS as given in Equation (10). ECAP is used to characterize ILT susceptibility on AAA wall (Di Achille et al., 2014). Critical threshold value of ECAP is stated as 1.4 Pa^{-1}, where above this value, there is a high potential of ILT formation (Kelsey et al., 2016). Therefore, as ECAP increases due to emergence of circulatory flows in diseased states, there is a higher chance of wall inflammation.

$$ECAP = \frac{OSI}{TAWSS} \tag{10}$$

Fluid Properties and Flow Regime

Blood has non-Newtonian characteristics where the viscosity decreases with increased shear rate. AAA flow is inherently pulsatile and has a turbulent nature particularly at mid-diastolic phase. At the systolic phase, peak blood flow velocity in AAA can reach up to 20 cm/s (Casciaro et al., 2018). Larger aneurysmal diameters lead to higher turbulence intensity and large recirculating vortices increasing the blood residence time in the aneurysm sac, particularly at the diastolic phase of the physiological pulsatile flow (Khanafer et al., 2007).

In many studies, AAA flow is considered as unsteady laminar flow (Scotti et al., 2008; Chandra et al., 2013; Morris et al., 2013; Soudah et al., 2013; Owen et al., 2016) due to not exceeding the threshold Reynolds number (2000–2300) for transition to turbulence in pipe flow. However, complex flow geometry, sudden lumen expansion in AAA sac and pulsatile nature of flow are the factors that might trigger the turbulence in low Reynolds numbers (Poelma et al., 2015). In order to resolve the turbulent effects accurately, Les et al. (2010) and Arzani et al. (2014) applied more demanding direct numerical simulation (DNS) approach, and Khanafer et al. (2007) used k-ω turbulence model.

Biochemical Transport

Oxygen (Sun et al., 2009), low density lipoproteins (Choudhury et al., 2019), and chemical species transported by blood flow have an influence on the AAA progression and ILT formation on the wall. Shear rate is an Eulerian measure that cannot quantify particle transport (Shadden and Arzani, 2015). Locally high surface concentration of chemical species are not always corresponds to the regions with low WSS that are determined using Eulerian mass transport (Choudhury et al., 2019). The residence time and flow path of the micro-particles can be determined using Lagrangian mass transport (Arzani et al., 2014, 2017). By this way, the particles in the blood flow can be tracked and their interaction with AAA wall can be modeled using convection, diffusion, and reaction equations coupled with the computed flow field (Biasetti et al., 2012). These fluid-chemical models provide better insight to understand AAA and ILT pathophysiology.

Setting Up and Solution of the Solid Domain via FEA

Defining Material Constants

AAA wall has hyperelastic (i.e., non-linear stress-strain behavior), viscoelastic (i.e., time varying response due to relaxation) and anisotropic (i.e., direction dependent) material properties due to its layered and fiber-oriented structure (Vande Geest et al., 2006a,b). In order to determine the wall deformation and stress in a reliable manner, constitutive equations are needed to model wall stress-strain behavior. As a first approximation, AAA wall can be modeled as a linearly elastic, homogeneous medium using elastic modulus of 2.7 MPa, Poisson's ratio of 0.45, and mass density of 2,000 kg/m^3 (Di Martino et al., 2001). For improved accuracy, non-linear stress-strain behavior should be taken into account using hyperelastic models (Scotti et al., 2008). Raghavan and Vorp (2000) obtained an experimental fit for non-linear stress-strain curve of AAA wall. Experimental data can be represented using Mooney-Rivlin hyperelastic material model considering a strain energy density function (W_s) given in Equation (11) (Rivlin and Saunders, 1951).

$$\begin{aligned} W_s = {} & c_{10}(I_1 - 3) + c_{01}(I_2 - 3) + c_{20}(I_1 - 3)^2 + \\ & c_{02}(I_2 - 3)^2 + c_{11}(I_1 - 3)(I_2 - 3) + c_{30}(I_2 - 3)^2 \end{aligned} \tag{11}$$

In Equation (11), I_i is the ith invariant of the left Cauchy-Green tensor, c_{ij} is the material parameter for fitting the experimental data. Chandra et al. (2013) used second order Mooney-Rivlin approach for modeling the AAA wall and ILT as given in Equations (12,13), respectively.

$$W_{wall} = c_{10}(I_1 - 3) + c_{20}(I_1 - 3)^2 \tag{12}$$

$$W_{ILT} = c_{01}(I_2 - 3) + c_{02}(I_2 - 3)^2 \tag{13}$$

Considering the population averages (Raghavan and Vorp, 2000; Vande Geest et al., 2006a,b), material parameters in Equations (12) and (13) are determined as c_{10}=17.4 N/cm^2, c_{20}=188.1 N/cm^2, c_{01}=7.98 N/cm^2, and c_{02}=8.71 N/cm^2. Mass

densities of AAA wall and ILT are assumed to be 1.2 and 1.1 g/cm^3, respectively.

Boundary Conditions in Solid Domain

In general, AAA tissue is isolated by applying zero translation and zero rotation fixed on the inlet and outlet of the solid domain (Scotti et al., 2005). The surrounding branch arteries of aorta produce tethering effect on the AAA model. This tethering effect is reflected to the wall either by using previously described zero displacement and rotation fixed on the inlet and outlet boundaries; or alternatively, an axial stretch can be defined on these solid inlet and outlet boundaries as suggested by Tang et al. (2005), since arterial wall is physiologically under tension in reality (Holzapfel et al., 2000). Scotti et al. (2008) applied 5% axial stretch on the inlet and outlet boundaries of the solid for modeling the tethering effect.

In addition to inlet and outlet boundaries, intra-abdominal pressure and contact of AAA with the surrounding tissues and organs can also be considered for defining boundary conditions (BC) in solid domain. Scotti et al. (2008) applied intra-abdominal pressure of 12 mmHg (Hinnen et al., 2005) on the outer AAA wall. In reality, AAA is located along the spinal column and there is a certain physical contact between AAA and spinal column which provides additional support on the posterior wall. This can be modeled with an additional BC on the posterior wall by fixing the contact surface with zero displacement (Scotti et al., 2008).

If solid FEA model is not coupled with a flow domain, then intraluminal pressure BC is applied on the inner AAA wall as a steady or transient load. This analysis is also known as computational solid stress (CSS) approach. In case of a FSI simulation, in which the solid FEA model is coupled with a flow domain, inner AAA wall is set as a FSI boundary surface.

Setting Up and Solution of the Fluid Domain Via Computational Fluid Dynamics

Modeling Non-Newtonian Fluid Viscosity

Computational fluid dynamics (CFD) simulations are performed to numerically determine the flow variables such as flow velocity, pressure and WSS by modeling the fluid viscosity. Newtonian fluids have constant viscosity, but for non-Newtonian fluids such as blood, the viscosity changes as function of shear rate. For large arteries, the shear strain rate in the flow exceeds 50 s^{-1} and the viscosity demonstrates nearly constant behavior depending on the high shear rate (Young, 1979). Therefore, modeling the blood as a Newtonian fluid is a common approach for the AAA flow. Recently, Arzani (2018) reported that blood residence time affects the viscosity and traditional non-Newtonian models may exaggerate the shear-dependent viscosity behavior of blood, thus it is recommended to use Newtonian models if minor portion of AAA is accompanied by high blood residence time.

Blood mass density is usually taken as 1.05 g/cm^3 with a constant dynamic viscosity (μ) of 0.035 Poise (Chandra et al., 2013). Khanafer et al. (2006) compared Newtonian and non-Newtonian fluid models for the same AAA geometry and stated that the maximum pressure and maximum WSS differences were 2.53 and 26.7%, respectively. The higher difference in maximum WSS is due to the effect of near-wall turbulence which is underestimated by Newtonian models. Non-Newtonian behavior of blood can be modeled using Carreau-Yasuda viscosity model parameters given in Equation (14).

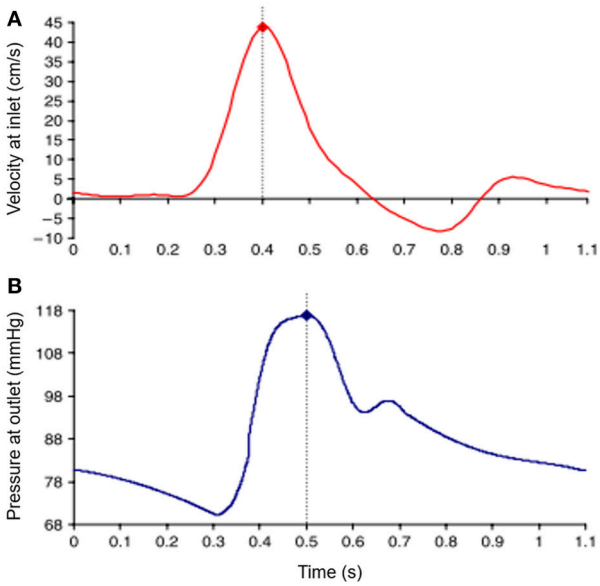

FIGURE 4 | Waveforms of applied boundary conditions at the inlet and the outlet of the fluid domain. Dash lines show the moment of peak values in the waveforms. **(A)** Sample inlet flow velocity profile. **(B)** Sample outlet pressure profile [The figure is adapted from Scotti et al. (2008) and used with permission].

$$\eta(\dot{\gamma}) = \eta_\infty + (\eta_0 - \eta_\infty)\left[1 + (\lambda\dot{\gamma})^a\right]^{(n-1)/a} \quad (14)$$

In Equation (14), $\dot{\gamma}$ is shear rate, η is shear rate dependent viscosity, η_∞ is viscosity at high shear rate, η_0 is viscosity at low shear rate, and λ, a, n are empirical constants. By approximating the blood viscosity measurements of Thurston (1979), empirical parameters yield as η_∞=0.00476 Pa s, η_0=0.0519 Pa s, a=0.409, n=0.191, and λ=0.438s.

Fluid Domain Boundary Conditions

Inlet and outlet BC are defined considering the physiological pulsatile flow. Commonly, time-varying flow velocity given in **Figure 4A** is defined at the inlet of fluid domain and time-varying intraluminal pressure given in **Figure 4B** is prescribed at the outlet (Scotti et al., 2008). No slip BC is applied on the wall considering the viscous blood flow.

The time-dependent inlet flow rate given in **Figure 4A** can be applied considering different velocity profiles. Applying plug velocity profile is the simplest approach where the axial flow velocity is uniform through the inlet boundary surface (Bluestein et al., 2009). Alternatively, fully developed velocity profile can be used considering Womersley profile which has zero velocity on the wall and has a parabolic distribution with maximum flow velocity at the midpoint of the inlet surface, which is more realistic due to including the effect of viscous boundary layer (Womersley, 1955; Papaharilaou et al., 2007). To enhance the

accuracy of the model, patient-specific inlet velocity profiles can also be applied by obtaining realistic profiles non-invasively using phase-contrast magnetic resonance images (PC-MRI) (Kose et al., 2006).

After determining patient-specific inlet BC, distribution of mass flow rate to the branches of mesenteric, renal, and iliac arteries should also be considered, since they are significantly affecting the mass flow rate at the outlet of AAA. One-dimensional arterial tree model can be used to determine appropriate inflow and outflow conditions to better reflect the reality for biological relevance (Formaggia et al., 2003; Wolters et al., 2005). Les et al. (2010) modeled the effect of branch arteries at the downstream vasculature using three-element Windkessel model considering the capacitance, proximal resistance and distal resistance at the downstream. Using PC-MRI scanning, mean flow rates at supraceliac and infrarenal locations are measured as 3.51 and 1.31 L/min, respectively. The difference of 2.2 L/min is distributed to the arterial branches between supraceliac (1 cm above celiac artery) and infrarenal (1 cm below the most distal renal artery) levels (Les et al., 2010). It is reported that using zero-pressure outlet BC is not sufficient, and Windkessel BC provides more realistic flow and pressure features.

For determining patient-specific outlet pressure BC, a catheter can be placed inside AAA sac, however this invasive procedure is not preferred by clinicians during AAA repair (Chandra et al., 2013). Alternatively, a non-invasive method can be applied to obtain patient-specific outlet pressure. van 't Veer et al. (2008) compared non-invasive brachial cuff blood pressure measurements with invasive catheter pressure measurements inside AAA sac. Brachial cuff pressure measurements resulted in 5% underestimation for systolic phase, and 12% overestimation for diastolic phase compared to the intraluminal pressure in AAA. Using these correlations, a patient-specific estimation of fluid outlet pressure can be predicted non-invasively.

Solution and Mesh Independence for Solid and Fluid Domains

Solid and fluid domains are spatially discretized using a generated mesh composed of tetrahedral, hexahedral or polyhedral elements as given in **Figure 5**. In fluid domain, mesh density should be relatively higher in the boundary layers close to the wall and in regions that are expected to have high velocity gradients as well. Obtaining a mesh-independent solution is a requirement prior to the in depth analysis of AAA hemodynamics. Typically, if a relative difference of 2% is achieved for variables obtained by different mesh sizes, the results can be considered as mesh-independent (Kelsey et al., 2016). The quality of CFD mesh resolution can also be checked using the minimum Kolmogorov length scale. For large eddy simulation approach, the ratio of mesh element size to the Kolmogorov length scale should be at most 20 and 40 for fine and coarse fluid meshes, respectively (Celik et al., 2009).

In order to check the mesh-independency of results, solution of first three cardiac cycles should be ignored. Because, periodically converged results are generally obtained after the third cycle. A time step of 0.001 s (~1/1,000th of cardiac cycle) is suitable for obtaining unsteady solutions (Les et al., 2010). If stability problems arise in the analysis, the time step can be decreased to achieve convergence. Courant number ($Co \equiv u\,(t)\,/x$) should be equal or lower than one for the increased stability. The Courant number shows how much information traverses (i.e., Flow velocity, u) the length of a mesh element (x) within a time step (t).

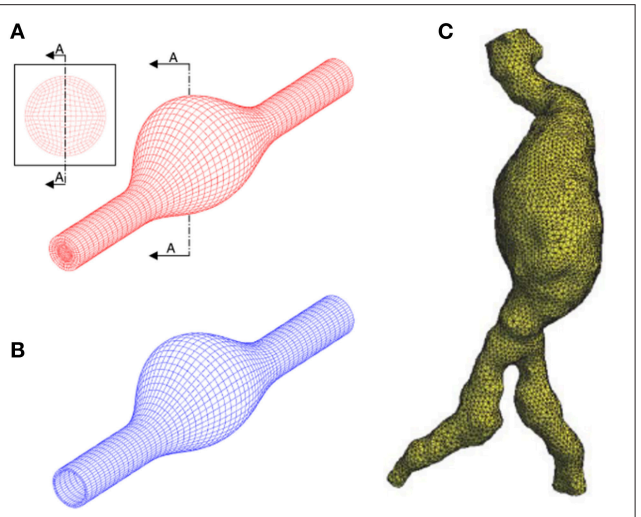

FIGURE 5 | Discretization of the problem domain using finite element meshes. **(A)** Structured hexahedral fluid mesh using idealized AAA model. **(B)** Structured hexahedral solid mesh using idealized AAA model. **(C)** Unstructured tetrahedral fluid mesh using patient-specific AAA model. [**A,B** are adapted from Scotti et al. (2008) and used with permission, **(C)** is adapted from Wolters et al. (2005) and used with permission].

Fluid-Structure Interaction (FSI)

To simulate deformation of AAA tissue under the effect of blood hemodynamics accurately, FSI approach needs to be adapted. This is because of the strong interactions between flowing blood and vessel walls. Blood flow generates unsteady forces on vessel walls that causes deformation of the walls. These deformations in turn influence blood flow patterns. Therefore, vessel wall behavior cannot be predicted accurately if these counter interacting forces are ignored. The commercial software packages such as ANSYS, ADINA, ABAQUS, COMSOL are commonly used for FSI modeling.

FSI modeling can be performed using three different numerical approaches, which are 1-way uncoupled (also known as FEA or CSS), explicit 2-way coupled and implicit 2-way coupled methods. 1-way uncoupled method is a static investigation where spatially uniform or non-uniform intraluminal pressure load is applied to the inner AAA wall without considering the effects of dynamic flow and only provides solid domain parameters such as wall stresses and wall displacements. In a related study (Scotti et al., 2008), it is stated that 1-way uncoupled approach underestimates the maximum wall stress due to neglecting the hemodynamic effects. To have a better understanding, FSI analysis should be performed using 2-way coupled methods. In a numerical investigation, 1-way

uncoupled and 2-way coupled FSI simulations are compared using the same patient-specific AAA model and it is reported that 1-way uncoupled FSI resulted in 14, 4, and 18% difference in peak principle stress (σ_1), principle strain (ε_1), and WSS, respectively (Chandra et al., 2013).

In 2-way coupled methods, a FSI boundary is defined between the blood and AAA wall. On this FSI boundary surface, solutions of solid and fluid domains are coupled considering displacement compatibility and traction equilibrium given in Equations (15,16) (Bathe et al., 1999). On FSI boundary, solid and fluid displacement vectors are denoted by $\mathbf{d}_s$ and $\mathbf{d}_f$; solid and fluid unit normal vectors are denoted by $\hat{\mathbf{n}}_s$ and $\hat{\mathbf{n}}_f$, respectively.

$$\mathbf{d}_s = \mathbf{d}_f \tag{15}$$

$$\boldsymbol{\tau}_s \cdot \hat{\mathbf{n}}_s = \boldsymbol{\tau}_f \cdot \hat{\mathbf{n}}_f \tag{16}$$

Two-way coupled FSI can be performed using explicit or implicit approaches depending on the level of physical interaction between the fluid and solid. When a strong interaction exists as present in AAA, explicit approach will be insufficient, and implicit approach should be preferred for enhanced accuracy (Amindari et al., 2017). For implicit approach, there are two options as iterative implicit or fully coupled. In fully coupled implicit method, all governing fluid and solid equations are solved simultaneously, requiring high computational memory and leading to an excessive solution time. However, iterative implicit approach requires less computational power, and consists of a number of coupling iterations until reaching interaction convergence at each time step. Using smaller time steps lead to more stable results. Increasing the number of coupling iterations and using relaxation factors will help to overcome the stability problems.

Recent Findings on Growth and Rupture Mechanics of AAAs From Computational Studies

It is now widely accepted that biomechanical factors play role in degeneration and eventual rupture of AAA tissue. There is controversy regarding which biomechanical parameters are important in rupture. Below we summarize the important findings by categorizing the effects of various parameters.

Effect of Wall Thickness and AAA Asymmetry

Scotti et al. (2005) investigated the effect of varying wall thicknesses by performing fully coupled FSI simulations using idealized AAA geometries based on medical images. The thickness of AAA wall has an average of 1.45 mm, but it can decrease to 0.23 mm near the rupture site (Raghavan et al., 2004, 2006). A variable thickness between 0.5 and 1.5 mm was distributed along the AAA wall as inversely proportional to the cross-sectional diameter. When variable wall thickness model was compared with a uniform wall thickness (1.5 mm) model, it was observed that peak wall stress was increased by four-times for the variable wall thickness case.

The same research group also investigated the effect of AAA asymmetry (Scotti et al., 2008). Different levels of asymmetry were modeled using idealized geometries with the same patient-specific inlet velocity BC. For the most asymmetric model with $\beta = 0.2$ (see Equation (1) for definition of β), AAA diameter expanded by 15.2% at the peak systolic pressure. When an axisymmetric ($\beta = 1$) AAA model is considered, the diameter expansion is observed as 12.8%, implying that increasing asymmetry resulted in higher AAA deformation and therefore higher peak wall stress on the wall. As AAA becomes more asymmetric, location of peak wall stress shifted from anterior to the posterior wall.

Effect of Proximal Neck and Iliac Bifurcation Angles

Drewe et al. (2017) performed FSI simulations to investigate the effects of proximal neck and lateral iliac bifurcation angles considering idealized AAA models. Recent morphological comparisons showed that AAAs with large iliac bifurcation angle have a lower rupture risk (Drewe et al., 2017). Proximal neck angle has less impact on AAA hemodynamics compared to the iliac bifurcation angle. When the iliac bifurcation angle increased from 30 to 150°, peak WSS increased more than 2-fold (from 2.91 to 6.19 Pa), peak von Mises wall stress increased about 30% (from 0.186 to 0.243 MPa) and ECAP decreased by 57% (from 11.41 to 7.25). Larger iliac bifurcation angle was more protective of ILT formation and AAA expansion due to provoking high WSS and low ECAP conditions (Drewe et al., 2017). However, excessive load on the iliac arteries with increased bifurcation angle may increase the risk of an iliac artery aneurysm initiation (Xenos et al., 2010).

Effect of AAA Diameter and Wall Stress

The maximum AAA diameter is the first indicator for the treatment. For the current practice, when maximum AAA diameter exceeds 5–6 cm or diameter growth rate is higher than 1 cm per year, open surgery or endovascular treatment methods are performed considering the life expectancy of the patient (Scott et al., 2002; Longo and Upchurch, 2005; Chandra et al., 2013). Canchi et al. (2018) performed a comparative FSI study, considering two patient-specific AAAs with maximum aneurysmal diameters of 3.5 and 7 cm. Maximum principle stresses were determined as 0.30 and 0.22 MPa for 3.5 and 7 cm AAA diameters, respectively, implying that size of AAA is not the sole determinant for the rupture risk. It is reported that maximum wall stress was 12% more accurate for predicting rupture compared to using maximum AAA diameter alone as an indicator (Fillinger et al., 2002, 2003).

The maximum wall stress is generally observed at the transition of sac to neck of AAA wall as shown in **Figure 6** (Chandra et al., 2013; Doyle et al., 2014). FEA investigations showed that peak wall stress on the posterior AAA wall was within the range of 290 to 450 kPa (Raghavan et al., 2000), while non-aneurysmal aorta had a peak stress around 120 kPa. Scotti et al. (2008) compared FSI and FEA approaches on the same AAA model, and showed that FSI resulted in 25% increased wall stresses (peak values between 275 and 398 kPa) compared to FEA. Chandra et al. (2013) also performed FSI and obtained relatively higher peak wall stresses between 750 and 870 kPa. The

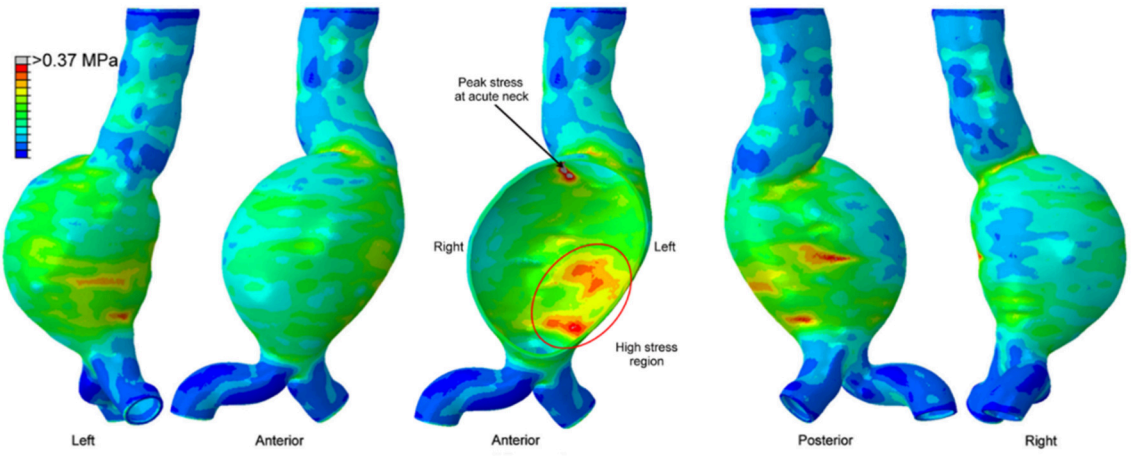

FIGURE 6 | Von Mises wall stress contour plot from different views, on a patient-specific AAA geometry at peak systolic pressure. The middle figure is a sectional view. High stress region exists in the posterior wall, however the peak wall stress is observed at the proximal neck of the aneurysm [The figure is adapted from Doyle et al. (2014) and used with permission].

reason for the high peak wall stress was considered to be the non-uniform AAA wall thickness which could increase the stresses at low thickness areas.

Effect of WSS and OSI

WSS and OSI are important hemodynamic parameters in turbulent AAA flow. Les et al. (2010) investigated patient-specific AAA hemodynamics using high-resolution CFD simulations (about 8-million mesh elements), hypothesizing that physical lower limb exercise might decrease the growth rate of AAA, since exercise resulted in a high amplitude WSS pattern and lowered OSI on AAA wall. Moderate turbulence was observed in AAA during exercise, while resting conditions led to mild turbulence. Rest-to-exercise TAWSS changes were found to be statistically significant. For example, at supraceliac level, TAWSS at rest was 3.6 dyn/cm^2, and it increased to 9.2 dyn/cm^2 during the exercise. At mid-aneurysm level, TAWSS at rest was 7.3 dyn/cm^2, while at exercise it was 21.7 dyn/cm^2. OSI values at rest were 0.28 and 0.27 for supraceliac and mid-aneurysm locations, respectively. These OSI values decreased to 0.18 and 0.21 during the exercise.

Qiu et al. (2018) performed CFD simulations using three ruptured and one non-ruptured patient-specific AAA models. The rupture sites were found to be near the fluid stagnation regions which have nearly zero WSS with high WSS gradients (WSSG). In **Figure 7**, the distribution of WSS and OSI are provided on a patient-specific model. Most researchers agree that the locations with low WSS, high OSI and high ECAP are prone to thrombus formation and have a higher risk of rupture (Les et al., 2010; Kelsey et al., 2016). On the other hand, in some studies reporting controversial results (O'Rourke et al., 2012; Arzani et al., 2014; Mohamied et al., 2015; Singh et al., 2018), it is stated that low WSS and high OSI regions do not coincide with thrombus deposition and atherosclerosis sites. Therefore, the exact effect of these hemodynamic parameters on the rupture mechanism is not yet fully understood.

Effect of Vascular Growth and Remodeling

Arterial growth and remodeling are investigated and modeled in several studies (Humphrey and Rajagopal, 2003; Watton et al., 2004; Gleason and Humphrey, 2005; Valentín et al., 2011, 2013; Humphrey and Holzapfel, 2012; Karšaj and Humphrey, 2012). In a recent study, Wu and Shadden (2015) presented a computational framework by coupling blood flow hemodynamics with vascular growth and remodeling (G&R). The wall is treated as a constrained mixture consisting of anisotropic collagen, elastin and smooth muscle fibers. Depending on the mechanical stimuli on the wall, the vessel has the ability of adaption for returning back to its homeostatic state by means of removal of old constituents and production of new ones. The lifespan of collagen is within 70–80 days (Wilson et al., 2013), where the flow simulation cycle has a time scale around 1 s. For computational efficiency, flow simulations only performed in cases when G&R caused severe change in geometry and boundary conditions, meaning that the last flow simulation results were used for all time in between until a new one is performed. The deviations of wall tension and WSS were used as the influencing factors for mass production rate on the vessel to return its homeostatic state. WSS changed about one order of magnitude in the aneurysm site and contributed to G&R. Stresses on the wall converged to homeostatic values after 110 G&R time steps (equivalent to about 800 days) and significant wall expansion was observed at the entire mass loss introduced regions.

Effect of Surgical and Endovascular Treatment Methods

Sughimoto et al. (2014) evaluated AAA surgery by comparing pre-operative and post-operative hemodynamics on CT-based geometries. AAA was replaced with a 30 mm straight graft under cardiopulmonary bypass. They proposed a novel parameter of pulsatile energy loss index (PELI)

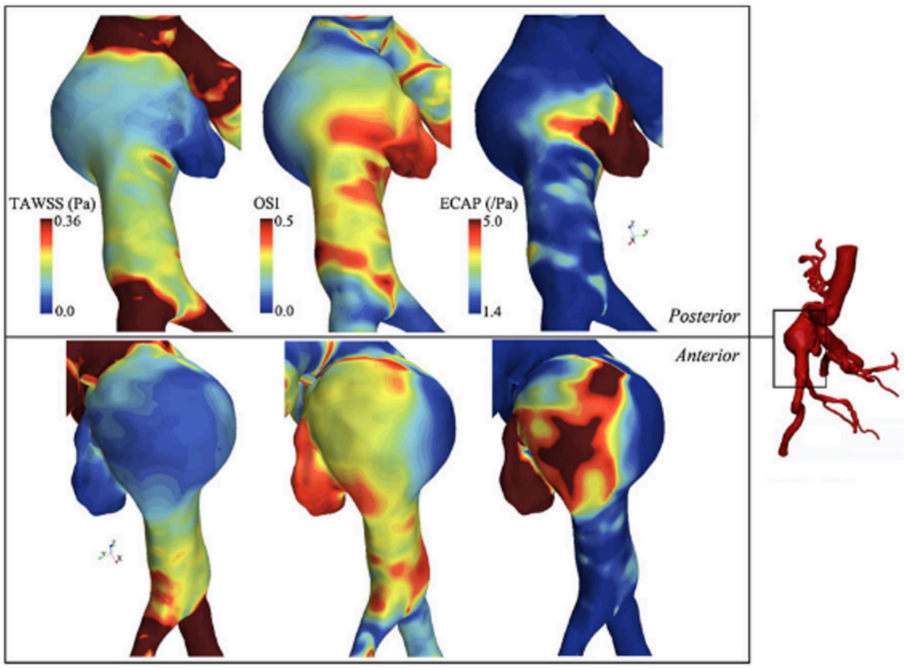

FIGURE 7 | TAWSS (Time averaged WSS), OSI, and ECAP contour plots on a patient specific AAA model. ILT formation is more likely to be observed in high ECAP regions. Rupture risk and aneurysm growth rate increase at regions with high OSI and low TAWSS [The figure is adapted from Kelsey et al. (2016) and used with permission].

which evaluates the energy loss between inlet and outlet of interested artery. After AAA treatment, PELI decreased from 0.986 (pre-operative value for the whole aorta) to 0.820 (see Sughimoto et al. (2014) for calculation of PELI), indicating that the grafting procedure improved the energy efficiency of blood flow delivery and reduced the left ventricle afterload. For a young healthy adult, PELI was measured as 0.0215, which was significantly low when compared to the AAA patient.

Casciaro et al. (2018) performed CFD simulations before and after two different endovascular surgical treatments of AAA. The Nellix endograft (Endologix, Irvine, California) proposed a method of AAA treatment based on endovascular aneurysm sealing (EVAS). For conventional endovascular aneurysm repair (EVAR), endografts have proximal fixation mechanism. The lateral neck angle (Kandail et al., 2015) and implantation position (Raptis et al., 2017) of the endografts alter the hemodynamics of EVAR. On the other hand, EVAS consists of two stents which are separately engaged to left and right common iliac arteries. Expandable endobags surround the stents and provide continuous sealing along the internal surface of the aneurysm (Böckler et al., 2015). Due to significant anatomic modifications after EVAS, 2-fold pressure increase was seen at the level of renal arteries. In addition, the peak flow velocity inside EVAS endograft stents was 60 cm/s, which was three-times higher than the peak blood flow velocity after EVAR treatment. This 3-fold increase in peak flow velocity after EVAS, also resulted in 60% higher WSS compared to EVAR (Casciaro et al., 2018).

EXPERIMENTAL INVESTIGATION OF HEMODYNAMICS OF AAAS

AAA hemodynamics is quite complex primarily due to irregular shape, flexible arteries, turbulent flow, and non-Newtonian behavior of blood. As computational methods have widely been used in investigation of hemodynamics and mechanical behavior of arterial tissue, experimental techniques are also utilized in characterization of flow dynamics through AAAs. Both approaches are crucial and complement each other with offering in depth analysis where the corresponding results depend on the assumptions in computational models and simplifications in experimental methods.

Various qualitative and quantitative flow measurement techniques have been utilized for experimental investigation of AAAs. In early studies, qualitative flow visualization techniques have been widely implemented, in which using localized injections, the patterns of dye as streaklines were generated (Ku et al., 1989). This simple method provides insights on overall behavior of flow structure in the region of interest. In terms of detailed velocity information in the AAAs, non-intrusive, and quantitative techniques such as MRI and Doppler Ultrasound Imaging (DUS) are appropriate for detailed anatomical analysis by means of tomographic slices. In MRI based system encoding the flow velocity is obtained by means of the changes in MR signal phase along a magnetic field gradient (Wang et al., 2016). Moreover, laser-based techniques including Laser Doppler Anemometry (LDA) and Particle Image Velocimetry (PIV) are also implemented for detailed velocity information. In

LDA, pointwise velocity measurements are performed by means of Doppler effect using two laser beams for each velocity component. This method has very high spatial and temporal resolutions (∼kHz) and allows to measure reverse flow and turbulent fluctuations, which is quite critical for understanding the growth and the rupture mechanics of AAAs (Yip and Yu, 2002). In PIV, two component velocity information on 2-D plane is obtained at relatively lower temporal resolution (∼Hz) using two laser sheets and an advanced camera, where in stereoscopic PIV three-velocity components are obtained on 2-D plane using two cameras. This method is quite effective in understanding the key parameters of disturbed hemodynamics of AAAs since it provides detailed velocity field information and therefore have widely been used recently (Deplano et al., 2013; Chen et al., 2014). For the quantification of three-dimensional velocity field, PIV offers two recent state of the art versions: Tomographic PIV and Holographic PIV, which are expected to appear in the studies of disturbed hemodynamics through AAAs in near future. Tomographic PIV has recently been applied to the hemodynamics of intracranial aneurysms (Roloff et al., 2017, 2018).

Experimental studies on blood flow inside AAAs is primarily categorized and populated in two major groups: the properties of the aorta phantom and conditions of the flow. Major consideration for the aorta phantom are elasticity of arterial wall and geometry of the aorta (change in wall diameter, aneurysm shape, artery bifurcation, etc.) whereas major considerations in flow conditions, include flow waveform (steady or physiological), type of working fluid (Newtonian, non-Newtonian), and pulse rate (exercise or resting). Considering the overall flow structure in aorta and AAAs, fully developed flow at the entrance of the AAA expands and creates counter rotating recirculation along with a jet flow at the center, which are due to the adverse pressure gradient imposed at the aneurysm bulge. Location and strength of the recirculation vortex primarily depend on the inlet flow waveform, bulge shape, and elasticity of arterial wall. For the steady inlet flow condition, which is not realistic, the recirculating vortex is larger in extent in average and located closer to downstream of the bulge, whereas in physiological flow condition recirculation region is alternating and moving back and forth due to periodic flow condition. It is also indicated that the spatial extent, the location, and the strength of the recirculation vortex are significantly affected by the bulge shape and the wall rigidity (Egelhoff et al., 1999; Yu, 2000; Deplano et al., 2007; Meyer et al., 2011). Flow structure inside the AAAs varies significantly according to these considerations, as reported by many experimental studies (Egelhoff et al., 1999; Yu, 2000; Deplano et al., 2007; Meyer et al., 2011).

Therefore, because of the complexities in geometry and flow conditions, the experimental set up for AAA investigations need to be designed to mimic natural realistic *in-vivo* conditions within AAA as close as possible to obtain accurate results. A typical experimental set up for the analysis of hemodynamics contains flow circulatory system including pump, piping, pressure compliance, test section that contains artery model, blood mimicking fluid, and flow measurement systems as briefly mentioned previously such as MRI, LDA, or PIV. In this part of the paper, the components of experimental set up and the techniques that are used widely in literature are explained in detail, and the results of recent experimental studies are discussed.

Flow Circulatory System

In cardiovascular biomechanics, it is difficult to measure hemodynamic quantities clinically due to the constraints of the system. Conducting *in vivo* animal studies are also very challenging because of the geometrical complexities and ethical issues. Therefore, in recent years, simulating *in vivo* conditions by using computational models or experimental setups become very popular. *In vitro* studies can be performed by generating the physiological flows through anatomical geometries of interest to simulate exact *in vivo* conditions in laboratory test setup; i.e., flow rates and pressure at the inlet and the exit, geometry of the artery and working fluid of a specific artery should be replicated physiologically. In **Figure 8**, an example of a test setup is presented. The main component of such a setup is the flow source, which is generally a pump, supplying a fluid flow into downstream. At the downstream, there are resistances to simulate physiological pressures. This is generally accomplished by using compliance chambers; in other words, vascular simulators to mimic realistic arterial pressures for specific arteries. Besides mimicking the physiological flow conditions, arterial phantoms which are desired to be studied should also be modeled and manufactured (Doyle et al., 2008, 2009b; Corbett et al., 2009). Finally, a blood mimicking fluid should be selected that matches biomechanical behaviors of blood.

Pump

Blood flows through arteries in an unsteady manner, which is characterized by a rhythmic repeatability and called pulsatile, i.e., such flows repeat themselves with a certain frequency. The pulsatile physiological flow profile, is presented in **Figure 4**, and has a complex waveform. In earlier studies, although it is far from the exact physiological conditions, researchers use constant flow rate in hemodynamic analyses. This is primarily due to the simplicities both in generating the steady flow in a circulatory loop and in performing flow measurements in such systems. In that sense, many experimental studies have been conducted at steady flow conditions using different type of flow generators, such as variable speed centrifugal or gear pumps (Ku et al., 1989; Asbury et al., 1995; Bluestein et al., 1996; Boutsianis et al., 2008), steady submersible pumps (Chen et al., 2014, 2015) or sometimes, by only using the effect of gravity, which requires placing a head tank (O'Rourke and McCullough, 2010).

However, a better description of hemodynamics of AAA closer to the physiological conditions is needed for the complete understanding of growth and rupture behavior of AAA. Indeed, comparison of steady and pulsatile flow conditions reveals important differences in hemodynamics which are also influenced by other system parameters including wall rigidity and AAA bulge shape (Yu, 2000). For example, with steady flow conditions, a vortex ring is localized at the distal end of the bulge, creating oscillations in wall shear stresses proximal to the

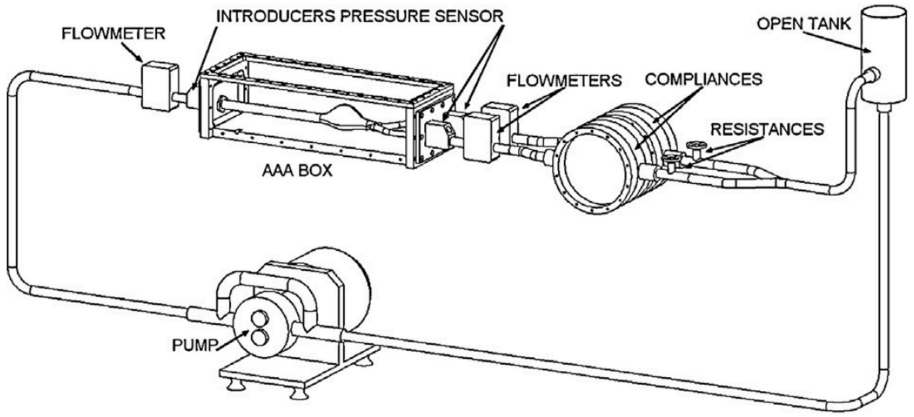

FIGURE 8 | Circulatory flow loop model for flow measurement system of abdominal aortic aneurysm containing tank, physiological flow generator, flowmeters, pressure sensors, compliances, and AAA box [The figure is adapted from Deplano et al. (2013) and used with permission].

corresponding localized region. On the other hand, with pulsatile flow case, the vortex ring is not localized and appears at the proximal site at the early systolic phase proceeding through the downstream throughout the cardiac cycle (Yu, 2000). This means that extrapolating steady flow results in extreme conditions might underestimate certain key parameters in physiological flow conditions. Considering the steady flow generators, centrifugal pumps, gravity-driven systems, and gear pumps have been commonly used. Later on, researchers have adapted various components to generate pulsatility at the downstream of these steady flow generators, including computer controlled valves (Egelhoff et al., 1999), piston-cylinder arrangements (Stamatopoulos et al., 2010, 2011), and gear pumps (Mechoor et al., 2016). In addition, commercial pumps which can generate either steady or pulsatile flow waveforms for several arteries are also available. All these alternatives for pumps are discussed along with addressing the pros and cons of each of them.

Steady flow generators

Centrifugal pumps. The most widely used flow generators are steady flow pumps, where the centrifugal pumps (Asbury et al., 1995; Bluestein et al., 1996) and submersible pumps (Chen et al., 2014, 2015) are generally used for that purpose. Centrifugal pumps are cost effective and are easily available in market with a very wide product range, however the flow rate is highly affected by the pressure drop, and thus, is not very convenient for hemodynamic analyses.

Gear pumps. Gear pumps are positive displacement pumps and are convenient for providing quite stable and constant flow rates at broad range of pressure drop conditions. In earlier studies, variable speed gear pumps have been employed in hemodynamics studies to generate steady flow conditions (Asbury et al., 1995; Boutsianis et al., 2008).

Gravity-driven systems. In gravity driven systems, the effect of gravity is used as the driving force with locating a head tank of fluid at certain elevation above the test section to maintain pressure and velocity distribution in AAA. With the effect of gravity, steady mean flow can be generated, but in order to maintain the physiological flow pattern, an additional equipment such as computer-controlled valves (Egelhoff et al., 1999) or piston-cylinder arrangements (Yu, 2000; Stamatopoulos et al., 2010, 2011) are needed to be used at the downstream.

Pulsatility generators

In order to generate pulsatility, additional computer-controlled equipment should be adapted to circulatory systems. For this purpose, the most common integrated systems include computer-controlled valves, piston-cylinder arrangements, or gear pumps.

Valves. In general, centrifugal pumps are adapted only for steady circulations, where in a very few studies, a flapper nozzle valve is adapted to the flow loop to produce pulsatility (Moore et al., 1992; Moore and Ku, 1994). In general, the desired waveform including physiological pattern with the reverse flow cannot be maintained properly in centrifugal pump driven systems. An application of valves in physiological flow generation is utilized by Egelhoff et al. (1999), where a gravity driven pump with a head tank kept 234 cm above the AAA test section to provide desired entrance flow conditions and a computer controlled diverter valve at the downstream of AAA model have been used to generate the pulsatility. The flow waveform for the corresponding setup is quite similar to realistic case, but deviates from the exact physiological waveform. A similar gravity driven set up with computer controlled rotating spherical valve downstream of the test section can also be used (Nikolaidis and Mathioulakis, 2002). Relatively enhanced version of the gravity driven flow generator with valves has been developed by Peattie et al. (2004), where two computer-controlled valves, one in the forward direction while the other is in the retrograde direction, were embedded to the system and more realistic waveform with backflow region was obtained with the improved control mechanism compared to Egelhoff et al. (1999) and Nikolaidis and Mathioulakis (2002).

Piston-cylinder arrangements. In piston-driven pumps, a piston is used as linear actuator to provide periodicity to the mean flow that is generated by a gear pump or a head tank located at a certain elevation above the test section, as explained previously. Piston-driven pumps serve better performance in terms of controllability to generate desired flow rate compared to previous orientations, but still physiological waveform, especially backflow regions, cannot be generated properly. In **Figure 9**, a test rig with a piston-driven pump is presented (Yu, 2000). The mean flow in the test section is generated by a head tank, which is fed by a submersible pump. Pulsatility is generated by means of a pulse generating module, which contains a DC gear-motor fitted with the circular cam of a small piston-cylinder assembly. DC gear-motor drives the piston by means of the circular cam to create necessary pulsating flow conditions (Yu, 2000; Yu and Zhao, 2000). The flow waveform generated in such a flow loop is periodic in sinusoidal form but again not physiological. To obtain more realistic flow waveforms, in later studies, a variable speed electrical motor is used to drive circular cam of linear reciprocating piston (Yip and Yu, 2001, 2002; Stamatopoulos et al., 2010, 2011). In some orientations, motors drive the reciprocating pistons with screw mechanisms such as rack and pinion and lead screw, rather than circular cam (Duclaux et al., 2010; Ene et al., 2011; Morris et al., 2013; Wang et al., 2016). In **Figure 10**, an example for piston with lead screw mechanism is shown (Tsai and Savaş, 2010). In that case, a gear pump provides the steady mean component of the desired flow waveform and piston arrangement provides the oscillatory component of the flow waveform with the help of a motor driven lead screw. The gear pump is preloaded with a back-pressure valve at its discharge, providing that the gears remain in constant contact to prevent reverse flow. Although the system is capable of generating different pulsatile waveforms, great deviations from physiological cases are reported, especially for the regions of steep changes in the waveform (Tsai and Savaş, 2010). Sometimes two-sided cylinders are also employed with such screw mechanisms. In such a case, a computer controlled motor driven rack mounted piston, divides a cylinder into two parts, and they are connected with a valve which ensures that pump is completely empty on one side of the cylinder while the other side is refilled to keep the flow direction same. The problem for two-sided piston cylinder assembly is its limited operating range in terms of peak flow because of the decreased stroke volume (Frayne et al., 1992; Salsac et al., 2006).

Gear pumps. In recent years, researchers have found that gear pumps are quite appropriate in physiological flow generation, where a controller needs to be integrated with a servo motor to run the gear pump. In that case, reverse flows can also be easily generated. An example of such system is presented in **Figure 11** (Mechoor et al., 2016). Different from the aforementioned systems that generate pulsatility, computer-controlled gear pumps operate continuously without requiring any additional equipment and can replicate the physiological waveforms quite accurately (Gaillard and Deplano, 2005; Deplano et al., 2007, 2013, 2014; Mechoor et al., 2016). In addition, Mechoor et al. (2016) developed a closed loop system with integrating a feedback mechanism from output flow to the computer controlled gear pump system to better match the desired physiological flows and pressure waveforms.

Commercially available pumps

Besides these component-based in-house built systems, there are commercially available physiological flow generators. Harvard Pump (Harvard Apparatus, Holliston, MA) and SuperPump (Vivitro Labs, Victoria, BC, Canada) are commercially available pumps that are partially programmable and offer several number of arterial waveforms. A fully programmable commercial pump is CardioFlow (Shelley Medical Imaging Technologies, London, ON, Canada), which is again a two-sided piston pump that generates pulsatile flow, by dividing the cylinder into two chambers, each with fluid ports at the end. Some of the studies that utilize these pumps in hemodynamic analysis of different arteries are Pahlevan and Gharib (2013), Groves et al. (2014), and Najjari and Plesniak (2016). Resulting waveforms for these commercial pumps are very similar to physiological cases of predefined arteries, but the range of arteries that they can replicate is limited.

Piping and Pressure Compliance

As a component of flow circulatory systems, piping is critical in terms of obtaining correct inlet waveforms. The main concerns in piping are the general arrangement and the distance between the pump exit and test section inlet, which determine whether the fully developed flow is generated at the inlet of the test section. Some researchers specify this required distance as 100 times the diameter of the tubing before flow enters the test section (Moore et al., 1992). In a latter study, Durst et al. (2005) have suggested a formula, as given in Equation (17).

$$\frac{L}{D} = \left[0.619^{1.6} + (0.0567Re)^{1.6}\right]^{1/1.6} \tag{17}$$

where D is the tube diameter (m), L is the entrance length (m) and *Re* is the Reynolds number. Tsai and Savaş (2010) states in the study of cerebral saccular aneurysms that the entrance length required for fully developed flow as given in Equation (18).

$$L = 0.058dRe \tag{18}$$

He and Ku (1994) have claimed that the maximum length of the inlet pipe to satisfy the requirement of fully developed flow conditions for pulsatile flow is smaller than the tube length for steady flow conditions.

In order to match the pressure waveform at the inlet of the test section, various methods have been implemented. Researchers frequently employing downstream vascular simulators, replicate the impedances along the arteries to generate pressure waveform at specific arteries, which are generally composed of flow resistances and compliance chambers. In some recent studies, resistor–capacitor–resistor (RCR) module is adapted, which is composed of proximal

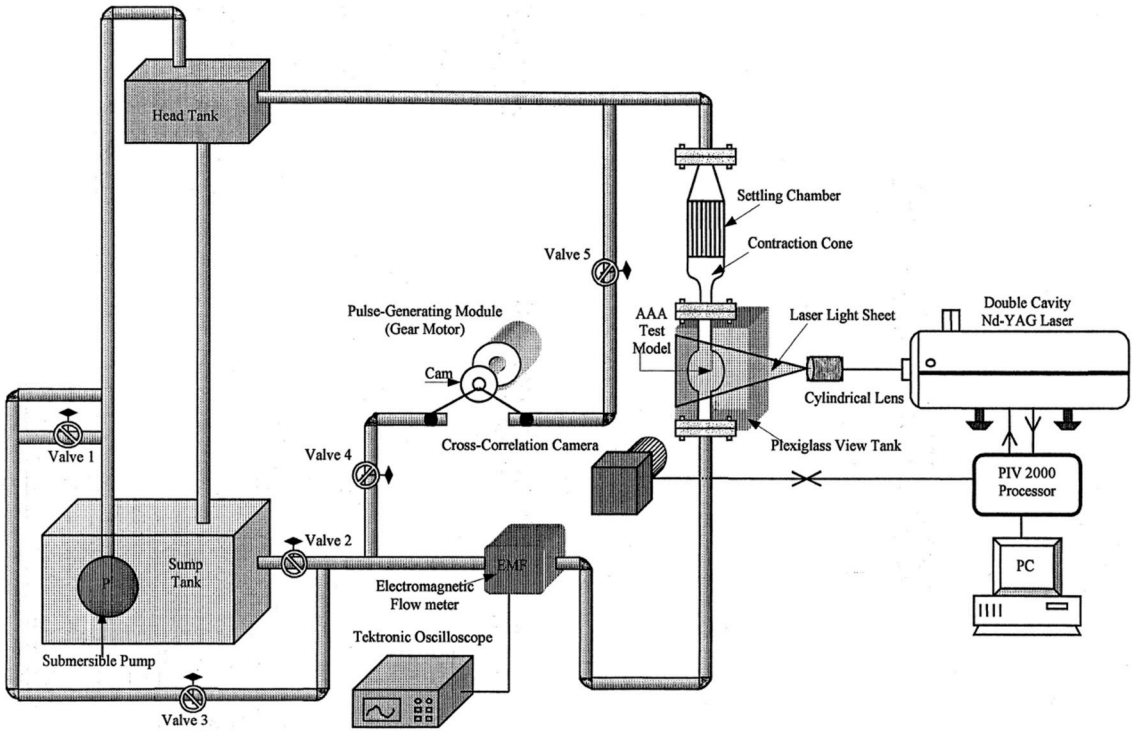

FIGURE 9 | Experimental test set up for AAA test model. The mean flow is generated by a head tank and pulsatility is added by piston cylinder assembly fitted with a circular cam, which is driven by a DC gear-motor [The figure is adapted from Yu (2000) and used with permission].

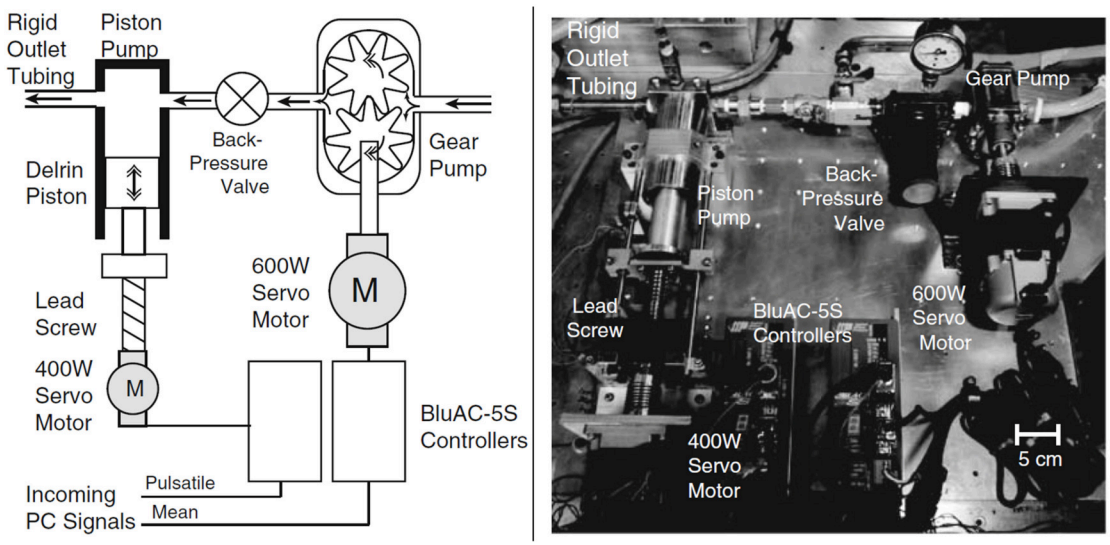

FIGURE 10 | Sketch and picture of flow circulatory system using gear pump and piston-cylinder arrangement with lead screw as flow generator. Steady flow is supplied by gear pump, while piston and servo motor combination generates the pulsation [The figure is adapted from Tsai and Savaş (2010) and used with permission].

and distal resistors (pinch valves) with a compliance chamber (air chamber) (Deplano et al., 2013; Mechoor et al., 2016). Besides all of these, reproducing physiological pressures throughout the aneurysm sac can be accomplished very accurately by the lumped-parameter boundary condition module, which is suggested by Kung et al. (2011). Such module is adapted downstream of aneurysm model to replicate outlet boundary condition, consisting of an inductance

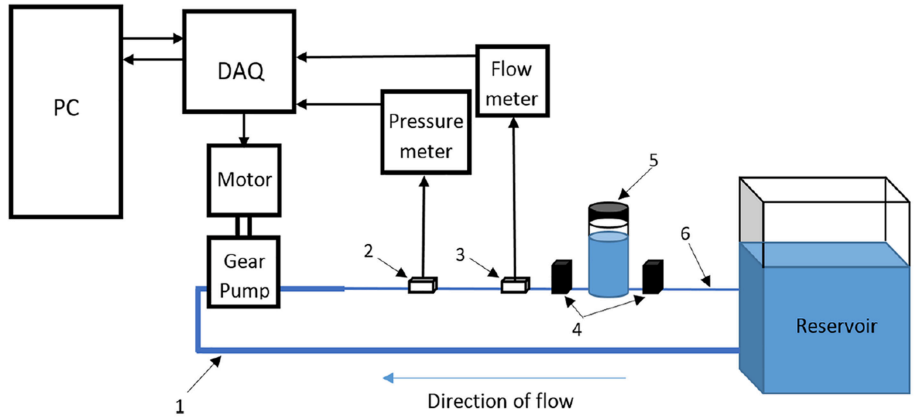

FIGURE 11 | Schematic representation of flow circulatory system using computer-controlled gear pump with a feedback mechanism to achieve desired physiological flow and pressure waveform [The figure is adapted from Mechoor et al. (2016) and used with permission].

(L), proximal resistance (Rp), capacitance (C), and distal resistance (Rd), which is, in total, called as four-element Windkessel model.

Test Section

Another component of a circulatory flow setup is the model of the artery of interest, or so called, anatomical phantom. In early studies, an aneurysm model, which has transparent rigid walls with simplified geometry, has been integrated to flow loop (Egelhoff et al., 1999). These simplified and rigid models cannot replicate the exact compliant nature of the vessels. However, they provide insight about the governing physical processes occurring inside the AAA, including but not limited to separation of the flow at the inlet of AAA, vortex generation and jet regions, transition to turbulence, oscillatory flow structure, and high or low wall shear stress regions. With such controllable geometries, the parametric studies regarding aspect ratio, bulge diameter, and bulge asymmetry can be characterized. In recent investigations, more realistic geometries have been implemented. Rigid aneurysm models with simplified geometries are in the form of straight tube with a concentric bulge, which can be described by an ellipse formula (Yu, 2000), and are generally manufactured from glass (Salsac et al., 2006), or resins (Biglino et al., 2013). On the other hand, in order to understand exact hemodynamics and biomechanical forces that are generated through the aneurysms, it is necessary to work with compliant arterial models (Deplano et al. (2007) to replicate *in vivo* condition by manufacturing patient-specific phantom.

Manufacturing the realistic and patient specific arterial model is quite challenging. Different techniques are applied in literature by using different materials like silicone, polyurethane, and latex, where in the most well-known technique polyjet printing is utilized to manufacture transparent, 3D, and compliant phantoms (Sulaiman et al., 2008; Biglino et al., 2013; Ionita et al., 2014). 3D patient-specific vascular imaging data generated by means of CT scanner or MR techniques are collected and exported into Standard Tessellation Language (STL) file format, and this STL file is imported into 3D polyjet printer. The printer head generates layers of liquid photopolymer and builds them up to create 3D models. This technique enables to utilize different materials with a high resolution. As another method 3D printed vessel lumens are used as molds of the real phantoms that are going to be casted (Ho et al., 2017). For non-transparent phantoms, other techniques with non-transparent materials are also available to manufacture patient specific artery models where Doppler Ultrasound measurements are conducted for flow quantification. As an example, embedding silicone-elastomer vessel model into the agar based tissue-mimicking material (TMM) having same acoustic properties with artery (Poepping et al., 2004), direct machining of phantom using numerically controlled milling rather than producing a mold (Wong et al., 2008) or some other techniques (Watts et al., 2007; Allard et al., 2013) can be given. Even though Doppler Ultrasound technique does not require transparent phantoms, which may be an advantage, it provides only the maximum velocity in a flow cross section. Therefore, detailed hemodynamics evaluation is not possible with Doppler Ultrasound technique.

Blood-Mimicking Fluid

Blood is a non-Newtonian fluid, where the viscosity changes with shear rate. In literature, most researchers have utilized Newtonian fluids as blood-mimicking fluid because blood behaves like a Newtonian fluid for certain shear rate values (Berger and Jou, 2000). However, its non-Newtonian behavior becomes critical when shear rate is low and Deplano et al. (2013) reports that wall shear rate in some regions of AAA drops to values of $1\,s^{-1}$. In this case, the blood acts as a non-Newtonian shear thinning fluid because viscosity decreases with increasing shear rate (Mandal, 2005). Non-Newtonian behavior of blood can be modeled using Carreau-Yasuda viscosity model, which is given in Equation (14). Most of the experimental studies utilize the Newtonian assumption, and generally pure water or the mixture of glycerin and water with different volumetric ratios have been widely used as blood mimicking fluid (Boutsianis et al., 2008; Stamatopoulos et al., 2010, 2011). There is only few studies that use non-Newtonian fluids of which behavior are very similar to

the blood, like Xanthane Gum solution with glycerin (Deplano et al., 2014; Najjari and Plesniak, 2016).

Flow Measurement System

In early studies, flow field is generally observed with the help of flow visualization technique (Budwig, 1994; Moore and Ku, 1994). The growing trend, which is the Particle Image Velocimetry (PIV) has been developed since the early 1980's to acquire velocity vector information of a whole flow field instantaneously with a high resolution (Adrian, 1991). Since 1993, PIV has been utilized in biologically important flows because of being a non-intrusive approach. In terms of the flow field information, different versions of PIV are available including 2D (planar) PIV, Stereoscopic PIV, Holographic PIV, and Tomographic PIV. In most of the AAA studies, planar PIV has been implemented, while Stereoscopic PIV has been utilized in a very few studies. As of authors knowledge, although Tomographic PIV has been applied to disturbed hemodynamics through intracranial aneurysms (Roloff et al., 2017, 2018), Holographic PIV and Tomographic PIV have not been applied to AAA studies yet.

Planar PIV is the mapping of average displacements of seeding particles within interrogation areas over a small time interval by means of two successive images of an illuminated plane in a fluid flow. Interrogation areas are small sub areas of each image, containing sufficient number of illuminated seeding particles. To find the displacements of particles for a short time interval, interrogation areas of two successive images are compared by means of cross correlation technique, resulting in determination of the most probable velocity vector for the particles inside of that interrogation areas, and this procedure continues until all interrogation areas are correlated and whole flow field velocity vectors are generated.

The fluid is seeded with neutrally buoyant particles, which should be sufficient in amount and size, typically varying from 5 to 50 μm, depending on the flow rate, magnification of the camera, and the field of view as well (Stamhuis, 2006). There are several types of seeding particles with respect to illumination characteristics, such as reflective, scattering, and fluorescent. Among all of these options, fluorescent particles have an advantage that fluorescent light can be distinguished from the illumination, which increases the visibility of the particles (Tsai and Savaş, 2010). Illumination of seeding particles with laser sheets and capturing the images with camera bring the refraction problem where the refractive indices of mediums and inclination angles of surfaces when lights passes through them are quite critical. Since the AAA models are curved in shape, in addition to the efforts given to match the refractive indices of working fluid and phantom, a box with flat surfaces perpendicular to the surface normal of camera lens plane covers the test section and is filled with working fluid to minimize refraction problems (Budwig, 1994).

In planar PIV, two component velocity information on 2-D plane is obtained using two laser sheets and an advanced camera, where in Stereoscopic PIV three-velocity components are obtained on 2-D plane using two cameras, as can be seen in **Figure 12**. Note that, lens planes and image planes of cameras are tilted to satisfy the Scheimpflug arrangement and plexiglass prisms in addition to the box for the test section are used to minimize refraction problems. In literature, there are many studies that utilize PIV technique to study the hemodynamics through AAA. In **Table 1**, PIV studies that have been conducted for the last 20 years are listed, considering the flow conditions at the inlet, type of blood mimicking fluids, wall types, geometry, and Reynolds number ranges.

Scaling Parameters

Pulsatile flow through the arteries is generally characterized by two non-dimensional parameters, Reynolds and Womersley numbers, which are defined as the Equations (19,20).

$$Re = \frac{UD}{\nu} \tag{19}$$

$$\alpha = 0.5D\sqrt{\frac{\omega}{\nu}} \tag{20}$$

where U is the velocity, D is the tube diameter, ν is the kinematic viscosity and ω is the frequency of periodicity (Womersley, 1955). Reynolds number is the ratio of inertia forces to viscous forces, which determines the flow regime and varies from 1 for very small arteries to ∼4,000 for aorta. Womersley number is the ratio of unsteady inertia forces to viscous forces, which can also be represented in terms of Reynolds number and Strouhal number. For low Womersley number flows, viscous forces dominate and velocity profile inside the arteries become parabolic, and velocity at the centerline oscillates with a phase of driving pressure gradient. For high Womersley number flows ($\alpha > 10$), unsteady inertia forces dominate and velocity profile has a nearly flat velocity profile, and in that case, flow represents situations with rapid acceleration and deceleration (Womersley, 1955; Ku, 1997). Womersley number value for femoral artery is nearly four, while for aorta, it reaches up to 22.

These non-dimensional parameters are required to be kept constant when scaling is conducted, enabling to perform similarity analysis. The artery models that are studied during the experiments might be scaled to a larger size because generally the vessels in human circulatory system are relatively small for macro scale investigations. In that case, the normal vessel is the prototype with exact dimensions and velocity values, while the artery model utilized in experiments might be the scaled version of the prototype. In that case, performing a similarity analysis by matching Reynolds and Womersley numbers of prototype and model will mimic physiological conditions and enables the simulation of performance of the prototype. By equating the Reynolds and Womersley numbers for the model and prototype, as given in Equations (21,22).

$$Re_m = Re_p, \qquad \frac{U_m D_m}{\nu_m} = \frac{U_p D_p}{\nu_p} \tag{21}$$

$$\alpha_m = \alpha_p, \qquad 0.5D_m\sqrt{\frac{\omega_m}{\nu_m}} = 0.5D_p\sqrt{\frac{\omega_p}{\nu_p}} \tag{22}$$

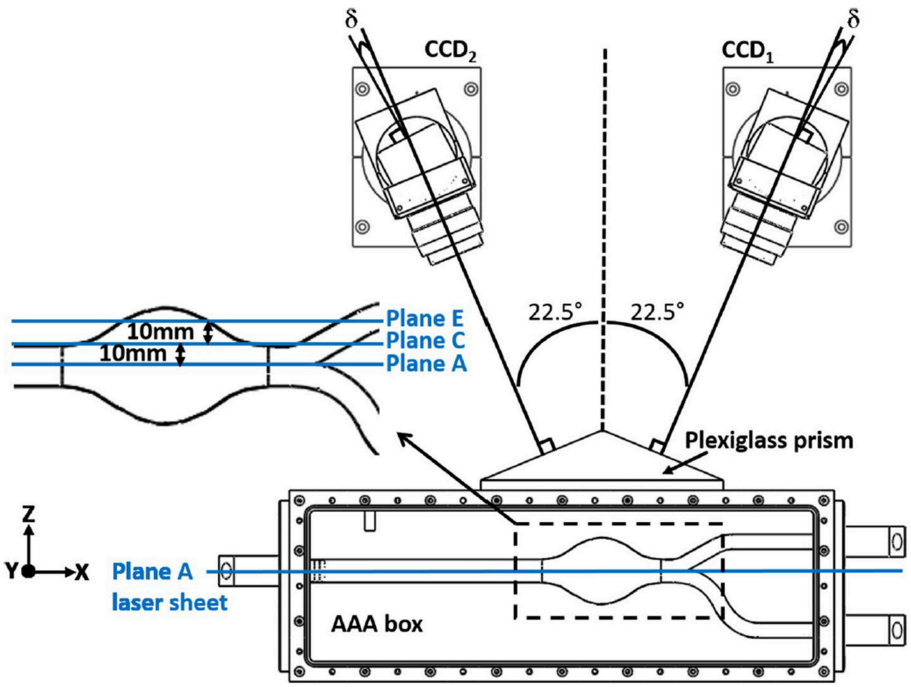

FIGURE 12 | Typical camera arrangement of the SPIV. δ is the angle between the lens plane and the image plane, and faces of plexiglass prism is perpendicular to corresponding camera, which is used to minimize refraction related problems [The figure is adapted from Deplano et al. (2016) and used with permission].

where subscript m is representing model and p is representing prototype and with the following ratio of diameters of arteries and kinematic viscosities, which is given in Equation (23).

$$L_r = \frac{D_p}{D_m} = constant, \quad \nu_r = \frac{\nu_p}{\nu_m} = constant \tag{23}$$

where L_r is diameter ratio and ν_r is the kinematic viscosity ratio of prototype to model, the velocity and frequency of the model become

$$U_m = \frac{U_p L_r}{\nu_r}, \quad \omega_m = \frac{\omega_p L_r^2}{\nu_r} \tag{24}$$

To increase the resolution of a small vessel by increasing its diameter, the velocity should be decreased by the ratio of $1/L_r$ to match the Reynolds number, while frequency should be decreased by the ratio of $1/L_r^2$ to match the Womersley number. In certain test setups, the frequency adjustment might be needed possibly due to the following two reasons: (1) Flow circulatory system could not reach the desired frequencies for the flow waveform, (2) Flow measurement system could not provide enough sample in one cycle. In that case, the desired velocity and diameter for the setup are determined accordingly. Similarly, if the flow rate in the setup is the limitation, then once the velocity is determined, diameter of the setup is adjusted according to the Reynolds number and finally the frequency of the waveform is set based on the Womersley number to ultimately reach the similarity.

Key Parameters to Study in Experimental Investigation of Hemodynamics of AAA

In experimental studies, researchers have generally reported the results of the hemodynamics in AAA in terms of velocity and vorticity parameters (Salsac et al., 2006; Stamatopoulos et al., 2010) obtained using several vortex identification techniques, such as swirling strength (Deplano et al., 2007). Swirling strength of a vortex is defined by λ_{ci}, while ${\lambda_{ci}}^2$ is called enstrophy, which is energy of vorticity and utilized for decreasing background noise (Zhou et al., 1999).

In recent years, with the utilization of Stereoscopic PIV technique, some researchers have also presented the 3D vortex evaluation through aneurysm sac (Deplano et al., 2016). In this technique, Deplano et al. (2016) have focused on the effect of transverse velocity component (w) measurement by means of comparing its magnitude to other velocity components, such as axial (u), vertical (v), or total velocity vector ($\mathbf{V}$), of which magnitude is

$$\|\mathbf{V}\| = \sqrt{u^2 + v^2 + w^2} \tag{25}$$

In addition, the magnitude of 2D velocity vector, ($\mathbf{V_{2D}}$), can also be written as

$$\|\mathbf{V_{2D}}\| = \sqrt{u^2 + v^2} \tag{26}$$

TABLE 1 | PIV studies conducted in the field of hemodynamics in AAA for the last 20 years.

References	Flow generator	Blood mimicking fluid	Wall type	Geometry	Reynolds numbers
Yu, 2000	Gravity driven pump with piston cylinder arrangement (Unsteady-Sinusoidal)	Newtonian fluid: A solution mixture of glycerin and water	Rigid wall-Pyrex glass tubes	Straight Tube and Axisymmetric, elliptical shaped bulge	Steady Flow: 400–1400 Unsteady Flow, Peak Value: 1,274
Salsac et al., 2006	Two sided piston cylinder arrangement (Unsteady-Physiological)	Newtonian fluid: Pure water	Rigid wall-Glass	Axisymmetric bulges with different diameters	Unsteady flow, Peak Value: 2,700
Deplano et al., 2007	Computer controlled pump (Unsteady-Physiological)	Newtonian fluid: Aqueous glycerin solution, 60% water	Rigid wall-Glass Compliant wall-Molded polyurethane	Asymmetric bulge	–
Boutsianis et al., 2008	Variable speed gear pump (Steady)	Newtonian fluid: A mixture of 40% water, 60% glycerol	Compliant wall-Silicone phantom	Patient-specific aneurysm, gathered by CT scanning	Steady flow: 560
Stamatopoulos et al., 2010	Linear reciprocating piston cylinder arrangement (Unsteady-Sinusoidal)	Newtonian fluid: A water and glycerin solution (40:60 by volume)	Rigid wall-Elastomer material (Sylgard-184)	Axisymmetric, elliptical shaped bulge	Steady Flow: 105–690 Unsteady Flow, 105–690
Stamatopoulos et al., 2011	Linear reciprocating piston cylinder arrangement (Unsteady-Physiological)	Newtonian fluid: A water and glycerin solution (40:60 by volume)	Compliant wall-Liquid silicon elastomer	Patient-specific aneurysm, gathered by CT scanning	Unsteady flow, Peak Value: 541
Deplano et al., 2013	Computer controlled pump (Unsteady-Physiological)	Newtonian fluid: Aqueous glycerin solution, 60% water	Compliant wall-Molded polyurethane	Asymmetric bulge with symmetric and asymmetric iliac bifurcation	Unsteady Flow, Peak Value: 1,876
Chen et al., 2014	Steady Submersible Pump	Newtonian fluid: A mixture of NaI and water	Rigid wall	Patient-specific aneurysm, produced by rapid prototyping	Steady Flow: 2,234
Deplano et al., 2014	Computer controlled pump (Unsteady-Physiological)	Shear-thinning fluid: Aqueous solution of Xanthane gum (XG)	Compliant wall-Molded polyurethane	Asymmetric bulge with asymmetric iliac bifurcation	Unsteady Flow, Peak Value: 1,941
Deplano et al., 2016	Computer controlled pump (Unsteady-Physiological)	Shear-thinning fluid: Aqueous solution of Xanthane gum (XG)	Compliant wall-Molded polyurethane	Asymmetric bulge with asymmetric iliac bifurcation	Unsteady Flow, Peak Value: 2,298
Wang et al., 2016	Piston cylinder arrangement (Unsteady-Physiological)	Newtonian fluid: Pure water	Rigid wall-Glass	Straight Tube and Axisymmetric, elliptical shaped bulge	

For each spatial point of different planes inside aneurysm, relative difference, *RD* between these two velocity magnitudes is calculated as

$$RD = \frac{\|\mathbf{V}\| - \|\mathbf{V_{2D}}\|}{\|\mathbf{V}\|} \times 100 \tag{27}$$

Once the *RD* values are calculated at each point, the mean value of the relative difference, *RD*, can be obtained on the corresponding planes. If *RD* is lower than 10%, it can be interpreted as u and v components are sufficient to represent flow behavior, whereas for higher mean relative difference values, w component needs to be included (Deplano et al., 2016). The quantities such as $\frac{|w|}{\|\mathbf{V}\|}$ contours and $\frac{|w|}{|u|}$, $\frac{|w|}{|v|}$, *RD* values, which underline the specific importance of w with respect to u and v components, can be utilized in order to investigate the importance of transverse velocity component (w) on hemodynamics and AAA progression. In addition, vortex ring and its strain dynamics which can also be obtained from Stereoscopic PIV data, are used to understand different flow instabilities and growth mechanism (Deplano et al., 2016). The rate of deformation tensor can be decomposed into rate of strain tensor, which is pure rate of deformation tensor S_{ij}, and pure rate of rotation tensor Ω_{ij}. The strain rate tensor S enables to visualize and quantify the direction of compression and stretching. If the eigenvalues S^*_{ij} of tensor S are positive, the fluid element is stretched while they are negative, the element is compressed (Bouremel et al., 2009).

Important Findings on Hemodynamics of AAAs From Experimental Studies

Hemodynamics in Undilated Aorta

In early studies, researchers have focused on hemodynamics inside undilated aorta to understand the effect of flow on dilation of arterial wall. Ku et al. (1989) investigated undilated abdominal aorta by using a realistic glass abdominal aorta model and observed steady flow inside that artery by injecting a dye into the model. Flow pattern at the infrarenal aorta, where AAA generation is observed, has more complex structure than in the suprarenal aorta because of the following reasons: (1) The aorta has a curvature at that section, which localizes transient separation to its posterior wall; (2) There are branches of arteries transferring blood to kidneys after the suprarenal and before the infrarenal segments. The blood flow transferred from these

branches creates secondary flows at the upstream of infrarenal aorta; (3) The bifurcation at the downstream of infrarenal aorta is creating a horseshoe vortex. All these unsteady flow structures make the infrarenal segment appropriate to generate an aneurysmal bulge.

Hemodynamics in AAA

Effect of pulsatility

In early studies on AAA (Nerem, 1984; Egelhoff et al., 1999; Yu, 2000), steady flow analysis has been conducted and as reported under laminar conditions, a jet of fluid passing though the core of the aneurysm is surrounded by a circulating vortex. The flow velocity through the center of the aneurysm is 40 times higher than the velocity at the recirculation region, and WSS value has the largest peak at the reattachment point of this recirculating flow. The WSS magnitude in the recirculation region is about ten times less than the value in the upstream tube, because the core flow separation at the bulge causes the negative WSS values. Scherer (1973) reports that the transition to turbulence begins at Re = 2900. Asbury et al. (1995) studied AAA without any bifurcation and utilized Color Doppler Flow Imaging (CDFI) method to visualize the flow and Laser Doppler Velocimetry (LDV) method to quantify the flow in order to address the effect of bulge diameter and turbulence on hemodynamics. They reported a correlation between the aneurysm size and rupture because especially in larger aneurysms turbulent flow is observed, which causes higher WSS values throughout the bulge (Asbury et al., 1995).

The cycle of physiological flow with strong acceleration and deceleration of flow in AAA has strong effects on vortex dynamics, which moves from proximal to the distal end creating significant fluctuations in WSS and pressure though the aneurysm bulge. Fukushima et al. (1989) conducted the first experimental and numerical study on pulsatile flow conditions for glass models of axisymmetric and asymmetric AAAs. They observed that primary and secondary vortices were present inside the bulge, and reported that the peak negative shear stress occurs at the distal end. Yu (2000) performed the first PIV experiments for both steady and pulsatile flow waveforms in pyrex glass aneurysm models without any iliac bifurcation to see the effects on sinusoidal waveform on hemodynamics. Yu and Zhao (2000) compared the steady and pulsatile flow dynamics in a straight tube with a side bulge using PIV, and they reported significant differences between flow patterns. Stamatopoulos et al. (2010) reported the difference between steady and pulsatile, sinusoidal flow in AAA, where the flow separation at the proximal end and reattachment at the distal end of aneurysm bulge is witnessed for steady case, but for unsteady case, these locations vary for each instant of cardiac cycle. However, the peak WSS values are observed at the model exit for both flow conditions.

Effects of wall material properties, working fluid properties, and geometric parameters on AAA hemodynamics

In most of the experimental studies, rigid axisymmetric models were used to investigate the hemodynamics in aneurysm bulge (Yu, 2000; Salsac et al., 2006; Stamatopoulos et al., 2010). Deplano et al. (2007) and Meyer et al. (2011) have tested two aneurysm models one having rigid and the other with compliant walls. The rigid aneurysm was made of glass while the compliant one was made of molded polyurethane, and both had the identical geometry as a simple bulge for comparison purposes. As can be seen in **Figure 13**, there is significant difference between the flow fields inside both of the aneurysms. In rigid model, there is only viscous dissipation, while in compliant model, viscoelastic dissipation is also observed, which is indicated as more critical. During the accelerating phase of the cycle, compliant walls absorb kinetic energy in the potential energy form, leading the walls become expanded. While the flow is decelerating, this stored kinetic energy retracts the walls. This expansion and retraction contribute the progression of vortices at the distal end of aneurysm during the deceleration phase. They conclude that increasing wall compliance causes collision of vortices with the walls, increasing both the local pressures and wall stresses especially at the distal end (Deplano et al., 2007; Meyer et al., 2011). Producing models with exact *in vivo* wall material properties and thicknesses are also important to decide rupture location. In literature, there are several studies focusing on identifying rupture location in compliant AAA models by means of tensile tests (Doyle et al., 2009a, 2010) and biaxial tests (O'Leary et al., 2014). Mechanical behaviors of ILT and wall calcification and their effects on rupture have also been characterized by means of these tests (Ene et al., 2011; O'Leary et al., 2013, 2015).

The real aneurysms also contain iliac bifurcation. Deplano et al. (2013) have studied asymmetric aorto-iliac bifurcation for a simple bulge. Two artery models, one with a straight outlet tube and the other with iliac bifurcation have been studied to observe the effect of bifurcation on flow structure. The results indicate that for the model with iliac bifurcations, intensity of the vortex ring impact on the anterior wall is about 90% higher than without bifurcation. When the vortex ring impinges on the wall, the forces generated by this impingement might possibly cause the rupture (Chu et al., 1995). For a compliant aneurysm bulge with aorta iliac bifurcation, stereoscopic PIV technique has been implemented to observe vortex ring impingement inside the aneurysm as 3D quantification (Deplano et al., 2016). In **Figure 14**, contours of $\frac{|w|}{\|\mathbf{V}\|}$ in six planes and four time instants of cardiac cycle is represented in order to understand the effect of transverse velocity component, *w*. During the deceleration phase, where T_a = 0.45, 0.55 *and* 0.85, the magnitude of the mean transverse velocity component, *w*, is 0.7 times the axial component and 1.7 times the vertical component, especially for C and D planes which are located within the AAA bulge.

The other important concern about AAA is intraluminal thrombus (ILT) developed inside the aneurysms, consisting of blood proteins, platelets, and cells. Platelets stick the vortex ring generated inside the aneurysm throughout the cardiac cycle, and are transported from proximal to distal end, released during vortex break up. They adhere to low wall shear stress sites, which will lead to thrombus formation (Biasetti et al., 2011; O'Rourke et al., 2012). The question that ILT formation decreases the rupture risk or not still has controversy. In an experimental and numerical study

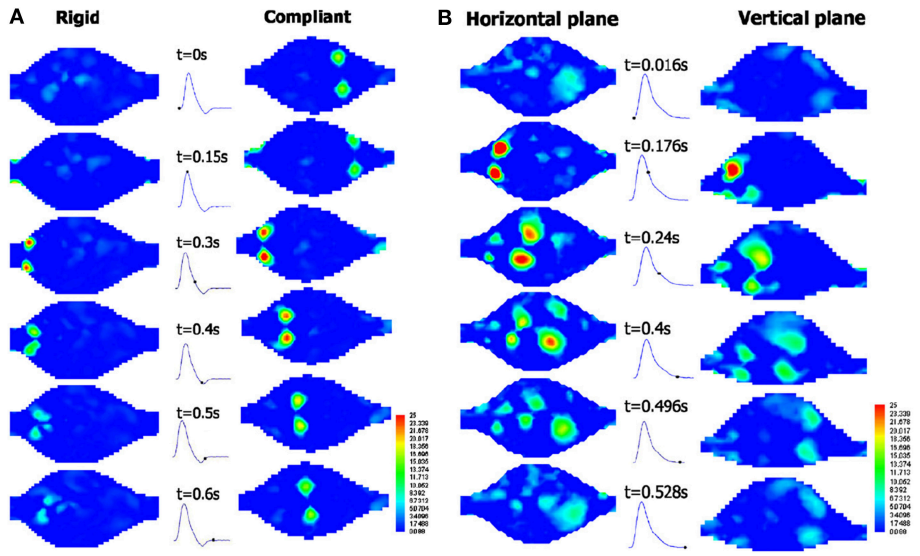

FIGURE 13 | Temporal evolution of the swirling strength λ_{ci} at different time instants in **(A)** the rigid model and the compliant model in horizontal plane, and **(B)** the compliant model at horizontal and vertical planes, under exercise conditions. During the deceleration phase for the compliant model, vortices impact on the walls and swirling strength increases, including vortex shedding occurrence [The figure is adapted from Deplano et al. (2007) and used with permission].

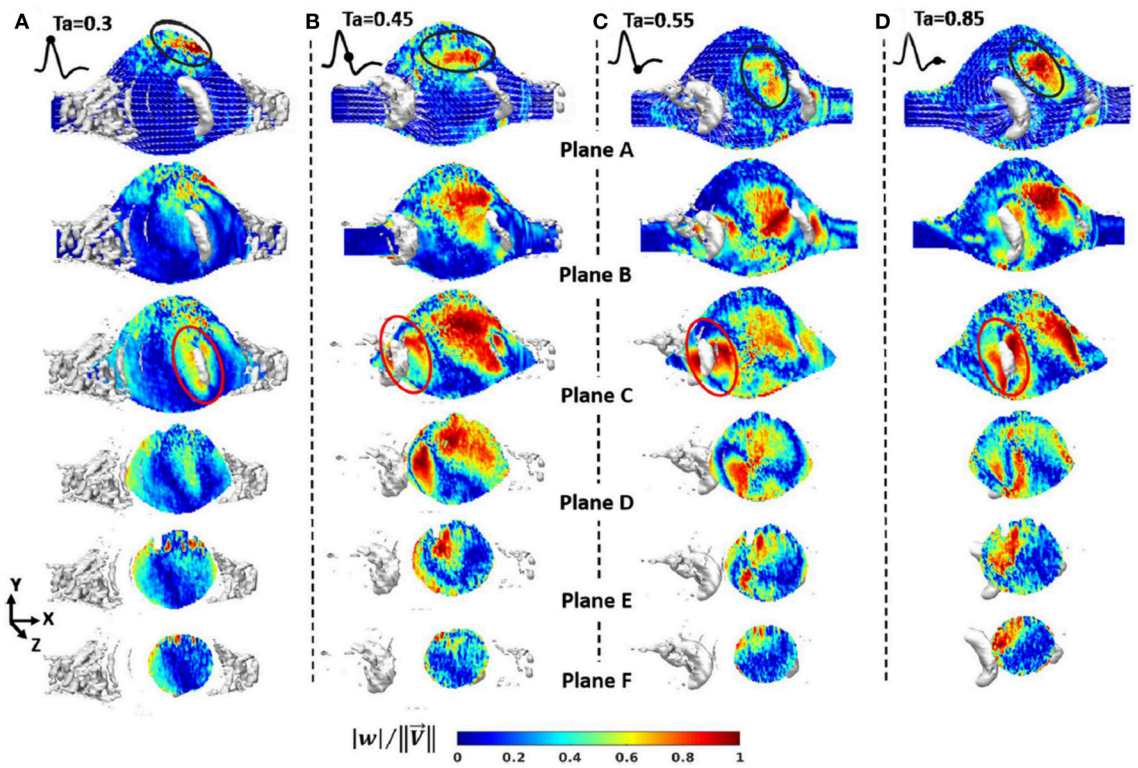

FIGURE 14 | Contours of $\frac{|w|}{\|\vec{V}\|}$ from Stereoscopic PIV measurements in six planes and four time instants of cardiac cycle **(A)** $T_a = 0.3$; maximum flow rate, **(B)** $T_a = 0.45$; decelerating flow rate, **(C)** $T_a = 0.55$; minimum flow rate, **(D)** $T_a = 0.85$; flow rate is nearly zero. Velocity vector projection and isosurface $\lambda_{ci} = 8$ (in white) is imposed on each plane. Flow stagnation area (in black) is represented by weak components of velocity vectors [The figure is adapted from Deplano et al. (2016) and used with permission].

on AAA with and without ILT, it is reported that a recirculation region is generated inside AAA without thrombus while it is disappeared in AAA with ILT (Chen et al., 2014), and there are several studies that are seeking the governing hemodynamic parameters affecting platelet deposition (Deplano et al., 2013, 2014).

As the patient-specific studies, there are a few examples such as Particle Tracking Velocimetry (PTV) study of Boutsianis et al. (2008) and PIV study of Stamatopoulos et al. (2011), where they report that WSS have the peak values at the proximal and distal sites, like in simplified bulges, and the velocity waveform at the anterior site is highly disturbed because the vortex is generated and transmitted to downstream at this site, rather than posterior.

For mimicking the shear stress and shear strain rate relation of blood, Deplano et al. (2014) have used Xanthane Gum dissolved in aqueous solutions of glycerol, a shear thinning fluid, where they report that shear thinning fluid model imposes higher shear stress values throughout the aneurysm bulge than Newtonian model. They conclude that the rheology of working fluid affects the hemodynamics inside aneurysm model, and should be taken into account for more realistic experimentation. On the other hand, in another study which is performed on a curved artery model with again a shear thinning fluid, mixture of fluids like Xanthane Gum, glycerin, water, and sodium iodide (Najjari and Plesniak, 2016). The results are very similar to the studies for curved arteries with Newtonian fluids, concluding that for large arteries with large flow rates, rheology of the blood does not affect the flow structure. However, at that point it is important to note that, they have utilized comparatively high sodium iodide concentration in their mixture than required to resolve the refractive index problems, leading that their working fluid is less viscoelastic than the blood.

CONCLUSION

Experimental and computational studies indicate that a certain number of parameters can be interpreted as the indicators of the rupture. Typically, the peak values of WSS and wall stress (structural stress) are interpreted as the footprints of an upcoming rupture. Some key parameters that are derived from WSS, such as TAWSS, OSI, and ECAP are also utilized to detect candidate locations of the rupture (Arzani and Shadden, 2015; Arzani, 2018; Singh et al., 2018). Unfortunately, determining the exact location of rupture by deciding the most effective hemodynamic parameter is still a controversial issue. For improved rupture risk assessment, ILT and plaque formations, patient-specific boundary conditions, arterial thickness variation, and heterogeneous material properties of arterial wall should be considered in a comprehensive computational analysis. For the experimental studies, flow loop should exactly replicate the *in-vivo* characteristics using a programmable, real time physiological pump that can supply re-producible and realistic inflow conditions to test model (Mechoor et al., 2016). In addition, lumped-parameter outlet boundary condition modules should be used to produce physiological pressures together with a compliant artery model having a patient specific geometry. The main purpose of these studies, in the end, should be to obtain a clinically useful tool in decision making step to understand whether the repair is necessary or not. In addition to mechanical analyses, the genetic aspect of the problem should be taken into account, since the disturbed biomechanical environment inside the aneurysm may affect gene expression patterns which may result in altered growth at later stages (Krishna et al., 2010).

AUTHOR CONTRIBUTIONS

HS and BR wrote the first draft and revised the manuscript. MY and HY structured, reviewed, and revised the manuscript. All authors read and approved the submitted version of the manuscript.

FUNDING

Qatar National Research Fund (QNRF), National Priority Research Program NPRP 10-0123-170222.

ACKNOWLEDGMENTS

The publication of this article was funded by the Qatar National Library.

REFERENCES

Adolph, R., Vorp, D. A., Steed, D. L., Webster, M. W., Kameneva, M. V., and Watkins, S. C. (1997). Cellular content and permeability of intraluminal thrombus in abdominal aortic aneurysm. *J. Vasc. Surg.* 25, 916–926. doi: 10.1016/S0741-5214(97)70223-4

Adrian, R. J. (1991). Particle-imaging Techniques for experimental fluid mechanics. *Annu. Rev. Fluid Mech.* 23, 261–304. doi: 10.1146/annurev.fl.23.010191.001401

Allard, L., Soulez, G., Chayer, B., Qin, Z., Roy, D., and Cloutier, G. (2013). A multimodality vascular imaging phantom of an abdominal aortic aneurysm with a visible thrombus. *Med. Phys.* 40:063701. doi: 10.1118/1.4803497

Amindari, A., Saltik, L., Kirkkopru, K., Yacoub, M., and Yalcin, H. C. (2017). Assessment of calcified aortic valve leaflet deformations and blood flow dynamics using fluid-structure interaction modeling. *Inf. Med. Unlock.* 9, 191–199. doi: 10.1016/j.imu.2017.09.001

Anjum, A., von Allmen, R., Greenhalgh, R., and Powell, J. T. (2012). Explaining the decrease in mortality from abdominal aortic aneurysm rupture. *BJS* 99, 637–645. doi: 10.1002/bjs.8698

Arzani, A. (2018). Accounting for residence-time in blood rheology models: do we really need non-Newtonian blood flow modelling in large arteries? *J. R. Soc. Interface* 15:20180486. doi: 10.1098/rsif.2018.0486

Arzani, A., Gambaruto, A., Chen, G., and Shadden, S. (2017). Wall shear stress exposure time: a Lagrangian measure of near-wall stagnation and concentration in cardiovascular flows. *Biomech. Model. Mechanobiol.* 16, 787–803. doi: 10.1007/s10237-016-0853-7

Arzani, A., and Shadden, S. C. (2015). Characterizations and correlations of wall shear stress in aneurysmal flow. *J. Biomech. Eng.* 138:014503. doi: 10.1115/1.4032056

Arzani, A., Suh, G.-Y., Dalman, R. L., and Shadden, S. C. (2014). A longitudinal comparison of hemodynamics and intraluminal thrombus deposition in

abdominal aortic aneurysms. *Am . J. Physiol. Heart Circ. Physiol.* 307, H1786–H1795. doi: 10.1152/ajpheart.00461.2014

Asbury, C. L., Ruberti, J. W., Bluth, E. I., and Peattie, R. A. (1995). Experimental investigation of steady flow in rigid models of abdominal aortic aneurysms. *Ann. Biomed. Eng.* 23, 29–39. doi: 10.1007/BF02368298

Bathe, K.-J., Hou, Z., and Ji, S. (1999). Finite element analysis of fluid flows fully coupled with structural interactions. *Comput. Struct.* 72, 1–16. doi: 10.1016/S0045-7949(99)00042-5

Bathe, K.-J., and Zhang, H. (2004). Finite element developments for general fluid flows with structural interactions. *Int. J. Numer. Methods Eng.* 60, 213–232. doi: 10.1002/nme.959

Bengtsson, H., and Bergqvist, D. (1993). Ruptured abdominal aortic aneurysm: a population-based study. *J. Vasc. Surg.* 18, 74–80. doi: 10.1067/mva.1993.42107

Berger, S. A., and Jou, L. D. (2000). Flows in Stenotic Vessels. *Annu. Rev. Fluid Mech.* 32, 347–382. doi: 10.1146/annurev.fluid.32.1.347

Biasetti, J., Hussain, F., and Gasser, T. C. (2011). Blood flow and coherent vortices in the normal and aneurysmatic aortas: a fluid dynamical approach to intra-luminal thrombus formation. *J. R. Soc. Interface.* 8, 1449–61. doi: 10.1098/rsif.2011.0041

Biasetti, J., Spazzini, P. G., Swedenborg, J., and Gasser, T. (2012). An integrated fluid-chemical model toward modeling the formation of intra-luminal thrombus in abdominal aortic aneurysms. *Front. Physiol.* 3:266. doi: 10.3389/fphys.2012.00266

Biglino, G., Verschueren, P., Zegels, R., Taylor, A. M., and Schievano, S. (2013). Rapid prototyping compliant arterial phantoms for *in-vitro* studies and device testing. *J. Cardiovasc. Magn. Reson.* 15:2. doi: 10.1186/1532-429X-15-2

Bluestein, D., Dumont, K., De Beule, M., Ricotta, J., Impellizzeri, P., Verhegghe, B., et al. (2009). Intraluminal thrombus and risk of rupture in patient specific abdominal aortic aneurysm – FSI modelling. *Comput. Methods Biomech. Biomed. Eng.* 12, 73–81. doi: 10.1080/10255840802176396

Bluestein, D., Niu, L., Schoephoerster, R. T., and Dewanjee, M. K. (1996). Steady flow in an aneurysm model: correlation between fluid dynamics and blood platelet deposition. *J. Biomech. Eng.* 118, 280–286. doi: 10.1115/1.2796008

Böckler, D., Holden, A., Thompson, M., Hayes, P., Krievins, D., de Vries, J.-P. P. M., et al. (2015). Multicenter nellix endovascular aneurysm sealing system experience in aneurysm sac sealing. *J. Vasc. Surg.* 62, 290–298. doi: 10.1016/j.jvs.2015.03.031

Bouremel, Y., Yianneskis, M., and Ducci, A. (2009). On the utilisation of vorticity and strain dynamics for improved analysis of stirred processes. *Chem. Eng. Res. Des.* 87, 377–385. doi: 10.1016/j.cherd.2008.11.016

Boutsianis, E., Guala, M., Olgac, U., Wildermuth, S., Hoyer, K., Ventikos, Y., et al. (2008). CFD and PTV steady flow investigation in an anatomically accurate abdominal aortic aneurysm. *J. Biomech. Eng.* 131:011008. doi: 10.1115/1.3002886

Budwig, R. (1994). Refractive index matching methods for liquid flow investigations. *Exp. Fluids* 17, 350–355. doi: 10.1007/BF01874416

Canchi, T., Saxena, A., Ng, E. Y. K., Pwee, E. C. H., and Narayanan, S. (2018). Application of fluid–structure interaction methods to estimate the mechanics of rupture in asian abdominal aortic aneurysms. *Bionanoscience* 8, 1035–1044. doi: 10.1007/s12668-018-0554-z

Casciaro, M. E., Dottori, J., El-Batti, S., Alsac, J.-M., Mousseaux, E., Larrabide, I., et al. (2018). Effects on aortoiliac fluid dynamics after endovascular sealing of abdominal aneurysms. *Vasc. Endovascular Surg.* 52, 621–628. doi: 10.1177/1538574418791059

Celik, I., Klein, M., and Janicka, J. (2009). Assessment measures for engineering LES applications. *J. Fluids Eng.* 131:031102. doi: 10.1115/1.3059703

Chandra, S., Raut, S. S., Jana, A., Biederman, R. W., Doyle, M., Muluk, S. C., et al. (2013). Fluid-structure interaction modeling of abdominal aortic aneurysms: the impact of patient-specific inflow conditions and fluid/solid coupling. *J. Biomech. Eng.* 135, 081001. doi: 10.1115/1.4024275

Chen, C.-Y., Antón, R., Hung, M.-Y., Menon, P., Finol, E. A., and Pekkan, K. (2014). Effects of intraluminal thrombus on patient-specific abdominal aortic aneurysm hemodynamics via stereoscopic particle image velocity and computational fluid dynamics modeling. *J. Biomech. Eng.* 136:031001. doi: 10.1115/1.4026160

Chen, C. Y., Hung, M. Y., Finol, E. A., and Pekkan, K. (2015). Experimental and computational investigation of the patient-specific abdominal aortic aneurysm pressure field AU - Antón, R. *Comput. Methods Biomech. Biomed. Eng.* 18, 981–992. doi: 10.1080/10255842.2013.865024

Choudhury, S., Anupindi, K., and Patnaik, B. S. V. (2019). Influence of wall shear stress and geometry on the lumen surface concentration of low density lipoprotein in a model abdominal aortic aneurysm. *Phys. Fluids* 31:011901. doi: 10.1063/1.5074125

Chu, C. C., Wang, C. T., and Chang, C. C. (1995). A vortex ring impinging on a solid plane surface—Vortex structure and surface force. *Phys. Fluids* 7, 1391–1401. doi: 10.1063/1.868527

Corbett, T. J., Doyle, B. J., Callanan, A., Walsh, M. T., and McGloughlin, T. M. (2009). Engineering silicone rubbers for *in vitro* studies: creating AAA models and ILT analogues with physiological properties. *J. Biomech. Eng.* 132:011008. doi: 10.1115/1.4000156

Cosford, P. A., and Leng, G. C. (2007). *Screening for Abdominal Aortic Aneurysm*. The Cochrane database of systematic reviews. Available online at: http://europepmc.org/abstract/MED/17443519 (accessed April 24, 2019)

Darling, R. C., Messina, C. R., Brewster, D. C., and Ottinger, L. W. (1977). Autopsy study of unoperated abdominal aortic aneurysms. The case for early resection. *Circulation* 56 (3 Suppl.), II161–164.

Deplano, V., Guivier-Curien, C., and Bertrand, E. (2016). 3D analysis of vortical structures in an abdominal aortic aneurysm by stereoscopic PIV. *Exp. Fluids* 57:167. doi: 10.1007/s00348-016-2263-0

Deplano, V., Knapp, Y., Bailly, L., and Bertrand, E. (2014). Flow of a blood analogue fluid in a compliant abdominal aortic aneurysm model: experimental modelling. *J. Biomech.* 47, 1262–1269. doi: 10.1016/j.jbiomech.2014.02.026

Deplano, V., Knapp, Y., Bertrand, E., and Gaillard, E. (2007). Flow behaviour in an asymmetric compliant experimental model for abdominal aortic aneurysm. *J. Biomech.* 40, 2406–2413. doi: 10.1016/j.jbiomech.2006.11.017

Deplano, V., Meyer, C., Guivier-Curien, C., and Bertrand, E. (2013). New insights into the understanding of flow dynamics in an *in vitro* model for abdominal aortic aneurysms. *Med. Eng. Phys.* 35, 800–809. doi: 10.1016/j.medengphy.2012.08.010

Di Achille, P., Tellides, G., Figueroa, C. A., and Humphrey, J. D. (2014). A haemodynamic predictor of intraluminal thrombus formation in abdominal aortic aneurysms. *Proc. R. Soc. A* 470:20140163. doi: 10.1098/rspa.2014.0163

Di Achille, P., Tellides, G., and Humphrey, J. D. (2016). Hemodynamics-driven deposition of intraluminal thrombus in abdominal aortic aneurysms. *Int. J. Numer. Method. Biomed. Eng.* 33:e2828. doi: 10.1002/cnm.2828

Di Martino, E., Mantero, S., Inzoli, F., Melissano, G., Astore, D., Chiesa, R., et al. (1998). Biomechanics of abdominal aortic aneurysm in the presence of endoluminal thrombus: experimental characterisation and structural static computational analysis. *Eur. J. Vasc. Endovasc. Surg.* 15, 290–299. doi: 10.1016/S1078-5884(98)80031-2

Di Martino, E. S., Guadagni, G., Fumero, A., Ballerini, G., Spirito, R., Biglioli, P., et al. (2001). Fluid–structure interaction within realistic three-dimensional models of the aneurysmatic aorta as a guidance to assess the risk of rupture of the aneurysm. *Med. Eng. Phys.* 23, 647–655. doi: 10.1016/S1350-4533(01)00093-5

Di Martino, E. S., and Vorp, D. A. (2003). Effect of variation in intraluminal thrombus constitutive properties on abdominal aortic aneurysm wall stress. *Ann. Biomed. Eng.* 31, 804–809. doi: 10.1114/1.1581880

Donea, J., Giuliani, S., and Halleux, J. P. (1982). An arbitrary lagrangian-eulerian finite element method for transient dynamic fluid-structure interactions. *Comput. Methods Appl. Mech. Eng.* 33, 689–723. doi: 10.1016/0045-7825(82)90128-1

Doyle, B. J., Cloonan, A. J., Walsh, M. T., Vorp, D. A., and McGloughlin, T. M. (2010). Identification of rupture locations in patient-specific abdominal aortic aneurysms using experimental and computational techniques. *J. Biomech.* 43, 1408–1416. doi: 10.1016/j.jbiomech.2009.09.057

Doyle, B. J., Corbett, T. J., Callanan, A., Walsh, M. T., Vorp, D. A., and McGloughlin, T. M. (2009a). An experimental and numerical comparison of the rupture locations of an abdominal aortic aneurysm. *J. Endovasc. Ther.* 16, 322–335. doi: 10.1583/09-2697.1

Doyle, B. J., Corbett, T. J., Cloonan, A. J., O'Donnell, M. R., Walsh, M. T., Vorp, D. A., et al. (2009b). Experimental modelling of aortic aneurysms: novel applications of silicone rubbers. *Med. Eng. Phys.* 31, 1002–1012. doi: 10.1016/j.medengphy.2009.06.002

Doyle, B. J., McGloughlin, T. M., Miller, K., Powell, J. T., and Norman, P. E. (2014). Regions of high wall stress can predict the future location of rupture of abdominal aortic aneurysm. *Cardiovasc. Intervent. Radiol.* 37, 815–818. doi: 10.1007/s00270-014-0864-7

Doyle, B. J., Morris, L. G., Callanan, A., Kelly, P., Vorp, D. A., and McGloughlin, T. M. (2008). 3D reconstruction and manufacture of real abdominal aortic aneurysms: from CT scan to silicone model. *J. Biomech. Eng.* 130:034501. doi: 10.1115/1.2907765

Drewe, C. J., Parker, L. P., Kelsey, L. J., Norman, P. E., Powell, J. T., and Doyle, B. J. (2017). Haemodynamics and stresses in abdominal aortic aneurysms: a fluid-structure interaction study into the effect of proximal neck and iliac bifurcation angle. *J. Biomech.* 60, 150–156. doi: 10.1016/j.jbiomech.2017.06.029

Duclaux, V., Gallaire, F., and Clanet, C. (2010). A fluid mechanical view on abdominal aortic aneurysms. *J. Fluid Mech.* 664, 5–32. doi: 10.1017/S0022112010003782

Durst, F., Ray, S., Ünsal, B., and Bayoumi, O.A. (2005). The development lengths of laminar pipe and channel flows. *J. Fluids Eng.* 127, 1154–1160. doi: 10.1115/1.2063088

Egelhoff, C. J., Budwig, R. S., Elger, D. F., Khraishi, T. A., and Johansen, K. H. (1999). Model studies of the flow in abdominal aortic aneurysms during resting and exercise conditions. *J. Biomech.* 32, 1319–1329. doi: 10.1016/S0021-9290(99)00134-7

Ene, F., Gachon, C., Delassus, P., Carroll, R., Stefanov, F., O'Flynn, P., et al. (2011). *In vitro* evaluation of the effects of intraluminal thrombus on abdominal aortic aneurysm wall dynamics. *Med. Eng. Phys.* 33, 957–966. doi: 10.1016/j.medengphy.2011.03.005

Ene-Iordache, B., and Remuzzi, A. (2012). Disturbed flow in radial-cephalic arteriovenous fistulae for haemodialysis: low and oscillating shear stress locates the sites of stenosis. *Nephrol. Dialysis Trans.* 27, 358–368. doi: 10.1093/ndt/gfr342

Feng, Y., Wada, S., Ishikawa, T., Tsubota, K.-I., and Yamaguchi, T. (2008). A rule-based computational study on the early progression of intracranial aneurysms using fluid-structure interaction: comparison between straight model and curved model. *J. Biomech. Sci. Eng.* 3, 124–137. doi: 10.1299/jbse.3.124

Field, D. A. (1988). Laplacian smoothing and delaunay triangulations. *Commun. Appl. Num. Methods* 4, 709–712. doi: 10.1002/cnm.1630040603

Fillinger, M. F., Marra, S. P., Raghavan, M. L., and Kennedy, F. E. (2003). Prediction of rupture risk in abdominal aortic aneurysm during observation: wall stress versus diameter. *J. Vasc. Surg.* 37, 724–732. doi: 10.1067/mva.2003.213

Fillinger, M. F., Raghavan, M. L., Marra, S. P., Cronenwett, J. L., and Kennedy, F. E. (2002). *In vivo* analysis of mechanical wall stress and abdominal aortic aneurysm rupture risk. *J. Vasc. Surg.* 36, 589–597. doi: 10.1067/mva.2002.125478

Formaggia, L., Lamponi, D., and Quarteroni, A. (2003). One-dimensional models for blood flow in arteries. *J. Eng. Math.* 47, 251–276. doi: 10.1023/B:ENGI.0000007980.01347.29

Franck, G., Dai, J., Fifre, A., Ngo, S., Justine, C., Michineau, S., et al. (2013). Reestablishment of the endothelial lining by endothelial cell therapy stabilizes experimental abdominal aortic aneurysms. *Circulation* 127, 1877–1887. doi: 10.1161/CIRCULATIONAHA.113.001677

Frayne, R., Holdsworth, D. W., Gowman, L. M., Rickey, D. W., Drangova, M., Fenster, A., et al. (1992). Computer-controlled flow simulator for MR flow studies. *J. Magn. Reson. Imaging* 2, 605–612. doi: 10.1002/jmri.1880020522

Fukushima, T., Matsuzawa, T., and Homma, T. (1989). Visualization and finite element analysis of pulsatile flow in models of the abdominal aortic aneurysm. *Biorheology* 26, 109–130. doi: 10.3233/BIR-1989-26203

Gaillard, E., and Deplano, V. (2005). Experimental study of the hemodynamics in an abdominal aortic aneurysm under physiological resting and exercise flow conditions. *Comput. Methods Biomech. Biomed. Engin.* 8, 109–110. doi: 10.1080/10255840512331388498

Gao, F., Ueda, H., Gang, L., and Okada, H. (2013). Fluid structure interaction simulation in three-layered aortic aneurysm model under pulsatile flow: comparison of wrapping and stenting. *J. Biomech.* 46, 1335–1342. doi: 10.1016/j.jbiomech.2013.02.002

Gleason, R. L., and Humphrey, J. D. (2005). Effects of a sustained extension on arterial growth and remodeling: a theoretical study. *J. Biomech.* 38, 1255–1261. doi: 10.1016/j.jbiomech.2004.06.017

Groves, E. M., Falahatpisheh, A., Su, J. L., and Kheradvar, A. (2014). The effects of positioning of transcatheter aortic valves on fluid dynamics of the aortic root. *ASAIO J.* 60, 545–552. doi: 10.1097/MAT.0000000000000107

He, X., and Ku, D. N. (1994). Unsteady entrance flow development in a straight tube. *J. Biomech. Eng.* 116, 355–360. doi: 10.1115/1.2895742

Hinnen, J.-W., Koning, O. H. J., Visser, M. J. T., and Van Bockel, H. J. (2005). Effect of intraluminal thrombus on pressure transmission in the abdominal aortic aneurysm. *J. Vasc. Surg.* 42, 1176–1182. doi: 10.1016/j.jvs.2005.08.027

Ho, C. K., Chee, A. J. Y., Yiu, B. Y. S., Tsang, A. C. O., Chow, K. W., and Yu, A. C. H. (2017). Wall-less flow phantoms with tortuous vascular geometries: design principles and a patient-specific model fabrication example. *IEEE Trans. Ultrason. Ferroelectr. Freq. Control* 64, 25–38. doi: 10.1109/TUFFC.2016.2636129

Holzapfel, G. A., Gasser, T. C., and Ogden, R. W. (2000). A new constitutive framework for arterial wall mechanics and a comparative study of material models. *J. Elasticity Phys. Sci. Solids* 61, 1–48. doi: 10.1007/0-306-48389-0_1

Houard, X., Rouzet, F., Touat, Z., Philippe, M., Dominguez, M., Fontaine, V., et al. (2007). Topology of the fibrinolytic system within the mural thrombus of human abdominal aortic aneurysms. *J. Pathol.* 212, 20–28. doi: 10.1002/path.2148

Hua, J., and Mower, W. R. (2001). Simple geometric characteristics fail to reliably predict abdominal aortic aneurysm wall stresses. *J. Vasc. Surg.* 34, 308–315. doi: 10.1067/mva.2001.114815

Humphrey, J. D., and Holzapfel, G. A. (2012). Mechanics, mechanobiology, and modeling of human abdominal aorta and aneurysms. *J. Biomech.* 45, 805–814. doi: 10.1016/j.jbiomech.2011.11.021

Humphrey, J. D., and Rajagopal, K. R. (2003). A constrained mixture model for arterial adaptations to a sustained step change in blood flow. *Biomech. Model. Mechanobiol.* 2, 109–126. doi: 10.1007/s10237-003-0033-4

Humphrey, J. D., and Taylor, C. A. (2008). Intracranial and abdominal aortic aneurysms: similarities, differences, and need for a new class of computational models. *Annu. Rev. Biomed. Eng.* 10, 221–246. doi: 10.1146/annurev.bioeng.10.061807.160439

Ionita, C. N., Mokin, M., Varble, N., Bednarek, D. R., Xiang, J., Snyder, K. V., et al. (2014). Challenges and limitations of patient-specific vascular phantom fabrication using 3D Polyjet printing. *Proc. SPIE–Int. Soc. Opt. Eng.* 9038:90380M. doi: 10.1117/12.2042266

Kandail, H., Hamady, M., and Xu, X. Y. (2015). Comparison of blood flow in branched and fenestrated stent-grafts for endovascular repair of abdominal aortic aneurysms. *J. Endovasc. Ther.* 22, 578–590. doi: 10.1177/1526602815587261

Karšaj, I., and Humphrey, J. D. (2012). A multilayered wall model of arterial growth and remodeling. *Mech. Mater.* 44, 110–119. doi: 10.1016/j.mechmat.2011.05.006

Kelsey, L. J., Powell, J. T., Norman, P. E., Miller, K., and Doyle, B. J. (2016). A comparison of hemodynamic metrics and intraluminal thrombus burden in a common iliac artery aneurysm. *Int. J. Numer. Method. Biomed. Eng.* 33:e2821. doi: 10.1002/cnm.2821

Khanafer, K., and Berguer, R. (2009). Fluid–structure interaction analysis of turbulent pulsatile flow within a layered aortic wall as related to aortic dissection. *J. Biomech.* 42, 2642–2648. doi: 10.1016/j.jbiomech.2009.08.010

Khanafer, K. M., Bull, J. L., Upchurch, G. R., and Berguer, R. (2007). Turbulence significantly increases pressure and fluid shear stress in an aortic aneurysm model under resting and exercise flow conditions. *Ann. Vasc. Surg.* 21, 67–74. doi: 10.1016/j.avsg.2006.10.009

Khanafer, K. M., Gadhoke, P., Berguer, R., and Bull, J. L. (2006). Modeling pulsatile flow in aortic aneurysms: effect of non-Newtonian properties of blood. *Biorheology* 43, 661–679.

Kontopodis, N., Metaxa, E., Papaharilaou, Y., Tavlas, E., Tsetis, D., and Ioannou, C. (2014). Advancements in identifying biomechanical determinants for abdominal aortic aneurysm rupture. *Vascular* 23, 65–77. doi: 10.1177/1708538114532084

Kose, U., Putter, S. D., Hoogeveen, R., and Breeuwer, M. (2006). "Computational fluid dynamics of abdominal aortic aneurysms with patient-specific inflow boundary conditions," in *Medical Imaging: SPIE* (San Diego, CA), 11. doi: 10.1117/12.649755

Krishna, S. M., Dear, A. E., Norman, P. E., and Golledge, J. (2010). Genetic and epigenetic mechanisms and their possible role in abdominal aortic aneurysm. *Atherosclerosis* 212, 16–29. doi: 10.1016/j.atherosclerosis.2010.02.008

Ku, D. N. (1997). Blood flow in arteries. *Annu. Rev. Fluid Mech.* 29, 399–434. doi: 10.1146/annurev.fluid.29.1.399

Ku, D. N., Glagov, S., Moore, J. E., and Zarins, C. K. (1989). Flow patterns in the abdominal aorta under simulated postprandial and exercise conditions: an experimental study. *J. Vasc. Surg.* 9, 309–316. doi: 10.1016/0741-5214(89)90051-7

Kung, E. O., Les, A. S., Medina, F., Wicker, R. B., McConnell, M. V., and Taylor, C. A. (2011). *In vitro* validation of finite-element model of AAA hemodynamics incorporating realistic outlet boundary conditions. *J. Biomech. Eng.* 133:041003. doi: 10.1115/1.4003526

Lasheras, J. C. (2006). The Biomechanics of Arterial Aneurysms. *Annu. Rev. Fluid Mech.* 39, 293–319. doi: 10.1146/annurev.fluid.39.050905.110128

Les, A. S., Shadden, S. C., Figueroa, C. A., Park, J. M., Tedesco, M. M., Herfkens, R. J., et al. (2010). Quantification of hemodynamics in abdominal aortic aneurysms during rest and exercise using magnetic resonance imaging and computational fluid dynamics. *Ann. Biomed. Eng.* 38, 1288–1313. doi: 10.1007/s10439-010-9949-x

Longo, C., and Upchurch, G. R. (2005). Abdominal aortic aneurysm screening: recommendations and controversies. *Vasc. Endovascular Surg.* 39, 213–219. doi: 10.1177/153857440503900301

Mandal, P. K. (2005). An unsteady analysis of non-Newtonian blood flow through tapered arteries with a stenosis. *Int. J. Non Linear Mech.* 40, 151–164. doi: 10.1016/j.ijnonlinmec.2004.07.007

McGloughlin Timothy, M., and Doyle Barry, J. (2010). New approaches to abdominal aortic aneurysm rupture risk assessment. *Arterioscler. Thromb. Vasc. Biol.* 30, 1687–1694. doi: 10.1161/ATVBAHA.110.204529

Mechoor, R. R., Schmidt, T., and Kung, E. (2016). A real-time programmable pulsatile flow pump for *in vitro* cardiovascular experimentation. *J. Biomech. Eng.* 138:111002. doi: 10.1115/1.4034561

Meyer, C. A., Bertrand, E., Boiron, O., and Deplano, V. (2011). Stereoscopically observed deformations of a compliant abdominal aortic aneurysm model. *J. Biomech. Eng.* 133:111004. doi: 10.1115/1.4005416

Mohamied, Y., Rowland, E. M., Bailey, E. L., Sherwin, S. J., Schwartz, M. A., and Weinberg, P. D. (2015). Change of direction in the biomechanics of atherosclerosis. *Ann. Biomed. Eng.* 43, 16–25. doi: 10.1007/s10439-014-1095-4

Moore, J. J. E., and Ku, D. N. (1994). Pulsatile velocity measurements in a model of the human abdominal aorta under simulated exercise and postprandial conditions. *J. Biomech. Eng.* 116, 107–111. doi: 10.1115/1.2895692

Moore, J. J. E., Ku, D. N., Zarins, C. K., and Glagov, S. (1992). Pulsatile flow visualization in the abdominal aorta under differing physiologic conditions: implications for increased susceptibility to atherosclerosis. *J. Biomech. Eng.* 114, 391–397. doi: 10.1115/1.2891400

Morris, L., Stefanov, F., and McGloughlin, T. (2013). Stent graft performance in the treatment of abdominal aortic aneurysms: The influence of compliance and geometry. *J. Biomech.* 46, 383–395. doi: 10.1016/j.jbiomech.2012.11.026

Mower, W. R., Quiñones, W. J., and Gambhir, S. S. (1997). Effect of intraluminal thrombus on abdominal aortic aneurysm wall stress. *J. Vasc. Surg.* 26, 602–608. doi: 10.1016/S0741-5214(97)70058-2

Najjari, M. R., and Plesniak, M. W. (2016). Evolution of vortical structures in a curved artery model with non-Newtonian blood-analog fluid under pulsatile inflow conditions. *Exp. Fluids* 57:100. doi: 10.1007/s00348-016-2188-7

Nerem, R. M. (1984). Atherogenesis: hemodynamics, vascular geometry, and the endothelium. *Biorheology* 21, 565–569. doi: 10.3233/BIR-1984-21415

Nikolaidis, N. M., and Mathioulakis, D. S. (2002). Axial and secondary flow study in a 90 deg bifurcation under pulsating conditions using PIV. *J. Fluids Eng.* 124, 505–511. doi: 10.1115/1.1470478

O'Leary, S., Kavanagh, E., Grace, P., McGloughlin, T., and Doyle, B. (2013). "Determination of layer and region specific mechanical properties of intraluminal thrombus (ILT): the importance of biaxial tensile testing," in *ASME 2013 Summer Bioengineering Conference* (Sunriver, OR). doi: 10.1115/SBC2013-14237

O'Leary, S. A., Kavanagh, E. G., Grace, P. A., McGloughlin, T. M., and Doyle, B. J. (2014). The biaxial mechanical behaviour of abdominal aortic aneurysm intraluminal thrombus: Classification of morphology and the determination of layer and region specific properties. *J. Biomech.* 47, 1430–1437. doi: 10.1016/j.jbiomech.2014.01.041

O'Leary, S. A., Mulvihill, J. J., Barrett, H. E., Kavanagh, E. G., Walsh, M. T., McGloughlin, T. M., et al. (2015). Determining the influence of calcification on the failure properties of abdominal aortic aneurysm (AAA) tissue. *J. Mech. Behav. Biomed. Mater.* 42, 154–167. doi: 10.1016/j.jmbbm.2014.11.005

O'Rourke, M. J., and McCullough, J. P. (2010). An investigation of the flow field within patient-specific models of an abdominal aortic aneurysm under steady inflow conditions. *Proc.Inst. Mech. Eng. H* 224, 971–988. doi: 10.1243/09544119JEIM694

O'Rourke, M. J., McCullough, J. P., and Kelly, S. (2012). An investigation of the relationship between hemodynamics and thrombus deposition within patient-specific models of abdominal aortic aneurysm. *Proc. Inst. Mech. Eng. Part H* 226, 548–564. doi: 10.1177/0954411912444080

Owen, B., Lowe, C., Ashton, N., Mandal, P., Rogers, S., Wein, W., et al. (2016). Computational hemodynamics of abdominal aortic aneurysms: three-dimensional ultrasound versus computed tomography. *Proc. Inst. Mech. Eng. Part H* 230, 201–210. doi: 10.1177/0954411915626742

Pahlevan, N. M., and Gharib, M. (2013). *In-vitro* investigation of a potential wave pumping effect in human aorta. *J. Biomech.* 46, 2122–2129. doi: 10.1016/j.jbiomech.2013.07.006

Papaharilaou, Y., Ekaterinaris, J. A., Manousaki, E., and Katsamouris, A. N. (2007). A decoupled fluid structure approach for estimating wall stress in abdominal aortic aneurysms. *J. Biomech.* 40, 367–377. doi: 10.1016/j.jbiomech.2005.12.013

Peattie, R. A., Asbury, C. L., Bluth, E. I., and Riehle, T. J. (1996). Steady flow in models of abdominal aortic aneurysms. Part II: Wall stresses and their implication for *in vivo* thrombosis and rupture. *J. Ultrasound Med.* 15, 689–696. doi: 10.7863/jum.1996.15.10.689

Peattie, R. A., Riehle, T. J., and Bluth, E. I. (2004). Pulsatile flow in fusiform models of abdominal aortic aneurysms: flow fields, velocity patterns and flow-induced wall stresses. *J. Biomech. Eng.* 126, 438–446. doi: 10.1115/1.1784478

Poelma, C., Watton Paul, N., and Ventikos, Y. (2015). Transitional flow in aneurysms and the computation of haemodynamic parameters. *J. R. Soc. Interface* 12:20141394. doi: 10.1098/rsif.2014.1394

Poepping, T. L., Nikolov, H. N., Thorne, M. L., and Holdsworth, D. W. (2004). A thin-walled carotid vessel phantom for Doppler ultrasound flow studies. *Ultrasound Med. Biol.* 30, 1067–1078. doi: 10.1016/j.ultrasmedbio.2004.06.003

Qiu, Y., Yuan, D., Wen, J., Fan, Y., and Zheng, T. (2018). Numerical identification of the rupture locations in patient-specific abdominal aortic aneurysmsusing hemodynamic parameters. *Comput. Methods Biomech. Biomed. Engin.* 21, 1–12. doi: 10.1080/10255842.2017.1410796

Raghavan, M., Kratzberg, J., and da Silva, E. S.o. (2004). "Heterogeneous, variable wall-thickness modeling of a ruptured abdominal aortic aneurysm," in *ASME International Mechanical Engineering Congress and Exposition* (Anaheim, CA), 271–272. doi: 10.1115/IMECE2004-60018

Raghavan, M. L., Kratzberg, J., Castro de Tolosa, E. M., Hanaoka, M. M., Walker, P., and da Silva, E. S. (2006). Regional distribution of wall thickness and failure properties of human abdominal aortic aneurysm. *J. Biomech.* 39, 3010–3016. doi: 10.1016/j.jbiomech.2005.10.021

Raghavan, M. L., and Vorp, D. A. (2000). Toward a biomechanical tool to evaluate rupture potential of abdominal aortic aneurysm: identification of a finite strain constitutive model and evaluation of its applicability. *J. Biomech.* 33, 475–482. doi: 10.1016/S0021-9290(99)00201-8

Raghavan, M. L., Vorp, D. A., Federle, M. P., Makaroun, M. S., and Webster, M. W. (2000). Wall stress distribution on three-dimensionally reconstructed models of human abdominal aortic aneurysm. *J. Vasc. Surg.* 31, 760–769. doi: 10.1067/mva.2000.103971

Raptis, A., Xenos, M., Georgakarakos, E., Kouvelos, G., Giannoukas, A., and Matsagkas, M. (2017). Hemodynamic profile of two aortic endografts accounting for their postimplantation position. *J. Med. Devices* 11:021003. doi: 10.1115/1.4035687

Rivlin, R. S., and Saunders, D. (1951). Large elastic deformations of isotropic materials VII. Experiments on the deformation of rubber. *Philos. Trans. R. Soc. Lond. Ser. A Math. Phys. Sci.* 243, 251–288. doi: 10.1098/rsta.1951.0004

Roloff, C., Berg, P., Redel, T., Janiga, G., and Thévenin, D. (2017). "Tomographic particle image velocimetry for the validation of hemodynamic simulations in an intracranial aneurysm," in *2017 39th Annual International Conference of the IEEE Engineering in Medicine and Biology Society (EMBC)* (Jeju Island), 1340–1343. doi: 10.1109/EMBC.2017.8037080

Roloff, C., Stucht, D., Beuing, O., and Berg, P. (2018). Comparison of intracranial aneurysm flow quantification techniques: standard PIV vs. stereoscopic PIV vs. tomographic PIV vs. phase-contrast MRI vs. CFD. *J. Neurointerven. Surg. Neurintsurg.* 11, 275–282. doi: 10.1136/neurintsurg-2018-013921

Sakalihasan, N., Limet, R., and Defawe, O. D. (2005). Abdominal aortic aneurysm. *Lancet* 365, 1577–1589. doi: 10.1016/S0140-6736(05)66459-8

Salsac, A.-V., Sparks, S. R., Chomaz, J.-M., and Lasheras, J. C. (2006). Evolution of the wall shear stresses during the progressive enlargement of symmetric abdominal aortic aneurysms. *J. Fluid Mech.* 560, 19–51. doi: 10.1017/S002211200600036X

Scherer, P. W. (1973). Flow in axisymmetrical glass model aneurysms. *J. Biomech.* 6, 695–700. doi: 10.1016/0021-9290(73)90025-0

Scott, R. A. P., Ashton, H. A., Lamparelli, M. J., Harris, G. J. C., and Stevens, J. W. (2002). A 14-year experience with 6 cm as a criterion for surgical treatment of abdominal aortic aneurysm. *BJS* 86, 1317–1321. doi: 10.1046/j.1365-2168.1999.01227.x

Scotti, C. M., and Finol, E. A. (2007). Compliant biomechanics of abdominal aortic aneurysms: a fluid–structure interaction study. *Comput. Struct.* 85, 1097–1113. doi: 10.1016/j.compstruc.2006.08.041

Scotti, C. M., Jimenez, J., Muluk, S. C., and Finol, E. A. (2008). Wall stress and flow dynamics in abdominal aortic aneurysms: finite element analysis vs. fluid–structure interaction. *Comput. Methods Biomech. Biomed. Eng.* 11, 301–322. doi: 10.1080/10255840701827412

Scotti, C. M., Shkolnik, A. D., Muluk, S. C., and Finol, E. A. (2005). Fluid-structure interaction in abdominal aortic aneurysms: effects of asymmetry and wall thickness. *Biomed. Eng. Online* 4:64. doi: 10.1186/1475-925X-4-64

Shadden, S. C., and Arzani, A. (2015). Lagrangian postprocessing of computational hemodynamics. *Ann. Biomed. Eng.* 43, 41–58. doi: 10.1007/s10439-014-1070-0

Simão da Silva, E., Rodrigues, A. J., Magalhães Castro de Tolosa, E., Rodrigues, C. J., Villas Boas do Prado, G., and Nakamoto, J. C. (2000). Morphology and diameter of infrarenal aortic aneurysms: a prospective autopsy study. *Cardiovasc. Surg.* 8, 526–532. doi: 10.1016/S0967-2109(00)00060-0

Simsek, F. G., and Kwon, Y. W. (2015). Investigation of material modeling in fluid–structure interaction analysis of an idealized three-layered abdominal aorta: aneurysm initiation and fully developed aneurysms. *J. Biol. Phys.* 41, 173–201. doi: 10.1007/s10867-014-9372-x

Singh, J., Brunner, G., Morrisett, J. D., Ballantyne, C. M., Lumsden, A. B., Shah, D. J., et al. (2018). Patient-specific flow descriptors and normalised wall index in peripheral artery disease: a preliminary study. *Comput. Methods Biomech. Biomed. Eng.* 6, 119–127. doi: 10.1080/21681163.2016.1184589

Soudah, E., Ng, E. Y. K., Loong, T. H., Bordone, M., Pua, U., and Narayanan, S. (2013). CFD modelling of abdominal aortic aneurysm on hemodynamic loads using a realistic geometry with CT. *Comput. Math. Methods Med.* 2013, 472564–472564. doi: 10.1155/2013/472564

Stamatopoulos, C., Mathioulakis, D. S., Papaharilaou, Y., and Katsamouris, A. (2011). Experimental unsteady flow study in a patient-specific abdominal aortic aneurysm model. *Exp. Fluids* 50, 1695–1709. doi: 10.1007/s00348-010-1034-6

Stamatopoulos, C., Papaharilaou, Y., Mathioulakis, D. S., and Katsamouris, A. (2010). Steady and unsteady flow within an axisymmetric tube dilatation. *Exp. Thermal Fluid Sci.* 34, 915–927. doi: 10.1016/j.expthermflusci.2010.02.008

Stamhuis, E. J. (2006). Basics and principles of particle image velocimetry (PIV) for mapping biogenic and biologically relevant flows. *Aquatic Ecol.* 40, 463–479. doi: 10.1007/s10452-005-6567-z

Stringfellow, M. M., Lawrence, P. F., and Stringfellow, R. G. (1987). The influence of aorta-aneurysm geometry upon stress in the aneurysm wall. *J. Surg. Res.* 42, 425–433. doi: 10.1016/0022-4804(87)90178-8

Sughimoto, K., Takahara, Y., Mogi, K., Yamazaki, K., Tsubota, K. I., Liang, F., et al. (2014). Blood flow dynamic improvement with aneurysm repair detected by a patient-specific model of multiple aortic aneurysms. *Heart Vessels* 29, 404–412. doi: 10.1007/s00380-013-0381-7

Sulaiman, A., Roty, C., Serfaty, J. M., Attia, C., Huet, L., and Douek, P. (2008). *In vitro*, nonrigid model of aortic arch aneurysm. *J. Vasc. Interven. Radiol.* 19, 919–924. doi: 10.1016/j.jvir.2008.02.009

Sun, N., Leung, J. H., Wood, N. B., Hughes, A. D., Thom, S. A., Cheshire, N. J., et al. (2009). Computational analysis of oxygen transport in a patient-specific model of abdominal aortic aneurysm with intraluminal thrombus. *Br. J. Radiol.* 82, S18–S23. doi: 10.1259/bjr/89466318

Swedenborg, J., and Eriksson, P. E. R. (2006). The intraluminal thrombus as a source of proteolytic activity. *Ann. N. Y. Acad. Sci.* 1085, 133–138. doi: 10.1196/annals.1383.044

Tang, D., Yang, C., Zheng, J., Woodard, P. K., Saffitz, J. E., Sicard, G. A., et al. (2005). Quantifying effects of plaque structure and material properties on stress distributions in human atherosclerotic plaques using 3D FSI models. *J. Biomech. Eng.* 127, 1185–1194. doi: 10.1115/1.2073668

Tanweer, O., Wilson, T. A., Metaxa, E., Riina, H. A., and Meng, H. (2014). A comparative review of the hemodynamics and pathogenesis of cerebral and abdominal aortic aneurysms: lessons to learn from each other. *J. Cerebrovasc. Endovasc. Neurosurg.* 16, 335–349. doi: 10.7461/jcen.2014.16.4.335

Taubin, G. (1995). "Curve and surface smoothing without shrinkage," in *Proceedings of IEEE International Conference on Computer Vision* (Cambridge, MA), 852–857. doi: 10.1109/ICCV.1995.466848

Thurston, G. B. (1979). Rheological parameters for the viscosity viscoelasticity and thixotropy of blood. *Biorheology* 16, 149–162. doi: 10.3233/BIR-1979-16303

Tong, J., and Holzapfel, G. A. (2015). Structure, mechanics, and histology of intraluminal thrombi in abdominal aortic aneurysms. *Ann. Biomed. Eng.* 43, 1488–1501. doi: 10.1007/s10439-015-1332-5

Tsai, W., and Savaş, Ö. (2010). Flow pumping system for physiological waveforms. *Med. Biol. Eng. Comput.* 48, 197–201. doi: 10.1007/s11517-009-0573-6

Valentín, A., Humphrey, J. D., and Holzapfel, G. A. (2011). A multi-layered computational model of coupled elastin degradation, vasoactive dysfunction, and collagenous stiffening in aortic aging. *Ann. Biomed. Eng.* 39, 2027–2045. doi: 10.1007/s10439-011-0287-4

Valentín, A., Humphrey, J. D., and Holzapfel, G. A. (2013). A finite element-based constrained mixture implementation for arterial growth, remodeling, and adaptation: Theory and numerical verification. *Int. J. Numer. Method. Biomed. Eng.* 29, 822–849. doi: 10.1002/cnm.2555

van 't Veer, M., Buth, J., Merkx, M., Tonino, P., van den Bosch, H., Pijls, N., et al. (2008). Biomechanical properties of abdominal aortic aneurysms assessed by simultaneously measured pressure and volume changes in humans. *J. Vasc. Surg.* 48, 1401–1407. doi: 10.1016/j.jvs.2008.06.060

Vande Geest, J. P., Sacks, M. S., and Vorp, D. A. (2006a). The effects of aneurysm on the biaxial mechanical behavior of human abdominal aorta. *J. Biomech.* 39, 1324–1334. doi: 10.1016/j.jbiomech.2005.03.003

Vande Geest, J. P., Sacks, M. S., and Vorp, D. A. (2006b). A planar biaxial constitutive relation for the luminal layer of intra-luminal thrombus in abdominal aortic aneurysms. *J. Biomech.* 39, 2347–2354. doi: 10.1016/j.jbiomech.2006.05.011

Vollmer, J., Mencl, R., and Müller, H. (2001). Improved laplacian smoothing of noisy surface meshes. *Computer Graphics Forum* 18, 131–138. doi: 10.1111/1467-8659.00334

Vorp, D. A., Raghavan, M. L., Muluk, S. C., Makaroun, M. S., Steed, D. L., Shapiro, R. O. N., et al. (1996). Wall strength and stiffness of aneurysmal and nonaneurysmal abdominal aorta. *Ann. N. Y. Acad. Sci.* 800, 274–276. doi: 10.1111/j.1749-6632.1996.tb33330.x

Vorp, D. A., Raghavan, M. L., and Webster, M. W. (1998). Mechanical wall stress in abdominal aortic aneurysm: influence of diameter and asymmetry. *J. Vasc. Surg.* 27, 632–639. doi: 10.1016/S0741-5214(98)70227-7

Wang, Y., Joannic, D., Patrick, J., Keromnes, A., Aurélien, M., Lalande, A., et al. (2016). *Comparison of Flow Measurement by 4D Flow Magnetic Resonance Imaging and by Particles Image Velocimetry on Phantom of Abdominal Aortic Aneurysm*. SM Vasc Med, SM Online Scientific Resources LLC.

Watton, P. N., Hill, N. A., and Heil, M. (2004). A mathematical model for the growth of the abdominal aortic aneurysm. *Biomech. Model. Mechanobiol.* 3, 98–113. doi: 10.1007/s10237-004-0052-9

Watts, D. M., Sutcliffe, C. J., Morgan, R. H., Meagher, S., Wardlaw, J., Connell, M., et al. (2007). Anatomical flow phantoms of the nonplanar carotid bifurcation, Part I: computer-aided design and fabrication. *Ultrasound Med. Biol.* 33, 296–302. doi: 10.1016/j.ultrasmedbio.2006.08.003

Wilson, J. S., Baek, S., and Humphrey, J. D. (2013). Parametric study of effects of collagen turnover on the natural history of abdominal aortic aneurysms. *Proc. R. Soc. A* 469:20120556. doi: 10.1098/rspa.2012.0556

Wolters, B. J. B. M., Rutten, M. C. M., Schurink, G. W. H., Kose, U., de Hart, J., and van de Vosse, F. N. (2005). A patient-specific computational model of fluid–structure interaction in abdominal aortic aneurysms. *Med. Eng. Phys.* 27, 871–883. doi: 10.1016/j.medengphy.2005.06.008

Womersley, J. R. (1955). Method for the calculation of velocity, rate of flow and viscous drag in arteries when the pressure gradient is known. *J. Physiol.* 127, 553–563. doi: 10.1113/jphysiol.1955.sp005276

Wong, E. Y., Thorne, M. L., Nikolov, H. N., Poepping, T. L., and Holdsworth, D. W. (2008). Doppler ultrasound compatible plastic material for use in rigid flow models. *Ultrasound Med. Biol.* 34, 1846–1856. doi: 10.1016/j.ultrasmedbio.2008.01.002

Wu, J., and Shadden, S. C. (2015). Coupled simulation of hemodynamics and vascular growth and remodeling in a subject-specific geometry. *Ann. Biomed. Eng.* 43, 1543–1554. doi: 10.1007/s10439-015-1287-6

Xenos, M., Alemu, Y., Zamfir, D., Einav, S., Ricotta, J. J., Labropoulos, N., et al. (2010). The effect of angulation in abdominal aortic aneurysms: fluid–structure interaction simulations of idealized geometries. *Med. Biol. Eng. Comput.* 48, 1175–1190. doi: 10.1007/s11517-010-0714-y

Yip, T. H., and Yu, S. C. M. (2001). Cyclic transition to turbulence in rigid abdominal aortic aneurysm models. *Fluid Dyn. Res.* 29:81. doi: 10.1016/S0169-5983(01)00018-1

Yip, T. H., and Yu, S. C. M. (2002). Oscillatory flows in straight tubes with an axisymmetric bulge. *Exp. Thermal Fluid Sci.* 26, 947–961. doi: 10.1016/S0894-1777(02)00214-5

Young, D. F. (1979). Fluid mechanics of arterial stenoses. *J. Biomech. Eng.* 101, 157–175. doi: 10.1115/1.3426241

Yu, S. C. M. (2000). Steady and pulsatile flow studies in abdominal aortic aneurysm models using particle image velocimetry. *Int. J. Heat Fluid Flow* 21, 74–83. doi: 10.1016/S0142-727X(99)00058-2

Yu, S. C. M., and Zhao, J. B. (2000). A particle image velocimetry study on the pulsatile flow characteristics in straight tubes with an asymmetric bulge. *Proc. Inst. Mech. Eng. Part C* 214, 655–671. doi: 10.1243/09544060015 23678

Zhang, H., Zhang, X., Ji, S., Guo, Y., Ledezma, G., Elabbasi, N., et al. (2003). Recent development of fluid–structure interaction capabilities in the ADINA system. *Comput. Struct.* 81, 1071–1085. doi: 10.1016/S0045-7949(03)00009-9

Zhou, J., Adrian, R. J., Balachandar, S., and Kendall, T. M. (1999). Mechanisms for generating coherent packets of hairpin vortices in channel flow. *J. Fluid Mech.* 387, 353–396. doi: 10.1017/S002211209900467X

Conflict of Interest Statement: The authors declare that the research was conducted in the absence of any commercial or financial relationships that could be construed as a potential conflict of interest.

frontiers in Bioengineering and Biotechnology

REVIEW
published: 05 June 2019
doi: 10.3389/fbioe.2019.00133

A Review of *in vitro* Platforms for Understanding Cardiomyocyte Mechanobiology

Ian L. Chin[1], *Livia Hool*[1,2] *and Yu Suk Choi*[1]*

[1] School of Human Sciences, The University of Western Australia, Perth, WA, Australia, [2] Victor Chang Cardiac Research Institute, Sydney, NSW, Australia

Mechanobiology—a cell's interaction with its physical environment—can influence a myriad of cellular processes including how cells migrate, differentiate and proliferate. In many diseases, remodeling of the extracellular matrix (ECM) is observed such as tissue stiffening in rigid scar formation after myocardial infarct. Utilizing knowledge of cell mechanobiology in relation to ECM remodeling during pathogenesis, elucidating the role of the ECM in the progression—and perhaps regression—of disease is a primary focus of the field. Although the importance of mechanical signaling in the cardiac cell is well-appreciated, our understanding of how these signals are sensed and transduced by cardiomyocytes is limited. To overcome this limitation, recently developed tools and resources have provided exciting opportunities to further our understandings by better recapitulating pathological spatiotemporal ECM stiffness changes in an *in vitro* setting. In this review, we provide an overview of a conventional model of mechanotransduction and present understandings of cardiomyocyte mechanobiology, followed by a review of emerging tools and resources that can be used to expand our knowledge of cardiomyocyte mechanobiology toward more clinically relevant applications.

Keywords: heart disease, biomaterials, hydrogels, cardiovascular disease, mechanosensation, elasticity, biophysical environment, extracellular matrix (ECM)

OPEN ACCESS

Edited by:
Sara Baratchi,
RMIT University, Australia

Reviewed by:
Milena Bellin,
Leiden University Medical Center, Netherlands
Leighton Izu,
University of California, Davis, United States

***Correspondence:**
Yu Suk Choi
yusuk.choi@uwa.edu.au

Specialty section:
This article was submitted to Biomechanics, a section of the journal Frontiers in Bioengineering and Biotechnology

Received: *28 March 2019*
Accepted: *17 May 2019*
Published: *05 June 2019*

Citation:
Chin IL, Hool L and Choi YS (2019) A Review of in vitro Platforms for Understanding Cardiomyocyte Mechanobiology. Front. Bioeng. Biotechnol. 7:133. doi: 10.3389/fbioe.2019.00133

INTRODUCTION

Great progress has been made in understanding the various stimuli that regulate and maintain function in the beating heart. It is widely accepted that mechanical signaling is important for the coordination and regulation of cardiac function, and that the physical properties of the cardiac tissue change with aging and disease, however it remains unclear how the heart receives and responds to these mechanical signals.

Over the past decade, cell mechanobiology—the multidisciplinary study of interactions between cells and their physical environment—has illustrated that integrin-mediated sensation and transduction of mechanical signals plays an important role in controlling cellular behavior. New understandings from integrin-mediated mechanotransduction have contributed to advances in many fields, notably in stem cell technologies and understanding cancer progression. With respect to the importance of mechanical signaling in the heart, it is reasonable to suggest that interactions between cardiomyocytes and their physical environment would also be integral to the heart's function.

In this review, we provide a summary of the present understanding of cardiomyocyte mechanobiology, with a focus on integrin mediated mechanotransduction, and then provide an insight toward emerging tools and techniques that can be used to further expand understandings of cell mechanobiology in the heart.

FOUNDATIONS OF MECHANOBIOLOGY

Mechanisms of Mechanosensation and Mechanotransduction

Cells receive many mechanical signals and cues from the extracellular matrix (ECM). These can include topographical variations in the substrate, the changes in stiffness over time and changes in stiffness over space. The ECM is formed from many proteins, glycosaminoglycans, and proteoglycans which all serve structural and non-structural roles in supporting and guiding cellular behavior. The components of the ECM and the roles thereof have been reviewed here (Bonnans et al., 2014). Notable protein constituents of the ECM are collagens, laminins, and fibronectins. These proteins act as ligands for cell adhesion as well as serving as being significant in the structure and organization of the ECM. The exact composition of the ECM varies from tissue to tissue, for example adipose tissue is rich in non-fibrillar collagen VI (Mariman and Wang, 2010) whereas cardiac tissue primarily consists of fibrillar collagen I. The composition of ECM can change over time, notably due to disease, which can result in marked remodeling of the ECM. Heart attack is an example of this, where, following a myocardial infarction, there is a dramatic increase in the proportion of collagen I at the site of the infarct as scar tissue is formed to replace dead cardiac tissue.

The ECM is key to carrying and providing mechanical cues to cells (**Figure 1**), which are in turn received by the cell through membrane bound integrins; heterodimers consisting of an alpha and beta subunit. Cellular interactions with the ECM can be mediated by the integrins that are expressed at the cell membrane. In mammals, there are 24 unique combinations of alpha and beta subunits, each binding to a specific set of ligands (Israeli-Rosenberg et al., 2014). Due to the specificity of integrins, the types and quantity of integrins on a cell membrane are believed to play a key role in determining the signals received by a cell and how the cell responds.

Integrins are connected to the cytoskeleton through a group of proteins known as the focal adhesion complex (FAC). FAC involves a number of adapter proteins, such as talin, α-actinin, and vinculin (Belkin and Koteliansky, 1987; Bois et al., 2006; Ye et al., 2014), which link integrins to filamentous actin of the cytoskeleton (Ye et al., 2014). These adapter proteins are believed to act like a "molecular clutch" because like a clutch in a car, these adapter proteins determine the level of engagement between the ECM and the cytoskeleton, which in turn determines how efficiently mechanical forces are transmitted between the ECM and the cytoskeleton (Swaminathan and Waterman, 2016). Talin and vinculin are believed to be mechanosensitive because talin has cryptic binding sites for vinculin, which are revealed through mechanical stretching (del Rio et al., 2009) and vinculin appears

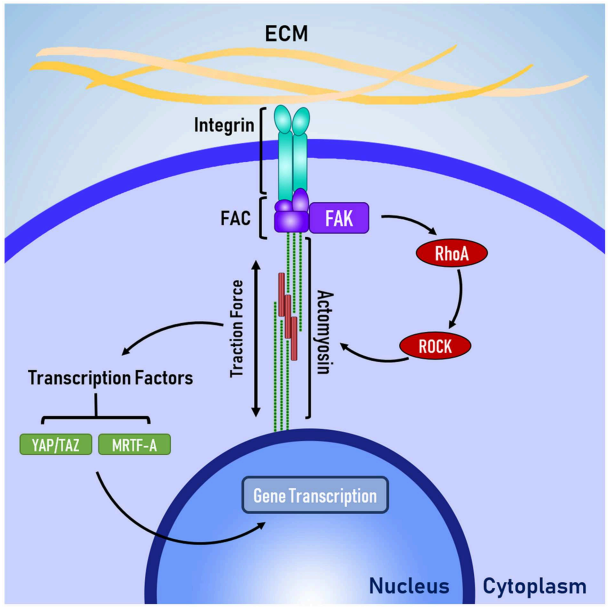

FIGURE 1 | The basic mechanotransduction pathway. Mechanical forces transmitted through the ECM are received by the cell at integrins. Integrins are connected to the cytoskeleton via the focal adhesion complex (FAC). Adapter proteins within the FAC transduce mechanical signals in to biochemical signals, triggering RhoA-ROCK mediated contraction of non-muscle actomyosin. Traction forces are generated by actomyosin activity, which activate transcription factors that enact changes to gene transcription in the nucleus.

to have force-mediated recruitment and activation (Balaban et al., 2001) via mitogen activated protein kinase (MAPK) binding (Holle et al., 2013).

The FAC can be a site of signal transduction, where mechanical signals are transformed into biochemical signals. One of the key signal-transduction pathways is the RhoA-ROCK pathway, where focal adhesion kinase (FAK) phosphosrylates RhoA, which leads to the activation of Rho associated protein kinase 1 (ROCK). FAK has also been implicated heavily in the development of cancer and researchers are currently investigating whether FAK could be a therapeutic target for treating various forms of cancer (Lee et al., 2015; Hirt et al., 2018). Laboratory studies have identified several promising inhibitors, which are progressing through the early stages of clinical testing (Lee et al., 2015; Lv et al., 2018).

The RhoA-ROCK pathway is responsible for cellular force generation through the phosphorylation of myosin light chain, which leads to contraction of non-muscle actin-myosin filaments generation traction forces. Traction forces exerted by the cell are resisted by the cellular microenvironment, which leads to changes in cell shape and controls the level of force applied to the membrane-bound integrins. Because the generation of traction forces are mediated by the physical properties of the cellular microenvironment (e.g., topography, stiffness, and ligand availability), it is believed that the generation of tractions forces is a mechanisms for cells to actively probe and respond the mechanical properties of their microenvironment (Lo et al., 2000; Ingber, 2003; Eyckmans et al., 2011). Beyond

the generation of traction forces, the RhoA-ROCK pathway has been implicated in several other mechanosensitive processes, such as the translocation of the co-transcription factors YAP/TAZ (Dupont et al., 2011) and MRTF-A (Yu et al., 2016), which shuttle between the cytoplasm and the nucleus to signal changes in gene transcription.

Protein Markers of Mechanosensation

A number of proteins that are sensitive to changes in the mechanical environment have been identified and it has been suggested that these proteins could be used to better understand the relationship between cellular functions and mechanosensation. Using immunocytochemistry, several studies have quantified the expression of these proteins and used protein expression as a measure of mechanosensation. Key proteins are described below, and their mechanosensitive expression is visually illustrated in **Figure 2**.

Lamin-A

Lamin-A is one of the intermediate filaments that constitute the nuclear lamina. Lamin-A is believed to play a key role in determining nuclear stiffness and to have a regulatory role in gene expression through interactions between DNA and the nuclear lamina (Swift et al., 2013). Lamin-A is also essential for post-natal growth as knockout of lamin-A in mouse models results in severe growth retardation and premature death (Sullivan et al., 1999; Jahn et al., 2012). Lamin-A expression has been used an indicator of mechanosensation as Lamin-A expression scales with tissue stiffness *in vivo* and substrate stiffness *in vitro*, whereby increased substrate stiffness results in increased lamin-A expression (Swift and Discher, 2014).

YAP/TAZ

Yes-associated protein (YAP) and transcriptional coactivator with PDZ-binding motif (TAZ) are co-transcription factors that have been implicated as major regulators of mechanotransduction. YAP/TAZ are believed to relay mechanical signals from the cytoplasm to the nucleus, where they enact changes in gene expression. Several experiments have shown that increased traction force increases nuclear YAP localization and that inhibition of mechanotransduction abolishes this response (Dupont et al., 2011; Hadden et al., 2017). YAP/TAZ localization is useful as a tool for measuring the level of mechanotransduction within a cell.

MRTF-A

Myocardin related transcription factor A (MRTF-A), also known as MKL1, is a transcription factor that shuttles between the cytoplasm and the nucleus. When inactive, MRTF-A is bound to globular actin (G-actin) and is localized within the cytoplasm. MRTF-A becomes active when G-actin dissociates from MRFT-A to be polymerised to form actomyosin. Upon dissociation, MRTF-A is sequestered in to the nucleus where it can enact changes to gene expression (Yu et al., 2016). Similar to YAP/TAZ, the degree of MRTF-A nuclear or cytoplasmic localization can be used as an indicator of mechanosensation (Hadden et al., 2017).

Mechanical Cues Control Major Cellular Processes

Traditionally, mechanobiology has been studied using 2-dimensional (2D), spatially and temporally static hydrogel platforms. Hydrogels have been made from naturally derived materials, such as collagen or hyaluronic acid (HA), and synthetic materials, such as polyacrylamide (PA) and polyethylene glycol (PEG). The advantages of each material has been debated in past and has been reviewed in more detail here (Ruedinger et al., 2014; Thiele et al., 2014), however all have been used to reveal foundational insights toward cell mechanobiology.

In many cell types, morphology, apopotosis, and proliferation are controlled through mechanosensation. Conventionally on a 2D substrate, cells are small and circular on a soft matrix and large and spread on a stiff matrix (Wang et al., 2000; Engler et al., 2006; Hadden et al., 2017) and in fibroblasts cultured on collagen hydrogels (Hadjipanayi et al., 2009) or collagen coated PA (Wang et al., 2000) increased rates of proliferation and decreased rates of apoptosis were observed on stiffer substrates.

Mechanical signaling is involved differentiation and migration. An early demonstration of this used PA hydrogels of different substrate stiffness to guide the differentiation of mesenchymal stem cells (MSC) cultured in identical serum conditions (Engler et al., 2006). Using early markers of lineage specification, it was found that cells preferentially differentiated toward tissues that were similar in stiffness to the substrates they were cultured on. For example, a soft matrix (<1 kPa) promoted neurogenic differentiation whereas a stiff matrix (>25 kPa) promoted osteogenic differentiation. It has been shown that similar outcomes can be achieved by controlling cell shape (McBeath et al., 2004; Kilian et al., 2010; Major and Choi, 2018), whereby increasing cell size promoted osteogenic differentiation and smaller cell size promoted adipogenic differentiation. Stiffness-mediated and shape-mediated changes to cell behavior are believed to both be a consequence of traction force generation, as traction forces can be controlled through both substrate stiffness and cell shape (Califano and Reinhart-King, 2010; Rape et al., 2011).

Further studies demonstrated that many cells, including adipose-derived stem cells (ASC) (Hadden et al., 2017), MSCs (Vincent et al., 2013), and fibroblasts (Hartman et al., 2017) preferentially migrate toward stiffer substrates through the process of durotaxis. Durotaxis has been demonstrated through time lapse microscopy of cells cultured on hydrogels patterned with a stiffness gradient. Durotaxis is mediated by ECM ligands that the cells are exposed to Hartman et al. (2017) and has been shown in ASC to only occur above a threshold stiffness gradient (8.2 kPa/mm) (Hadden et al., 2017).

CURRENT UNDERSTANDING OF CARDIAC MECHANOBIOLOGY

Cardiomyocytes Are Mechanosensitive

In the context of cardiac physiology, it is accepted that cardiomyocytes are mechanosensitive, however the mechanisms

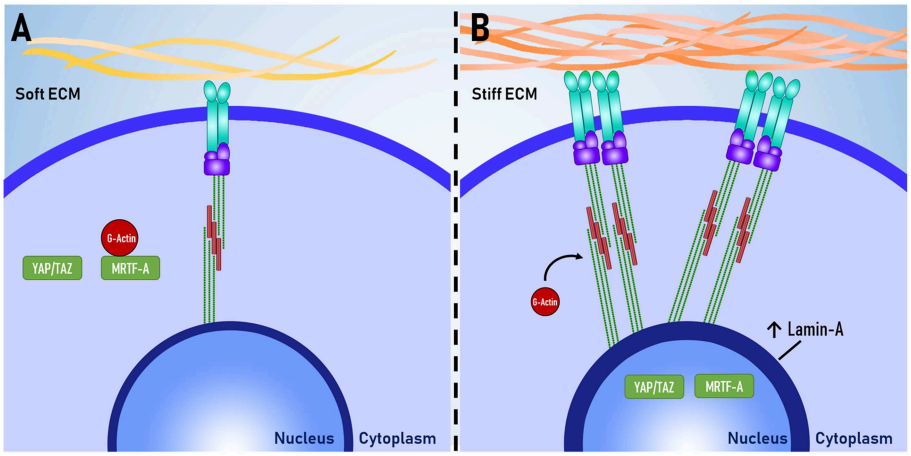

FIGURE 2 | Proteins as mechanomarkers. Expression of Lamin A, YAP and MRTF-A are dependent on mechanical signaling. When exposed to **(A)** soft ECM, YAP/TAZ and MRTF-A are inactive. When exposed to a **(B)** stiff ECM, there is increased assembly of non-muscle actomyosin stress fibers and focal adhesion complexes. MRTF-A dissociates from globular actin (G-actin) and both YAP/TAZ and MRTF-A translocate to the nucleus. The expression of Lamin-A in the nuclear lamina also increases.

and implication of cardiomyocyte mechanosensation are not well-understood.

There is evidence that appropriately matching substrate stiffness can promote the maturation of induced pluripotent stem cell (iPSC) derived cardiomyocytes (Herron et al., 2016) and of embryonic cardiomyocytes (Young and Engler, 2011). Cardiomyocytes derived from iPSC and cultured on polydimethylsiloxane (PDMS) membranes had more mature electrophysiology compared to cells cultured on glass, shown by action potential configuration and conduction, and connexin 43 expression. Embryonic chicken cardiomyocytes demonstrated increased levels of the late cardiac marker troponin-T and a time-dependent decrease in the early cardiac marker NKX2.5 when cultured on a modified hyaluronic acid (HA) that stiffened over time as opposed to cells cultured temporally static hydrogels (Young and Engler, 2011). In conjunction with the observations from derived cardiomyocytes, it appears that substrate stiffness plays an important role in the maturation of cardiac muscle and that these changes are time dependent.

Substrate stiffness is also known to alter the phenotype of cardiomyocytes. In embryonic quail and neonatal rat cardiomyocytes grown on 2D polyacrylamide (PA) hydrogels, cell shape and the level of sarcomere organization were found to be stiffness dependent (Engler et al., 2008; Jacot et al., 2008). In both cases, it was found that approximately 10 kPa was the optimal stiffness for the growth of cardiomyocytes, where the shape was more myocyte-like, the sarcomeres showed clear striations and functionally cells were better capable of maintaining constant spontaneous beating.

Substrate stiffness also appears to play an important role in force generation during contraction (Hersch et al., 2013; Ribeiro et al., 2015). Hersch et al. used traction force microscopy to measure the force of contraction of single rat cardiomyocytes cultured on PDMS substrates of varying stiffness. As substrate stiffness increased, the length of contraction remained constant and the force of contraction increased accordingly (Hersch et al., 2013). In this study, the authors did not observe any structural differences between cardiomyocytes cultured on different substrate stiffnesses, potentially because late embryonic cardiomyocytes were used which may have been more terminally differentiated than cardiomyocytes used in other studies. Based on these observations, the authors suggested that cardiomyocytes may be able to quickly adapt the force of contraction in response to mechanical resistance from the cellular microenvironment without significant reorganization of the cytoskeleton.

There appear to be two main pathways for mechanotransduction in cardiomyocytes: through integrins and through cadherins. Chopra et al. demonstrated this by culturing neonatal rat cardiomyocytes on PA gels coated in either type I collagen or in N-cadherin, neonatal rat cardiomyocytes demonstrated many similar trends in cell shape, cytoskeletal organization and the generation of traction forces (Chopra et al., 2011). N-cadherin is a major constituent of the intercalated discs, a strong mechanical linkage between cardiomyocytes, and has been shown to be essential for the development of the heart (Kostetskii et al., 2005). The intercalated disc is a characteristic feature of mature cardiomyocytes not typically found in the mesenchymal cells used to model mechanotransduction. This study suggested that cardiomyocytes are sensitive to N-cadherin mediated mechanical signaling and possibly also cell-cell mechanical signaling through the intercalated discs. Other studies have suggested that the loss of intercalated disks plays a role in age-related loss of cardiac function and that reinforcement of the intercalated disks may help preserve cardiac function (Kaushik et al., 2015; Sessions et al., 2018).

The Cardiac Cellular Microenvironment

The heart is unique as an organ in the way that it spontaneously contracts in a coordinated fashion. Accordingly, cardiomyocytes are unique in their cellular structure and organization to support

the function of the heart. Mechanotransduction is often modeled using stem cells, however there are several key structural differences between cardiomyocytes and stem cells, outlined in **Figure 3**.

Like most ECM, the cardiac ECM is constituted of many components, and has been reviewed here (Nielsen et al., 2017), however the key elements are summarized here. Structurally, the ECM can be divided in to the interstitial matrix, the ECM that exists between cells, and the basement membrane, the ECM that immediately surrounds the cells. In the heart, the interstitial matrix is comprised mostly of fibrillar collagen I, and primarily provides structural support for the cell. The basement membrane contains a mixture of proteins including laminin, collagen, and many proteoglycans. Throughout the ECM are non-structural matricellular proteins, such as osteopontin and matrix metalloproteins, which help in organizing the structure of the ECM and can provide important chemical signals to cells. With regards to the physical properties of healthy cardiac tissue, the stiffness is typically around 10 kPa (Berry et al., 2006; Janmey and Miller, 2011). Following myocardial infarction, tissue stiffness changes dramatically at the site of the infarct, initially softening as dead cells are removed and then increasing to approximately 40 kPa during scar formation (Berry et al., 2006). *In vitro* matching substrate stiffness to physiological values (∼10 kPa) has been found to promote maturation and improve contractility in neonatal cardiomyocytes whereas pathological stiffnesses (>35 kPa) result in hypertrophy and reduced contractility (Engler et al., 2004; Jacot et al., 2008; McCain et al., 2014).

Cardiomyocytes adhere to ECM primarily through α1β1, α5β1, and α7β1 integrins, which bind to collagen, fibronectin, and laminin, respectively (Israeli-Rosenberg et al., 2014). Integrin expression varies as a consequence of development and disease. For example, the expression of the α5 subunit is reduced and the expression of the α7 subunit increases during post-natal development (Brancaccio et al., 1998) and ischemia can promote the expression of both the α5 and α7 subunits (Nawata, 1999).

The cellular structure and organization of cardiomyocytes have been reviewed in depth by Lyon et al. (2015) and so will be only briefly covered by this review. There are two key function-specific structures in cardiomyocytes: the sarcomere and the intercalated disk. The sarcomere is the basic contractile unit within the cardiomyocyte and the degree of sarcomeric organization is often used as an indicator of cardiomyocyte differentiations and maturation. Sarcomeres are often visualized using α-actinin (Ribeiro et al., 2015; Pandey et al., 2018), troponin-I (Annabi et al., 2013; Li et al., 2016) and troponin-T (Yahalom-Ronen et al., 2015; Li et al., 2017) and other sarcomeric proteins, such as myosin heavy chain and myosin light chain, are used as indicators of cardiac differentiation and maturation (Choi et al., 2010; Higuchi et al., 2013; Yahalom-Ronen et al., 2015; Li et al., 2017). As traction forces play a significant role in mechanosensation, it is unclear how the additional contractile apparatus affects the rest of mechanotransduction pathway.

The intercalated disc is a characteristic feature of mature cardiomyocytes not typically found in the mesenchymal cells used to model mechanotransduction. Intercalated discs form the major link between adjacent cardiomyocytes and are essential for coordinating contraction and transmitting electrical and mechanical signals between cells. N-cadherin is a major component of intercalated discs, being involved in the formation of fascia adherens junctions and area composita, two junctions that mechanically link the intercalated disc to the cytoskeleton (Mezzano and Sheikh, 2012). In mouse models, knockout of N-cadherin leads to a loss of intercalated discs, morphological changes to the heart that resemble a dilated cardiomyopathy and leads to sudden death (Kostetskii et al., 2005). There is evidence that cadherins can mediate mechanotransduction independent of integrins. Chopra et al. demonstrated this by culturing neonatal rat cardiomyocytes on PA gels coated in either type I collagen or in N-cadherin, neonatal rat cardiomyocytes demonstrated

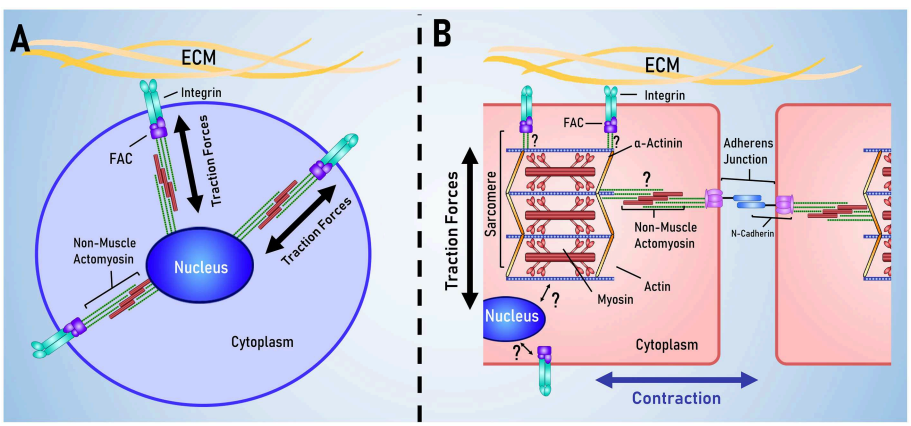

FIGURE 3 | Key differences between stem cell and cardiac mechanotransduction. **(A)** In stem cell models of mechanotransduction, mechanical signals are received by membrane bound integrins, transduced in to biochemical signals that result in traction force generation by non-muscle actomyosin. **(B)** Cardiomyocytes are characterized by having aligned muscle actomyosin and intercalated disks; intercellular links for electrical and mechanical coordination of contraction. It is currently unclear how the sarcomere and nucleus are mechanically linked to membrane bound integrins and the cadherins that link cells together.

many similar trends in cell shape, cytoskeletal organization and the generation of traction forces (Chopra et al., 2011). This study suggested that cardiomyocytes are sensitive to N-cadherin mediated mechanical signaling and possibly also cell-cell mechanical signaling through the intercalated discs.

EMERGING MATERIALS AND METHODS FOR UNDERSTANDING CARDIAC MECHANOBIOLOGY

Whilst simple platforms have provided us with a basic understanding of cardiac mechanobiology, the *in vivo* cardiac environment combines a number of complex mechanical signals. Cardiac tissue is striated, temporally dynamic, 3-dimensional (3D), and viscoelastic. To emulate this, materials would need to incorporate spatial patterning, temporal patterning, support 3D culture, have tuneable viscoelastic elements and furthermore would also need to combine all these elements to reveal how each signal interacts with one another. Similar challenges are faced across the field of mechanobiology and to this end, new materials and methods have been developed that can allow for more comprehensive mimicry of the cellular microenvironment. To bridge the gap between *in vitro* platforms and the *in vivo* environment, we should take inspiration from these materials and methods used to study mechanobiology in other cells, such as stem cells, fibroblasts or cancer cells, and adapt them to expand upon our understanding of cardiomyocyte mechanobiology.

Spatial Patterning

Recent developments in spatially patterned platforms have presented some interesting solutions to some of the challenges in studying cardiomyocytes. A number of techniques have been developed to create platforms with a stiffness gradient, as a high-throughput system for analyzing mechanosensitive properties of cells (Hartman et al., 2016; Hadden et al., 2017). These platforms were used to generate higher resolution data than past studies by examining protein expression, cell morphology, and cell migration on a continuous gradient rather than at discrete stiffnesses. These platforms were developed using PA and took utilized chemical gradients during fabrication to generate a mechanical gradient, however there are other approaches to developing patterned hydrogels. A promising approach is to use photolithography, where controlled light exposure is used to create mechanical patterns in hydrogels during fabrication. This can be achieved using hydrogels with a photoinitiated fabrication process, such as gelatin methacyloyl (GelMA), where a photomask can be used to vary light exposure across the hydrogel during fabrication, allowing for a stiffness pattern to be incorporated in to the hydrogel.

Spatial patterning of hydrogels can also involve controlling the area available for cells to grow. In the past, this has involved microcontact stamping, to control the spatial distribution of ligands across the substrate (Engler et al., 2004) or microcontact printing, to control the physical area available for cell adhesion (McBeath et al., 2004; Kilian et al., 2010; Major and Choi, 2018). Typically, microcontact printing involves fabricating PDMS stamps that are used to define an area where an ECM protein, such as fibronectin, could be applied allowing cells to adhere to the area marked by the PDMS stamp, but not elsewhere. In the past, this technique has been primarily used to guide differentiation, in mixed differentiation media, by controlling cell shape. McBeath et al. found that restricted cell spreading promoted adipogenesis and larger spreading areas promoted osteogenesis (McBeath et al., 2004). Kilian et al. confirmed this result and found that the key to guiding differentiation was cell contractility, measured through myosin IIa expression, rather than cell size itself (Kilian et al., 2010). Major and Choi further investigated cell spreading and size work in conjunction with substrate stiffness to determine differentiation, however this study found that under more complex conditions, signals can compete and mask one another. For example, under adipogenic stiffness conditions, increasing cell spreading area would promote the expression of the osteogenic differentiation marker RUNX2 however when cultured on osteogenic stiffness conditions, cell size-induced differences in RUNX2 expression were attenuated. This illustrates the potential complications using complex platforms as well as the importance of developing and studying combinatorial platforms.

Patterning hydrogels like this allows the distribution of cells to be controlled, making it possible to examine the differences between cell-ECM and cell-cell signaling in cardiomyocyte mechanobiology. In light of the known importance of intercalated discs in cardiac function (Sheikh et al., 2009; Lyon et al., 2015) and the differences between integrin and N-cadherin mediated mechanosensation (Chopra et al., 2011), it would be valuable to understand how different forms of mechanical signaling effects cardiomyocytes and the implications this might have if the relationship between the cells and their microenvironment were to change.

Temporal Patterning

Given that many diseases change the stiffness of the ECM over time, it is possible that the ECM could be a target for treatments. This concept has been investigated in the context of cancer, however the importance of time-dependent stiffness changes is not well-understood. Temporal elements in hydrogel platforms are invaluable in understanding the importance of time dependent changes as they reveal the interplay between mechanical signals across time, something which is not captured by temporally static platforms.

A major limitation of many dynamically stiffened hydrogels is that the stiffness changes are irreversible and so cannot investigate the reversibility of stiffness-induced cellular changes. Rosales et al. (2017) overcame this challenge by developing a material that combined two independent chemistries; one chemistry that is photodegradable and one chemistry for photocrosslinking, so that the material could be both softened and stiffened on demand. Using this material, the investigators were able to soften the material from 14.8 to 3.5 kPa and then stiffen the material to 27.7 kPa, illustrating the range of stiffnesses achievable by the material. Using this platform, the investigators probed the capacity of human MSCs to respond to dynamic environmental stiffness changes, chiefly

examining cell size, shape and nuclear YAP localization. It was found that, as demonstrated by temporally static platforms, that reducing substrate stiffness reduced cell size, increased the roundness of the cells and decreased the level of nuclear YAP localization and the opposite for increasing substrate stiffness. Interestingly, whilst increasing substrate stiffness did partially restore cell size, shape and YAP localization to pre-softening levels, complete recovery was not observed despite the post-stiffening stiffness being double that of the initial stiffness. These findings suggest that there are time-dependent characteristics of mechanosensation, not captured by static hydrogel platforms.

These observations are supported by Abdeen et al. (2016), who performed a similar experiment using a hydrogel material functionalised with magnetic particles. Using their magnetoactive hydrogel, substrate stiffness can be reversibly increased from 0.1 to 90 kPa by applying a magnetic field to the hydrogel. Investigators measured cell size and Runx2 expression as cells were exposed to various regimes of substrate softening and stiffening and similar to Rosales et al. it was observed that the relationship between cell size and Runx2 expression and substrate stiffness was dependent on the regime the cells were exposed to.

Findings from these temporally dynamic platforms has illustrated that the dimension of time is an important consideration for the study of mechanobiology and potentially treatments targeting the ECM. With regards to heart disease, understanding time-dependent changes to cardiac mechanobiology would inform us of appropriate time frames for treatments or the suitability of certain treatments, given the degree of ECM remodeling observed in disease, such as myocardial infarction coupled with limitations in our capacity to alter the physical characteristics of the *in vivo* environment.

Dimensionality

Introducing dimensionality has been a large focus of recent works as it is generally appreciated that many cells do not grow in a 2D monolayer but in a 3D environment, however until recently there were few platforms that were suitable or able to sustain a 3D culture. There are now several materials that are available for encapsulating cells, such as GelMA (Loessner et al., 2016) and modified HA (Caliari et al., 2016), which have shown that the trends observed in 2D are not necessarily representative of the trends observed in 3D. Notably, cell spreading and YAP/TAZ nuclear localization were reduced as stiffness increased in 3D, which is the inverse of what is traditionally observed in 2D (Caliari et al., 2016). Possible explanations to this could be related to the pore size of the material, which is coupled to the stiffness of the material and could be restricting the volume expansion of cells, which has been suggested as a key regulator of cellular functions (Lee et al., 2019). This idea is supported by Caliari et al. who found that increasing the susceptibility of the hydrogel to enzymatic degradation enhanced cell spreading and the nuclear translocation of YAP (Caliari et al., 2016), suggesting that cell volume itself may play a key role in regulating cellular function.

Viscoelasticity

Many hydrogel materials used for past *in vitro* studies, such as PA, are purely elastic, however for many tissues, including myocardium, the ECM is actually viscoelastic (Urban et al., 2013; Wang et al., 2016). As a viscoelastic material, the ECM has time-dependent characteristics in the way that it responds to stress (force applied per unit of area) and strain (the degree to which an object is deformed). These properties are generally described by strain-rate dependence, stress-relaxation and creep, which are best explained by engineering textbooks such as "Mechanical Response of Polymers: An Introduction" (Wineman and Rajagopal, 2000). Presently, the viscoelasticity in many hydrogel materials has not been well-characterized and there are few materials where viscoelastic properties can be tuned, however based on the materials that are available, it has been shown that viscoelasticity can have a significant effect on cell behavior and growth.

In one example, a modified alginate-based hydrogel material was used to investigate the role of stress-relaxation in stem cell differentiation. The material had mobile crosslinks that become restructured as stresses and strains were applied, and could be modified to tune the stress-relaxation time of the material. In samples with the same initial elastic modulus, it was found that the stress relaxation time mediated cell spreading in 3D and could guide stem cell differentiation synergistically with other differentiation cues (Chaudhuri et al., 2016; Lee et al., 2017). In another study, PA was used to study viscoelasticity, through varying the proportions of acrylamide and bis-acrylamide to generate gels with the same elasticity but different creep responses (Cameron et al., 2011) and it was found that creep influenced the morphology, proliferation and differentiation potential of human MSCs.

Viscoelasticity is a property of biomaterials that in past has had limited exploration due to limitations of the materials available, however emerging materials have highlighted that cells can detect and respond the viscoelasticity of their environment. This makes viscoelasticity an important consideration in trying to understand mechanosensation and mechanotransduction, notably in 3D culture environments, and is another facet of the cellular microenvironment that can be emulated.

FROM BENCHTOP TO BEDSIDE

Many innovative and creative strategies have been devised to overcome the challenges involved in mimicking the *in vivo* environment *in vitro*. This has involved adapting simple materials to be used in complex applications and opening new opportunities through the development of new materials, allowing us greater control over the way we mimic the spatial and temporal elements of the cellular microenvironment in 2D and 3D. With these developments in mind, there are now many resources available for study the role of mechanosensation in the transition from healthy to pathological states and the possibility of manipulating the physical environment, or cells perception thereof, as

a form of treatment. There is also potential in devising combinatorial platforms that combine biochemical, electrical and mechanical signaling in order enhance the efficacy of *in vitro* studies.

Major challenges still exist, notably difficulties in studying viscoelasticity and understanding the discrepancies between mechanosensation in 2D and 3D. Despite this, the frontier of our mechanobiology understandings have expanded through the development of tools and resources, and in bridging the gap between *in vitro* studies and *in vivo* observations.

AUTHOR CONTRIBUTIONS

All authors listed have made a substantial, direct and intellectual contribution to the work, and approved it for publication.

FUNDING

This work was supported by National Health and Medical Research Council Project Grant 1098449 and Research Fellowship 1117366 and Heart Foundation Future Leader Fellowship 101173.

REFERENCES

Abdeen, A. A., Lee, J., Bharadwaj, N. A., Ewoldt, R. H., and Kilian, K. A. (2016). Temporal modulation of stem cell activity using magnetoactive hydrogels. *Adv. Healthc. Mater.* 5, 2536–2544. doi: 10.1002/adhm.201600349

Annabi, N., Tsang, K., Mithieux, S. M., Nikkhah, M., Ameri, A., Khademhosseini, A., et al. (2013). Highly elastic micropatterned hydrogel for engineering functional cardiac tissue. *Adv. Funct. Mater.* 23, 4950–4959. doi: 10.1002/adfm.201300570

Balaban, N. Q., Schwarz, U. S., Ishizaki, T., and Narumiya, S. (2001). Focal contacts as mechanosensors externally applied local mechanical force induces growth of focal. *J. Cell Biol.* 153, 1175–1185. doi: 10.1083/jcb.153.6.1175

Belkin, A. M., and Koteliansky, V. E. (1987). Interaction of iodinated vinculin, metavinculin and α-actinin with cytoskeletal proteins. *FEBS Lett.* 220, 291–294. doi: 10.1016/0014-5793(87)80832-3

Berry, M. F., Engler, A. J., Woo, Y. J., Pirolli, T. J., Bish, L. T., Jayasankar, V., et al. (2006). Mesenchymal stem cell injection after myocardial infarction improves myocardial compliance. *Am. J. Physiol. Heart Circ. Physiol.* 290, H2196–H2203. doi: 10.1152/ajpheart.01017.2005

Bois, P. R., O'Hara, B. P., Nietlispach, D., Kirkpatrick, J., and Izard, T. (2006). The vinculin binding sites of talin and α-actinin are sufficient to activate vinculin. *J. Biol. Chem.* 281, 7228–7236. doi: 10.1074/jbc.M510397200

Bonnans, C., Chou, J., and Werb, Z. (2014). Remodelling the extracellular matrix in development and disease. *Nat. Rev. Mol. Cell Biol.* 15, 786–801. doi: 10.1038/nrm3904

Brancaccio, M., Cabodi, S., Belkin, A. M., Collo, G., Tomatis, D., Altruda, F., et al. (1998). Differential onset of expression of ?7 and ?1D integrins during mouse heart and skeletal muscle development. *Cell Adhes. Commun.* 5, 193–205. doi: 10.3109/15419069809040291

Caliari, S. R., Vega, S. L., Kwon, M., Soulas, E. M., and Burdick, J. A. (2016). Dimensionality and spreading influence MSC YAP/TAZ signaling in hydrogel environments. *Biomaterials* 103, 314–323. doi: 10.1016/j.biomaterials.2016.06.061

Califano, J. P., and Reinhart-King, C. A. (2010). Substrate stiffness and cell area predict cellular traction stresses in single cells and cells in contact. *Cell. Mol. Bioeng.* 3, 68–75. doi: 10.1007/s12195-010-0102-6

Cameron, A. R., Frith, J. E., and Cooper-White, J. J. (2011). The influence of substrate creep on mesenchymal stem cell behaviour and phenotype. *Biomaterials* 32, 5979–5993. doi: 10.1016/j.biomaterials.2011.04.003

Chaudhuri, O., Gu, L., Klumpers, D., Darnell, M., Bencherif, S. A., Weaver, J. C., et al. (2016). Hydrogels with tunable stress relaxation regulate stem cell fate and activity. *Nat. Mater.* 15, 326–334. doi: 10.1038/nmat4489

Choi, Y. S., Matsuda, K., Dusting, G. J., Morrison, W. A., and Dilley, R. J. (2010). Engineering cardiac tissue *in vivo* from human adipose-derived stem cells. *Biomaterials* 31, 2236–2242. doi: 10.1016/j.biomaterials.2009.11.097

Chopra, A., Tabdanov, E., Patel, H., Janmey, P. A., and Kresh, J. Y. (2011). Cardiac myocyte remodeling mediated by N-Cadherin-dependent mechanosensing. *AJP Heart Circ. Physiol.* 300, H1252–H1266. doi: 10.1152/ajpheart.00515.2010

del Rio, A., Perez-Jimenez, R., Liu, R., Roca-Cusachs, P., Fernandez, J. M., and Sheetz, M. P. (2009). Stretching single talin rod molecules activates vinculin binding. *Science* 323, 638–641. doi: 10.1126/science.1162912

Dupont, S., Morsut, L., Aragona, M., Enzo, E., Giulitti, S., Cordenonsi, M., et al. (2011). Role of YAP/TAZ in mechanotransduction. *Nature* 474, 179–184. doi: 10.1038/nature10137

Engler, A. J., Carag-Krieger, C., Johnson, C. P., Raab, M., Tang, H. Y., Speicher, D. W., et al. (2008). Embryonic cardiomyocytes beat best on a matrix with heart-like elasticity: scar-like rigidity inhibits beating. *J. Cell Sci.* 121, 3794–3802. doi: 10.1242/jcs.029678

Engler, A. J., Griffin, M. A., Sen, S., Bönnemann, C. G., Sweeney, H. L., and Discher, D. E. (2004). Myotubes differentiate optimally on substrates with tissue-like stiffness: pathological implications for soft or stiff microenvironments. *J. Cell Biol.* 166, 877–887. doi: 10.1083/jcb.200405004

Engler, A. J., Sen, S., Sweeney, H. L., and Discher, D. E. (2006). Matrix elasticity directs stem cell lineage specification. *Cell* 126, 677–689. doi: 10.1016/j.cell.2006.06.044

Eyckmans, J., Boudou, T., Yu, X., and Chen, C. S. (2011). A Hitchhiker's guide to mechanobiology. *Dev. Cell* 21, 35–47. doi: 10.1016/j.devcel.2011.06.015

Hadden, W. J., Young, J. L., Holle, A. W., McFetridge, M. L., Kim, D. Y., Wijesinghe, P., et al. (2017). Stem cell migration and mechanotransduction on linear stiffness gradient hydrogels. *Proc. Natl. Acad. Sci. USA.* 114, 5647–5652. doi: 10.1073/pnas.1618239114

Hadjipanayi, E., Mudera, V., and Brown, R. A. (2009). Close dependence of fibroblast proliferation on collagen scaffold matrix stiffness. *J. Tissue Eng. Regen. Med.* 3, 77–84. doi: 10.1002/term.136

Hartman, C. D., Isenberg, B. C., Chua, S. G., and Wong, J. Y. (2016). Vascular smooth muscle cell durotaxis depends on extracellular matrix composition. *Proc. Natl. Acad. Sci. USA.* 113, 11190–11195. doi: 10.1073/pnas.1611324113

Hartman, C. D., Isenberg, B. C., Chua, S. G., and Wong, J. Y. (2017). Extracellular matrix type modulates cell migration on mechanical gradients. *Exp. Cell Res.* 359, 361–366. doi: 10.1016/j.yexcr.2017.08.018

Herron, T. J., Rocha, A. M., Campbell, K. F., Ponce-Balbuena, D., Willis, B. C., Guerrero-Serna, G., et al. (2016). Extracellular matrix–mediated maturation of human pluripotent stem cell–derived cardiac monolayer structure and electrophysiological function. *Circ. Arrhythm. Electrophysiol.* 9, 1–12. doi: 10.1161/CIRCEP.113.003638

Hersch, N., Wolters, B., Dreissen, G., Springer, R., Kirchgeßner, N., Merkel, R., et al. (2013). The constant beat: cardiomyocytes adapt their forces by equal contraction upon environmental stiffening. *Biol. Open* 2, 351–361. doi: 10.1242/bio.20133830

Higuchi, S., Lin, Q., Wang, J., Lim, T. K., Joshi, S. B., Anand, G. S., et al. (2013). Heart extracellular matrix supports cardiomyocyte differentiation of mouse embryonic stem cells. *J. Biosci. Bioeng.* 115, 320–325. doi: 10.1016/j.jbiosc.2012.10.004

Hirt, U. A., Waizenegger, I. C., Schweifer, N., Haslinger, C., Gerlach, D., Braunger, J., et al. (2018). Efficacy of the highly selective focal adhesion kinase inhibitor BI 853520 in adenocarcinoma xenograft models is linked to a mesenchymal tumor phenotype. *Oncogenesis* 7:21. doi: 10.1038/s41389-018-0032-z

Holle, A. W., Tang, X., Vijayraghavan, D., Vincent, L. G., Fuhrmann, A., Choi, Y. S., et al. (2013). *In situ* mechanotransduction via vinculin regulates stem cell differentiation. *Stem Cells* 31, 2467–2477. doi: 10.1002/stem.1490

Ingber, D. E. (2003). Mechanosensation through integrins: cells act locally but think globally. *Proc. Natl. Acad. Sci.* 100, 1472–1474. doi: 10.1073/pnas.0530201100

Israeli-Rosenberg, S., Manso, A. M., Okada, H., and Ross, R. S. (2014). Integrins and integrin-associated proteins in the cardiac myocyte. *Circ. Res.* 114, 572–586. doi: 10.1161/CIRCRESAHA.114.301275

Jacot, J. G., McCulloch, A. D., and Omens, J. H. (2008). Substrate stiffness affects the functional maturation of neonatal rat ventricular myocytes. *Biophys. J.* 95, 3479–3487. doi: 10.1529/biophysj.107.124545

Jahn, D., Schramm, S., Schnölzer, M., Heilmann, C. J., de Koster, C. G., Schütz, W., et al. (2012). A truncated lamin A in the Lmna -/- mouse line: implications for the understanding of laminopathies. *Nucleus.* 3, 463–474. doi: 10.4161/nucl.21676

Janmey, P. A., and Miller, R. T. (2011). Mechanisms of mechanical signaling in development and disease. *J. Cell Sci.* 124, 9–18. doi: 10.1242/jcs.071001

Kaushik, G., Spenlehauer, A., Sessions, A. O., Trujillo, A. S., Fuhrmann, A., Fu, Z., et al. (2015). Vinculin network–mediated cytoskeletal remodeling regulates contractile function in the aging heart. *Sci. Transl. Med.* 7:292ra99. doi: 10.1126/scitranslmed.aaa5843

Kilian, K. A., Bugarija, B., Lahn, B. T., and Mrksich, M. (2010). Geometric cues for directing the differentiation of mesenchymal stem cells. *Proc. Natl. Acad. Sci.* 107, 4872–4877. doi: 10.1073/pnas.0903269107

Kostetskii, I., Li, J., Xiong, Y., Zhou, R., Ferrari, V. A., Patel, V. V., et al. (2005). Induced deletion of the N-Cadherin gene in the heart leads to dissolution of the intercalated disc structure. *Circ. Res.* 96, 346–354. doi: 10.1161/01.RES.0000156274.72390.2c

Lee, B. Y., Timpson, P., Horvath, L. G., and Daly, R. J. (2015). Pharmacology and therapeutics FAK signaling in human cancer as a target for therapeutics. *Pharmacol. Ther.* 146, 132–149. doi: 10.1016/j.pharmthera.2014.10.001

Lee, H. P., Gu, L., Mooney, D. J., Levenston, M. E., and Chaudhuri, O. (2017). Mechanical confinement regulates cartilage matrix formation by chondrocytes. *Nat. Mater.* 16, 1243–1251. doi: 10.1038/nmat4993

Lee, H. P., Stowers, R., and Chaudhuri, O. (2019). Volume expansion and TRPV4 activation regulate stem cell fate in three-dimensional microenvironments. *Nat. Commun.* 10:529. doi: 10.1038/s41467-019-08465-x

Li, J., Minami, I., Shiozaki, M., Yu, L., Yajima, S., Miyagawa, S., et al. (2017). Human pluripotent stem cell-derived cardiac tissue-like constructs for repairing the infarcted myocardium. *Stem Cell Rep.* 9, 1546–1559. doi: 10.1016/j.stemcr.2017.09.007

Li, Y., Shi, X., Tian, L., Sun, H., Wu, Y., Li, X., et al. (2016). AuNP–collagen matrix with localized stiffness for cardiac-tissue engineering: enhancing the assembly of intercalated discs by ?1-integrin-mediated signaling. *Adv. Mater.* 28, 10230–10235. doi: 10.1002/adma.201603027

Lo, C. M., Wang, H. B., Dembo, M., and Wang, Y. L. (2000). Cell movement is guided by the rigidity of the substrate. *Biophys. J.* 79, 144–152. doi: 10.1016/S0006-3495(00)76279-5

Loessner, D., Meinert, C., Kaemmerer, E., Martine, L. C., Yue, K., Levett, P. A., et al. (2016). Functionalization, preparation and use of cell-laden gelatin methacryloyl-based hydrogels as modular tissue culture platforms. *Nat. Protoc.* 11, 727–746. doi: 10.1038/nprot.2016.037

Lv, P. C., Jiang, A. Q., Zhang, W. M., and Zhu, H. L. (2018). FAK inhibitors in cancer, a patent review. *Expert Opin. Ther. Pat.* 28, 139–145. doi: 10.1080/13543776.2018.1414183

Lyon, R. C., Zanella, F., Omens, J. H., and Sheikh, F. (2015). Mechanotransduction in cardiac hypertrophy and failure. *Circ. Res.* 116, 1462–1476. doi: 10.1161/CIRCRESAHA.116.304937

Major, L. G., and Choi, Y. S. (2018). Developing a high-throughput platform to direct adipogenic and osteogenic differentiation in adipose-derived stem cells. *J. Tissue Eng. Regen. Med.* 12, 2021–2028. doi: 10.1002/term.2736

Mariman, E. C., and Wang, P. (2010). Adipocyte extracellular matrix composition, dynamics and role in obesity. *Cell. Mol. Life Sci.* 67, 1277–1292. doi: 10.1007/s00018-010-0263-4

McBeath, R., Pirone, D. M., Nelson, C. M., Bhadriraju, K., and Chen, C. S. (2004). Cell shape, cytoskeletal tension, and RhoA regulate stemm cell lineage commitment. *Dev. Cell* 6, 483–495. doi: 10.1016/S1534-5807(04)00075-9

McCain, M. L., Yuan, H., Pasqualini, F. S., Campbell, P. H., and Parker, K. K. (2014). Matrix elasticity regulates the optimal cardiac myocyte shape for contractility. *Am. J. Physiol. Heart Circ. Physiol.* 306, H1525–H1539. doi: 10.1152/ajpheart.00799.2013

Mezzano, V., and Sheikh, F. (2012). Cell-cell junction remodeling in the heart: possible role in cardiac conduction system function and arrhythmias? *Life Sci.* 90, 313–321. doi: 10.1016/j.lfs.2011.12.009

Nawata, J. (1999). Differential expression of ?1, ?3 and ?5 integrin subunits in acute and chronic stages of myocardial infarction in rats. *Cardiovasc. Res.* 43, 371–381. doi: 10.1016/S0008-6363(99)00117-0

Nielsen, S. H., Mouton, A. J., DeLeon-Pennell, K. Y., Genovese, F., Karsdal, M., and Lindsey, M. L. (2017). Understanding cardiac extracellular matrix remodeling to develop biomarkers of myocardial infarction outcomes. *Matrix Biol.* 75–76, 1–15. doi: 10.1016/j.matbio.2017.12.001

Pandey, P., Hawkes, W., Hu, J., Megone, W. V., Gautrot, J., Anilkumar, N., et al. (2018). Cardiomyocytes sense matrix rigidity through a combination of muscle and non-muscle myosin contractions. *Dev. Cell* 44, 326–336.e3. doi: 10.1016/j.devcel.2017.12.024

Rape, A. D., Guo, W. H., and Wang, Y. L. (2011). The regulation of traction force in relation to cell shape and focal adhesions. *Biomaterials* 32, 2043–2051. doi: 10.1016/j.biomaterials.2010.11.044

Ribeiro, M. C., Tertoolen, L. G., Guadix, J. A., Bellin, M., Kosmidis, G., D'Aniello, C., et al. (2015). Functional maturation of human pluripotent stem cell derived cardiomyocytes *in vitro* - correlation between contraction force andelectrophysiology. *Biomaterials* 51, 138–150. doi: 10.1016/j.biomaterials.2015.01.067

Rosales, A. M., Vega, S. L., DelRio, F. W., Burdick, J. A., and Anseth, K. S. (2017). Hydrogels with reversible mechanics to probe dynamic cell microenvironments. *Angew. Chem. Int. Ed.* 56, 12132–12136. doi: 10.1002/anie.201705684

Ruedinger, F., Lavrentieva, A., Blume, C., Pepelanova, I., and Scheper, T. (2014). Hydrogels for 3D mammalian cell culture: a starting guide for laboratory practice. *Appl. Microbiol. Biotechnol.* 99, 623–636. doi: 10.1007/s00253-014-6253-y

Sessions, A. O., Min, P., Cordes, T., Weickert, B. J., Divakaruni, A. S., Murphy, A. N., et al. (2018). Preserved cardiac function by vinculin enhances glucose Oxidation and extends health- and life-span. *APL Bioeng.* 2:036101. doi: 10.1063/1.5019592

Sheikh, F., Ross, R. S., and Chen, J. (2009). Cell-cell connection to cardiac disease. *Trends Cardiovasc. Med.* 19, 182–190. doi: 10.1016/j.tcm.2009.12.001

Sullivan, T., Escalante-Alcalde, D., Bhatt, H., Anver, M., Bhat, N., Nagashima, K., et al. (1999). Loss of A-type lamin expression compromises nuclear envelope integrity leading to muscular dystrophy. *J. Cell Biol.* 147, 913–919. doi: 10.1083/jcb.147.5.913

Swaminathan, V., and Waterman, C. M. (2016). The molecular clutch model for mechanotransduction evolves. *Nat. Cell Biol.* 18, 459–461. doi: 10.1038/ncb3350

Swift, J., and Discher, D. E. (2014). The nuclear lamina is mechano-responsive to ECM elasticity in mature tissue. *J. Cell Sci.* 127, 3005–3015. doi: 10.1242/jcs.149203

Swift, J., Ivanovska, I. L., Buxboim, A., Harada, T., Dingal, P. C., Pinter, J., et al. (2013). Nuclear lamin-A scales with tissue stiffness and enhances matrix-directed differentiation. *Science* 341:1240104. doi: 10.1126/science.1240104

Thiele, J., Ma, Y., Bruekers, S. M., Ma, S., and Huck, W. T. (2014). 25th anniversary article: designer hydrogels for cell cultures: a materials selection guide. *Adv. Mater.* 26, 125–148. doi: 10.1002/adma.201302958

Urban, M. W., Pislaru, C., Nenadic, I. Z., Kinnick, R. R., and Greenleaf, J. F. (2013). Measurement of viscoelastic properties of *in vivo* swine myocardium using lamb wave dispersion ultrasound vibrometry (LDUV). *IEEE Trans. Med. Imaging* 32, 247–261. doi: 10.1109/TMI.2012.2222656

Vincent, L. G., Choi, Y. S., Alonso-Latorre, B., del Álamo, J. C., and Engler, A. J. (2013). Mesenchymal stem cell durotaxis depends on substrate stiffness gradient strength. *Biotechnol. J.* 8, 472–484. doi: 10.1002/biot.201200205

Wang, H. B., Dembo, M., and Wang, Y. L. (2000). Substrate flexibility regulates growth and apoptosis of normal but not transformed cells. *Am. J. Physiol. Cell Physiol.* 279, C1345–C1350. doi: 10.1152/ajpcell.2000.279.5.C1345

Wang, Z., Golob, M. J., and Chesler, N. C. (2016). Viscoelastic Properties of Cardiovascular Tissues. In *Viscoelastic and Viscoplastic Materials*, 2:64. InTech. doi: 10.5772/64169

Wineman, A. S., and Rajagopal, K. R. (2000). *Mechanical Response of Polymers: An Introduction*. Cambridge: Cambridge University Press.

Yahalom-Ronen, Y., Rajchman, D., Sarig, R., Geiger, B., and Tzahor, E. (2015). Reduced matrix rigidity promotes neonatal cardiomyocyte dedifferentiation, proliferation and clonal expansion. *Elife* 4, 1–18. doi: 10.7554/eLife.07455

Ye, N., Verma, D., Meng, F., Davidson, M. W., Suffoletto, K., and Hua, S. Z. (2014). Direct observation of α-actinin tension and recruitment at focal adhesions during contact growth. *Exp. Cell Res.* 327, 57–67. doi: 10.1016/j.yexcr.2014.07.026

Young, J. L., and Engler, A. J. (2011). Hydrogles with time-dependent material properties enhance cardiomyocyte differentiation *in vitro*. *Biomaterials* 32, 1002–1009. doi: 10.1016/j.biomaterials.2010.10.020

Yu, O. M., Miyamoto, S., and Brown, J. H. (2016). Myocardin-related transcription factor A and yes-associated protein exert dual control in G protein-coupled receptor- and RhoA- mediated transcriptional regulation and cell proliferation. *Mol. Cell. Biol.* 36, 39–49. doi: 10.1128/MCB.00772-15

Conflict of Interest Statement: The authors declare that the research was conducted in the absence of any commercial or financial relationships that could be construed as a potential conflict of interest.

frontiers in Bioengineering and Biotechnology

REVIEW
published: 16 July 2019
doi: 10.3389/fbioe.2019.00162

Innovative Tools for Mechanobiology: Unraveling Outside-In and Inside-Out Mechanotransduction

Danahe Mohammed[1], *Marie Versaevel*[1], *Céline Bruyère*[1], *Laura Alaimo*[1], *Marine Luciano*[1], *Eléonore Vercruysse*[1], *Anthony Procès*[1,2] *and Sylvain Gabriele*[1]*

[1] Mechanobiology and Soft Matter Group, Interfaces and Complex Fluids Laboratory, Research Institute for Biosciences, University of Mons, Mons, Belgium, [2] Department of Neurosciences, Research Institute for Biosciences, University of Mons, Mons, Belgium

Cells and tissues can sense and react to the modifications of the physico-chemical properties of the extracellular environment (ECM) through integrin-based adhesion sites and adapt their physiological response in a process called mechanotransduction. Due to their critical localization at the cell-ECM interface, transmembrane integrins are mediators of bidirectional signaling, playing a key role in "outside-in" and "inside-out" signal transduction. After presenting the basic conceptual fundamentals related to cell mechanobiology, we review the current state-of-the-art technologies that facilitate the understanding of mechanotransduction signaling pathways. Finally, we highlight innovative technological developments that can help to advance our understanding of the mechanisms underlying nuclear mechanotransduction.

Keywords: mechanobiology, mechanotransduction, cytoskeleon, integrins, microsystem and macrosystem approaches, force, signaling/signaling pathways

OPEN ACCESS

Edited by:
Sara Baratchi,
RMIT University, Australia

Reviewed by:
Yubing Sun,
University of Massachusetts Amherst, United States
Gerald A. Meininger,
University of Missouri, United States
Anthony John Ricci,
Stanford University, United States

***Correspondence:**
Sylvain Gabriele
sylvain.gabriele@umons.ac.be

Specialty section:
This article was submitted to Biomechanics, a section of the journal Frontiers in Bioengineering and Biotechnology

Received: *31 January 2019*
Accepted: *20 June 2019*
Published: *16 July 2019*

Citation:
Mohammed D, Versaevel M, Bruyère C, Alaimo L, Luciano M, Vercruysse E, Procès A and Gabriele S (2019) Innovative Tools for Mechanobiology: Unraveling Outside-In and Inside-Out Mechanotransduction. Front. Bioeng. Biotechnol. 7:162. doi: 10.3389/fbioe.2019.00162

INTRODUCTION

During the last two decades, increasing evidence has suggested that the physico-chemical properties of the cell microenvironment and the physical forces exerted by cells and tissues play critical roles in the regulation of physiological and pathological situations. In both contexts, cells must adapt their behavior by converting physical signals into biochemical signals and changes in gene expression by using mechanochemical transduction, or mechanotransduction, signaling pathways.

Adherent cells are connected to the extracellular matrix (ECM) through the transmembrane receptor integrins. Mechanical signals can be detected via focal adhesion (FA) sites and translated into biochemical information through integrin-related signaling pathways. The inside tension generated by the actomyosin contractility can be transferred to the ECM through integrins at FAs. As a consequence, FAs serve as crucial sites for both outside-in and inside-out mechanotransduction (**Figure 1**). Although it is clear that integrins play a crucial role in translating outside-in and inside-out signals, it remains unclear how cells can be able to sense mechanical forces and convert mechanical signals into biological responses (Jaalouk and Lammerding, 2009). Moreover, this global mechanism is further complicated by the highly dynamic behavior of cells that can adapt their morphology and cytoskeletal organization in response to mechanical forces. In addition, specialized mechanoreceptors can enhance mechanosensation for critical processes such as blood pressure, auditory function or touch sensation by using specific organelles that can detect a wide range of stimulus frequencies (Peng et al., 2011). For instance, the so-called "hair" cells transduce mechanical vibrations into electrical signals that propagate to the brain. Located

on the apical surface of sensory hair cells, hair bundles are filled with actin, named stereocilia. The mechanical deflection of the stereocilia toward the tall edge opens gated ion channels, while opposite deflection closes channels (Katta et al., 2015). Indeed, the actin filament sliding generates a force that changes the conformation of a transmembrane protein, leading to the transient entry of calcium ions. Other mechanisms such as the modifications of intracellular protein conformations or the direct transmission of forces to the cell nucleus are only being explored (Chu et al., 2019). To address this issue, the mechanobiology field has become very active at the forefront of current research (Roca-Cusachs et al., 2017). Mechanobiology is an interdisciplinary field that focuses on physical forces and their impact on cell mechanics. A major challenge in mechanobiology is to understand mechanotransduction mechanisms by which mechanical signals are transduced into a cascade of biochemical events (Humphrey et al., 2014) and to understand how these molecular events contribute to development, physiology and disease.

To answer these open questions, current studies need to stimulate mechanically living cells and tissues and then determine their mechanical and functional responses. Current studies on cell mechanotransduction are mostly limited by the techniques that are available to impose mechanical stimulation at both single cell and tissue levels and, in turn, allow to measure biomechanical and biochemical cell responses. Here, we introduce some basic concepts of mechanobiology and we review recent experimental developments that have significant implications for addressing challenging questions in cellular mechanotransduction.

BASIC CONCEPTS OF MECHANOBIOLOGY

The concept of force in cell biology can be intuitively related to pushing or pulling actions exerted by individual or assembly of cells. Even if the concept of force in cell biology is difficult to define, it exists a wide range of physiological situations where mechanical events are crucial to the establishment of cellular functions. For instance, the division of eukaryote cells requires the assembly of a bipolar spindle, which the morphology mostly depends on the activities of molecular motors that generate pushing or pulling forces on the microtubule-based mitotic spindle (Shimamoto et al., 2015). The quantification of cellular forces requires the development of micro- or nano-sensors capable of converting forces into mechanical deformations, knowing the material properties of the force sensor (i.e., the spring constant or the elastic modulus). Micro- or nano-sensors provide therefore an exact readout of forces from the material deformation within a range from few piconewtons to hundreds of nanonewtons.

Force assays allow to probe the mechanical properties of cells, which describe the cell deformation over time in response to an applied stress. The elastic modulus corresponds to the scaling between stress and strain of cells and depends on the deformation mode (**Figures 2A–C**). The Young's modulus corresponds to the cell elasticity with a unit of pascals (Pa) under extension. This fundamental property of living cells and tissues is involved in the establishment of their three-dimensional (3D) shapes under a mechanical stress. However, one must consider that living cells and tissues need to be considered as viscoelastic living materials (**Figure 2D**). Viscoelastic materials undergoing a mechanical deformation store and dissipate mechanical energy (Coppée et al., 2011). The viscoelastic behavior of cells and tissues leads to the relaxation of the mechanical stress and the increase of the deformation over time (Moeendarbary and Harris, 2014) (**Figures 2E,F**). Various rheological models, such as the standard linear solid model, have been proposed to describe the viscoelastic behavior of cells and tissues (**Figure 2D**).

In addition to the investigation of the mechanical properties of cells themselves, forces applied by cells on their surrounding are key for understanding inside-out mechanotransduction pathways. Contractile cellular forces are transmitted to other cellular neighbors via cell-cell adhesive interactions (i.e., cadherins) and to their local microenvironment through cell-matrix interactions (i.e., integrins). Cellular tractions forces occur across small-length scales (nano- to micrometers) in the range of pico to nanonewtons, making challenging a direct experimental measurement. Interestingly, ion channels have been proposed for decades to be central for sensing mechanical forces, but their identity remained largely elusive until the discovery of Piezo 1 and Piezo 2 channels (Coste et al., 2010). The current view suggests that cellular mechanotransduction signaling is largely mediated by transmembrane proteins, however the Piezo1 ion channel has been suggested to be involved in the emergence of traction forces and can therefore revisit the current concept (Murthy et al., 2017; Nourse and Pathak, 2017).

In the human body, the magnitude of forces exerted by cells varies significantly and mainly depends on the physiological location of the cells. Indeed, each type of tissue construct is characterized by both specific physico-chemical and mechanical properties. For this reason, a large effort has been made in the last two decades to propose novel synthetic materials that can recapitulate the physico-chemical properties of the complex native cellular microenvironment.

SYNTHETIC MATRICES TO REPRODUCE THE COMPLEXITY OF THE NATIVE CELL MICROENVIRONMENT

In human tissues, the ECM is a highly 3D dynamic structure where cells have interactions with a myriad of biochemical (e.g., soluble factors) and biophysical (e.g., stiffness/stress) cues that direct their functions. Cells are constantly remodeling the ECM through synthesis, degradation and chemical modifications. These processes imply important changes in ECM properties (e.g., stiffness and porosity), which in turn drive cell fate and maintain tissue homeostasis (Baker et al., 2015). The biochemical composition of the ECM is complex and mainly consists of branched glycosaminoglycan structures (e.g., heparin sulfate and

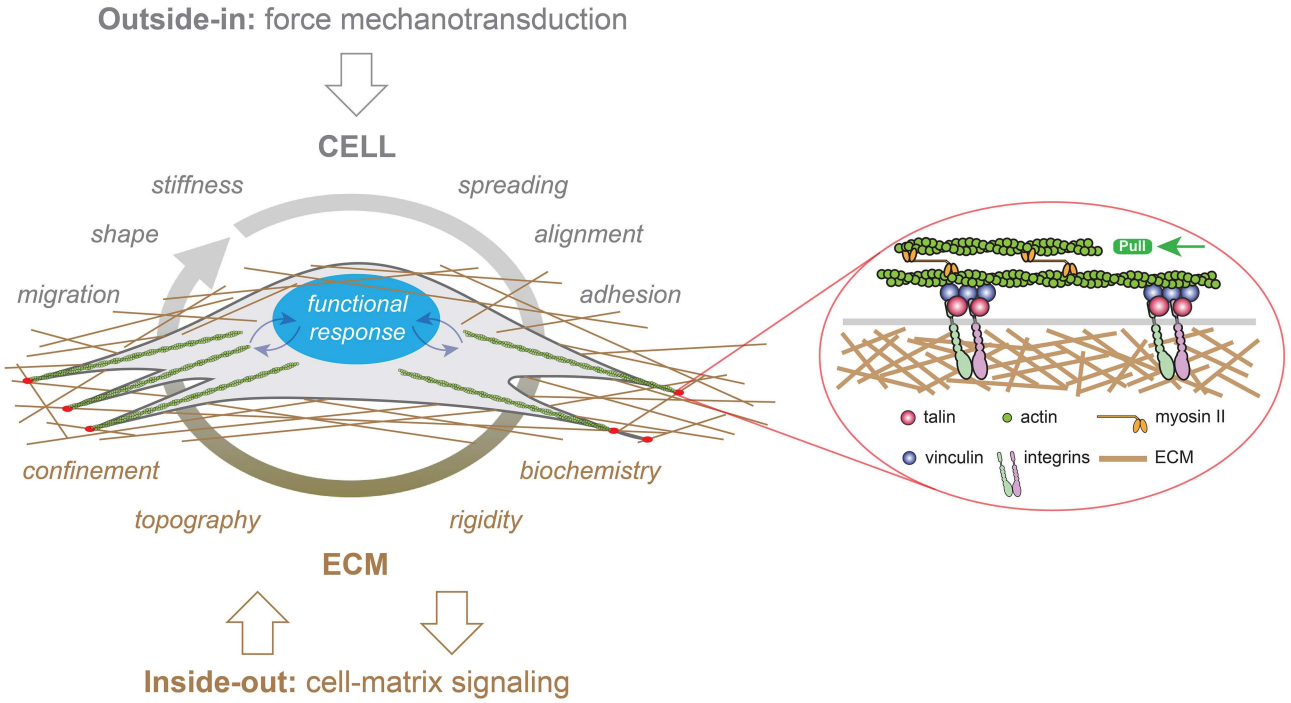

FIGURE 1 | Representation of "outside-in" (in gray) and "inside-out" (in brown) mechanotransduction signals in a cell growing in a three-dimensional (3D) fibrous matrix. External forces applied to eukaryotic cells modulate their migration, shape, stiffness, spreading, alignment or adhesion behaviors, whereas the ECM provides multiple cues to cells such as confinement, topography, rigidity and biochemistry. Focal adhesion (FAs, in red) serve as crucial sites for both outside-in and inside-out mechanotransduction through the recruitment of transmembrane integrins. Mechanical signals (curved blue arrows) are converted in biological responses by the nucleus, which is depicted in blue.

chondroitin sulfate) (Karp, 2015) and high molecular weight proteins (e.g., collagen, fibronectin, and laminin). All of these macromolecules form a 3D fibrillar network that provides a unique bioactive micro-environment. Most of the ECM components contain adhesive binding sites that are involved in the transduction of mechanical signals exerted from the local micro-environment (Humphries, 1990). The mechanisms used by cells to receive and process mechanical signals are still not understood due to the complexity of the native cell micro-environment. In addition, cell-ECM interactions typically involve coordinated presentation of multiple factors (e.g., cell-ligand density, porosity or stiffness) that can be presented over multiple time scales. To overcome this barrier, smart hydrogels have emerged as a promising alternative strategy to standard plastic dishes for cell culture.

Hydrogels are defined as crosslinked water-swollen biomacromolecules that form a three-dimensional structure. The large amount of water in hydrogels allows the diffusion of biomolecules secreted by cells. The design of hydrogels suitable for cell culture requires to reproduce both the biochemical and mechanical properties of their native microenvironment. Water-swollen polymers such as poly(ethyleneglycol) (PEG), poly(vinyl alcohol) (PVA), poly(2-hydroxyethylmethacrylate) (PHEMA) and poly(acrylamide) (PAAm) can form elastic hydrogels that can reproduce some basic mechanical aspects of soft tissues (**Figure 3A**) (Annabi et al., 2014). Although still not fully understood, growing evidence suggests that cells interpret elasticity through integrin-mediated mechanotransduction signals that trigger outside-in signaling cascades. The seminal work of Engler and coworkers was performed with polyacrylamide hydrogels in order to modulate human mesenchymal stem cells (hMSCs) differentiation by tuning the hydrogel elastic modulus (Engler et al., 2006). Promising matrix candidate for studying mechanobiology *in vitro*, PAAm hydrogels have received a large attention in order to overcome its native non-adhesive properties, for instance using heterobifunctional cross-linker sulfo-SANPAH (Wang and Discher, 2007), hydrazine and protein oxidation by periodate (Damljanovic et al., 2005), deep UV exposure (Tseng et al., 2011) or HS-ester during the polymerization phase (Polio et al., 2012). However, most of these methods present difficulties for controlling easily the cell–ligand density and decoupling the relative contribution of mechanotransduction cues. In order to address this limitation, Grevesse et al. introduced a new PAAm hydrogel, called hydroxy-PAAm, that incorporates hydroxyl groups to allow the functionalization of PAAm hydrogels with ECM proteins with minimal requirements in cost or expertise (**Figure 3B**) (Grevesse et al., 2013). Hydroxy-PAAm has been shown to be an effective biomaterial for immobilizing any desired proteins and tuning important physico-chemical parameters of the matrix (Grevesse et al., 2014), such as ligand density and matrix stiffness (**Figures 3C,D**), while keeping superior

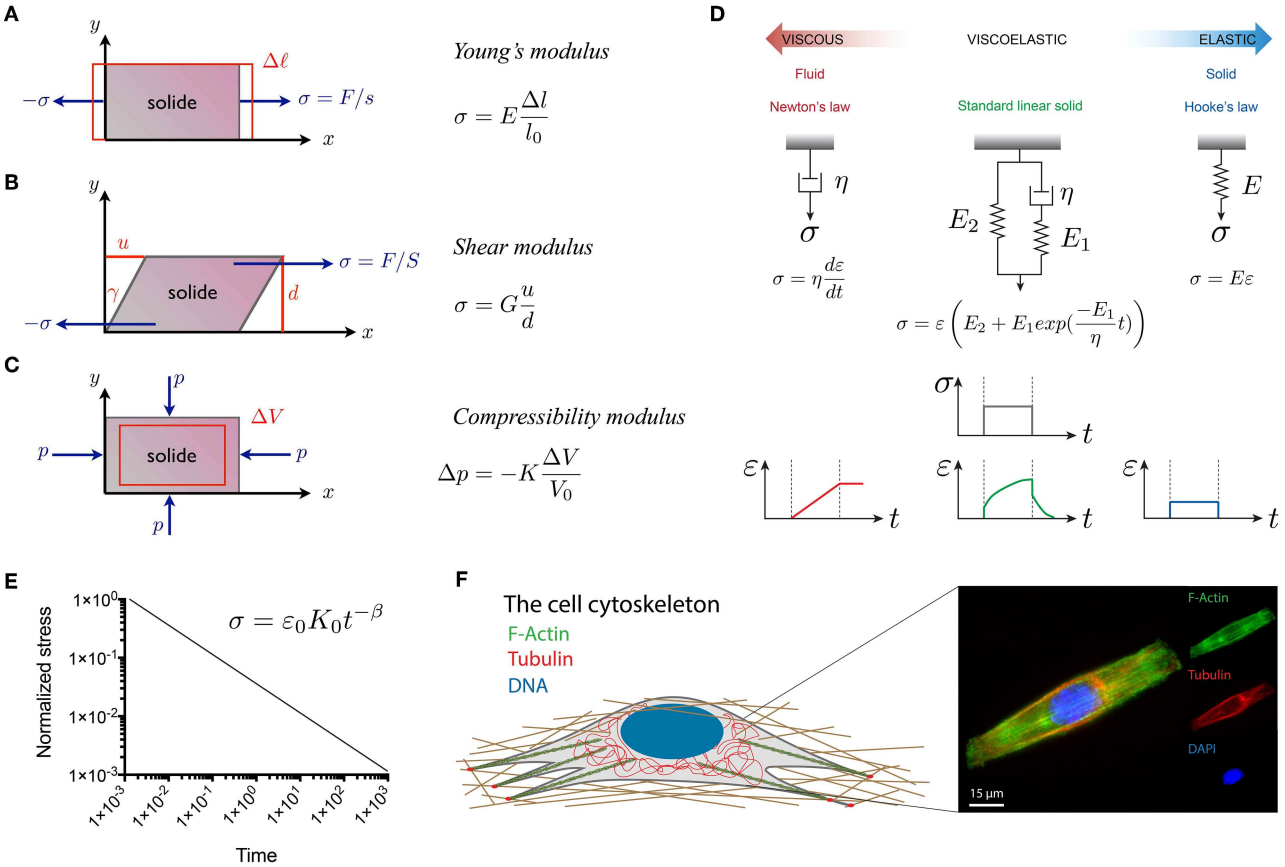

FIGURE 2 | Representation of the fundamental quantities involved in the three main modes of deformation used in material characterization: **(A)** linear elongation, **(B)** shear deformation and **(C)** isotropic compression. **(D)** Viscoelastic models, such as the standard linear model in green, can be obtained from the association of dashpots, that represent viscous Newtonian fluids (in red), and springs that represent ideal elastic solids (in blue). **(E)** The power law type of relaxation in log–log scale is a line with a slope β, which is the power law exponent. The power law exponents are $\beta = 0$ and $\beta = 1$ for purely elastic and viscous materials, respectively. Elastic and viscous mechanisms contribute to a complex relaxation response when $0 < \beta < 1$ (Grevesse et al., 2015). **(F)** The composition and spatial organization of cytoskeletal components significantly influence the cell rheological properties. Epifluorescence image of a C2C12 myoblast immunostained for F-actin (in green), microtubules (in red) and DNA (in blue). The scale bar is 15 µm.

optical properties (**Figure 3E**). For instance, hydroxy-PAAm hydrogels were used to show the individual role of αvβ3 and α5β1 integrins in the matrix rigidity sensing of highly motile cells (Riaz et al., 2016) and that matrix rigidity can modulate the axon growth, the density of synapses and the electrophysiological activity of neuronal networks (Lantoine et al., 2016). Due to the elastic nature of PAAm hydrogels, most of the cellular mechanotransduction studies have converged upon the idea that ECM elasticity is the main physical cue sensed by cells. However, *in vivo* matrices exhibit viscoelastic behavior characterized with stress relaxation properties that can regulate cell functions (Chauduri et al., 2015, 2016; Bauer et al., 2017; Vining et al., 2019). Recently, Charrier et al. reported the synthesis of gels with an independent tuning of elastic and viscous moduli. By altering systematically the hydrogel viscosity, the authors demonstrated the time dependence of cellular mechanosensing and the influence of viscous dissipation on cell phenotype (Charrier et al., 2018). Despite many advantages to mimic the structure of native tissues, one major drawback of PAAm hydrogels is that porosity changes with variations in stiffness, leading to changes in cell-fate decisions (Trappman et al., 2012).

In addition to these works, magnetic hydrogels (M-gel systems) (Niland et al., 2001) and photoresponsive hydrogels (PRHs) that include photochromic chromophores as the photoreactive groups within the 3D hydrogels network (Tomatsu et al., 2011) were developed to mimic the mechanical environment of the ECM (Dong et al., 2018). Diverse photoreactions have been used to tune the properties and functions of hydrogels such as degradability (Kloxin et al., 2009), polarity (Liu et al., 2005) or adhesion (Bryant et al., 2007), which has made photoresponsive hydrogels useful for engineering a dynamic cell microenvironment for mechanotransduction assays (Zhang et al., 2015).

Even if considerable efforts have been made to design synthetic hydrogels with finely tunable physico-chemical and mechanical properties, ECM fiber networks remain more

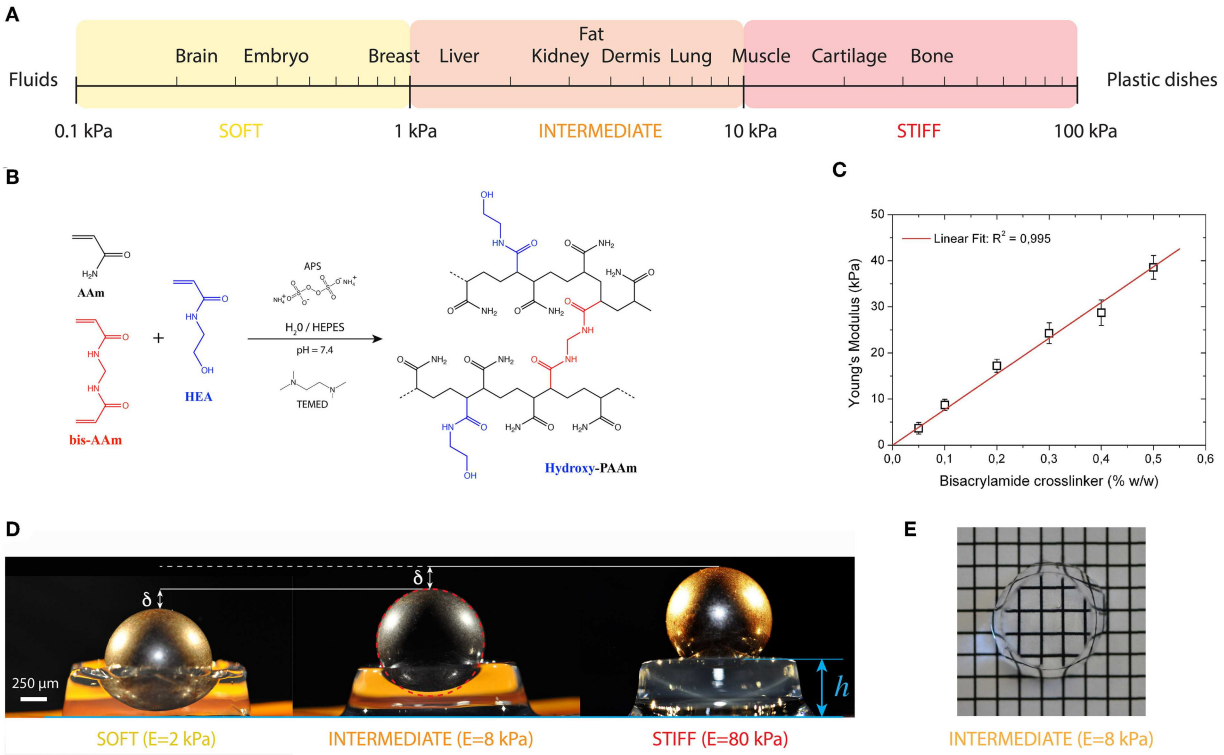

FIGURE 3 | (A) The elasticity of living tissues spans a wide range of rigidities which are organized in three domains: soft (0.1 ≤ E ≤ 1kPa), intermediate (1 ≤ E ≤10 kPa) and stiff (10 ≤ E ≤ 100 kPa). **(B)** Acrylamide (AAm, in black) and bisacrylamide (bis-AAm, in blue) and N-hydroxyethylacrylamide (HEA, in red) monomers were co-polymerized to form a hydrophilic network of polyacrylamide containing hydroxyl groups (hydroxy-PAAm) by random radical polymerization (Grevesse et al., 2013, 2014). **(C)** The amount of bis-AAm cross-linker allows to modulate the stiffness of hydroxy-PAAm hydrogels. **(D)** Images of three hydroxy-PAAm hydrogels of various rigidities (from left to right: soft in yellow, intermediate in orange and stiff in red) deformed by a static steel ball that exerts a constant load. The resistance of the hydroxy-PAAm hydrogels against the deformation imposed by the steel ball is proportional to the elastic modulus of the hydrogels. **(E)** Hydroxy-PAAm hydrogels have superior optical properties, such as high transparency, that do not depend on their mechanical properties.

complex than their synthetic analogs. Indeed, native ECM fibers can be mechanically stretched by cell-generated forces that will upregulate their Young's modulus (Liu et al., 2006), activate cryptic sites (Klotzsch et al., 2009) or inhibit binding sites (Chabria et al., 2010; Kubow et al., 2015). Furthermore, because most ECM fibers, such as fibronectin, have enzymatic cleavage sites, particularly for metalloproteinases (MMPs), they can be enzymatically degraded causing the release of peptide fragments that may play a crucial role in regulating inflammatory processes (Modol et al., 2014). In addition to MMP-degradable hydrogel platforms (Lueckgen et al., 2018; Xiaomeng et al., 2018), novel technologies to create synthetic matrices with stretched fibers will be essential to learn whether and how cell-cell and cell-ECM mechanotransduction crosstalk is regulated by ECM fiber tension (Vogel, 2018).

STANDARDIZING CELL-SUBSTRATE INTERACTIONS WITH MICROFABRICATED TOOLS

Interactions of cells with the ECM determine their fate through the modulation of cell shape, cell-surface adhesions and cell spreading. The ability to produce precisely engineered surfaces for cell culture that can provide robust *in vitro* assays to control cell adhesion is crucial for understanding inside-out and outside-in mechanotransduction signals.

In conventional two-dimensional (2D) cultures, cells grow until confluence without any specific spatial organization. Major drawbacks of conventional cultures are therefore the difficulty to manage complex parameters involved in mechanotransduction signaling pathways. To address this limitation, a large effort has been made during the last two decades to develop robust micropatterning techniques for manipulating cell adhesion patterns. Although the first micropatterning methods were introduced more than 40 years ago (Carter, 1967; Harris, 1973), they only became commercially available recently. Among a wide range of patterning techniques, the microcontact printing (μCP) technique mainly developed by the Whitesides group at Harvard University (Whitesides et al., 2001) has become the most popular and widely used technique for cell biology assays (**Figure 4A**). Controlling cell adhesion through adhesive micropatterns allows to impose boundary conditions in cell culture in order to control both cell shape and structure. Cell shape can be precisely controlled to minimize variations of cell morphologies inherent to any cell types (**Figures 4B–E**).

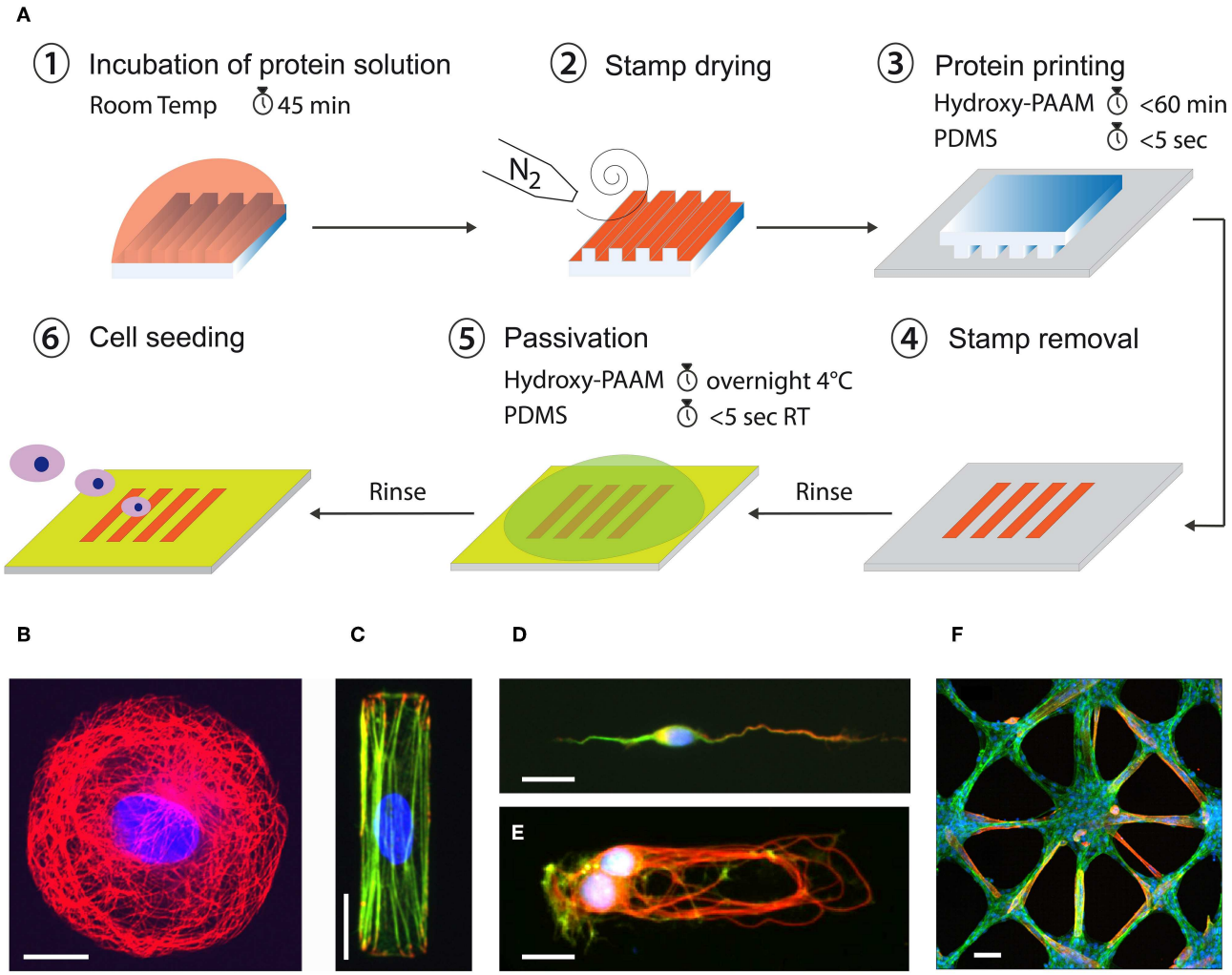

FIGURE 4 | (A) Microcontact printing allows to from 2D micropatterns of proteins on flat culture substrates from a PDMS structured microstamp (Grevesse et al., 2013; Versaevel et al., 2014b). Example of fluorescent images of different cell types grown at the single cell and tissue levels on adhesive micropatterns of various geometries and protein coatings. Human Umbilical Vein Endothelial Cell (HUVEC) were grown on **(B)** a circular micropattern of fibronectin (FN) and stained for tubulin (in red) and DNA (in blue), **(C)** a rectangular micropattern of FN and stained for vinculin (in red), actin (in green) and DNA (in blue). **(D)** A cortical neuron was grown on a stripe of laminin (LM) and stained for MAP2 (in green), Tau (in red) and DNA (in blue). **(E)** A doublet of cortical neurons was grown on a rectangular micropattern of LM and stained for tubulin (in red), actin (in green), and DNA (in blue). **(F)** A 2D tissue of C2C12 myoblasts was grown on a star-shaped micropattern of FN and stained for actin (in green), troponin T (in red) and DNA (in blue) after differentiation in myotubes. Scale bars are **(B)** 10 μm, **(C)** 20 μm, **(D)** 10 μm, **(E)** 20 μm, and **(F)** 50 μm.

Adhesive micropatterns were used to demonstrate that cells need to spread, to extend spatially, to generate forces and not only to have the biochemical factors to survive and grow (Chen et al., 1997). Micropatterns have been used for instance to demonstrate that the geometry of the adhesive micropattern influences the cell division through the reorientation of the mitotic spindle (Thery et al., 2005; Fink et al., 2011). Using endothelial cells grown on a wide range of micropattern geometries, it has been shown that compressive forces exerted by the actomyosin filaments regulate nuclear orientations and deformations (Versaevel et al., 2012). Changes in cell shape imposed by the geometry of the adhesive micropattern modulate cell proliferation through chromatin condensation, demonstrating a mechanotransduction signaling pathway. It has been shown that the direction of the leading-edge extension can be controlled by constraining cell shape using adhesive micropatterns. For instance, square cells were found to reorient cell-substrate adhesions and stress fibers, concentrating therefore contractile forces in the corner regions (Parker et al., 2002). Using μCP, it has been suggested that mechanical interactions between cells and ECM that modulate cytoskeletal tension may therefore play a key role in the control of directional cell motility. In the context of cell migration, μCP was also used to study the influence of the 2D spatial confinement by using adhesive ratchets (Mahmud et al., 2009; Mohammed et al., 2019). Adhesive micropatterns were applied to the study of the influence of the adhesive micro-environment on the actin architecture and

contractility (Mandal et al., 2014). The study of the influence of the geometry on multicellular systems (**Figure 4F**) has shown that cells propagate the alignment observed at the edges over hundreds of micrometers into the cell monolayer (Duclos et al., 2014). Wide adhesive stripes have been used to demonstrate that cells self-organize in a nematic phase developing a shear flow close to the edges, while the cells align perfectly with the direction of the stripe and the net flow vanishes on stripes narrower than a critical width (Duclos et al., 2018). More recently, micropatterns were used to study how cells distinguish between positive and negative curvatures in their physical environment. The authors found that concave edges promote polarized actin structures with actin flow directed toward the cell edge, whereas convex edges were characterized by an actin retrograde flow (Chen et al., 2019). Proteins micropatterns have also started to be used for studying early embryonic spatial patterning during development (Warmflash et al., 2015). For instance, a neuroectoderm model based on micropatterned human pluripotent stem (hPS) cells was developed by Xue et al. for mimicking *in vitro* the neuroectomderm regionalization observed during early neurulation *in vivo* (Xue et al., 2018). Most of the previous studies that controlled cell shape for studying cell-matrix interactions have been done using 2D micropatterned surfaces. However, a large number of cell types experience *in vivo* complex 3D environments with different physico-chemical properties.

The design of well-defined micro- and nano-structured surfaces can help to understand interactions of cells with topographical features. It has been observed that epithelial cells align along the preferential direction of nano-grooves, suggesting that the ECM topography encountered by cells *in vivo* is involved in cell polarization (Teixeira et al., 2003). Interestingly most of the components of the cytoskeleton were found to be correlated to the cell orientation, as well as the nucleus. By patterning microchannels using polyacrylamide hydrogels with a stiffness ranging from 400 Pa to 120 kPa, Pathak and Kumar found that migration velocity increased with the matrix stiffness in narrow microchannels (Pathak and Kumar, 2012). They attribute this behavior to an increased induction of polarity in actin stress fibers and traction forces in cells seeded in these narrow channels. However, this technique does not reproduce the subcellular fibrillar architecture of the ECM that can be sensed by migrating cells. To address this limitation, the Reinhart-King's group introduced a micromolding technology to form collagen microtracks that produce a 3D micro-environment which reproduce the physiological structure of native tracks found in proteolytically active cancer cells (Kraning-Rush et al., 2013). Microtracks of collagen have been used to show that adhesion and contractility mechanisms uniquely regulate migration through 3D collagen matrices. Interestingly, migration in collagen microtracks was found to be insensitive to matrix density and also independent of cell-matrix mechano-coupling, which are both important regulators of migration within the 3D matrix (Carey et al., 2015). A migration assay consisting of micro-channels with narrow constrictions has been used to show that nuclear deformation during cell migration leads to transient opening of the nuclear envelope, and that the ESCRT III complex is required to seal rapidly the nucleo-cytoplasmic barrier (Raab et al., 2016). This transient opening of the nuclear membrane causes a mixing of nucleo-cytoplasmic components, that may lead to DNA damages. More recently, large efforts have been made to replicate out-of-plane curvatures, such as tubular structures involved in ductal elongation *in vivo*. Lumens of epithelial cell sheets grown inside narrow microtubes exhibited migration modes that depend on both confinement and curvature levels (Xi et al., 2017).

MECHANICAL PROBING OF MECHANOTRANSDUCTION SIGNALING PATHWAYS

The characterization of the cells mechanical properties requires to apply well-controlled external forces to induce measurable deformations. The quantification of the mechanical deformation as a function of time and its dependence on the loading frequency allows to determine the viscoelastic behaviors of living cells and tissues. Over the last few years, original methods have been developed to apply well-controlled forces to living cells and tissues. For instance, a parallel plate method based on the bending of glass microplates of calibrated stiffness enables quantifying either passive (i.e., cell deformability) or active (i.e., cell traction) forces. Interestingly, this technique can be combined with confocal microscopy or total internal reflection fluorescence (TIRF) microscopy for studying the dynamics of cell-substrate interactions (Mitrossilis et al., 2010; Fouchard et al., 2014; Bufi et al., 2015).

However, the implementation of these techniques in the broader biological community remains challenging due to the inherently multidisciplinary expertise required to conduct and interpret mechanical measurements. Interestingly, some of these force assays can be also used for studying how external forces are transduced into biochemical and functional responses and to identify the corresponding mechanotranduction signaling pathways, in normal or pathological situations (Chen, 2008). In this section, we will review five techniques working at different levels of force and used for interrogating mechanotransduction pathways (**Figure 5**).

At the lowest force levels, Atomic Force Microscopy (AFM) has progressively emerged as a key platform for mapping the mechanical properties of living biological samples on spatially defined areas ranging from few nanometers to several tens of micrometers. By using AFM to probe fibroblasts seeded on polyacrylamide hydrogels with varying stiffness, Solon *et al.* demonstrated that fibroblasts are able to adapt their own stiffness to match the elastic modulus of its substrate (Solon et al., 2007). The use of cantilevers with a spherical tip protects the cells against damage during force application and enables to use the AFM as a local indenter (Charras and Horton, 2002). This technique was used by Elosegui-Artola et al. to indent the nucleus of fibroblasts and elegantly demonstrate that forces applied to the nucleus translocate the transcription factor YAP to the nucleus (Elosegui-Artola et al., 2017). Recently, AFM has started to be combined with complementary techniques

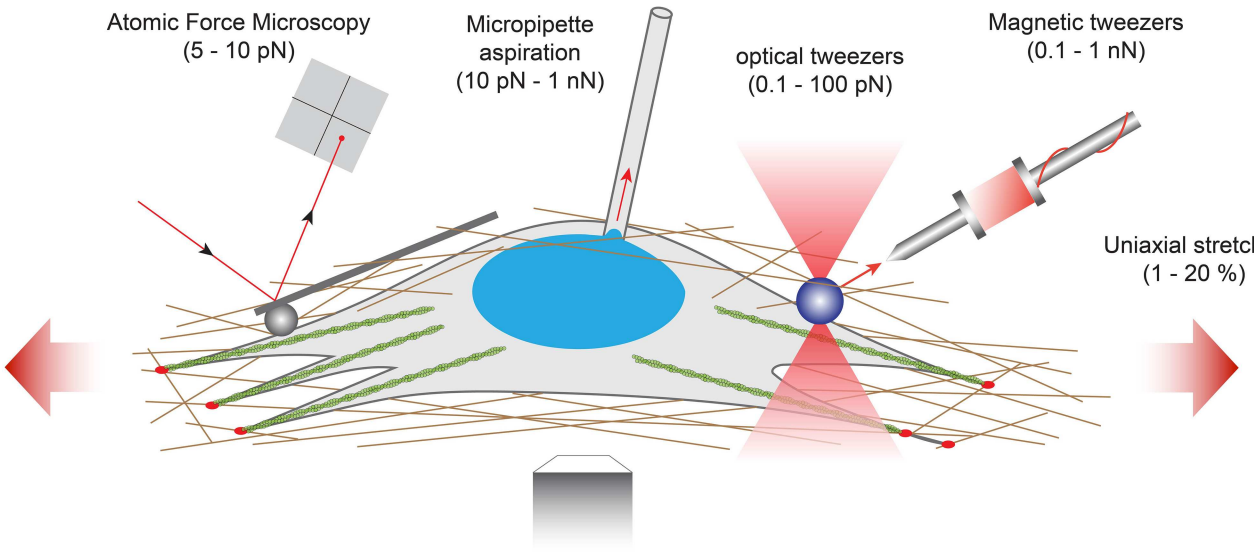

FIGURE 5 | Examples of force-application techniques used to probe the rheological properties of cells or to apply well-defined external loads for studying mechanotransduction pathways. From left to right: atomic force microscopy (AFM), micropipette aspiration, optical tweezers, magnetic tweezers and uniaxial stretcher.

including confocal microscopy, super-resolution microscopy or microfluidic devices to relate the 3D distribution of mechanical responses of biological specimen to their morphologies (Krieg et al., 2019). Indeed, the combination of AFM with additional techniques has been required to investigate the interactions among molecules (Zhou et al., 2017; Bhat et al., 2018). Such combinations of complementary techniques allow to generate multicomplexed mechanical and biochemical data from live cells and tissues in real time.

For larger levels of forces, other techniques have emerged such as optical tweezers (Killian et al., 2018), magnetic tweezers (Kollmannsberger and Fabry, 2007; Sarkar and Rybenkov, 2016), micropipette aspiration (Hochmuth, 2000) or uniaxial stretcher (**Figure 5**). Optical tweezers (also called optical traps or laser traps) consist of highly focused laser beam that provides an attractive or repulsive force. The laser beam is focused through a microscope objective. The narrowest point of the focused beam, known as the beam waist, contains a very strong electric field gradient. As a consequence, dielectric particles are attracted along the gradient to the region of strongest electric field, which is the center of the beam. The magnitude of the force (typically on the order of 0.1–100 piconewtons) depends on the relative refractive index between the particle and the surrounding medium and allows to physically hold and move micrometer-scale objects, similar to tweezers. Because the trapping force decreases with decreasing object volume, the typical object size ranges from 0.5 to 10 μm in diameter to ensure that objects are trapped efficiently. In addition, the force acting on a bead is dependent on the distance between the laser focal point and the center of the particle. Optical tweezers have been used to study membrane cell elasticity in many cell types such as neurons and red blood cells (Sleep et al., 1999). Optical tweezers were integrated with a microfluidic device to locally apply mechanical tensile and compressive force on single cells, providing an efficient platform for further studies of mechanotransduction in single cells (Honarmandi et al., 2011). More recently, an oscillatory optical trap has been used to apply forces to the cell membrane in the piconewton range. Even if the time-scale of these experiments was very short, this mechanical stimulation produced a local membrane indentation that induces cellular calcium transients, which were observed to be dependent on the stimulus strength and the force pulse frequency (Falleroni et al., 2018). Optical tweezers were usually used to manipulate molecules, but some groups have developed new methodologies based on optical tweezers to probe viscoelastic properties of cells (Yareni et al., 2016). Interestingly, the photo-induced effects caused by laser trapping were found to be negligible, giving the possibility to use optical tweezers for dynamic monitoring of viscoelastic behaviors in living cells and tissues (Lyubin et al., 2012).

Magnetic tweezers rely on the manipulation of paramagnetic beads by applying a controlled magnetic field that exerts pulling forces on the beads. Paramagnetic beads can be chemically functionalized to present adhesion proteins at their surface that can be recognized by the cell cytoskeleton. For instance, Grevesse et al. used fibronectin-coated microbeads to link the cytoskeleton of cortical neurons and probe the mechanical properties of the two main subcellular compartments (soma vs. axon) (Grevesse et al., 2015). Creep experiments revealed two opposite rheological behaviors within cortical neurons: the cell body was soft and characterized by a solid-like response, whereas the neurite compartment was stiffer and viscous-like. The authors suggested that the opposite rheological properties of neuronal microcompartments predict axonal vulnerability in brain injury. The neurite is a mechanosensitive compartment that becomes softer and adopts a pronounced viscous state on soft matrices. Furthermore, they found that local deformations of the cell body induce a significant condensation of chromatin, which results from nuclear shape remodeling that leads to a

force-dependent stiffening of the nucleus, providing a robust explanation of the stress stiffening behavior of the soma. Magnetic tweezers were also used to apply high pulsatile forces to fibronectin-coated magnetic beads bound to normal and alpha-actinin depleted cells to demonstrate the role of alpha-actinin in focal adhesion maturation (Roca-Cusachs et al., 2013). Recently, Tajik et al. applied precisely controlled oscillating forces to magnetic beads attached to individual cells. The authors demonstrate that external forces are transmitted to the nucleus, leading to chromatin stretching and changes in gene transcription (Tajik et al., 2016). Indeed, external mechanical stresses were transmitted to the nucleus, where they induced deformation of a bacterial artificial chromosome (BAC) reporter inserted into the cells. By using magnetic tweezers, Tajik and coworkers showed therefore that external forces can modulate the structure of chromatin and the transcription of specific genes (Tajik et al., 2016).

Micropipette aspiration partially aspirates a single cell by applying a subatmospheric pressure through a glass micropipette. This technique was first used on circulating white blood cells (Tsai et al., 1993) and then performed on adherent cells, leading to the estimation of the cell cortical thickness which has been estimated on the order of 0.1 μm (Zhelev et al., 1994).

Other techniques, such as membrane stretching, allow to apply a fixed strain to single cells or a cell sheet by deforming an elastic substrate. The mechanical deformation is thus transmitted to the cells through integrin-related adhesions and involved outside-in mechanotransduction signaling pathways. Silicone elastomers such a poly(dimethylsiloxane), PDMS, are usually used to form elastic membranes. Strain rates commonly vary from 0.1 to 10 Hz with a typical strain percentage ranging from 1 to 30% to keep the membrane deformation in the linear elastic regime. Uniaxial or biaxial strain field can be applied, depending on the complexity of the strain device. One dimensional (1D), or uniaxial strain, corresponds to the membrane stretch in one direction. In this configuration, the two free edges must be constrained to avoid compression in the direction perpendicular to the strain as a result of the Poisson effect. In two-dimensional (2D) strain devices, a uniform biaxial deformation is obtained from the stretching of a thin elastic membrane. Membrane stretching presents the advantage of being applicable on 2D tissues, providing an average readout from millions of cells. In addition, PDMS membranes are optically transparent and could be prepared with thicknesses ranging from 50 to 250 μm, which are particularly well-suited to perform live stretching experiments on an inverted microscope. Uniaxial stretching experiments have been performed to mimic the deformation of brain tissues during traumatic events. Indeed, it was found that traumatic stimulations of integrins are an important etiological contributor to mild Traumatic Brain Injury (mTBI). Cultures of cortical neurons were stretched with an abrupt one-dimensional strain to reproduce *in vitro* TBI. Stretching experiments revealed that the Rho signaling pathway can be activated through integrins and may contribute to the diffuse axonal injury reported in mTBI (Hemphill et al., 2011). By integrating a cell-stretching assay with micropillars, Shao and coworkers found a cell shape-dependent mechanotransduction process in stretched vascular endothelial cells. Combining experiments with theoretical modeling, the authors showed that the global architecture of contractile actomyosin filaments is a key determinant of the mechanotransduction process under uniaxial stretch (Shao et al., 2014).

MEASURING QUANTITATIVELY PROTRUSIVE AND CONTRACTILE FORCES

Actin filaments (AFs) are semiflexible polymers with a persistence length of ∼17 μm (Gittes et al., 1993), which is defined as the distance over which the filament is bent by thermal forces (Morse, 1998). AFs are ∼7 nm in diameter, functionally polar in nature and built from dimer pairs of globular actin monomers. Actin polymerization produces most of the driving force required for membrane protrusion (Parekh et al., 2005). When the end of an AF is exposed to a concentration of monomeric actin that is above its critical concentration (Cc), the filament end binds monomers and grows by polymerization. Conversely, when the concentration of monomeric actin is below Cc, monomers detach from the filament end, and the actin filament shrinks by depolymerization. These two different critical actin concentrations are, respectively localized at both opposing ends of the filament, leading to the asymmetrical growth of AFs. When the actin monomer concentration is between the two critical concentrations, only the plus-end grows while the minus-end shrinks. This process allows to maintain a roughly constant length of the filament and is known as "treadmilling" (Wilson et al., 2010).

To test this experimentally, Prass and coworkers introduced a very elegant way to directly measure the protrusive forces exerted by the leading edge (Prass et al., 2006). Briefly, an AFM cantilever of calibrated spring constant was placed vertically perpendicular to the substrate surface in front of the leading edge (**Figure 6A**). The load force applied by a migrating cell on the advancing leading edge exerts in response an equal and opposite protrusive force to the cantilever. The vertical position of the cantilever was measured optically over time. Knowing the spring constant of the cantilever and measuring its deflection with time permits estimation of the temporal evolution of the load force. When the lamellipodium touched the cantilever, one can observe an initial increase of forces. The deflection increases linearly with time until the lamellipodium is stalled at higher forces. At this stage, the velocity of the lamellipodia decreases close to zero and the leading-edge stalls. The lamellipodial protrusive force was determined from the stall force, corresponding to the moment where the cantilever stops. The first derivative of the deflection-time curves allows to obtain the cantilever speed vs. time. The deflection of the cantilever provides therefore a direct measure of the protrusive forces exerted by the lamellipodium in the nanonewton range.

The actomyosin cytoskeleton of adherent cells generates contractile forces which are transmitted to the ECM

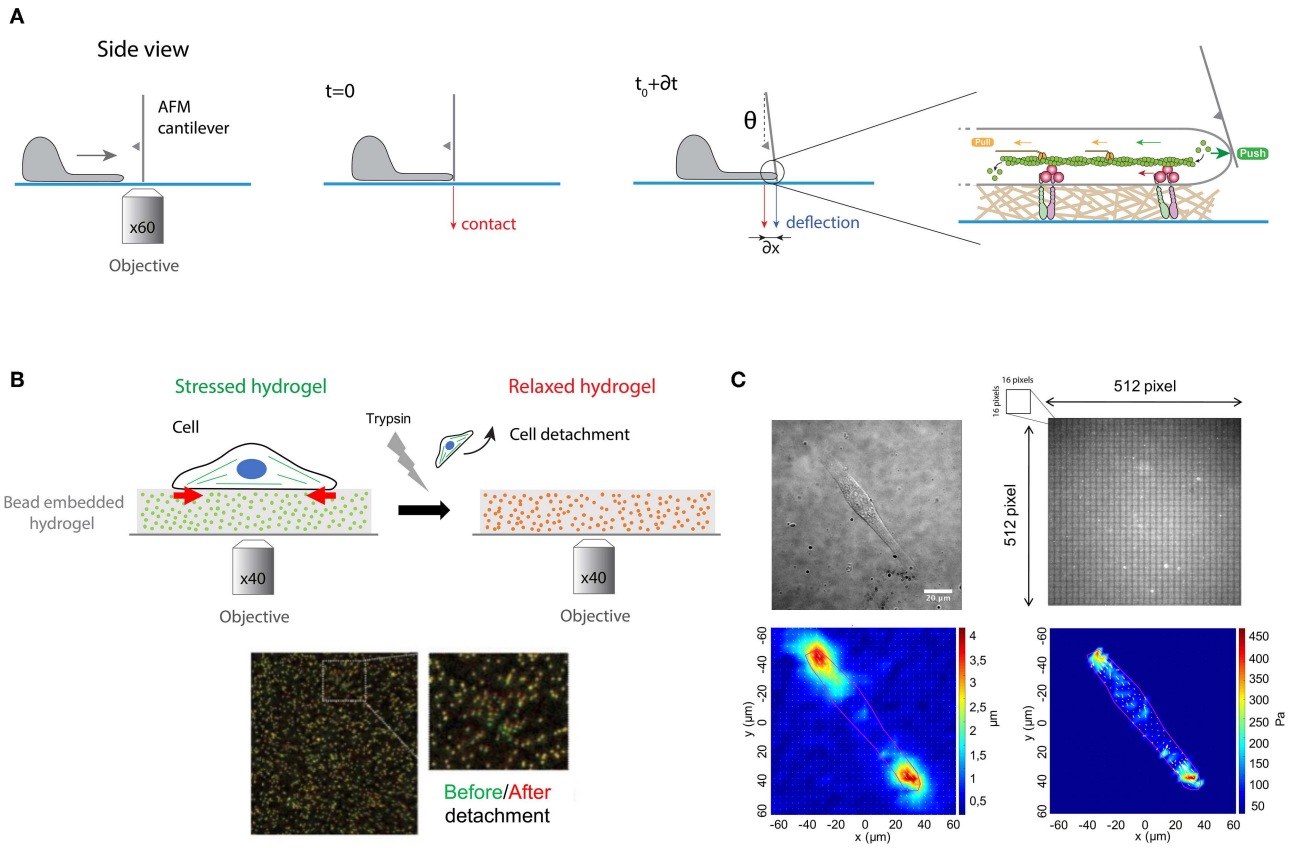

FIGURE 6 | (A) Protrusive forces exerted by the lamellipodia of migrating cells can be quantified by measuring the deflection of an AFM cantilever over time. A cantilever of calibrated spring constant is placed vertically perpendicular to the surface in front of the leading edge and its vertical position is measured optically over time. The polymerization of actomyosin filaments exerts a load force that pushes on the cell membrane that deflects the cantilever. **(B)** Traction force microscopy (TFM) measures the contractile forces exerted by adherent cells on an elastic hydrogel that contains fluorescent embedded beads of ∼200 nm in diameter. Cell spreads on the hydrogel, leading to its contraction (stressed state in green). After trypsin detachment, the contractile stress is released, and the fluorescent beads relax (in red). The differences of bead position between stressed and relaxed states serve as markers to visualize the hydrogel deformation in a 2D plane. **(C)** Gel deformations are estimated using a Fourier-based difference-with-interpolation image analysis. To characterize the contractile forces of each cell, the elastic strain energy stored in the polyacrylamide gel due to cell tractions is calculated as the product of local tractions and deformations, integrated over the spreading area of the cells. The scale bar is 20 µm.

through integrin-based adhesions (**Figure 1**). Contractile forces are crucial for physiological processes such as embryo morphogenesis or wound healing (DuFort et al., 2011) but also for pathological processes, such as cancer metastasis (Wirtz et al., 2011). Measuring cellular traction forces is therefore critical for a better understanding of the mechanisms involved in inside-out and outside-in mechanotransduction signals. To tackle this problem, Harris and coworkers developed the traction force microscopy (TFM) method (Harris et al., 1980). They showed that the wrinkling of an elastic rubber used as culture surface can be calibrated to assess the magnitude of contractile forces exerted by fibroblasts. However, the nonlinear deformation of silicone elastomers and the low spatial resolution lead to the further development of this technique to improve the resolution and reproducibility of traction force measurements (Dembo and Wang, 1999).

In this context, PAAm hydrogels with embedded fluorescent beads of ∼200 nm in diameter has emerged as a robust method to determine quantitatively traction forces exerted by adherent cells (**Figures 6B,C**). Adherent cells deform the substrate with cellular tractions that have a very small magnitude (pN—nN) and occur across small length scales (nm—µm). Due to their superior optical and mechanical properties, PAAm hydrogels are now considered as the substrate of choice to perform continuous traction force measurements. Indeed, PAAm hydrogels are optically transparent and their mechanical properties are also ideal since they are linearly elastic over a wide range of deformations. Traction forces can be estimated by comparing two images of fluorescent images of fluorescent markers embedded in the elastic hydrogel (**Figure 6B**). The first image corresponds to the stressed state where the cell is applying traction forces on the substrate, whereas the second corresponds to the fully relaxed state of the substrate. This reference image is obtained

by detaching cells with a trypsin treatment. Although TFM was originally conceived to compute a 2D force field exerted by a single cell on a flat substrate (Han et al., 2015), this method has been then successfully extended to multicellular clusters (Trepat et al., 2009). Recently a large effort has been made to compute 3D force fields of cells moving in complex fibrillar 3D microenvironment. Indeed, physiologically the ECM is mostly composed of fibers that behave as non-linear elastic materials. To address this problem 3D traction force fields were computed using synthetic polyethylene glycol (PEG) with matrix metalloprotease (MMP)-cleavable sites (Legant et al., 2010). Interestingly, 3D traction force approaches have shown that the traction force exerted by MDA-MB-231 breast carcinoma cells is independent of ECM concentration and stiffness (Steinwachs et al., 2016). It is important to note that determining the traction field from the displacement field represents a mathematical ill-posed problem that can be solved only by a small number of experts in force-field calculations. This limitation has been addressed by providing efficient open source codes (Schwarz and Soine, 2015). Recently, hydrogels labeled with a high density of fluorescent microspheres of two different colors have been developed (Sabass et al., 2008) to analyze both the distribution and dynamics of traction forces within individual focal adhesions (Plotnikov et al., 2012). In addition, light-based methods have been developed by employing molecular tension sensors, such as Förster resonance energy transfer (FRET) and deoxyribonucleic acid (DNA) (Jurchenko and Salaita, 2015). The combination of TFM with FRET-based molecular force sensors is an efficient tool to decipher the mechanisms of integrin-mediated mechanosensing (Grashoff et al., 2010; Blakely et al., 2014; Zhang et al., 2014; Jurchenko and Salaita, 2015). Moreover, novel strategies using membrane DNA tension probes allow to visualize tensile forces at cell junctions (Zhao et al., 2017).

In vivo cells exist within three-dimensional (3D) matrices, however measuring tractions of cells in 3D remains difficult and the nonlinear nature of collagen type I hydrogels, which is already used for 3D cell culture, prevents calculation of traction forces. To address this challenge, vertical cantilevers were molded from silicone elastomers in order to measure forces from tissue constructs composed of few 100 of cells (Legant et al., 2009). This device is now considered as a robust assay to determine contractile forces in cardiac tissues, providing quantitative information about the mechanotransduction signaling pathways that drive tissue formation (Boudou et al., 2012).

DETERMINING MECHANICAL AND FUNCTIONAL PROPERTIES OF THE CELL NUCLEUS

The mechanical stability of the nucleus defines its capability of maintaining a three-dimensional shape by minimizing deformations and recovering strain after a mechanical deformation. Interestingly, it has been demonstrated that large nuclear deformations increase the risk of modifying nuclear architecture and may lead to DNA damages and ultimately cell death (Versaevel et al., 2013; Denais et al., 2016).

The quantifications of deformations and recovery of nuclei are required for understanding the mechanisms involved in the nuclear response to forces and in the maintenance of its mechanical stability. To address this challenge, micropipette aspiration has been shown to be an interesting method by providing a robust way to characterize nuclear viscoelastic properties. This technique was used by Guilak and coworkers to demonstrate the individual contribution of each nuclear components. The authors conclude that nuclei behave as a viscoelastic material which is 3–4 times stiffer than the cytoplasm and nearly twice as viscous as the cytoplasm (Guilak et al., 2000). Dahl and coworkers used the micropipette aspiration technique to demonstrate that the nucleus is a stiff organelle that maintains its mechanical integrity at short times, but deforms at longer times (Dahl et al., 2005). Recently, (de-)adhesion kinetics on micropatterned substrates have been introduced as a robust assay for studying cellular and nuclear mechanics. Interestingly, this non-invasive technique can be extended to high-throughput assays for screening pharmacological candidates (Versaevel et al., 2017).

It has been shown that genome expression is affected by spatial positioning and chromatin motions (Misteli, 2004) but also by nuclear compartmentalization, and other factors that are all physically contained by the nuclear envelope (NE). The NE separates the chromatin from the cytoplasm and contains the peripheral protein lamina (Gruenbaum et al., 2003), which is attached by nuclear membrane proteins that stabilize the envelope and provide sites for chromatin binding and organization (**Figure 7A**) (Burke and Stewart, 2002).

The overall nuclear stiffness is mainly established by the remodeling of lamina and chromatin. It is therefore important to decipher their individual roles for a better understanding of the nuclear mechanics and the regulation of cellular functions. It has been shown that chromatin controls the resistance to small deformations, while lamina dictates the nuclear strain stiffening that dominates resistance to large deformations (Stephens et al., 2017). In a first approximation, the mechanical response of the lamina can be described by a Maxwell model that combines in series a purely elastic spring with a purely viscous damper. Recent works have shown that B-type lamins contribute primarily to the elastic response, whereas A-type lamins contribute to the viscosity (**Figure 7B**) (Swift et al., 2013). As a consequence, increasing A-type lamins relative to B-type lamins leads to slower nuclear deformation under stress (Swift et al., 2013). Recently, the loss of A-type lamins in human dermal fibroblasts was observed to correspond to large stress fibers and high traction forces, suggesting a role of A-type lamins in the balance between cytoskeletal tension and cell-substrate adhesions, which may contribute to mechanosensing defects as observed in laminopathies (Corne et al., 2017). It is now clear that there is a global connection between the physico-chemical properties of micro-environment and gene expression. Indeed, integrins at the focal adhesions link the cytoskeleton to the ECM proteins, which is in close interaction with the nuclear membrane through LINC complex (**Figure 7A**). Using Structured Illumination Microscopy

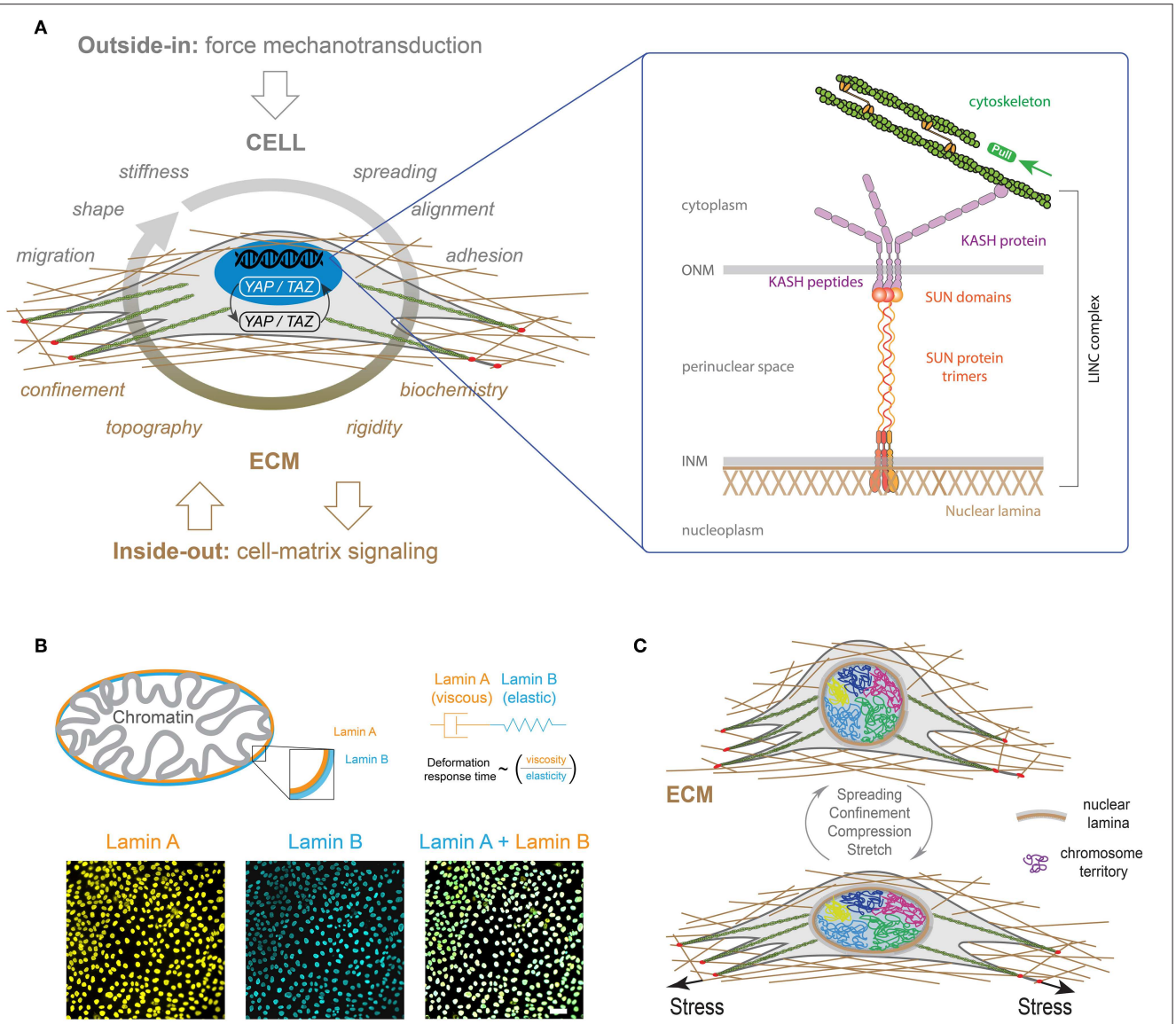

FIGURE 7 | (A) LINC complexes are made of the inner nuclear membrane (INM), SUN protein trimers, the outer nuclear membrane (ONM) and KASH proteins. KASH protein mediates interactions with actin cables through Nesprin 2. **(B)** A-type and B-type lamins (orange and blue, respectively) form individual polymer networks which are juxtaposed on the inside of the nuclear envelope. Both lamin types are found at the interface between chromatin and the cytoskeleton (Swift and Discher, 2014). The mechanical properties of the lamina can be described by viscoelastic models based on the combination of elastic (spring-like) springs and viscous (flowing) dahspots. The characteristic deformation time of the lamina is therefore related to the ratio of the viscous part (i.e., lamin A) on the elastic one (i.e., lamin B) (Swift et al., 2013). Typical images of nuclei of Madin-Darby Canine Kidney (MDCK) cells stained for lamin A (in orange) and lamin B (in blue). The scale bar is 10 μm. **(C)** Differential mechanical forces are applied on the nucleus, such as actin contractile forces or microtubules compressive forces, through LINC complexes. The three-dimensional organization of chromosomes is modulated by these mechanical signals, leading to new gene expression programs (Uhler and Shivashankar, 2017).

(SIM), it has been shown that nuclear indentations are generated by accumulated tension in apical actin stress fibers that deform the nuclear lamina. Indeed a local enrichment of LINC complexes has been observed at indented nuclear zones where apical actin fibers are anchored to the nuclear lamina. In addition, the deep deformations of the nuclear envelope indices the formation of segregated domains of condensed chromatin (Versaevel et al., 2014a). Finally, Lamina-associated domains (LADs) along DNA enables the interactions between chromosomes and nuclear membrane. This global structure suggests that modifications of the ECM can modulate the regulation of the genome architecture and cell-fate decisions (Shivashankar, 2019).

Cell shape changes have been found to modulate nuclear shape, DNA expression (Versaevel et al., 2012), histone acetylation and gene expression profile (Jain et al., 2013). Inside nuclei, DNA is packed into less condensed euchromatin and more condensed heterochromatin, that both form chromosomes. The spatial organization of chromosomes

into distinct chromosome territories inside the nucleus is crucial for regulation of gene expression (**Figure 7C**) (Bickmore and van Steensel, 2013). Interestingly, the reorganization of these territories has been observed during differentiation (Boney and Cavalli, 2016). In view of the linkage between the cellular micro-environment and the nucleus through the cytoskeleton and specific connectors, the question of the effect of external mechanical stresses applied to the cell on the spatial organization of chromatin was raised. To address this question, Wang et al. used fluorescence hybridization to demonstrate that the repositioning of chromosomes correlates with gene expression that were found to be cell geometry dependent (Wang et al., 2017). More recently, Roy et al. demonstrated the reversibility of the chromosome territories transitions by reprogramming fibroblasts into stem cell-like cells through laterally confined growth (Roy et al., 2018). Growing evidence suggests that a mechanical load on the nucleus drives the nuclear translocation of YAP by modulating molecular transport through nuclear pores (**Figure 7A**) (Elosegui-Artola et al., 2017). In addition, the stiffening of the ECM allows to connect the cytoskeleton and the nucleus, allowing the propagation of forces from focal adhesions to the nuclear envelope.

OPTOGENETIC METHODS TO INTERROGATE MECHANOTRANSDUCTION PATHWAYS

Optogenetics is a rapidly evolving technology that aims to control optically and precisely specific events in genetically targeted living cells and tissues. Optogenetic methods allow to deliver an optical control at high temporal (millisecond-scale) and spatial resolution in physiological or pathological situations (Deisseroth, 2011). The principle of optogenetics uses the heterologous expression of light-sensitive microbial membrane proteins, called opsins, to induce optically a cell depolarization or silencing on a millisecond time scale (**Figure 8A**). Optogenetics combines therefore optics, genetics and bioengineering to either stimulate or inhibit cellular activity via light-sensitive opsins (**Figure 8B**) (Nagel et al., 2002, 2003).

In 1979 Francis Crick described one of the major challenges facing neuroscience by the need to control one cell type in the brain while leaving other cell types unaltered. Since electrodes cannot be used to precisely target defined cells, Crick envisioned that light might be used to control and monitor the activity of genetically defined neuronal populations. However, it took more than 30 years for neuroscientists to develop the first approaches for optogenetics. In the early 2000s, Zemelman and Miesenbock (Sloan- Kettering Cancer center, New York) (Zemelman et al., 2003) and Trauner, Kramer and Isacoff (University of California, Berkeley) (Banghart et al., 2004) considered alternative strategies based on cascades or combination of different genes. In 2005, Deisseroth and coworkers used a light-sensitive microbial protein, Channelrhodopsin-2 (ChR2), expressed in neurons to activate neurons with light pulses in a temporally precise manner (Boyden et al., 2005). The current optogenetics tool box opens the door to experiments where neuronal activity can be controlled in real time.

Although it arose from neurosciences, optogenetics has started to address recently open questions about mechanotransduction mechanisms in various cell types. For instance, Bruegman *et al.* showed that optogenetic stimulations of skeletal muscles expressing the light-sensitive channel ChR2 can generate large forces, which could be useful for studying mechanotransduction signaling pathways in muscle cells (Bruegmann et al., 2015). More recently, Valon and coworkers reported the up- and down- regulation of contractile forces with optogenetic tools working at high spatiotemporal accuracy (Valon et al., 2017). The authors found a rapid increase of cellular traction forces in response to the translocation of RhoA activator ARHGEF11 to CRY2-mCherry (optoGEF-RhoA). Changes in cell contractility were found to be related to modifications in the transcriptional regulator YAP, demonstrating the ability of optogenetic approach to control mechanotransduction signaling pathways. More recently, Baaske and coworkers reported an optogenetic system based on an integrin engineered with a phytochrome-interacting factor domain (OptoIntegrin) and a red light-switchable phytochrome B-functionalized matrix (OptoMatrix) (Baaske et al., 2019). This receptor-ligand pair enables a reversible optogenetic control of integrin-matrix interaction, as well as the controlled activation of downstream mechanosensory signaling pathways.

SUMMARY AND FUTURE PERSPECTIVES

Novel techniques developed to probe cellular forces have reported a wide range of mechanisms acting over multiple length scales (from molecular forces to supra-cellular force patterns). As a consequence, physical forces cannot be only considered as basic switches of mechanotransduction signals, but as the key mechanism to propagate signals between cells. Interestingly, recent technological developments allow to study the molecular mechanisms used by cellular forces to alter gene activities by modulating the conversion of mechanical stimuli into biochemical signals. Advancements in force measurement methods will therefore permit to address many remaining open questions surrounding cell-substrate but also cell-cell interactions, such as cadherins. For instance, understanding how mechanical tension exerted on cadherins is converted into biochemical signals and how this signaling in turn leads to changes in cell expression remains an open question in cell biology.

The understanding of the molecular mechanisms involved in outside-in and inside-out mechanotransduction signaling pathways requires to elaborate integrated strategies combining super resolution fluorescence microscopy (e.g., stimulated emission depletion, STED—photo-activated localization microscopy, PALM—stochastic optical reconstruction microscopy, STORM) with biophysical probes and multipatterning of proteins. In addition to these combined imaging techniques, FRET biosensors could be applied to examine force transmission across the cytoskeleton to nuclear envelope proteins, chromatin remodeling or mechanically induced changes within the nucleus. FRET between fluorophores of a single type, known as homoFRET,

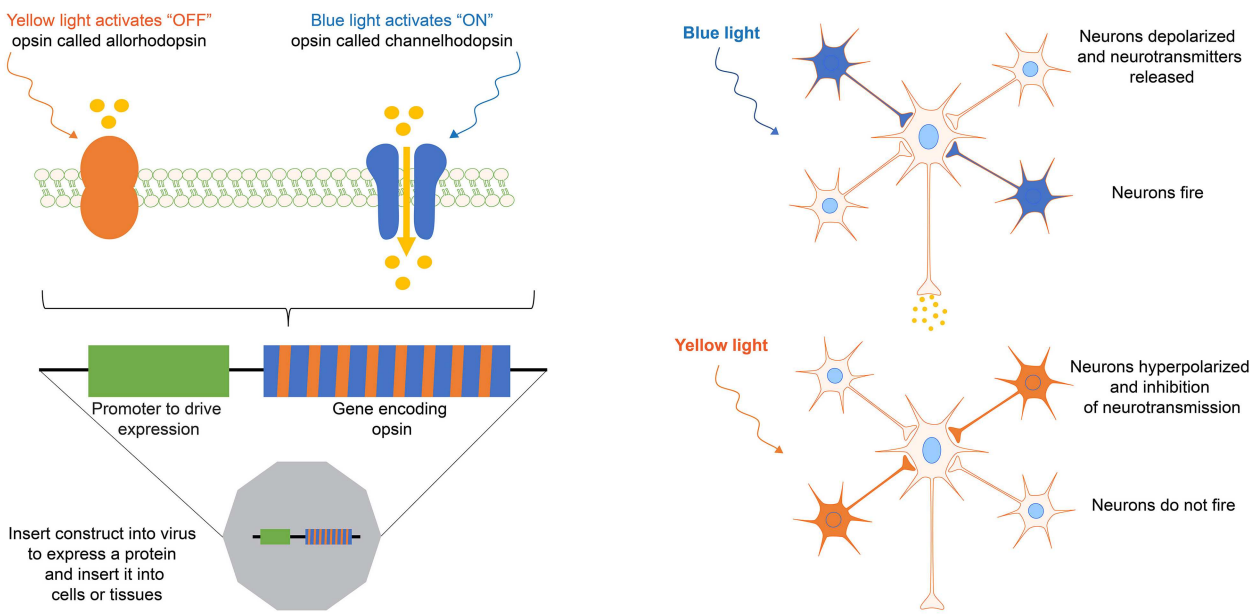

FIGURE 8 | (A) The optogenetic principle is based on light-sensitive proteins from algae called opsins. **(B)** Opsins can be expressed in single cells, cell clusters or tissues by using transfection with a gene construct inserted in viruses. By using different wavelengths, optogenetics allows to activate or inhibit for instance neurotransmission, or specific mechanotransduction signaling pathways in living cells, such as neurons.

is a promising method to visualize and quantitatively measure changes in protein ratios upon force application, based on the signal produced when molecules labeled with enhanced green fluorescent protein, such as G-actin, assemble into actin filaments.

A further challenge should be devoted to a better understanding of how ECM sensing can activate specific transcription factors and translocates them to the cell nucleus. Indeed, it remains unclear whether chromosome configurations can be altered in response to the modifications of the mechanical properties of the nucleus that can be modulated by changes in the ECM physico-chemical properties. Furthermore, several aspects of Piezo channels must be addressed in the near future to determine the role of specific mechanotransduction processes in regulating physiological and pathological processes. For instance, it will be important to decouple the role of Piezo 1 and 2 that makes them such versatile mechanosensors. In addition, questions about conformational changes leading to channel (in-)activation remain to be answered.

Finally, a major technical challenge in cellular mechanotransduction concerns the development of synthetic models of the stem cell niche to manipulate the biophysical and biochemical properties of the stem cell microenvironment. Indeed, the discovery of induced pluripotent stem (iPS) cells as patient-specific stem cells represents a breakthrough for the basic cell biology and new therapies. Understanding how stem cell behavior can be regulated by mechanical forces can provide fundamental insights for the design of artificial niches for regenerative therapies. In this context, we envision exciting technical developments for the light-controlled activation of cellular forces, dynamic organoid systems and synthetic niches with a spatiotemporally controlled release of proteins and growth factors. Smart stem cell niches that integrate the control of material properties (stiffness, topography, etc.) and protein patterning to recapitulate cell-cell and cell-matrix interactions is required to identify the ECM cues which are relevant to niche-like regulation of stem cell fate. By guiding collections of stem cells that can assemble in 3D, organ-on-a-chip platforms represent a valuable technology to form realistic *in vitro* models of organ-level systems required to interrogate mechanotransduction pathways in stem cells but also to realize a precision medicine approach by testing important differences in varied patient cohorts.

AUTHOR CONTRIBUTIONS

DM and SG designed the content of the article. All authors performed literature survey, prepared the figures and wrote the article. All authors edited and reviewed the article before submission.

FUNDING

This work was financially supported by the FEDER project PROSTEM, the Belgian National Fund for Scientific Research (F.R.S.-FNRS, Crédits de Recherches–J009916F and J0191.17) and the MAT(T)ISSE project financially supported by Interreg France-Wallonie-Vlaanderen (Fonds Européen de

Développement Régional, FEDER-ERDF). DM, LA, CB, EV, ML, and AP are financially supported by FRIA (F.R.S.-FNRS). The Mechanobiology and Soft Matter group belongs to the French research consortium GDR 3070 CellTiss.

ACKNOWLEDGMENTS

The authors apologize to the many colleagues whose work could not be cited due to space constraints.

REFERENCES

Annabi, N., Tamayol, A., Uquillas, J. A., Akbari, M., Bertassoni, L. E., Cha, C., et al. (2014). 25th anniversary article: rational design and applications of hydrogels in regenerative medicine. *Adv. Mater. Weinheim.* 26, 85–123. doi: 10.1002/adma.201303233

Baaske, J., Mülhäuser, W. W. D., Sasha Yousefi, O., Zanner, S., Radziwill, G., Hörner, M. et al. (2019). Optogenetic control of integrin-matrix interaction. *Commun. Biol.* 2:15. doi: 10.1038/s42003-018-0264-7

Baker, B. M., Trappmann, B., Wang, W. Y., Sakar, M. S., Kim, I. L., Shenoy, V. B., et al. (2015). Cell-mediated fibre recruitment drives extracellular matrix mechanosensing in engineered fibrillar microenvironments. *Nat. Mater.* 14, 1262–1268. doi: 10.1038/nmat4444

Banghart, M., Borges, K., Isacoff, E., Trauner, D., and Kramer, R. H. (2004). Light-activated ion channels for remote control of neuronal firing. *Nat. Neurosci.* 7, 1381–1386. doi: 10.1038/nn1356

Bauer, A., Gu, L., Kwee, B., Li, W. A., Dellacherie, M., Celiz, A. D., et al. (2017). Hydrogel substrate stress-relaxation regulates the spreading and proliferation of mouse myoblasts. *Acta Biomater.* 62, 82–90. doi: 10.1016/j.actbio.2017.08.041

Bhat, S. V., Sultana, T., Körnig, A., McGrath, S., Shahina, Z., and Dahms, T. E. S. (2018). Correlative atomic force microscopy quantitative imaging-laser scanning confocal microscopy quantifies the impact of stressors on live cells in real-time. *Sci. Rep.* 8:8305. doi: 10.1038/s41598-018-26433-1

Bickmore, W. A., and van Steensel, B. (2013). Genome architecture: domain organization of interphase chromosomes. *Cell* 152, 1270–1284. doi: 10.1016/j.cell.2013.02.001

Blakely, B. L., Dumelin, C. E., Trappman, B., McGregor, L. M., Choi, C. K., Anthony, P. C., et al. (2014). A DNA-based molecular probe for optically reporting cellular traction forces. *Nat. Methods* 11, 1229–1232. doi: 10.1038/nmeth.3145

Boney, B., and Cavalli, G. (2016). Organization and function of the 3D genome. *Nat. Rev. Genet.* 17, 661–678. doi: 10.1038/nrg.2016.112

Boudou, T., Legant, W. R., Mu, A., Borochin, M. A., Thavandiran, N., Radisic, M., et al. (2012). A microfabricated platform to measure and manipulate the mechanics of engineered cardiac microtissues. *Tissue Eng. Part A* 18, 910–919. doi: 10.1089/ten.tea.2011.0341

Boyden, E. S., Zhang, F., Bamberg, E., Nagel, G., and Deisseroth, K. (2005). Millisecond-timescale, genetically targeted optical control of neural activity. *Nat. Neurosci.* 8, 1263–1268. doi: 10.1038/nn1525

Bruegmann, T., van Bremen, T., Vogt, C. C., Send, T., Fleischmann, B. K., and Sasse, P. (2015). Optogenetic control of contractile function in skeletal muscle. *Nat. Commun.* 2:7153. doi: 10.1038/ncomms8153

Bryant, S. J., Cuy, J. L., Hauch, K. D., and Ratner, B. D. (2007). Photo-patterning of porous hydrogels for tissue engineering. *Biomaterials* 28, 2978–2986. doi: 10.1016/j.biomaterials.2006.11.033

Bufi, N., Durand-Smet, P., and Asnacios, A. (2015). Single-cell mechanics: the parallel plates technique. *Methods Cell Biol.* 125, 187–209. doi: 10.1016/bs.mcb.2014.11.002

Burke, B., and Stewart, C. L. (2002). Life at the edge: the nuclear envelope and human disease. *Nat. Rev. Mol. Cell Biol.* 3, 575–585. doi: 10.1038/nrm879

Carey, S. P., Rahman, A., Kraning-Rush, C. M., Romero, B., Somasegar, S., Torre, O. M., et al. (2015). Comparative mechanisms of cancer cell migration through 3D matrix and physiological microtracks. *Am. J. Physiol. Cell Physiol.* 308, C436–C447. doi: 10.1152/ajpcell.00225.2014

Carter, S. B. (1967). Haptotactic islands – a method of confining single cells to study individual cell reactions and clone formation. *Exp. Cell Res.* 48, 189–193. doi: 10.1016/0014-4827(67)90298-4

Chabria, M., Hertig, S., Smith, M. L., and Vogel, V. (2010). Stretching fibronectin fibres disrupts binding of bacterial adhesins by physically destroying an epitope. *Nat. Commun.* 1:135. doi: 10.1038/ncomms1135

Charras, G. T., and Horton, M. A. (2002). Single cell mechanotransduction and its modulation analyzed by atomic force microscope indentation. *Biophys. J.* 82, 2970–2981. doi: 10.1016/S0006-3495(02)75638-5

Charrier, E. E., Pogoda, K., Wells, R. G., and Janmey, P. (2018). Control of cell morphology and differentiation by substrates with independently tunable elasticity and viscous dissipation. *Nat. Comm.* 9:449. doi: 10.1038/s41467-018-02906-9

Chauduri, O., Gu, L., Darnell, M., Klumpers, D., Bencherif, S. A., Weaver, J. C., et al. (2015). Substrate stress relaxation regulates cell spreading. *Nat. Commun.* 6:6365. doi: 10.1038/ncomms7365

Chauduri, O., Gu, L., Klumpers, D., Darnell, M., Bencherif, S. A., Weaver, J. C., et al. (2016). Hydrogels with tunable stress relaxation regulate stem cell fate and activity. *Nat. Mater.* 15, 326–334. doi: 10.1038/nmat4489

Chen, C. S. (2008). Mechanotransduction - a field pulling together? *J. Cell Sci.* 121, 285–3292. doi: 10.1242/jcs.023507

Chen, C. S., Mrksich, M., Huang, S., Whitesides, G. M., and Ingber, D. E. (1997). Geometric control of cell life and death. *Science* 276, 425–428. doi: 10.1126/science.276.5317.1425

Chen, T., Callan-Jones, A., Fedorov, E., Ravasio, A., Brugues, A., Ong, H. T., et al. (2019). Large-scale curvature sensing by directional actin flow drives cellular migration mode switching. *Nat. Phys.* 15, 393–402. doi: 10.1038/s41567-018-0383-6

Chu, S. H., Lo, L. H., Lai, R. L., Yang, T. T., Weng, R. R., Liao, J. C., et al. (2019). A microfluidic device for in situ fixation and super-resolved mechanosensation studies of primary cilia. *Biomicrofluidics* 13:014105. doi: 10.1063/1.5081756

Coppée, S., Gabriele, S., Jonas, A., Jestin, J., and Damman, P. (2011). Influence of Chain Interdiffusion between Immiscible Polymers on Dewetting Dynamics. *Soft Matter* 7, 9951–9955. doi: 10.1039/c1sm05486d

Corne, T. D. J., Sieprath, T., Vandenbussche, J., Mohammed, D., te Lindert, M., Gabriele, S., et al. (2017). Deregulation of focal adhesion formation and cytoskeletal tension due to loss of A-type lamins. *Cell Adh. Migr.* 11, 447–463. doi: 10.1080/19336918.2016.1247144

Coste, B., Mathur, J., Schmidt, M., Early, T. J., Ranade, S., Petrus, M. J., et al. (2010). Piezo1 and Piezo2 are essential components of distinct mechanically activated cation channels. *Science* 330, 55–60. doi: 10.1126/science.1193270

Dahl, K. N., Engler, A. J., Pajerowski, J. D., and Discher, D. E. (2005). Power-law rheology of isolated nuclei with deformation mapping of nuclear substructures. *Biophys. J.* 89:2855. doi: 10.1529/biophysj.105.062554

Damljanovic, V., Lagerholm, B. C., and Jacobson, K. (2005). Bulk and micropatterned conjugation of extracellular matrix proteins to characterized polyacrylamide substrates for cell mechanotransduction assays. *BioTechniques* 39, 847–851. doi: 10.2144/000112026

Deisseroth, K. (2011). Optogenetics. *Nat. Methods* 8, 26–29. doi: 10.1038/nmeth.f.324

Dembo, M., and Wang, Y. L. (1999). Stresses at the cell-to-substrate interface during locomotion of fibroblasts. *Biophys. J.* 76, 2307–2316. doi: 10.1016/S0006-3495(99)77386-8

Denais, C. M., Gilbert, R. M., Isermann, P., McGregor, A. L., te Lindert, M., Weigelin, B., et al. (2016). Nuclear envelope rupture and repair during cancer cell migration. *Science* 352, 353–358. doi: 10.1126/science.aad7297

Dong, Y., Jin, G., Hong, Y., Zhu, H., Lu, T. J., Xu, F., et al. (2018). Engineering the cell microenvironment using novel photoresponsive hydrogels. *ACS Appl. Mater. Interfaces* 10, 12374–12389. doi: 10.1021/acsami.7b17751

Duclos, G., Blanch-Mercader, C., Yashunsky, V., Salbreux, G., Joanny, J. F., Prost, J., et al. (2018). Spontaneous shear flow in confined cellular nematics. *Nat. Phys.* 14, 728–732. doi: 10.1038/s41567-018-0099-7

Duclos, G., Garcia, S., Yevick, H. G., and Silberzan, P. (2014). Perfect nematic order in confined monolayers of spindle-shaped cells. *Soft Matter* 10, 2346–2353. doi: 10.1039/C3SM52323C

DuFort, C. C., Paszek, M. J., and Weaver, V. M. (2011). Balancing forces: architectural control of mechanotransduction. *Nat. Rev. Mol. Cell Biol.* 12, 308–319. doi: 10.1038/nrm3112

Elosegui-Artola, A., Andreu, I., Beedle, A. E. M., Lezamiz, A., Uroz, M., Kosmalska, A. J., et al. (2017). Force triggers YAP nuclear entry by regulating transport across nuclear pores. *Cell* 171, 1397–1410. doi: 10.1016/j.cell.2017.10.008

Engler, A. J., Sen, S., Sweeney, H. L., and Discher, D. E. (2006). Matrix elasticity directs stem cell lineage specification. *Cell* 126, 677–689. doi: 10.1016/j.cell.2006.06.044

Falleroni, F., Torre, V., and Cojoc, D. (2018). Cell mechanotransduction with piconewton forces applied by optical tweezers. *Front. Cell. Neurosci.* 12:130. doi: 10.3389/fncel.2018.00130

Fink, J., Carpi, N., Betz, T., Betard, A., Chebah, M., Azioune, A., et al. (2011). External forces control mitotic spindle positioning. *Nat. Cell Biol.* 13, 771–778. doi: 10.1038/ncb2269

Fouchard, J., Bimbard, C., Bufi, N., Durant-Smet, P., Proag, A., Richert, A., et al. (2014). Three-dimensional cell body shape dictates the onset of traction force generation and growth of focal adhesions. *Proc. Natl. Acad. Sci. U.S.A* 111, 13075–13080. doi: 10.1073/pnas.1411785111

Gittes, F., Mickey, B., Nettleton, J., and Howard, J. (1993). Flexural rigidity of microtubules and actin filaments measured from thermal fluctuations in shape. *J. Cell Biol.* 120, 923–934. doi: 10.1083/jcb.120.4.923

Grashoff, C., Hoffman, B. D., Brenner, M. D., Zhou, R., Parsons, M., Yang, M. T., et al. (2010). Measuring mechanical tension across vinculin reveals regulation of focal adhesion dynamics. *Nature* 466, 263–267. doi: 10.1038/nature09198

Grevesse, T., Dabiri, B. E., Parker, K. K., and Gabriele, S. (2015). Opposite rheological properties of neuronal microcompartments predict axonal vulnerability in brain injury. *Sci. Rep.* 5:9475. doi: 10.1038/srep09475

Grevesse, T., Versaevel, M., Circelli, G., Desprez, S., and Gabriele, S. (2013). A simple route to functionalize polyacrylamide hydrogels for the independent tuning of mechanotransduction cues. *Lab Chip* 13:777. doi: 10.1039/c2lc41168g

Grevesse, T., Versaevel, M., and Gabriele, S. (2014). Preparation of Hydroxy-PAAm Hydrogels for decoupling the effects of mechanotransduction cues. *J. Vis. Exp.* 90:e51010. doi: 10.3791/51010

Gruenbaum, Y., Goldman, R. D., Meyuhas, R., Mills, E., Margalit, A., Fridkin, A., et al. (2003). The nuclear lamina and its functions in the nucleus. *Int. Rev. Cytol.* 226, 1–62. doi: 10.1016/S0074-7696(03)01001-5

Guilak, F., Tedrow, J. R., and Burgkart, R. (2000). Viscoelastic properties of the cell nucleus. *Biochem. Biophys. Res. Commun.* 269, 781–786. doi: 10.1006/bbrc.2000.2360

Han, S. J., Oak, Y., Groisman, A., and Danuser, G. (2015). Traction microscopy to identify force modulation in subresolution adhesions. *Nat. Methods* 12, 653–656. doi: 10.1038/nmeth.3430

Harris, A. (1973). Behavior of cultured cells on substrata of variable adhesiveness. *Exp. Cell Res.* 77, 285–297. doi: 10.1016/0014-4827(73)90579-X

Harris, A. K., Wild, P., and Stopak, D. (1980). Silicone rubber substrata: a new wrinkle in the study of cell locomotion. *Science* 208, 177–179. doi: 10.1126/science.6987736

Hemphill, M. A., Dabiri, B. E., Gabriele, S., Kerscher, L., Franck, C., Goss, J. A., et al. (2011). A possible role for integrin signaling in Diffuse Axonal Injury. *PLoS ONE* 6:e22899. doi: 10.1371/journal.pone.0022899

Hochmuth, R. M. (2000). Micropipette aspiration of living cells. *J. Biomech.* 33, 15–22. doi: 10.1016/S0021-9290(99)00175-X

Honarmandi, P., Lee, H., Lang, M. J., and Kamm,R. D. (2011). A microfluidic system with optical laser tweezers to study mechanotransduction and focal adhesion recruitment. *Lab Chip*. 11, 684–694. doi: 10.1039/C0LC00487A

Humphrey, J. D., Dufresne, E. R., and Schwartz, M. A. (2014). Mechanotransduction and extracellular matrix homeostasis. *Nat. Rev. Mol. Cell Biol.* 12, 802–812. doi: 10.1038/nrm3896

Humphries, M. J. (1990). The molecular basis and specificity of integrin-ligand interactions. *J. Cell Sci.* 97, 585–592.

Jaalouk, D. E., and Lammerding, J. (2009). Mechanotransduction gone awry. *Nat. Rev. Mol. Cell Biol.* 10, 63–73. doi: 10.1038/nrm2597

Jain, N., Venkatesan Iyer, K., Kumar, A., and Shivashankar, G. V. (2013). Cell geometric constraints induce modular gene-expression patterns via redistribution of HDAC3 regulated by actomyosin contractility. *Proc. Natl. Acad. Sci. U.S.A.* 110, 11349–11354. doi: 10.1073/pnas.1300801110

Jurchenko, C., and Salaita, K. S. (2015). Lighting up the force: investigating mechanisms of mechanotransduction using fluorescent tension probes. *Mol. Cell. Biol.* 35, 2570–2582. doi: 10.1128/MCB.00195-15

Karp, G. (2015). *Cell and Molecular Biology: Concepts and Experiments*. New York, NY: John Wiley & Sons, Inc.

Katta, S., Krieg, M., and Goodman, M. B. (2015). Feeling force: physical and physiological principles enabling sensory mechanotransduction. *Annu. Rev. Cell Dev. Biol.* 31, 347–371. doi: 10.1146/annurev-cellbio-100913-013426

Killian, J. L., Ye, F., and Wang, M. D. (2018). Optical Tweezers: a force to be reckoned with *Cell* 175, 1445–1448. doi: 10.1016/j.cell.2018.11.019

Klotzsch, E., Smith, M. L., Kubow, K. E., Muntwyler, S., Little, W. C., Beyeler, F., et al. (2009). Fibronectin forms the most extensible biological fibers displaying switchable force-exposed cryptic binding sites. *Proc. Natl. Acad. Sci. U.S.A.* 106, 18267–1872. doi: 10.1073/pnas.0907518106

Kloxin, A. M., Kasko, A. M., Salinas, C. N., and Anseth, K. S. (2009). Photodegradable hydrogels for dynamic tuning of physical and chemical properties. *Science* 324, 59–63 doi: 10.1126/science.1169494

Kollmannsberger, P., and Fabry, B. (2007). High-Force Magnetic tweezers with force feedback for biological applications. *Rev. Sci. Instrum.* 78:14301. doi: 10.1063/1.2804771

Kraning-Rush, C. M., Carey, S. P., Lampi, M. C., and Reinhart-King, C. A. (2013). Microfabricated collagen tracks facilitate single cell metastatic invasion in 3D. *Integr. Biol.* 5, 606–616. doi: 10.1039/c3ib20196a

Krieg, M., Fläschner, G., Alsteens, D., Gaub, B. M., Roos, W. H., Wuite, G. J. L., et al. (2019). Atomic force microscopy-blased mechanobiology. *Nat. Rev. Phys.* 1, 41–57. doi: 10.1038/s42254-018-0001-7

Kubow, K. E., Vukmirovic, R., Zhe, L., Klotzsch, E., Smith, M. L., Gourdon, D., et al. (2015). Mechanical forces regulate the interactions of fibronectin and collagen I in extracellular matrix. *Nat. Commun.* 6:8026. doi: 10.1038/ncomms9026

Lantoine, J., Grevesse, T., Villers, A., Delhaye, G., Mestdagh, C., Versaevel, M., et al. (2016). Matrix stiffness modulates formation and activity of neuronal networks of controlled architectures. *Biomaterials* 89:14e24. doi: 10.1016/j.biomaterials.2016.02.041

Legant, W. R., Miller, J. S., Blakely, B. L., Cohen, D. M., Genin, G. M., and Chen, C. S. (2010). Measurement of mechanical tractions exerted by cells in three-dimensional matrices. *Nat. Methods* 7, 969–971. doi: 10.1038/nmeth.1531

Legant, W. R., Pathak, A., Yang, M. T., Deshpande, V. S., McMeeking, R. M., and Chen, C. S. (2009). Microfabricated tissue gauges to measure and manipulate forces from 3D microtissues. *Proc. Natl. Acad. Sci. U.S.A.* 106, 10097–10102. doi: 10.1073/pnas.0900174106

Liu, W., Jawerth, L. M., Sparks, E. A., Falvo, M. R., Hantgan, R. R., Superfine, R., et al. (2006). Fibrin fibers have extraordinary extensibility and elasticity. *Science* 313:634. doi: 10.1126/science.1127317

Liu, X. M., Yang, B., and Wang, Y. L. (2005). Photoisomerisable cholesterol derivatives as photo-trigger of liposomes: effect of lipid polarity, temperature, incorporation ratio, and cholesterol. *Biochim. Biophys. Acta* 1720, 28–34. doi: 10.1016/j.bbamem.2005.10.016

Lueckgen, A., Garske, D. S., Ellinghaus, A., Desai, R. M., Stafford, A. G., Mooney, D. J., et al. (2018). Hydrolytically-degradable click-crosslinked alginate hydrogels. *Biomaterials* 181, 189–198. doi: 10.1016/j.biomaterials.2018.07.031

Lyubin, E. V., Khokhlova, M. D., Skryabina, M. N., and Fedyanin, A. A. (2012). Cellular viscoelasticity probed by active rheology in optical tweezers. *J. Biomed. Opt.* 17:101510. doi: 10.1117/1.JBO.17.10.101510

Mahmud, G., Campbell, C. J., Bishop, K. J. M., Komarova, Y. A., Chaga, O., Soh, S., et al. (2009). Directing cell motions on micropatterned ratchets. *Nat. Phys.* 5, 606–612. doi: 10.1038/nphys1306

Mandal, K., Wang, I., Vitiello, E., Orellana, L. A. C., and Balland, M. (2014). Cell dipole behaviour revealed by ECM sub-cellular geometry. *Nat. Commun.* 5:5749. doi: 10.1038/ncomms6749

Misteli, T. (2004). Spatial positioning; a new dimension in genome function. *Cell.* 119, 153–156. doi: 10.1016/j.cell.2004.09.035

Mitrossilis, D., Fouchard, J., Pereira, D., Postic, F., Richert, A., Saint-Jean, M., et al. (2010). Real-time single-cell response to stiffness. *Proc. Natl. Acad. Sci. U.S.A.* 107, 16518–16523. doi: 10.1073/pnas.1007940107

Modol, T., Brice, N., Ruiz de Galarreta, M., Garcia Garzon, A., Iraburu, M. J., Martínez–Irujo, J. J., et al. (2014). Fibronectin peptides as potential regulators of hepatic fibrosis through apoptosis of hepatic stellate cells. *J. Cell. Physiol.* 230, 546–553. doi: 10.1002/jcp.24714

Moeendarbary, E., and Harris, A. R. (2014). Cell mechanics: principles, practices, and prospects. *Wiley Interdiscip. Rev. Syst. Biol. Med.* 6, 371–388. doi: 10.1002/wsbm.1275

Mohammed, D., Charras, G., Vercruysse, E., Versaevel, M., Lantoine, J., Alaimo, L., et al. (2019). Substrate area confinement is a key determinant of cell velocity in collective migration. *Nat. Phys.* doi: 10.1038/s41567-019-0543-3

Morse, D. C. (1998). Viscoelasticity of concentrated isotropic solutions of semi-flexible polymers. 1. model and stress tensor; 2. linear response. *Macromolecules* 31, 7030–7044. doi: 10.1021/ma9803032

Murthy, S. E., Dubin, A. E., and Patapoutian, A. (2017). Piezos thrive under pressure: mechanically activated ion channels in health and disease. *Nat. Rev. Mol. Cell Biol.* 18, 771–783. doi: 10.1038/nrm.2017.92

Nagel, G., Ollig, D., Fuhrmann, M., Kateriya, S., Musti, A. M., Bamberg, E., et al. (2002). Channelrhodopsin-1: a light-gated proton channel in green algae. *Science* 296, 2395–2398. doi: 10.1126/science.1072068

Nagel, G., Szellas, T., Huhn, W., Kateriya, S., Adeishvili, N., Berthold, P., et al. (2003). Channelrhodopsin-2, a directly light-gated cation-selective membrane channel. *Proc. Natl. Acad. Sci. U.S.A.* 100, 13940–13945. doi: 10.1073/pnas.1936192100

Niland, S., Cremer, A., Fluck, J., Eble, J. A., Krieg, T., Sollberg, S., et al. (2001). Contraction-dependent apoptosis of normal dermal fibroblasts. *J. Invest. Dermatol.* 116, 686–692. doi: 10.1046/j.1523-1747.2001.01342.x

Nourse, J. L., and Pathak, M. M. (2017). How cells channel their stress: interplay between Piezo1 and the cytoskeleton. *Semin. Cell Dev. Biol.* 71, 3–12. doi: 10.1016/j.semcdb.2017.06.018

Parekh, S. H., Chaudhuri, O., Theriot, J. A., and Fletcher, D. A. (2005). Loading history determines the velocity of actin-network growth. *Nat. Cell Biol.* 7, 1219–1223. doi: 10.1038/ncb1336

Parker, K. K., Brock, A. L., Brangwynne, C., Mannix, R. J., Wang, N., Ostuni, E., et al. (2002). Directional control of lamellipodia extension by constraining cell shape and orienting cell tractional forces. *FASEB J.* 16, 1195–1204 doi: 10.1096/fj.02-0038com

Pathak, A., and Kumar, S. (2012). Independent regulation of tumor cell migration by matrix stiffness and confinement. *Proc. Natl. Acad. Sci. U.S.A.* 109, 10334–10339. doi: 10.1073/pnas.1118073109

Peng, A. W., Salles, F. T., Pan, B., and Ricci, A. J. (2011). Integrating the biophysical and molecular mechanisms of auditory hair cell mechanotransduction. *Nat. Commun.* 2:523. doi: 10.1038/ncomms1533

Plotnikov, S. V., Pasapera, A. M., Sabass, B., and Waterman, C. M. (2012). Force fluctuations within focal adhesions mediate ECM-rigidity sensing to guide directed cell migration. *Cell* 151, 1513–1527. doi: 10.1016/j.cell.2012.11.034

Polio, R., Rothenberg, K. E., Stamenovic, D., and Smith, M. L. (2012). A micropatterning and image processing approach to simplify measurement of cellular traction forces. *Acta Biomater.* 8, 82–88. doi: 10.1016/j.actbio.2011.08.013

Prass, M., Jacobson, K., Mogilner, A., and Radmacher, M. (2006). Direct measurement of the lamellipodial protrusive force in a migrating cell. *J. Cell Biol.* 174, 767–772. doi: 10.1083/jcb.200601159

Raab, M., Gentili, M., de Belly, H., Thiam, H. R., Vargas, P., Jimenez, A. J., et al. (2016). ESCRT III repairs nuclear envelope ruptures during cell migration to limit DNA damage and cell death. *Science* 352, 359–362. doi: 10.1126/science.aad7611

Riaz, M., Versaevel, M., Glinel, K., Mohammed, M., and Gabriele, S. (2016). Persistence of fan-shaped keratocytes is a matrix-rigidity-dependent mechanism that requires α5β1 integrin engagement. *Sci. Rep.* 6:34141. doi: 10.1038/srep34141

Roca-Cusachs, P., Conte, V., and Trepat, X. (2017). Quantifying forces in cell biology. *Nat. Cell Biol.* 19, 742–751. doi: 10.1038/ncb3564

Roca-Cusachs, P., del Rio, A., Puklin-Faucher, E., Gauthier, N. C., Biais, N., and Sheetz, M. P. (2013). Integrin-dependent force transmission to the extracellular matrix by α-actinin triggers adhesion maturation. *Proc. Natl. Acad. Sci. U.S.A.* 110, E1361–E1370. doi: 10.1073/pnas.1220723110

Roy, B., Venkatachalapathy, S., Ratna, P., Wang, Y., Jokhun, D. S., Nagarajan, M., et al. (2018). Laterally confined growth of cells induces nuclear reprogramming in the absence of exogenous biochemical factors. *Proc. Natl. Acad. Sci. U.S.A.* 115, E4741–E4750. doi: 10.1073/pnas.1714770115

Sabass, B., Gardel, M. L., Waterman, C. M., and Schwarz, U. S. (2008). High resolution traction force microscopy based on experimental and computational advances. *Biophys. J.* 94, 207–220. doi: 10.1529/biophysj.107.113670

Sarkar, R., and Rybenkov, V. V. (2016). A guide to magnetic tweezers and their application *Front. Phys.* 4:48. doi: 10.3389/fphy.2016.00048

Schwarz, U. S., and Soine, J. R. (2015). Traction force microscopy on soft elastic substrates: a guide to recent computational advances. *Biochim. Biophys. Acta* 1853, 3095–3104. doi: 10.1016/j.bbamcr.2015.05.028

Shao, Y., Mann, J. M., Chen, W., and Fu, J. (2014). Global architecture of the F-actin cytoskeleton regulates cell shape-dependent endothelial mechanotransduction. *Integr. Biol.* 6, 300–311. doi: 10.1039/c3ib40223a

Shimamoto, Y., Forth, S., and Kapoor, T. M., Measuring (2015). Pushing and braking forces generated by ensembles of Kinesin-5 crosslinking two microtubules. *Dev. Cell* 34, 669–681. doi: 10.1016/j.devcel.2015.08.017

Shivashankar, G. V. (2019). Mechanical regulation of genome architecture and cell-fate decision. *Curr. Opin. Cell Biol.* 56, 115–121. doi: 10.1016/j.ceb.2018.12.001

Sleep, J., Wilson, D., Simmons, R., and Gratzer, W. (1999). Elasticity of the red cell membrane and its relation to hemolytic disorders: an optical tweezers study. *Biophys. J.* 77, 3085–3095. doi: 10.1016/S0006-3495(99)77139-0

Solon, J., Levental, I., Sengupta, K., Georges, P. C., and Janmey, P. (2007). Fibroblast adaptation and stiffness matching to soft elastic substrates. *Biophys. J.* 93, 4453–4461. doi: 10.1529/biophysj.106.101386

Steinwachs, J., Metzner, C., Skodzek, K., Lang, N., Thievessen, I., Mark, C., et al. (2016). Three-dimensional force microscopy of cells in biopolymer networks. *Nat. Methods* 13, 171–176. doi: 10.1038/nmeth.3685

Stephens, A. D., Banigan, E. J., Adam, S. A., Goldman, R. D., and Marko, J. F. (2017). Chromatin and lamin A determine two different mechanical response regimes of the cell nucleus. *Mol. Biol. Cell.* 28, 1984–1996. doi: 10.1091/mbc.e16-09-0653

Swift, J., and Discher, D. E. (2014). The nuclear lamina is mechano-responsive to ECM elasticity in mature tissue. *J. Cell Sci.* 127, 3005–3015. doi: 10.1242/jcs.149203

Swift, J., Ivanovska, I. L., Buxboim, A., Harada, T., Dingal, P. C., Pinter, J., et al. (2013). Nuclear lamin-A scales with tissue stiffness and enhances matrix-directed differentiation. *Science* 341:1240104. doi: 10.1126/science.1240104

Tajik, A., Zhang, Y., Wei, F., Sun, J., Jia, Q., Zhou, W., et al. (2016). Transcription upregulation via force-induced direct stretching of chromatin. *Nat. Mater.* 15, 1287–1296. doi: 10.1038/nmat4729

Teixeira, A. I., Abrams, G. A., Bertics, P. J., Murphy, C. J., and Nealey, P. F. (2003). Epithelial contact guidance on well-defined micro- and nanostructured substrates. *J. Cell Sci.* 116, 1881–1892. doi: 10.1242/jcs.00383

Thery, M., Racine, V., Pepin, A., Piel, M., Chen, Y., Sibarita, J. B., et al. (2005). The extracellular matrix guides the orientation of the cell division axis. *Nat. Cell Biol.* 7, 947–953. doi: 10.1038/ncb1307

Tomatsu, I., Peng, K., and Kros, A. (2011). Photoresponsive hydrogels for biomedical applications. *Adv. Drug Delivery Rev.* 63, 1257–1266. doi: 10.1016/j.addr.2011.06.009

Trappman, B., Gautrot, J. E., Connelly, J. T., Strange, D. G. T., Yuan, L., Oyen, M. L., et al. (2012). Extracellular-matrix tethering regulates stem-cell fate. *Nat. Mater.* 11, 642–649. doi: 10.1038/nmat3339

Trepat, X., Wasserman, M. R., Angelini, T. E., Millet, E., Weitz, D. A., Butler, J. P., et al. (2009). Physical forces during collective cell migration. *Nat. Phys.* 5, 426–430. doi: 10.1038/nphys1269

Tsai, M. A., Frank, R. S., and Waugh, R. E. (1993). Passive mechanical behavior of human neutrophils: power-law fluid. *Biophys. J.* 65, 2078–2088. doi: 10.1016/S0006-3495(93)81238-4

Tseng, Q., Wang, I., Duchemin-Pelletier, E., Azioune, A., Carpi, N., Gao, J., et al. (2011). A new micropatterning method of soft substrates reveals that different tumorigenic signals can promote or reduce cell contraction levels. *Lab Chip* 11, 2231–2240. doi: 10.1039/c0lc00641f

Uhler, C., and Shivashankar, G. V. (2017). Regulation of genome organization and gene expression by nuclear mechanotransduction. *Nat. Rev. Mol. Cell Biol.* 18, 717–727. doi: 10.1038/nrm.2017.101

Valon, L., Marin-Llaurado, W., T., Charras, G., and Trepat, X. (2017). Optogenetic control of cellular forces and mechanotransduction. *Nat. Commun.* 8:14396. doi: 10.1038/ncomms14396

Versaevel, M., Braquenier, J. B., Riaz, M., Grevesse, T., Lantoine, J., and Gabriele, S. (2014a). Super-resolution microscopy reveals LINC complex recruitment at nuclear indentation sites. *Sci. Rep*. 4:7362. doi: 10.1038/srep07362

Versaevel, M., Grevesse, T., and Gabriele, S. (2012). Spatial coordination between cell and nuclear shape within micropatterned endothelial cells. *Nat. Commun.* 14:671. doi: 10.1038/ncomms1668

Versaevel, M., Grevesse, T., Riaz, M., Lantoine, J., and Gabriele, S. (2014b). Micropatterning Hydroxy-PAAm hydrogels and Sylgard 184 silicone elastomers with tunable elastic moduli. *Methods Cell Biol.* 121, 33–48. doi: 10.1016/B978-0-12-800281-0.00003-8

Versaevel, M., Riaz, M., Corne, T., Grevesse, T., Lantoine, J., Mohammed, D., et al. (2017). Probing cytoskeletal pre-stress and nuclear mechanics in endothelial cells with spatiotemporally controlled (de-)adhesion kinetics on micropatterned substrates. *Cell Adh. Migr.* 11, 98–109. doi: 10.1080/19336918.2016.1182290

Versaevel, M., Riaz, M., Grevesse, T., and Gabriele, S. (2013). Cell confinement: putting the squeeze on the nucleus. *Soft Matter* 9:6665. doi: 10.1039/c3sm00147d

Vining, K. H., Stafford, A., and Mooney, D. J. (2019). Sequential modes of crosslinking tune viscoelasticity of cell-instructive hydrogels. *Biomaterials* 188, 187–197. doi: 10.1016/j.biomaterials.2018.10.013

Vogel, V. (2018). Unraveling the mechanobiology of extracellular matrix. *Annu. Rev. Physiol.* 80, 353–387. doi: 10.1146/annurev-physiol-021317-121312

Wang, Y., Nagarajan, M., Uhler, C., and Shivashankar, G. V. (2017). Orientation and repositioning of chromosomes correlate with cell geometry-dependent gene expression. *Mol. Biol. Cell* 28, 1997–2009. doi: 10.1091/mbc.e16-12-0825

Wang, Y. L., and Discher, D. E. (2007). "Cell mechanics," in *Methods in Cell Biology*, Vol. 83 (New York, NY: Elsevier), 521–524. doi: 10.1016/S0091-679X(07)83026-3

Warmflash, A., Sorre, B., Etoc, F., Siggia, E. D., and Brivanlou, A. H. (2015). A method to recapitulate early embryonic spatial patterning in human embryonic stem cells. *Nat. Methods* 8, 847–854. doi: 10.1038/nmeth.3016

Whitesides, G. M., Ostuni, E., Takayama, S., Jiang, X., and Ingber, D. E. (2001). Soft lithography in biology and biochemistry. *Annu. Rev. Biomed. Eng.* 3, 335–373. doi: 10.1146/annurev.bioeng.3.1.335

Wilson, C. A., Tsuchida, M. A., Allen, G. M., Barnhart, E. L., Applegate, K. T., Yam, P. T., et al. (2010). Myosin II contributes to cell-scale actin network treadmilling through network disassembly. *Nature* 46, 373–379. doi: 10.1038/nature08994

Wirtz, D., Konstantopoulos, K., and Searson, P. C. (2011). The physics of cancer: the role of physical interactions and mechanical forces in metastasis. *Nat. Rev. Cancer* 11, 512–522. doi: 10.1038/nrc3080.

Xi, W., Sonam, S., Saw, T. B., Ladoux, B., and Lim, C. T. (2017). Emergent patterns of collective cell migration under tubular confinement. *Nat. Commun.* 8:1517. doi: 10.1038/s41467-017-01390-x

Xiaomeng, L., Qingqing, S., Qian, L., Naoki, K., and Guoping, C. (2018). Functional hydrogels with tunable structures and properties for tissue engineering applications. *Front. Chem.* 6:499. doi: 10.3389/fchem.2018.00499

Xue, X., Sun, Y., Resto-Irizarry, A. M., Yuan, Y., Yong, K. M. A., Zheng, Y., et al. (2018). Mechanics-guided embryonic patterning of neuroectoderm tissue from human pluripotent stem cells. *Nat. Mater.* 17, 633–641. doi: 10.1038/s41563-018-0082-9

Yareni, A. A., Pontes, B., Ether, D. S., Pires, L. B., Araujo, G. R., Frases, S., et al. (2016). Rheological properties of cells measured by optical tweezers *BMC Biophys.* 9:5. doi: 10.1186/s13628-016-0031-4

Zemelman, B. V., Nesnas, N., Lee, G. A., and Miesenböck, G. (2003). Photochemical gating of heterologous ion channels: remote control over genetically designated populations of neurons. *Proc. Natl. Acad. Sci. U.S.A.* 100, 1352–1357. doi: 10.1073/pnas.242738899

Zhang, X., Liu, M., Li, Y., Dong, Y., Pingguan-Murphy, B., Lu, T. J., et al. (2015). Engineering cell microenvironment using novel functional hydrogels. *Eur. Polym. J.* 72, 590–601. doi: 10.1016/j.eurpolymj.2015.03.019

Zhang, Y., Ge, C., Zhu, C., and Salaita, K. (2014). DNA-based digital tension probes reveal integrin forces during early cell adhesion. *Nat. Commun.* 5:5167. doi: 10.1038/ncomms6167

Zhao, B., O'Brien, C., Karunanayake Mudiyanselage, A. P. K. K., Li, N., Bagheri, Y., Wu, R., et al. (2017). Visualizing Intercellular Tensile Forces by DNA-based membrane molecular probes. *J. Am. Chem. Soc.* 139, 18182–18185. doi: 10.1021/jacs.7b11176

Zhelev, D. V., Needham, D., and Hochmuth, R. M. (1994). Role of the membrane cortex in neutrophil deformation in small pipets. *Biophys. J.* 67, 696–705. doi: 10.1016/S0006-3495(94)80529-6

Zhou, L., Cai, M., Tong, T., and Wang, H. (2017). Progress in the correlative atomic force microscopy and optical microscopy. *Sensors* 17:938. doi: 10.3390/s17040938

Conflict of Interest Statement: The authors declare that the research was conducted in the absence of any commercial or financial relationships that could be construed as a potential conflict of interest.

Advantages of publishing in Frontiers

OPEN ACCESS
Articles are free to read for greatest visibility and readership

FAST PUBLICATION
Around 90 days from submission to decision

HIGH QUALITY PEER-REVIEW
Rigorous, collaborative, and constructive peer-review

TRANSPARENT PEER-REVIEW
Editors and reviewers acknowledged by name on published articles

Frontiers
Avenue du Tribunal-Fédéral 34
1005 Lausanne | Switzerland

Visit us: www.frontiersin.org
Contact us: info@frontiersin.org | +41 21 510 17 00

REPRODUCIBILITY OF RESEARCH
Support open data and methods to enhance research reproducibility

DIGITAL PUBLISHING
Articles designed for optimal readership across devices

FOLLOW US
@frontiersin

IMPACT METRICS
Advanced article metrics track visibility across digital media

EXTENSIVE PROMOTION
Marketing and promotion of impactful research

LOOP RESEARCH NETWORK
Our network increases your article's readership